IMAGING IN THE VISUAL SYSTEM DISORDERS

EDITED BY: Dehui Xiang, Haoyu Chen, Vishal Jhanji and Jian Zheng
PUBLISHED IN: Frontiers in Neuroscience and Frontiers in Psychology

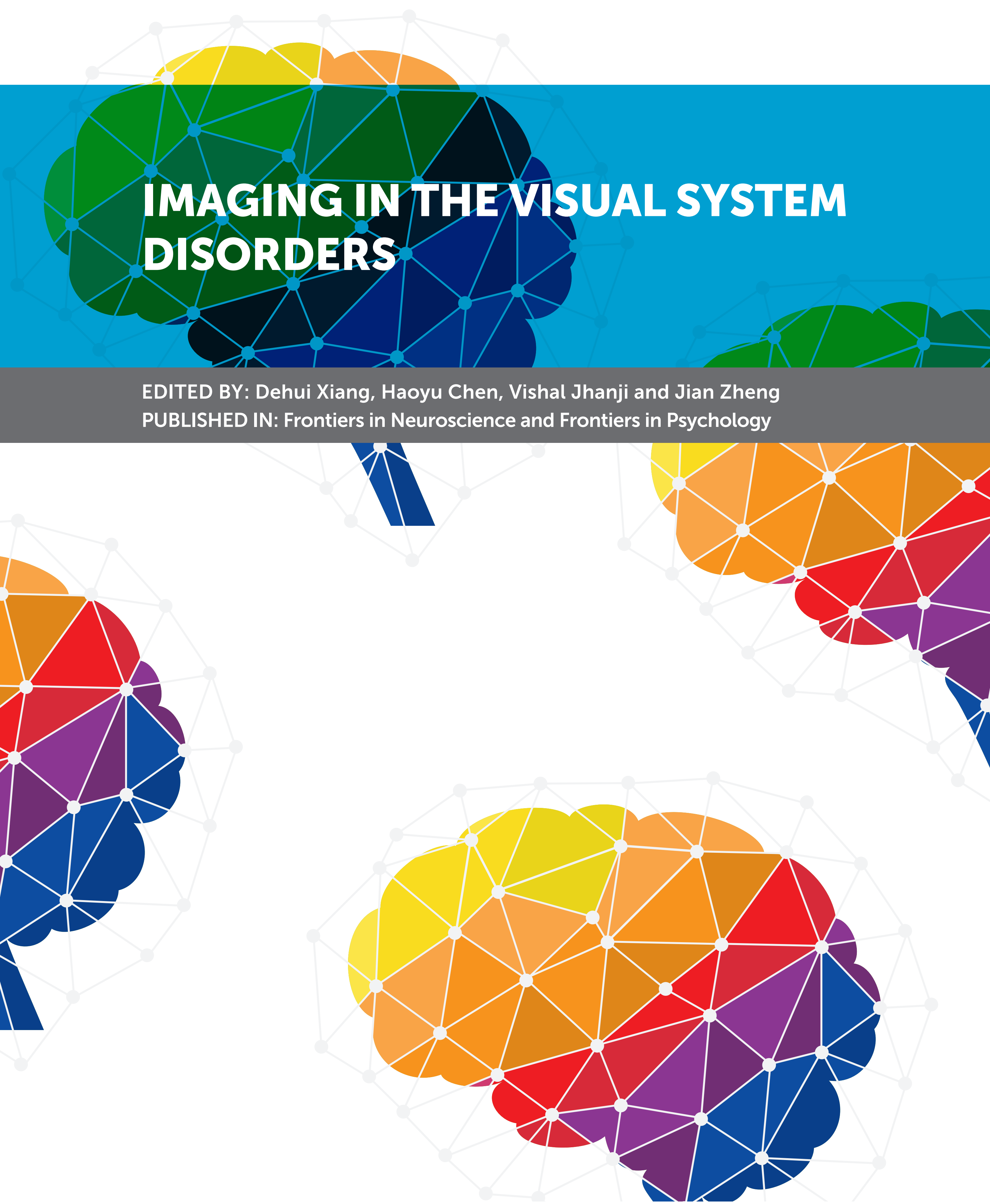

frontiers Research Topics

ISSN 1664-8714
ISBN 978-2-88976-812-7
DOI 10.3389/978-2-88976-812-7

About Frontiers

Frontiers is more than just an open-access publisher of scholarly articles: it is a pioneering approach to the world of academia, radically improving the way scholarly research is managed. The grand vision of Frontiers is a world where all people have an equal opportunity to seek, share and generate knowledge. Frontiers provides immediate and permanent online open access to all its publications, but this alone is not enough to realize our grand goals.

Frontiers Journal Series

The Frontiers Journal Series is a multi-tier and interdisciplinary set of open-access, online journals, promising a paradigm shift from the current review, selection and dissemination processes in academic publishing. All Frontiers journals are driven by researchers for researchers; therefore, they constitute a service to the scholarly community. At the same time, the Frontiers Journal Series operates on a revolutionary invention, the tiered publishing system, initially addressing specific communities of scholars, and gradually climbing up to broader public understanding, thus serving the interests of the lay society, too.

Dedication to Quality

Each Frontiers article is a landmark of the highest quality, thanks to genuinely collaborative interactions between authors and review editors, who include some of the world's best academicians. Research must be certified by peers before entering a stream of knowledge that may eventually reach the public - and shape society; therefore, Frontiers only applies the most rigorous and unbiased reviews.
Frontiers revolutionizes research publishing by freely delivering the most outstanding research, evaluated with no bias from both the academic and social point of view. By applying the most advanced information technologies, Frontiers is catapulting scholarly publishing into a new generation.

What are Frontiers Research Topics?

Frontiers Research Topics are very popular trademarks of the Frontiers Journals Series: they are collections of at least ten articles, all centered on a particular subject. With their unique mix of varied contributions from Original Research to Review Articles, Frontiers Research Topics unify the most influential researchers, the latest key findings and historical advances in a hot research area! Find out more on how to host your own Frontiers Research Topic or contribute to one as an author by contacting the Frontiers Editorial Office: frontiersin.org/about/contact

IMAGING IN THE VISUAL SYSTEM DISORDERS

Topic Editors:
Dehui Xiang, Soochow University, China
Haoyu Chen, Shantou University & the Chinese University of Hong Kong, China
Vishal Jhanji, University of Pittsburgh, United States
Jian Zheng, Suzhou Institute of Biomedical Engineering and Technology, Chinese Academy of Sciences (CAS), China

Citation: Xiang, D., Chen, H., Jhanji, V., Zheng, J., eds. (2022). Imaging in the Visual System Disorders. Lausanne: Frontiers Media SA.
doi: 10.3389/978-2-88976-812-7

Table of Contents

frontiers | Frontiers in Neuroscience

EDITORIAL
published: 30 May 2022
doi: 10.3389/fnins.2022.904854

Editorial: Imaging in the Visual System Disorders

Dehui Xiang[1], *Haoyu Chen*[2*], *Jian Zheng*[3] *and Vishal Jhanji*[4]

[1] School of Electronics and Information Engineering, Soochow University, Suzhou, China, [2] Joint Shantou International Eye Center, Shantou University and the Chinese University of Hong Kong, Shantou, China, [3] Department of Medical Imaging, Suzhou Institute of Biomedical Engineering and Technology, Chinese Academy of Sciences, Suzhou, China, [4] Department of Ophthalmology, University of Pittsburgh, Pittsburgh, PA, United States

Keywords: visual system, medical imaging, deep learning, eye disease, ophthalmology

Editorial on the Research Topic

Imaging in the Visual System Disorders

More than 80% of the information we need to perceive the world is delivered by vision. According to the World Health Organization World Report on Vision 2019, there are at least 2.2 billion visually impaired people worldwide, with at least 1 billion possessing a vision impairment that should have been prevented or that is yet to be tackled (World Health Organization, 2019). Visual disorders place significant economic burdens on the patients, their families, and the healthcare system. The diseases of the eye, optic nerve, and brain may cause vision impairment. Early detection and diagnosis of these pathologies would enable clinicians to forestall visual loss.

Imaging is an important technique for diagnosing these diseases (Chen et al., 2019). In the past decades, advances in imaging techniques have provided us tools to improve our understanding of visual system disorders, and facilitate the diagnosis and management of patients with visual system disorders. However, there are still considerable challenges in the field of imaging in visual system disorders, such as precise segmentation of lesions on images, lack of sizeable labeled datasets, correlation of novel imaging biomarkers with clinical diagnosis or management, and correlation of ocular imaging biomarkers with central nervous system disorders or parameters.

An interdisciplinary Research Topic was hosted by the Perception Science section of Frontiers in Neuroscience to cover recent advances in various imaging techniques in diagnosis and management of visual system disorders. In this issue, we aim to address some of these issues surrounding different imaging modalities in visual disorders.

Classification and segmentation of structures and lesions remain challenging for ocular imaging. Recently, artificial intelligence (AI) has dramatically advanced various medical research fields, including imaging segmentation and classification. Numerous deep learning-based ophthalmological image processing algorithms have been proposed to analyze optical coherence tomography (OCT) images, optical coherence tomography angiography (OCTA) images, fundus photographs, and fluorescein staining slit-lamp images. Wang, L. et al. proposed a dynamic multi-hierarchical weighting segmentation network (DW-Net) for the simultaneous segmentation of retinal layers and choroid neovascularization in retinal OCT images. The proposed network was composed of a residual aggregation encoder path to select informative features, a multi-hierarchical weighting connection for the fusion of detailed information and abstract information, and a dynamic decoder path. Their method achieved DICE scores of 0.9484 and 0.9538 for the segmentation of choroidal neovascularization and seven retinal layers, respectively. Wan et al. proposed an optimized Unet to segment parapapillary atrophy in color fundus photos. An edge attention module and a reverse attention module were fused into the UNet (Ronneberger et al., 2015), such that their method achieved a high area under curve (AUC) of 0.9235 over the original

Edited and reviewed by:
Rufin VanRullen,
Centre National de la Recherche
Scientifique (CNRS), France

****Correspondence:***
Haoyu Chen
drchenhaoyu@gmail.com

Specialty section:
This article was submitted to
Perception Science,
a section of the journal
Frontiers in Neuroscience

Received: *26 March 2022*
Accepted: *13 April 2022*
Published: *30 May 2022*

Citation:
Xiang D, Chen H, Zheng J and
Jhanji V (2022) Editorial: Imaging in
the Visual System Disorders.
Front. Neurosci. 16:904854.
doi: 10.3389/fnins.2022.904854

UNet of 0.7917. The proposed method worked better for large parapapillary atrophy than small parapapillary atrophy. Xu et al. implemented and investigated the application of a deep learning system based on EfficientNet-B6 in diagnosing pterygium using anterior segment photographs. Their system can judge the presence of pterygium and classify the severity of pterygium. The accuracy of the system was 0.9468.

In the AI-based medical image processing field, it is expensive and time-consuming to obtain the labels of medical data. Therefore, it is advisable to utilize unlabeled data to improve the performance of the algorithms. Meng et al. proposed a multi-scale information fusion network (MF-Net) to segment choroidal neovascularization in retinal OCT images. Their method was evaluated with 1,522 labeled OCT images with choroidal neovascularization and the DICE score was 0.9290. Furthermore, they used a semi-supervised MF-Net with pseudo labels for unlabeled data which improved the DICE score to 0.9307. Wang, T. et al. proposed a semi-supervised multi-scale self-transformer generative adversarial network (Semi-MsST-GAN), which can improve corneal ulcer segmentation in fluorescein staining slit-lamp images by leveraging unlabeled images. Their method achieved a DICE of 0.9093 in evaluating the public SUSTech-SYSU dataset.

This special issue also highlighted a few novel parameters in ocular imaging. Dong et al. used a deep learning-based algorithm for the segmentation of corneal and epithelial thickness on anterior segment-OCT with 1,430 images and characterized the epithelial and corneal thickness changes at different stages of the keratoconus progression. They identified that both epithelial and corneal thickness decreased with the progression of keratoconus, except the epithelial thickness in the scarring stage, which had irregular fluctuation. Ye et al. found that on OCTA, radial peripapillary capillary density, but not peripapillary retinal nerve fiber layer thickness, decreased in pathological myopia compared to simple myopia. Peripapillary capillary density showed the highest AUC for pathological myopia (AUC = 0.962). Furthermore, the best-corrected visual acuity was affected by peripapillary capillary density, axial length, and their interaction.

The eye is a window for the brain and vascular system. Many systemic diseases such as diabetes, cerebral vascular diseases, cardiovascular diseases, and Parkinson's disease may be investigated from ocular parameters (Abràmoff et al., 2010). Zhang et al. used retinal photography and cerebral magnetic resonance imaging (MRI) to evaluate the correlation between retinal microvascular abnormalities in patients with type 2 diabetes and the presence of cerebral small vessel lesions. They found that the degree of diabetic retinopathy and retinal arteriole and venule calibers were associated with MRI burden of cerebral small vessel disease. Zhao et al. used a context encoder network to segment outer retinal layers on OCT images and found that subjects with white matter hyperintensities had a thinner Henle fiber layer, outer nuclear layers, and photoreceptor outer segments, while Parkinson's disease patients had a thicker interdigitation zone and retinal pigment epithelium. Zhou et al. used OCTA and visual evoked potential to study the retinal changes in Parkinson's disease. They found that macular vessel density, but not ganglion cell-inner plexiform layer thickness or the retinal nerve fiber layer decreased in Parkinson's disease. Macular vessel density was also correlated with visual evoked potential. They suggested that retinal microvasculature change may be a biomarker for early diagnosis of Parkinson's disease.

With the development of imaging engineering techniques and the collaboration between clinicians and engineering scientists, we would be able to develop more automatic and precise techniques, which can help clinicians to diagnose and manage patients with visual system disorders, and benefit the patients.

AUTHOR CONTRIBUTIONS

DX conceived the idea. HC, JZ, and VJ critically reviewed the manuscript and revised the paper. All authors contributed to the article and approved the submitted version.

FUNDING

This work was supported in part by the National Nature Science Foundation of China (61971298, 61771326, and 81871352) by the Suzhou Science and Technology Bureau under Grant SJC2021023, and by the National Key R&D Program of China (2018YFA0701700).

REFERENCES

Abràmoff, M. D., Garvin, M. K., and Sonka, M. (2010). Retinal imaging and image analysis. *IEEE Rev. Biomed. Eng.* 3, 169–208. doi: 10.1109/RBME.2010.2084567

Chen, X., Shi, F., and Chen, H., (Eds.). (2019). *Retinal Optical Coherence Tomography Image Analysis*. Singapore: Springer Singapore.

Ronneberger, O., Fischer, P., and Brox, T. (2015). "U-net: convolutional networks for biomedical image segmentation," in *International Conference on Medical Image Computing and Computer-Assisted Intervention* (Cham: Springer), 234–241.

World Health Organization (2019). *World Report on Vision*. Geneva.

Conflict of Interest: The authors declare that the research was conducted in the absence of any commercial or financial relationships that could be construed as a potential conflict of interest.

frontiers
in Neuroscience

ORIGINAL RESEARCH
published: 12 August 2021
doi: 10.3389/fnins.2021.718820

Visual Impairments Are Associated With Retinal Microvascular Density in Patients With Parkinson's Disease

Min Zhou[1†], Lei Wu[2†], Qinyuan Hu[1], Congyao Wang[1], Jiacheng Ye[1], Tingting Chen[1] and Pengxia Wan[1]*

[1] Department of Ophthalmology, The First Affiliated Hospital, Sun Yat-sen University, Guangzhou, China, [2] Department of Neurology, The First Affiliated Hospital, Sun Yat-sen University, Guangzhou, China

Objective: This study aimed to evaluate retinal microvascular density in patients with Parkinson's disease (PD) and its correlation with visual impairment.

Methods: This cross-sectional study included 24 eyes of 24 patients with PD and 23 eyes of 23 healthy controls. All participants underwent ophthalmic examination, visual evoked potential (VEP) test, 25-item National Eye Institute Visual Function Questionnaire (NEI VFQ-25), and optical coherence tomography angiography (OCTA) examination. The correlation between retinal microvascular density and visual parameter was evaluated using Spearman correlation analysis, and the area under receiver operating characteristic curve (AUROC) was calculated.

Results: Parkinson's disease patients had prolonged P100 latency ($P = 0.041$), worse vision-related quality of life (composite score and 3 of 12 subscales in NEI VFQ-25), and decreased vessel density (VD) in all sectors of 3-mm-diameter region (all $P < 0.05$) compared with healthy controls. There were no statistical differences in the ganglion cell-inner plexiform layer (GCIPL) thickness and retinal nerve fiber layer (RNFL) thickness between the two groups. A negative correlation was found between P100 latency and nasal and superior sectors of macular VD in a 3-mm-diameter region ($r = -0.328$, $P = 0.030$; $r = -0.302$, and $P = 0.047$, respectively). Macular VD in a 3-mm-diameter region showed diagnostic capacities to distinguish PD patients from healthy controls (AUROCs, ranging from 0.655 to 0.723).

Conclusion: This study demonstrated that decreased retinal microvascular density was correlated with visual impairment in PD patients. Retinal microvasculature change may occur earlier than visual decline and retinal structure change and has the potential to be a promising diagnostic marker for early PD.

Keywords: visual impairment, retinal microvascular density, Parkinson's disease, optical coherence tomography angiography, visual evoked potential

Edited by:
Haoyu Chen,
Shantou University, The Chinese University of Hong Kong, China

Reviewed by:
Kazuyuki Hirooka,
Hiroshima University, Japan
Chunxin Liu,
Third Affiliated Hospital of Sun Yat-sen University, China

Correspondence:
Pengxia Wan
wanpengx@mail.sysu.edu.cn

†These authors share first authorship

Specialty section:
This article was submitted to Perception Science, a section of the journal Frontiers in Neuroscience

Received: *01 June 2021*
Accepted: *14 July 2021*
Published: *12 August 2021*

Citation:
Zhou M, Wu L, Hu Q, Wang C, Ye J, Chen T and Wan P (2021) Visual Impairments Are Associated With Retinal Microvascular Density in Patients With Parkinson's Disease. Front. Neurosci. 15:718820. doi: 10.3389/fnins.2021.718820

Abbreviations: PD, Parkinson's disease; CNS, central nervous system; OCTA, optical coherence tomography angiography; OCT, optical coherence tomography; VEP, visual evoked potential; MMSE, Mini-Mental State Examination; UPDRS III, Unified Parkinson's Disease Rating Scale III; H&Y, Hoehn and Yahr; BCVA, best-corrected visual acuity; IOP, intraocular pressure; NEI VFQ-25, 25-item National Eye Institute Visual Function Questionnaire; ONH, optic nerve head; VD, vessel density; SCP, superficial capillary plexus; FAZ, foveal avascular zone; CST, central subfield thickness; GCIPL, ganglion cell-inner plexiform layer; RNFL, retinal nerve fiber layer; SD, standard deviation; IQR, interquartile range; AUROC, the area under receiver operating characteristic curve; LogMAR, logarithm of the minimum angle of resolution.

INTRODUCTION

Parkinson's disease (PD) is the second most common neurodegenerative disease characterized by a wide range of motor and non-motor symptoms (Lee and Gilbert, 2016). Visual symptoms together with other non-motor disorders such as cognitive deficits, hyposmia, and gastrointestinal dysfunctions were widely recognized to affect the life quality of PD patients and may occur several years before the onset of cardinal motor signs (Berg et al., 2015; Mahlknecht et al., 2015). Studies have reported as high as 78% of PD patients had at least one visual symptom, such as reading difficulties, double vision, and misjudgment of objects and distances (Archibald et al., 2011; Urwyler et al., 2014). The impact of visual disorders is particularly annoying for patients with PD, because they have impairments in control of movement and postural stability, and which could be compensated through visual guidance (Azulay et al., 1999; Davidsdottir et al., 2005).

The underlying pathogenesis of these visual disorders is regarded as relevant with α-synuclein deposition (Bodis-Wollner et al., 2014) and dopamine deficiency (Harnois and Di Paolo, 1990) in the retina, and similar to the pathological features of PD in the brain. Recently, vessel degeneration has been considered to be an additional factor contributing to the progression of PD. In postmortem brain tissue of PD patients, capillaries were shorter in average length, were less in number, and had fewer branches those in age-matched controls (Guan et al., 2013). And decreased cerebral blood flow has also been found in non-demented patients with PD, suggesting that perfusion abnormality may be a potential predictor upstream of cognitive impairment and neurodegeneration (Syrimi et al., 2017). However, the detections for brain vasculature are expensive and time-consuming. As a constituent of the central nervous system (CNS), the retina shows a striking resemblance to the brain and spinal cord. The cellular and molecular mechanisms implicated in retinal neurodegenerative processes are similar to those in the CNS (London et al., 2013; Maresca et al., 2013).

Therefore, the retina can serve as a window to observe microcirculation in the brain. Optical coherence tomography angiography (OCTA) is a functional extension of optical coherence tomography (OCT) imaging that facilitates the visualization of microvascular and morphological structure non-invasively in the retina (Spaide et al., 2018). Recently, several research findings described the decreased retinal microvascular density in patients with PD, which can serve as a surrogate biomarker for the diagnosis of PD (Kwapong et al., 2018; Zou et al., 2020). However, studies focusing on whether altered retinal microvasculature affects visual function were scarce.

Thus, the aim of our study was to determine the microvasculature alterations in the retina and its relationship with visual function in patients with PD.

MATERIALS AND METHODS

Participants

The protocol of this study was approved by the Ethics Committee of the First Affiliated Hospital of Sun Yat-sen University. Participants provided informed written consent, and the tenets of the Declaration of Helsinki were followed throughout. Consecutive patients were recruited from the neurology outpatient clinic of the First Affiliated Hospital of Sun Yat-sen University, and healthy subjects were recruited from the patients' non-consanguineous families or friends *via* asking for their willingness to participate. Idiopathic PD was defined by an experienced neurologist based on the United Kingdom Brain Bank criteria (Reichmann, 2010), and medical records including the duration of disease and treatment were carefully collected. Eligible patients were aged 40 years or older and only received drug treatment without any surgical intervention (e.g., deep brain stimulation treatment). The exclusion criteria were as follows: patients with psychiatric or neurological diseases other than PD, such as dementia or multiple sclerosis; diabetes, uncontrolled hypertension, or other systemic diseases which could affect the visual system; history of ocular trauma or surgery; family history of glaucoma; high refractive error (± 6.00D spherical equivalent); intraocular pressure (IOP) > 21 mmHg; media opacifications; concomitant ocular diseases such as corneal disease, glaucoma, or retinal disease. After preliminary screening, patients were asked to refrain from drug administration the night before, and on the day of examination. Each participant was first scored clinically and neuropsychologically by the neurologist and subsequently examined by the ophthalmologists using visual evoked potential (VEP), and OCTA. Clinicians were blind to each other's results during the assessment.

Neuropsychological and Clinical Assessments

All patients were evaluated for cognitive function and disease severity by the same experienced neurologist (LW). Cognitive function was assessed using the Mini-Mental State Examination (MMSE). MMSE is a 30-point questionnaire that assesses orientation, memory, attention, language, and visuospatial ability, and scores < 27 points are indicative of likely cognitive impairment (Folstein et al., 1975). Disease severity was evaluated using the Unified Parkinson's Disease Rating Scale III (UPDRS III) (Goetz et al., 2008) and Hoehn and Yahr (1967) [H&Y] stage. Patients were assessed in the "off" state before the regular dose of the drug.

Ophthalmologic Examination

All participants received a complete ophthalmic examination, including best-corrected visual acuity (BCVA), IOP, and examination of the anterior segment, and fundus by an experienced ophthalmologist. Vision-related quality of life was assessed using the 25-item National Eye Institute Visual Function Questionnaire (NEI VFQ-25). After the NEI VFQ-25 was administered, scores were recorded according to the guideline provided. Scores range from 0 to 100, with higher scores indicating better visual function (Mangione et al., 2001). All subjects were evaluated with VEP (MKWHAMD, CN-V1.4, Huzhou Medconova Medical Technology Co., Ltd., Huzhou, China) in a dark and quiet room. Stimulation was monocular after covering the other eye, and visual stimuli followed a checkerboard pattern.

Optical Coherence Tomography Angiography

The imaging of all subjects was performed using the Zeiss Cirrus HD-OCT 5000 with an AngioPlex OCTA instrument (Cirrus; Zeiss, Dublin, CA, United States). A standard 3 × 3 mm scan was performed centered on the fovea, while the 6 × 6 mm scan was performed centered on the optic nerve head (ONH) as well as fovea. Vessel density (VD) (defined as the total length of the perfused vasculature per unit area in the region of measurement) of the superficial capillary plexus (SCP) (from the layer of the inner limiting membrane to the inner plexiform layer) was measured automatically in all 3 × 3 mm and 6 × 6 mm scans. Images of VD were calculated separately at various distances from the fovea: central (1-mm-diameter region), inner ring (1–3-mm-diameter region), outer ring (3–6-mm-diameter region), and full area (6-mm-diameter region). Furthermore, inner-ring and outer-ring regions were divided into four quadrants. The foveal avascular zone (FAZ) was assessed automatically in the 3 × 3 mm scan. The central subfield thickness (CST) (from the layer of the inner limiting membrane to the retinal pigment epithelium at the fovea) and ganglion cell-inner plexiform layer (GCIPL) thickness were measured using a macular cube 512 × 128 scan. Peripapillary retinal nerve fiber layer (RNFL) thickness was measured using an optic disk cube 200 × 200 scan. All scans were performed by the same experienced examiner (MZ). All of the scan images were reviewed by an experienced ophthalmologist (CW) for further quality control with the following exclusion criteria: (1) poor scan quality (less than 7/10 signal strength index); (2) motion artifacts; (3) inaccurate segmentation; (4) focal signal loss; and (5) blurred images.

Images were analyzed automatically using the AngioPlex OCTA software (version 10.0.0.14618, Carl Zeiss Meditec). Moreover, the FAZ boundaries were carefully reviewed and manually corrected if an obvious error of automated segmentation is observed.

Data Analysis

One eye with a higher-quality image on the 3 × 3 mm OCTA scan from each subject was selected for the analyses. All data were analyzed using the SPSS 22.0 statistical software package (SPSS, Armonk, NY, United States).

Quantitative variables were described as mean (SD, standard deviation) or median (IOR, interquartile range), while categorical variables were described using frequencies and percentages. The *t*-test was used to evaluate normally distributed data. For non-normally distributed data, we used the Mann–Whitney *U*-test. Correlations between OCTA parameters and other clinical features were evaluated using Spearman correlation analysis. $P < 0.05$ was accepted as statistically different. The area under the receiver operating characteristic curve (AUROC) was calculated to determine the diagnostic accuracy of the analyzed parameters discriminating between PD patients and healthy controls.

RESULTS

Clinical Characteristics of Enrolled Patients and Healthy Controls

A total of 39 patients with a definite diagnosis of idiopathic PD and 30 healthy controls were recruited from the Neurology Department of the First Affiliated Hospital of Sun Yat-sen University between October 2019 and November 2020. After the ophthalmic assessment, seven PD patients and four controls expired, due to concomitant ocular diseases or non-cooperation. Eight patients and three controls were excluded because of insufficient image quality. **Figure 1** details the reasons for exclusion from statistical analyses. Ultimately, 24 patients (24 eyes) and 23 controls (23 eyes) were included in the analyses. The PD patients had a mean age of 65.88 years, and 75.0% were male. The healthy controls had a mean age of 63.43 years, and 47.8% were male. There was no significant difference between PD patients and controls with regard to age, and sex. The mean disease duration of PD patients was 5.3 years, and the mean score of UPDRS III was 26.5. The demographics of PD patients and controls are summarized in **Table 1**.

Visual Function of Enrolled Patients and Healthy Controls

There were no significant differences in BCVA and IOP between PD patients and healthy controls. Compared with healthy controls, P100 latency was significantly longer in patients with PD (113.3 ± 14.7 ms vs. 107.6 ± 12.6 ms, $P = 0.041$), whereas P100 amplitude was not significantly different between the two groups (**Table 2**). The NEI VFQ-25 scores were significantly worse in PD patients for the composite score (80 ± 10 vs. 84 ± 13, $P = 0.031$) and 3 of 12 subscales, including general health (29 ± 16 vs. 52 ± 20, $P < 0.001$), near vision (71 ± 17 vs. 80 ± 22, $P = 0.037$), and role limitations (68 ± 27 vs. 87 ± 19, $P = 0.008$) (**Figure 2**). The correlations between the general health subscale and other subscales of NEI VFQ-25 were undertaken in order to analyze whether the general health status of PD had an impact on the vision-related quality-of-life assessments. No correlation was found between the general health subscale and other subscales in NEI VFQ-25.

Macular and Peripapillary Microvascular Density Parameters

Parkinson's disease patients had significantly lower macular VD than healthy controls in the inner superior sector (13.6 ± 4.1 mm vs. 15.6 ± 3.9 mm^{-1}, $P = 0.030$) of the 6-mm-diameter region (**Figures 3A,C** and **Supplementary Table 1**). Health controls had higher signal strength than PD patients in the 6 × 6 mm scan centered on the macular (8.7 ± 1.0 vs. 7.7 ± 1.1, $P = 0.008$). In the 6-mm-diameter region centered on the ONH, the peripapillary VD in the outer superior sector (16.9 ± 2.2 mm^{-1} vs. 18.6 ± 1.4 mm^{-1}, $P = 0.003$) of PD patients was significantly lower than those of controls, while the differences in other regions were not statistically significant (**Supplementary Table 2**). In the 3-mm-diameter region, macular VD was significantly decreased in all sectors in PD patients compared with healthy controls

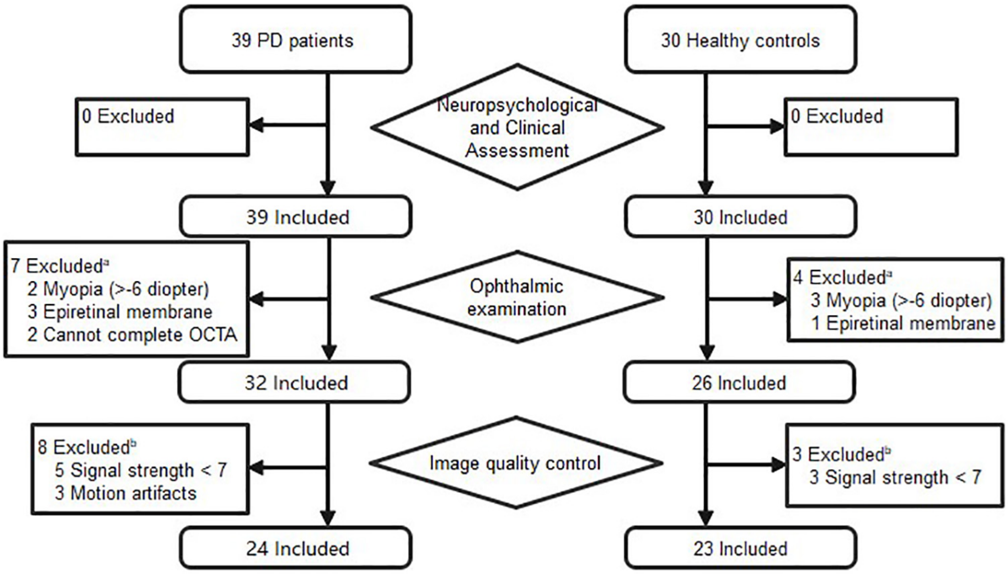

FIGURE 1 | Flow diagram of excluded subjects prior to analysis. [a]Patients were excluded if one eye had concomitant ocular diseases. [b]Patients were included if one eye's images met the inclusion criteria.

(full area: 16.0 ± 3.0 mm^{-1} vs. 18.0 ± 2.0 mm^{-1}, $P = 0.010$) (**Figures 3B,D** and **Table 3**). The signal strength between the two groups was not significantly different in the 3 × 3 mm scan centered on the macular or the 6 × 6 mm scan centered on the ONH (all $P > 0.05$). No significant difference was seen in the FAZ area between the two groups (0.31 ± 0.10 mm^2 vs. 0.28 ± 0.10 mm^2, $P = 0.464$).

CST, RNFL, and GCIPL Thicknesses

The differences between the RNFL thickness (average: 93.4 ± 10.7 μm vs. 98.0 ± 9.4 μm, $P = 0.128$) and CST (average: 272.8 ± 10.3 μm vs. 274.7 ± 11.0 μm, $P = 0.534$) of the two groups were not statistically significant (**Supplementary Tables 3, 4**). No significant thinning was shown in the GCIPL thickness of PD patients when compared with the healthy controls (average: 80.5 ± 5.6 μm vs. 82.3 ± 6.2 μm, $P = 0.303$) (**Supplementary Table 5**).

TABLE 1 | Demographic characteristics of all enrolled participants.

Variable	Mean (SD)		
	PD	**HC**	***P***
	***N* = 24**	***N* = 23**	
Age (year)	65.88 (6.50)	63.43 (7.11)	0.225
Male sex, No. (%)	18/24 (75.0)	11/23 (47.8)	0.055
PD history (year)	5.3 (4.2)	/	/
UPDRS III rating	26.5 (12.3)	/	/
H&Y rating	2.0 (0.3)	/	/
MMSE	28.5 (1.6)	/	/

PD, Parkinson's disease; HC, healthy controls; UPDRS III, Unified Parkinson's Disease Rating Scale III; H&Y, Hoehn and Yahr; MMSE, Mini-Mental State Examination.

Correlations Among Visual Function and Disease Duration, Severity, and Cognition in PD Patients

A significant negative correlation was shown between disease severity using the UPDRS III and composite scores of NEI VFQ-25 ($r = -0.587$, $P = 0.005$). The BCVA, VEP P100 latency, and amplitude were not statistically associated with disease duration, severity, and MMSE scores. Spearman correlation coefficients and their corresponding *P*-values are listed in **Table 4**.

Correlations Between Microvascular Density and Clinical Data in PD Patients

The nasal sector and inner ring of macular VD were negatively correlated with disease duration ($r = -0.442$, $P = 0.035$; $r = -0.431$, and $P = 0.040$; respectively), while no significant correlation between disease severity and cognitive function and macular VD of 3-mm-diameter region in PD group (**Supplementary Table 6**). P100 latency was negatively correlated with the nasal and superior sectors of macular VD in 3-mm-diameter region ($r = -0.328$, $P = 0.030$; $r = -0.302$, and $P = 0.047$, respectively). There was no significant correlation between visual function parameters and other regions of macular VD in the 3-mm-diameter region (**Table 5**).

Diagnostic Abilities of Macular Microvascular Density Indices

The AUROCs of macular VD in the 3-mm-diameter region for discriminating PD patients from healthy controls were highest for the temporal sector (0.723), followed by the full

TABLE 2 | Ophthalmologic and VEP information of all enrolled participants.

Variable	**PD (*N* = 24)**		**HC (*N* = 23)**		***P***
	Mean (SD)	**Median (range)**	**Mean (SD)**	**Median (range)**	
BCVA (LogMAR)	0.088 (0.122)	0.000 (0.000–0.191)	0.097 (0.117)	0.097 (0.000–0.097)	0.591
IOP (mmHg)	14.7 (2.4)	14 (13–16)	15.6 (2.8)	16 (13–17)	0.287
P100 latency (ms)	113.3 (14.7)	113.0 (106.0–116.5)	107.6 (12.6)	105.0 (101.5–110.5)	0.041[a]
P100 amplitude (μV)	6.6 (5.1)	5.5 (3.4–8.6)	5.6 (3.9)	4.7 (3.1–7.7)	0.597
NEI VFQ-25 composite score	80 (10)	79 (76–88)	84 (13)	89 (81–93)	0.031[a]

VEP, visual evoked potential; PD, Parkinson's disease; HC, healthy controls; BCVA, best-corrected visual acuity; LogMAR, logarithm of the minimum angle of resolution; IOP, intraocular pressure; NEI VFQ-25, 25-item National Eye Institute Visual Function Questionnaire.

[a]*$P < 0.05$.*

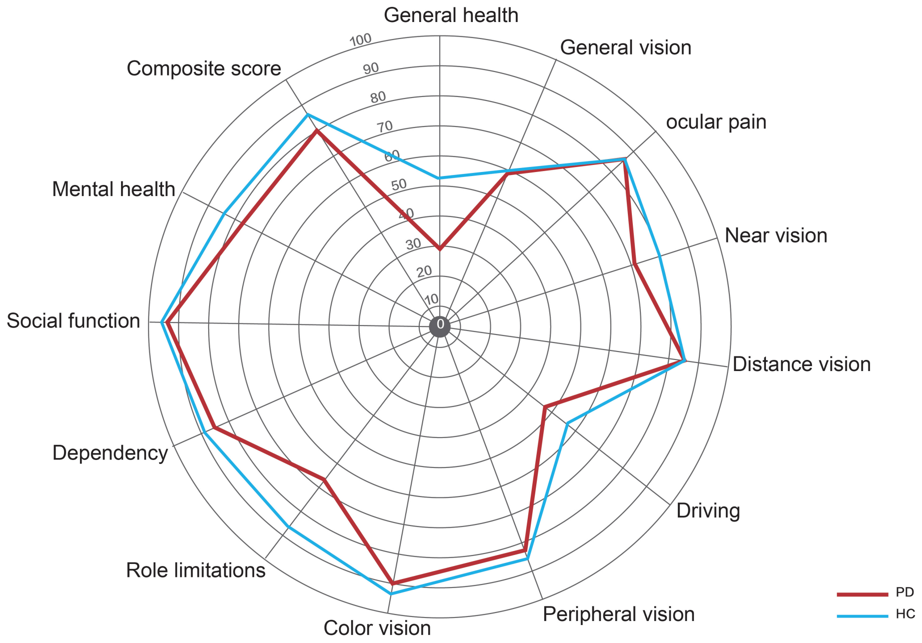

FIGURE 2 | Radar graph representing the mean scores for the various scales in the NEI VFQ-25. The red line represents the patients with PD, and the blue line represents the healthy controls.

area (0.720), inner ring (0.716), nasal sector (0.678), superior sector (0.668), inferior sector (0.668), and central sector (0.655) (**Figure 4**).

DISCUSSION

In this study, we observed that PD patients had no significant visual decline compared with healthy controls but experienced a worse vision-related quality of life, which implied that visual impairment existed in PD patients. Compared with those in healthy controls, prolonged P100 latency and decreased VD in both the macula and ONH were observed in PD patients, but there were no differences in retinal structure between the two groups. In addition, there was a significant correlation between visual impairment and retinal VD. Therefore, our results indicated that the macular microvascular alterations may occur earlier than the changes in retinal structure and may associate with visual impairment.

Symptoms of visual dysfunction have been widely reported and may contribute to the overall disabilities in PD patients (Uc et al., 2005). NEI VFQ-25 is a questionnaire developed by the National Eye Institute used for measuring the self-reported, vision-targeted health status of people with chronic eye diseases (Mangione et al., 2001). Although there was no significant difference in BCVA between the two groups, PD patients had significantly lower near vision, role limitations, and overall composite scores of NEI VFQ-25 compared with healthy controls. Furthermore, the composite score was strongly inversely related to disease severity. These outcomes suggested that PD patients had substantial problems and restrictions in everyday activities due to vision impairment, and worsen along disease progression. It is worth mentioning that the MMSE scores of the PD group were all within the normal range,

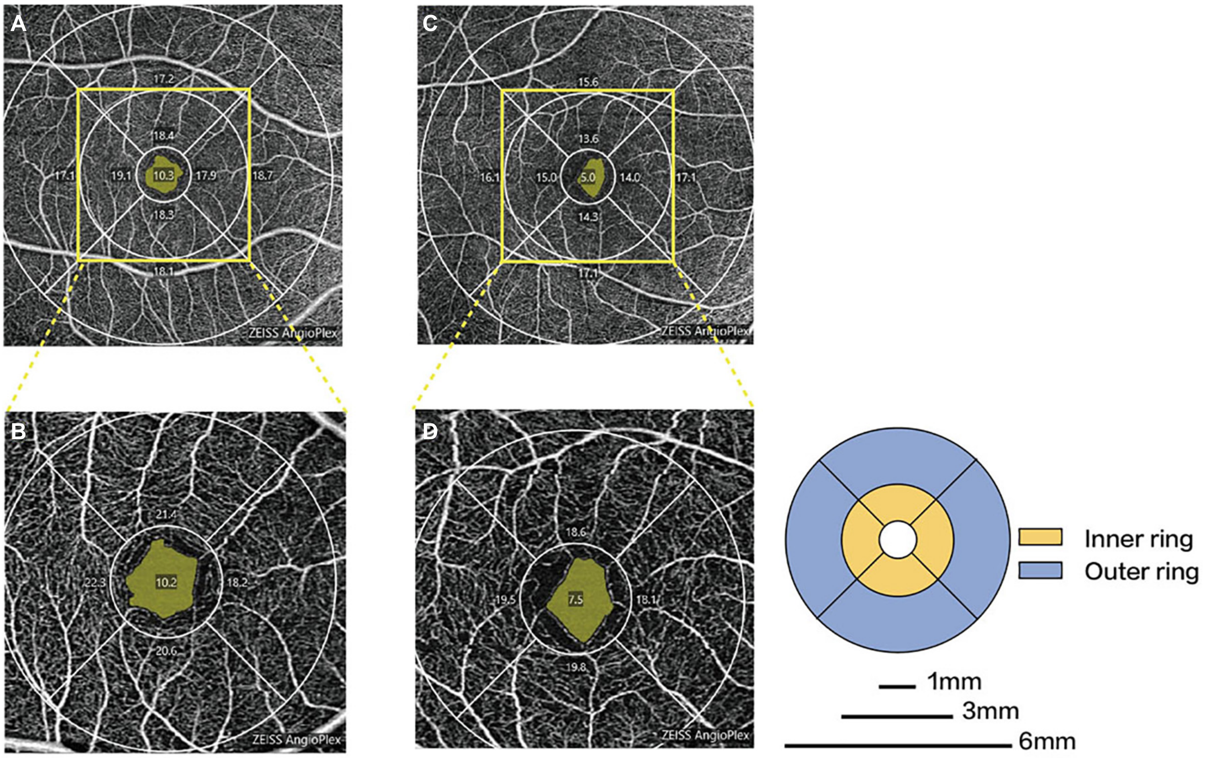

FIGURE 3 | Representative OCTA images in patients with PD and healthy controls. Macular microvascular density of healthy controls **(A)** and PD patients **(C)** in the 6-mm-diameter region. Macular microvascular density of healthy controls **(B)** and PD patients **(D)** in the 3-mm-diameter region.

TABLE 3 | Comparison of macular microvascular density and FAZ area between the PD patients and healthy controls in the 3-mm-diameter region.

Variable	**PD (N = 24)**		**HC (N = 23)**		***P***
	Mean (SD)	**Median (range)**	**Mean (SD)**	**Median (range)**	
Nasal (mm^{-1})	17.4 (3.5)	17.8 (15.0–19.3)	19.4 (2.6)	19.5 (17.6–21.3)	0.029^{a}
Temporal (mm^{-1})	17.2 (3.6)	17.8 (16.0–20.0)	19.7 (1.9)	19.5 (18.6–21.5)	0.009^{a}
Superior (mm^{-1})	17.1 (4.1)	18.1 (14.5–20.3)	19.4 (2.6)	19.8 (17.6–21.8)	0.049^{a}
Inferior (mm^{-1})	17.1 (3.1)	17.9 (14.9–19.4)	18.8 (2.5)	19.1 (17.1–20.9)	0.049^{a}
Central (mm^{-1})	6.6 (2.6)	6.7 (4.9–8.6)	8.2 (2.3)	7.9 (6.5–9.9)	0.032^{a}
Inner ring (mm^{-1})	17.2 (3.2)	17.3 (15.9–19.4)	19.3 (2.1)	19.4 (17.9–21.1)	0.011^{a}
Full area (mm^{-1})	16.0 (3.0)	16.1 (14.5–18.2)	18.0 (2.0)	18.4 (16.5–19.7)	0.010^{a}
FAZ area (mm^{2})	0.31 (0.10)	0.31 (0.22–0.37)	0.28 (0.10)	0.28 (0.23–0.37)	0.464

FAZ, foveal avascular zone; PD, Parkinson's disease; HC, healthy controls.
$^{a}P < 0.05$.

and the general health score did not correlate with any other subscales. Therefore, it is reasonable to assume that NEI VFQ-25 scores were reliable and not affected by cognitive function, and health status of PD patients. Almer et al. (2012) found that most subscales in NEI VFQ-25 were worse in PD patients than in controls and that near activities seemed to be more greatly affected by disease severity. They suggested that the decline in vision-targeted life quality of PD patients was probably ascribed to the ocular motor function because acuity, color vision, and contrast sensitivity did not vary significantly from those of controls. Compared with those in our study, PD patients in their group had a worse vision-related quality of life. This discrepancy might be ascribed to the difference in the disease course in which the subjects of Almer et al. (2012) had longer disease duration (10.9 ± 6.8 years). A better understanding of the vision-related life quality is important for the optimal care of PD patients, and we strongly encourage PD patients to undergo the assessment of NEI VFQ-25, which is simple, fast, and convenient.

Abnormal VEP in our study also reflected functional impairment in the visual pathway of PD patients. VEP was used as a non-invasive technique to evaluate bioelectrical function of

TABLE 4 | Correlations between visual function and clinical data in PD patients.

	BCVA (LogMAR)	P100 latency	P100 amplitude	Composite score
PD history (year)	−0.188 (0.391)	0.243 (0.288)	0.418 (0.060)	0.051 (0.816)
UPDRS III rating	−0.085 (0.715)	−0.253 (0.282)	−0.267 (0.255)	−0.587 (0.005[a])
MMSE	−0.048 (0.828)	−0.098 (0.673)	−0.089 (0.701)	−0.023 (0.919)

PD, Parkinson's disease; UPDRS III, Unified Parkinson's Disease Rating Scale III; MMSE, Mini-Mental State Examination; BCVA, best-corrected visual acuity; LogMAR, logarithm of the minimum angle of resolution.

[a]*$P < 0.05$.*

the entire visual pathway from the retina to higher cortical visual pathways. VEP latency was considered to be a more sensitive measure of foveal electrical activity than amplitude and less likely to be affected by dopaminergic drugs. Due to the relatively small individual difference, the P100 latency was commonly used to confirm the abnormalities of the visual pathway. In our study, the P100 latency of VEP was prolonged in patients with PD than in controls, and whereas the difference in P100 amplitude was not significant. This result was consistent with a meta−analysis that contained 20 case–control studies (He et al., 2018). The possible mechanism of VEP abnormalities is that dopaminergic neuron degeneration and decrease in dopamine production and secretion in PD patients may affect the function of the inner plexiform cells and horizontal cells in the retina, disrupting the transmission of visual signals (Büttner et al., 1996). The thinning of intraretinal layers in PD patients as shown by OCT also supports this conclusion to some extent (Garcia-Martin et al., 2014). However, we did not observe such a decrease in the retinal structure, and no significant thinning was shown in RNFL, CST, and GCIPL thicknesses between PD patients and controls in our study. Instead, we found altered retinal microvasculature in PD patients, and microvascular density was lower in PD patients than in controls, particularly in the macular area. As retinal vasculature has embryologic origins similar to cerebral vasculature, it might be postulated that these two shared a common vascular pathophysiology (Gariano and Gardner, 2005; Nadal et al., 2020). Cerebral small-vessel disease was proven to be associated with incident parkinsonism and may be an underlying etiology (Bohnen and Muller, 2016). A recent study has demonstrated that α-synuclein was deposited in the retinal ganglion cell layer as well as the vessel wall of retina arteries in transgenic animal models of PD (Price et al., 2016). Few studies have investigated the relationship between visual function and OCTA in PD. Intriguingly, we found a negative correlation between P100 latency and nasal, and superior sectors of macular VD in the 3-mm-diameter region. It can be speculated that the deposition of α-synuclein in intraretinal layers and retinal vessels, leading to abnormal VEP and microvasculature alterations, and ultimately results in visual dysfunction in PD patients. Likely, the nasal and superior sectors of retinal vessels might be the most affected site, leading to a potential change in the visual pathway at an early stage in PD patients. However, this conjecture must be corroborated by further research.

We also found that PD patients had decreased macular VD in all sectors of the 3-mm-diameter region compared with healthy subjects through the 3 × 3 mm scan without significant difference in signal strength. However, within the same matching area in the 6 × 6 mm scan, macular VD decreased only in the superior sector. We suspect that the discrepancy might be derived from the different scan protocols. In the 6 × 6 mm scan pattern, a total number of 350 B-scans were sampled and repeated twice in the vertical dimension, with each B-scan having 350 A-scans in the horizontal dimension. As for the 3 × 3 mm scan, there were 245 A-scans in each B-scan along the horizontal dimension, and 245 B-scans were repeated four times at each location. Therefore, the 3 × 3 mm scan pattern provides a denser sampling spacing (12.2 μm) than the 6 × 6 mm scanning pattern (17.1 μm), as well as better lateral resolution (Rosenfeld et al., 2016). This enables the 3 × 3 mm scan pattern to acquire more detailed information of the microvasculature and has a greater ability to discriminate the capillaries. Furthermore, a previous study has proved that a direct comparison between the two is not possible, given the different resolutions (Xiao et al., 2020). Considering that capillary deficits could be the earliest change of retinal vessels in PD patients, the 3 × 3 mm scan may more accurately reflect the foveal microvasculature in PD patients. Several studies have adopted OCTA as the main evaluation method to quantify the retinal microvasculature in PD patients. Decreased macular VD and perfusion density, as well as choroidal structural changes, were found in patients with PD in a recent study with a large sample size of 137 healthy controls, and 69 patients. Likewise, no significant difference was found in the retinal structure (Robbins et al., 2020). Furthermore, decreased retinal microvascular density was found only in the SCP but not in the deep capillary plexus in a study by Kwapong et al. (2018). However, in contrast to our results, they detected retinal thinning in PD patients, which was correlated with SCP, and suggesting that retinal microvascular abnormalities may contribute to the neurodegeneration in PD patients (Kwapong et al., 2018). Shi et al. (2020) used three different algorithms to quantify the retinal capillaries based on the OCTA images. They found that the retinal capillary skeleton and perfusion densities and capillary complexity of SCP were significantly lower in PD patients than in healthy controls (Shi et al., 2020). Unlike our results, in the study by Rascunà et al. (2020) no significant difference in microvascular density was observed between PD patients and healthy controls. These results were variable and inconsistent, possibly due to the study design, and patient selection. Furthermore, a prior study showed that different OCTA devices had different effects on VD measurements in subjects with media opacity, possibly due to different OCTA flow algorithms (Zhang et al., 2020). In addition, VD measurements and the OCTA repeatability were significantly affected by the signal strength (Lee et al., 2019; Yu et al., 2019). Therefore, the type of OCTA devices and the signal strength of OCTA images need to be taken into account when interpreting the results. Although results from these studies differed, most of them supported the notion that macular VD was decreased in PD patients. The details of different studies and their findings are elucidated in **Supplementary Table 7**. Our results

TABLE 5 | Correlations between visual function and macular microvascular density in the 3-mm-diameter region.

	Nasal	Temporal	Superior	Inferior	Central	Inner ring	Full area
BCVA (LogMAR)	0.004 (0.979)	−0.109 (0.466)	−0.060 (0.689)	−0.009 (0.952)	0.066 (0.658)	−0.074 (0.620)	−0.046 (0.761)
P100 latency (ms)	−0.328 (0.030[a])	−0.113 (0.465)	−0.302 (0.047[a])	−0.154 (0.318)	−0.176 (0.253)	−0.257 (0.092)	−0.288 (0.058)
P100 amplitude (μV)	0.022 (0.888)	0.243 (0.112)	0.168 (0.275)	0.271 (0.075)	0.169 (0.273)	0.154 (0.319)	0.193 (0.209)
Composite score	0.256 (0.082)	0.175 (0.240)	0.247 (0.094)	0.024 (0.872)	−0.028 (0.849)	0.226 (0.127)	0.194 (0.191)

BCVA, best-corrected visual acuity; LogMAR, logarithm of the minimum angle of resolution.
[a]*$P < 0.05$.*

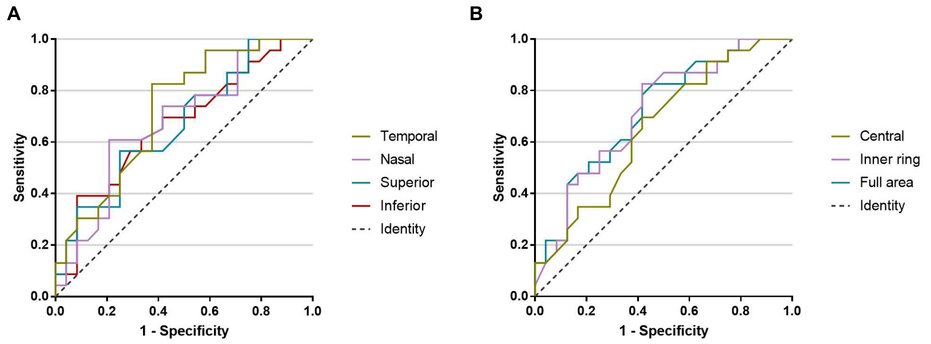

FIGURE 4 | The AUROCs for discriminating PD patients from healthy controls. **(A)** Macular microvascular density of the 3-mm-diameter region: temporal sector (0.723), nasal sector (0.678), superior sector (0.668), and inferior sector (0.668). **(B)** Macular microvascular density of the 3-mm-diameter region: central sector (0.655), inner ring (0.716), and full area (0.720).

suggested that retinal microvascular changes might precede vision decline and be detected earlier than retinal structure changes in PD patients. Furthermore, macular microvascular density showed diagnostic capacities to distinguish PD patients from healthy controls (AUROCs, ranged from 0.655 to 0.723). Within our study, PD patients were at a mean H&Y stage of 2, which indicated that our patients were in a relatively early stage of the disease. Thus, retinal microvasculature changes show promise as biomarkers for the diagnosis of PD in the early stage.

The present study had several notable advantages. First, we assessed the PD patients' UPDRS III and H&Y stage in the "off" state, which could more accurately reflect the severity of the disease without the impact of medications. Second, NEI VFQ-25 was used to evaluate vision-related quality of life, which could more closely mirror the actual practice of visual function. Third, different from prior studies, we analyzed the correlation between VEP parameters and retinal microvascular density. Of note is that both of these are objective measurements without subjective bias. However, there are some limitations of this study that merit considerations. The current sample size was small, so the results must be carefully interpreted because some of the detected correlations could be statistical anomalies. Although we assessed the BCVA, one of the primary indices of visual impairment, we did not evaluate specific visual symptoms, such as ocular motor function, contrast sensitivity, color perception, and illusions, which are reported commonly in PD and may also contribute to the lower life quality. Even we excluded the poor quality of images, the healthy group had higher-quality OCTA images than the PD group in the 6 × 6 mm scan centered on the macular, which may cause bias when interpreting these results. Another noteworthy point is that PD patients in the severe stage have difficulty cooperating with the OCTA examination, so we could not acquire the data from this group. However, on the basis of our results, we remain convinced that retinal microvascular density might be valuable in the diagnosing and monitoring for early PD. Future studies are needed to further investigate clinical implications of our findings.

CONCLUSION

Our study showed that retinal microvascular density decreased in PD patients and correlated with visual impairment. Retinal microvasculature was altered early even when the visual decline and retinal structure changes are not detectable, and may be a promising diagnostic marker for PD patients.

DATA AVAILABILITY STATEMENT

The raw data supporting the conclusions of this article will be made available by the authors, without undue reservation.

ETHICS STATEMENT

The studies involving human participants were reviewed and approved by Ethics Committee of the First Affiliated Hospital of

Sun Yat-sen University. The patients/participants provided their written informed consent to participate in this study.

AUTHOR CONTRIBUTIONS

MZ and LW: study and original manuscript writing. PW, MZ, and LW: conception and design. CW, JY, and TC: data collection. MZ and QH: analysis and interpretation. CW and PW: manuscript revision. PW: funding. All authors contributed to the article and approved the submitted version.

FUNDING

This work was supported by Guangdong Clinical Drug Research Funding (No. 2019XQ).

SUPPLEMENTARY MATERIAL

The Supplementary Material for this article can be found online at: https://www.frontiersin.org/articles/10.3389/fnins.2021.718820/full#supplementary-material

REFERENCES

Almer, Z., Klein, K. S., Marsh, L., Gerstenhaber, M., and Repka, M. X. (2012). Ocular motor and sensory function in Parkinson's disease. *Ophthalmology* 119, 178–182. doi: 10.1016/j.ophtha.2011.06.040

Archibald, N. K., Clarke, M. P., Mosimann, U. P., and Burn, D. J. (2011). Visual symptoms in Parkinson's disease and Parkinson's disease dementia. *Mov. Disord.* 26, 2387–2395.

Azulay, J. P., Mesure, S., Amblard, B., Blin, O., Sangla, I., and Pouget, J. (1999). Visual control of locomotion in Parkinson's disease. *Brain* 122(Pt 1), 111–120. doi: 10.1093/brain/122.1.111

Berg, D., Postuma, R. B., Adler, C. H., Bloem, B. R., Chan, P., Dubois, B., et al. (2015). MDS research criteria for prodromal Parkinson's disease. *Mov. Disord.* 30, 1600–1611. doi: 10.1002/mds.26431

Bodis-Wollner, I., Kozlowski, P. B., Glazman, S., and Miri, S. (2014). α-synuclein in the inner retina in parkinson disease. *Ann. Neurol.* 75, 964–966. doi: 10.1002/ana.24182

Bohnen, N. I., and Muller, M. L. (2016). Cerebral small vessel disease and incident parkinsonism: the RUN DMC study. *Neurology* 86, 1268–1269. doi: 10.1212/wnl.0000000000002554

Büttner, T., Kuhn, W., Müller, T., Heinze, T., Pühl, C., and Przuntek, H. (1996). Chromatic and achromatic visual evoked potentials in Parkinson's disease. *Electroencephalogr. Clin. Neurophysiol.* 100, 443–447. doi: 10.1016/0168-5597(96)95700-7

Davidsdottir, S., Cronin-Golomb, A., and Lee, A. (2005). Visual and spatial symptoms in Parkinson's disease. *Vision Res.* 45, 1285–1296. doi: 10.1016/j.visres.2004.11.006

Folstein, M. F., Folstein, S. E., and Mchugh, P. R. (1975). "Mini-mental state". A practical method for grading the cognitive state of patients for the clinician. *J. Psychiatr Res.* 12, 189–198.

Garcia-Martin, E., Larrosa, J. M., Polo, V., Satue, M., Marques, M. L., Alarcia, R., et al. (2014). Distribution of retinal layer atrophy in patients with Parkinson disease and association with disease severity and duration. *Am. J. Ophthalmol.* 157, 470–478.e472.

Gariano, R. F., and Gardner, T. W. (2005). Retinal angiogenesis in development and disease. *Nature* 438, 960–966. doi: 10.1038/nature04482

Goetz, C. G., Tilley, B. C., Shaftman, S. R., Stebbins, G. T., Fahn, S., Martinez-Martin, P., et al. (2008). Movement disorder society-sponsored revision of the unified Parkinson's disease rating scale (MDS-UPDRS): scale presentation and clinimetric testing results. *Mov. Disord.* 23, 2129–2170. doi: 10.1002/mds.22340

Guan, J., Pavlovic, D., Dalkie, N., Waldvogel, H. J., O'carroll, S. J., Green, C. R., et al. (2013). Vascular degeneration in Parkinson's disease. *Brain Pathol.* 23, 154–164. doi: 10.1111/j.1750-3639.2012.00628.x

Harnois, C., and Di Paolo, T. (1990). Decreased dopamine in the retinas of patients with Parkinson's disease. *Invest. Ophthalmol. Vis. Sci.* 31, 2473–2475.

He, S. B., Liu, C. Y., Chen, L. D., Ye, Z. N., Zhang, Y. P., Tang, W. G., et al. (2018). Meta-analysis of visual evoked potential and Parkinson's disease. *Parkinsons Dis.* 2018:3201308.

Hoehn, M. M., and Yahr, M. D. (1967). Parkinsonism: onset, progression and mortality. *Neurology* 17, 427–442. doi: 10.1212/wnl.17.5.427

Kwapong, W. R., Ye, H., Peng, C., Zhuang, X., Wang, J., Shen, M., et al. (2018). Retinal Microvascular impairment in the early stages of Parkinson's disease. *Invest. Ophthalmol. Vis. Sci.* 59, 4115–4122. doi: 10.1167/iovs.17-23230

Lee, A., and Gilbert, R. M. (2016). Epidemiology of Parkinson disease. *Neurol. Clin.* 34, 955–965.

Lee, T. H., Lim, H. B., Nam, K. Y., Kim, K., and Kim, J. Y. (2019). Factors affecting repeatability of assessment of the retinal microvasculature using optical coherence tomography angiography in healthy subjects. *Sci. Rep.* 9:16291.

London, A., Benhar, I., and Schwartz, M. (2013). The retina as a window to the brain-from eye research to CNS disorders. *Nat. Rev. Neurol.* 9, 44–53. doi: 10.1038/nrneurol.2012.227

Mahlknecht, P., Seppi, K., and Poewe, W. (2015). The concept of prodromal Parkinson's disease. *J. Parkinsons Dis.* 5, 681–697.

Mangione, C. M., Lee, P. P., Gutierrez, P. R., Spritzer, K., Berry, S., and Hays, R. D. (2001). Development of the 25-item national eye institute visual function questionnaire. *Arch. Ophthalmol.* 119, 1050–1058. doi: 10.1001/archopht.119.7.1050

Maresca, A., La Morgia, C., Caporali, L., Valentino, M. L., and Carelli, V. (2013). The optic nerve: a "mito-window" on mitochondrial neurodegeneration. *Mol. Cell Neurosci.* 55, 62–76. doi: 10.1016/j.mcn.2012.08.004

Nadal, J., Deverdun, J., De Champfleur, N. M., Carriere, I., Creuzot-Garcher, C., Delcourt, C., et al. (2020). Retinal vascular fractal dimension and cerebral blood flow, a pilot study. *Acta Ophthalmol.* 98, e63–e71.

Price, D. L., Rockenstein, E., Mante, M., Adame, A., Overk, C., Spencer, B., et al. (2016). Longitudinal live imaging of retinal α-synuclein::GFP deposits in a transgenic mouse model of Parkinson's Disease/Dementia with Lewy Bodies. *Sci. Rep.* 6:29523.

Rascunà, C., Russo, A., Terravecchia, C., Castellino, N., Avitabile, T., Bonfiglio, V., et al. (2020). Retinal thickness and microvascular pattern in early Parkinson's disease. *Front. Neurol.* 11:533375.

Reichmann, H. (2010). Clinical criteria for the diagnosis of Parkinson's disease. *Neurodegener. Dis.* 7, 284–290.

Robbins, C. B., Thompson, A. C., Bhullar, P. K., Koo, H. Y., Agrawal, R., Soundararajan, S., et al. (2020). Characterization of retinal microvascular and choroidal structural changes in Parkinson disease. *JAMA Ophthalmol.* 139, 182–188. doi: 10.1001/jamaophthalmol.2020.5730

Rosenfeld, P. J., Durbin, M. K., Roisman, L., Zheng, F., Miller, A., Robbins, G., et al. (2016). ZEISS Angioplex$^{\text{TM}}$ spectral domain optical coherence tomography angiography: technical aspects. *Dev. Ophthalmol.* 56, 18–29. doi: 10.1159/000442773

Shi, C., Chen, Y., Kwapong, W. R., Tong, Q., Wu, S., Zhou, Y., et al. (2020). Characterization by fractal dimension analysis of the retinal capillary network in Parkinson disease. *Retina* 40, 1483–1491. doi: 10.1097/iae.0000000000002641

Spaide, R. F., Fujimoto, J. G., Waheed, N. K., Sadda, S. R., and Staurenghi, G. (2018). Optical coherence tomography angiography. *Prog. Retin. Eye Res.* 64, 1–55. doi: 10.5005/jp/books/18041_2

Syrimi, Z. J., Vojtisek, L., Eliasova, I., Viskova, J., Svatkova, A., Vanicek, J., et al. (2017). Arterial spin labelling detects posterior cortical hypoperfusion in non-demented patients with Parkinson's disease. *J. Neural. Transm. (Vienna)* 124, 551–557. doi: 10.1007/s00702-017-1703-1

Uc, E. Y., Rizzo, M., Anderson, S. W., Qian, S., Rodnitzky, R. L., and Dawson, J. D. (2005). Visual dysfunction in Parkinson disease without dementia. *Neurology* 65, 1907–1913. doi: 10.1212/01.wnl.0000191565.11065.11

Urwyler, P., Nef, T., Killen, A., Collerton, D., Thomas, A., Burn, D., et al. (2014). Visual complaints and visual hallucinations in Parkinson's disease. *Parkinsonism Relat. Disord.* 20, 318–322. doi: 10.1016/j.parkreldis.2013.12.009

Xiao, H., Liu, X., Liao, L., Tan, K., Ling, Y., and Zhong, Y. (2020). Reproducibility of foveal avascular zone and superficial macular retinal vasculature measurements in healthy eyes determined by two different scanning protocols of optical coherence tomography angiography. *Ophthalmic. Res.* 63, 244–251. doi: 10.1159/000503071

Yu, J. J., Camino, A., Liu, L., Zhang, X., Wang, J., Gao, S. S., et al. (2019). Signal Strength Reduction Effects in OCT Angiography. *Ophthalmol. Retina* 3, 835–842. doi: 10.1016/j.oret.2019.04.029

Zhang, J., Tang, F. Y., Cheung, C. Y., and Chen, H. (2020). Different effect of media opacity on vessel density measured by different optical coherence tomography angiography algorithms. *Transl. Vis. Sci. Technol.* 9:19. doi: 10.1167/tvst.9.8.19

Zou, J., Liu, K., Li, F., Xu, Y., Shen, L., and Xu, H. (2020). Combination of optical coherence tomography (OCT) and OCT angiography increases diagnostic efficacy of Parkinson's disease. *Quant. Imag. Med. Surg.* 10, 1930–1939. doi: 10.21037/qims-20-460

Conflict of Interest: The authors declare that the research was conducted in the absence of any commercial or financial relationships that could be construed as a potential conflict of interest.

The reviewer CL declared a shared affiliation, with no collaboration, with the authors to the handling editor at the time of the review.

frontiers in Neuroscience

ORIGINAL RESEARCH
published: 14 September 2021
doi: 10.3389/fnins.2021.741651

Outer Retinal Layer Thickness Changes in White Matter Hyperintensity and Parkinson's Disease

Yitian Zhao [1,2,3†], Jinyu Zhao [1,4†], Yuanyuan Gu [1,2,3†], Bang Chen [1], Jiaqi Guo [1], Jianyang Xie [1], Qifeng Yan [1], Yuhui Ma [1], Yufei Wu [5], Jiong Zhang [1*], Qinkang Lu [5*] and Jiang Liu [6*]

[1] Cixi Institute of Biomedical Engineering, Ningbo Institute of Materials Technology and Engineering, Chinese Academy of Sciences, Ningbo, China, [2] Zhejiang International Scientific and Technological Cooperative Base of Biomedical Materials and Technology, Ningbo Institute of Materials Technology and Engineering, Chinese Academy of Sciences, Ningbo, China, [3] Zhejiang Engineering Research Center for Biomedical Materials, Ningbo Institute of Materials Technology and Engineering, Chinese Academy of Sciences, Ningbo, China, [4] School of Mechanical Engineering, Southwest Jiaotong University, Chengdu, China, [5] The Affiliated People's Hospital of Ningbo University, Ningbo, China, [6] Department of Computer Science and Engineering, Southern University of Science and Technology, Shenzhen, China

OPEN ACCESS

Edited by:
Jian Zheng,
Suzhou Institute of Biomedical Engineering and Technology (CAS), China

Reviewed by:
Dongxu Gao,
University of Liverpool, United Kingdom
Lei Wang,
Wenzhou Medical University, China

***Correspondence:**
Jiong Zhang
zhangjiong@nimte.ac.cn
Qinkang Lu
luqinkang@163.com
Jiang Liu
liuj@sustech.edu.cn

† These authors have contributed equally to this work and share first authorship

Specialty section:
This article was submitted to Perception Science, a section of the journal Frontiers in Neuroscience

Received: *15 July 2021*
Accepted: *18 August 2021*
Published: *14 September 2021*

Citation:
Zhao Y, Zhao J, Gu Y, Chen B, Guo J, Xie J, Yan Q, Ma Y, Wu Y, Zhang J, Lu Q and Liu J (2021) Outer Retinal Layer Thickness Changes in White Matter Hyperintensity and Parkinson's Disease. Front. Neurosci. 15:741651. doi: 10.3389/fnins.2021.741651

Purpose: To investigate the thickness changes of outer retinal layers in subjects with white matter hyperintensities (WMH) and Parkinson's Disease (PD).

Methods: 56 eyes from 31 patients with WMH, 11 eyes from 6 PD patients, and 58 eyes from 32 healthy controls (HC) were enrolled in this study. A macular-centered scan was conducted on each participant using a spectral-domain optical coherence tomography (SD-OCT) device. After speckle noise reduction, a state-of-the-art deep learning method (i.e., a context encoder network) was employed to segment the outer retinal layers from OCT *B*-scans. Thickness quantification of the outer retinal layers was conducted on the basis of the segmentation results.

Results: WMH patients had significantly thinner Henle fiber layers, outer nuclear layers (HFL+ONL) and photoreceptor outer segments (OS) than HC ($p = 0.031$, and $p = 0.005$), while PD patients showed a significant increase of mean thickness in the interdigitation zone and the retinal pigment epithelium/Bruch complex (IZ+RPE) (19.619 ± 4.626) compared to HC (17.434 ± 1.664). There were no significant differences in the thickness of the outer plexiform layer (OPL), the myoid and ellipsoid zone (MEZ), and the IZ+RPE layer between WMH and HC subjects. Similarly, there were also no obvious differences in the thickness of the OPL, HFL+ONL, MEZ and the OS layer between PD and HC subjects.

Conclusion: Thickness changes in HFL+ONL, OS, and IZ+RPE layers may correlate with brain-related diseases such as WMH and PD. Further longitudinal study is needed to confirm HFL+ONL/OS/IZ+RPE layer thickness as potential biomarkers for detecting certain brain-related diseases.

Keywords: white matter hyperintensities, Parkinson's disease, outer retinal layers, OCT images, deep learning

1. INTRODUCTION

White matter, gray matter and substantia nigra are three important components of the central nervous system. There exists strong evidence showing that white matter hyperintensities (WMH) is an important clinical markers of several brain diseases, such as stroke, dementia, in both cross-sectional and longitudinal studies (Balakrishnan et al., 2021; Song et al., 2021). Degeneration of the nigra cells leads to a decrease in dopamine neurons, which causes Parkinson's disease (PD). Therefore, efficient detection of hyperintense lesions in cerebral white matter and substantia nigra damage is of potential importance in the further study of diseases of the brain.

White matter hyperintensities (WMH) is the area of brain tissue that show up as increased brightness in T2-weighted magnetic resonance imaging (MRI) (Wardlaw et al., 2013). In clinical practice, a structural MRI (Zhuang et al., 2017) can be used for quantitative calculation of the volume of brain tissue for the diagnosis of WMH, while diffusion tensor imaging (DTI) (Etherton et al., 2017, 2019) is used to detect early micro-structural changes in white matter. The arterial spin labeling (ASL) (Van Dalen et al., 2016) method employed blood as an endogenous tracer for 3D flair scanning, in which the WMH volume was inversely proportional to the regional perfusion level. In addition, carotid ultrasound, cerebral angiogram, and echocardiogram have also been used to identify WMH.

PD is a neurodegenerative disorder, mainly affected by dopaminergic neurons in a specific area of the brain called the substantia nigra (Shen et al., 2021). Currently, PD is usually diagnosed based on motor symptoms (Oh et al., 2018). Common lab tests from blood, urine, or cerebrospinal fluid (CSF) can be used to detect PD. Meanwhile, brain imaging techniques [e.g., MRI, and Positron Emission Tomography (PET)] have also been proved as highly sensitive tools for identifying PD. However, most detection methods for WMH and PD are cost-intensive and invasive (usually involving the injection of a dye into the patient to make blood vessels stand out more prominently). It's necessary to explore a cheap and non-invasive alternative detection method.

It is commonly accepted that there are various relationships between eye and brain (Baker et al., 2008). The retina develops from the diencephalon in the embryonic period. Retinal vessels possess similar anatomic and physiological characteristics to cerebral vessels. There is also a blood-retinal barrier analogous to blood-brain barrier. In many chronic diseases, changes in retinal vessels may reflect, or even precede changes in cerebral vessels. Furthermore, the retina is the only organ whose vascular imaging can be acquired noninvasively *in vivo*. Therefore, considerable efforts have been made to investigate the progression of brain-related disorders based on retinal signs. Lindley et al. (2009) found that, lacunar stroke was more likely to produce retinal micro-vessel signs, such as focal arteriolar narrowing, arteriovenous nipping, generalized retinal arteriolar narrowing, small retinal arteriole to venule ratio, and retinal venular widening, compared with other stroke subtypes. Optical coherence tomography (OCT) is an efficient cross-sectional bioimaging modality that has become indispensable to retinal examination. Wang et al. (2014) employed spectral-domain OCT to detect localized retinal nerve fiber layer defects (RNFLDs) and confirmed that they were strongly associated with acute ischemic stroke, or prior cerebral stroke. Moreno-Ramos et al. (2013) revealed a significant decrease in the thickness of the retinal nerve fiber layer (RNFL) in AD, PD, and Lewy body dementia compared to normal controls, but the thickness changes were not statistically significant between these three diseases. Thomson et al. (2015) conducted a meta-analysis of RNFL change in dementia and concluded that the RNFL thickness had the potential to distinguish AD, or mild cognitive impairment (MCI) from healthy controls (HC). Thinning of the ganglion cell-inner plexiform layer (GC-IPL) may be found at the preclinical stage of AD (Fyfe, 2018; Cheung et al., 2019; Ma et al., 2021). Bulut et al. (2018) analyzed retinal vascular density (RVD), the foveal avascular zone (FAZ), choroidal thickness (CT), and outer retinal and choroidal flow rate in AD patients and HC via OCT angiography (OCTA) imaging, and highlighted the potential role of those metrics in the early diagnosis of AD. Ma et al. (2018) studied potential correlations between PD and retinal changes using OCT, finding that the average RNFL thickness, total macular thickness and MV were significantly decreased in PD patients compared to HC. Matlach et al. (2018) carried out some correlation analysis, but ruled out macular inner retinal thickness and peripapillary RNFL thickness to be effective biomarkers of PD patients. Chrysou et al. (2019) performed a relatively detailed meta-analysis of retinal changes in PD, and confirmed significant thinning of peripapillary RNFL and combined GC-IPL in PD.

For retinal structural changes associated with AD/PD/dementia, most prior work focused on the thickness of the RNFL, GCL, and/or GC-IPL. However, the retina is usually composed of inner layers and outer layers, as shown in **Figure 1**. The inner retinal layers include the RNFL, GCL, inner plexiform layer (IPL), and inner nuclear layer (INL), while the outer retinal layers comprise the outer plexiform layer (OPL), the Henle fiber layer and outer nuclear layer (HFL+ONL), the myoid and ellipsoid zone (MEZ), the photoreceptor outer segments (OS), the interdigitation zone and the retinal pigment epithelium/Bruch complex (IZ+RPE). On one hand, RPE layer in the outer retina may produce levodopa, a precursor to dopamine (McKay et al., 2006). The degeneration of dopaminergic neurons is an important feature of Parkinson's Disease. On the other hand, the INL+HFL and OS layers in the outer retina contain axons and dendrites of photoreceptor cells, respectively (Lujan et al., 2011). The NFL containing ganglion cell axons, and the IPL containing ganglion cell dendrites were confirmed to be thinner in WMH patients. To the best of our knowledge, the study of associations between thickening in any of the outer retinal layers and brain-related diseases has remained relatively unexplored. In this study, we use a deep learning model to segment the outer retinal layer automatically from OCT images, and measure the thickness of each layer. We then utilize these thickness indicators to investigate outer retinal layer alterations within the PD, WMH and HC groups, respectively, in order to find a potential retina-related index for the auxiliary diagnosis of these diseases.

2. EXPERIMENTS

Ethical approval for all experiments was provided by the institutional ethics committees, and written informed consent was obtained from each individual in accordance with Declaration of Helsinki.

2.1. Data Collection

2.1.1. Healthy Controls

There were 32 participants of similar age and sex to the WMH and PD patients. HC were subjects without cognitive impairment. Any subject with any of certain ocular diseases (such as glaucoma, macular degeneration, cataract, or high myopia) or with a systematic/neurological disease (such as diabetes, hypertension or multiple sclerosis) or prior ocular surgery was excluded from this study.

2.1.2. WMH and PD Participants

In total 56 eyes from 31 WMH patients and 11 eyes from 6 PD patients were enrolled in this study. Demographic data (age and sex) of WMH and PD participants were obtained through self-reporting questionnaires. WMH cases were evaluated by MRI technique, using a spin density image to estimate the total volume of subcortical white matter signal abnormalities. Participants were divided into WMH and HC groups by their total Fazekas scores, according to the reference standards of the presence of white matter abnormalities (Fazekas et al., 1987).

PD patients were diagnosed according to the UK Parkinson's Disease Society Brain Bank Clinical Diagnostic Criteria (Hughes et al., 1992). To satisfy the diagnosis of bradykinesia, a patient should have at least one of the following symptoms: muscular rigidity, 4–6 Hz rest tremor, and postural instability that are not caused by primary visual, vestibular, cerebellar, or proprioceptive dysfunction.

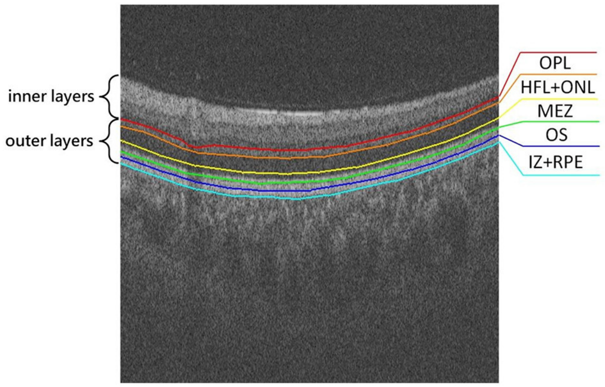

FIGURE 1 | Illustration of the outer retina layered structure, from top to bottom: outer plexiform layer (OPL), Henle fiber layer and outer nuclear layer (HFL+ONL), myoid and ellipsoid zone (MEZ), photoreceptor outer segments (OS), interdigitation zone and retinal pigment epithelium/Bruch complex (IZ+RPE).

2.2. OCT Image Acquisition

The RTVue XR Avanti SD-OCT system (Optovue Inc., Fremont, California, USA) was employed to perform a macular-centered OCT scan for each participant. Each scanned volume comprised 400 B-scans with a resolution of 400 × 400 × 640 pixels, and covered a field of view of $6.00 \times 6.00 \times 1.99\ mm^3$.

2.3. Methods

A senior ophthalmologist manually annotated 160 OCT images for our validation. The labeled mask containing 5 layers of outer retinal sublayer based on our internally developed labeling software. Due to the characteristics of coherent light imaging, OCT is susceptible to coherent/speckle noise, resulting in significant degradation in spatial resolution and image quality. In order to overcome these quality defects, a multi-frame fusion-based super-resolution reconstruction algorithm (Yan et al., 2020) was adopted as a preprocessing step before segmentation to improve the resolution of the OCT images. A deep learning-based algorithm (i.e., context encoder network namely CE-Net Gu et al., 2019) was then employed to segment the outer retinal layers from the volumetric images (Please see Appendix in **Supplementary Material** and **Figure 5** for more details). CE-Net was originally proposed for medical image segmentation specifically to overcome feature resolution reduction caused by consecutive pooling or convolution striding, and it has been proven to be effective in retinal OCT layer segmentation.

In the training stage, we input the super-resolution reconstructed OCT image which were cropped to 512 × 400 pixels automatically to the CE-Net, and calculate the Dice loss function (Crum et al., 2006) for the predicted map of the network output with the paired label. During the training, batch size was set to 4 and we adopt the SGD optimizer with a weight decay of 5e-4 to train the entire network end-to-end. The learning rate we set to 2e-4.

In this work, we first employed the CE-Net to detect the outer retinal layer boundaries, then we asked an ophthalmologist to review the automated detection results. The boundaries with poor segmentation performance were manual adjusted by using open source software ImageJ (https://imagej.nih.gov/ij/). Finally, thickness quantification of the outer retinal layers was performed on the basis of previous segmentation results. By calculating the thickness of the outer retinal layer for each B-scan of the same subject, the global thickness indicator of the corresponding person was obtained.

TABLE 1 | Basic characteristics of WMH, PD, and HC groups.

Characteristics	WMH (n = 31)	PD (n = 6)	HC (n = 32)	P_1	P_2
Eyes (OD), n	56 (28)	11 (5)	58 (28)	N/A	N/A
Age, years	63.58 ± 7.12	62.67 ± 11.48	60.56 ± 5.72	$0.239^{\diamond}$	$0.492^{\diamond}$
Female, n	12	4	20	$0.059^{\ddagger}$	$0.846^{\ddagger}$

OD represents the right eyes.

P_1 and P_2 denote the significance between WMH and HC, and PD and HC, respectively.

$P^{\diamond}$ value was obtained by Student's t-test and $P^{\ddagger}$ value was obtained by chi-square test.

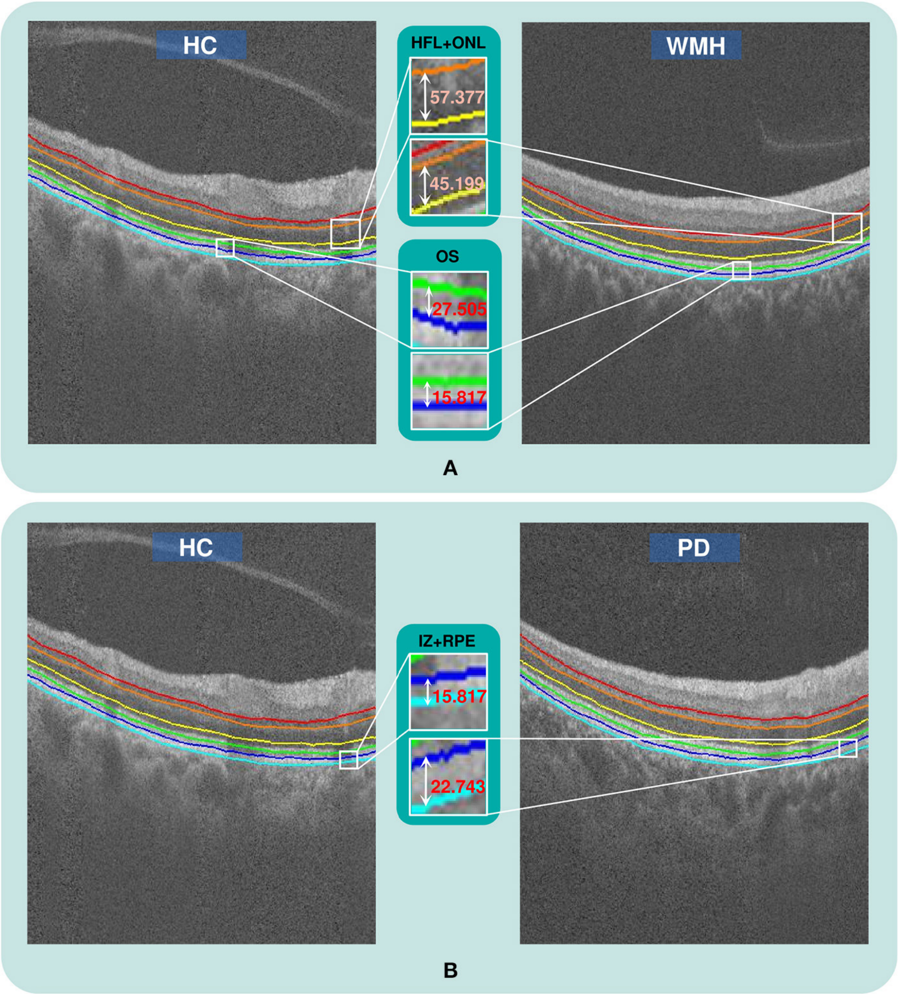

FIGURE 2 | The qualitative comparison of outer retinal layer thickness. **(A)** The thickness of the HFL+ONL and OS layers in a WMH case is obviously reduced compared with a healthy subject from the HC group, **(B)** The thickness of the IZ+RPE layer in a PD case is obviously greater than in a HC case.

2.4. Statistical Analysis

The statistical analysis was performed using IBM SPSS Statistics v22.0 software (IBM Inc., Armonk, NY, USA). To compare the characteristics of subjects among groups, Student's *t*-tests and chi-square tests were performed for continuous variables and categorical ones, respectively. If the samples across each group meet the hypothesis of homogeneity of variance, the One-way ANOVA models is applied to analyze the thickness difference among three groups. Otherwise, the Kruskal Wallis test for independent samples was applied for continuous variables, and the chi-square test for cateforical variables. Furthermore, associations between incidence of disease and the thickness information of the retinal layers were assessed using multivariate logistic regression analysis, in which the models of the WMH and PD groups were adjusted for age and gender. $p < 0.05$ was regarded as statistically significant. The basic demographics of the subjects are shown in **Table 1**. There was no significant difference in either age or sex between groups.

2.5. Results

2.5.1. Descriptive Statistics

The visual comparison results of outer retinal layer segmentation of 3 example images from different groups are shown in **Figure 2**. The box plots in **Figure 3** illustrate median, 1st/3rd quartile and lower/upper values within 1.5 interquartile ranges of 5 outer retinal layers. To quantitatively evaluate disease correlation, thickness comparisons between the WMH, PD and HC groups are summarized in **Table 2**. In the joint thickness of HFL and OPL, there is a significant difference ($p = 0.031$) between the WMH, PD and HC groups, while the MEZ thickness also shows a significant difference between the three groups ($p = 0.042$). The OS thickness of the WMH group exhibits an obvious decrease compared with the PD and HC groups ($p = 0.008$). Moreover, it is worth mentioning that the mean thickness of IZ+RPE in the PD group was significantly thicker than that in the other two groups. However, due to small sample size, the variance is non-homogeneous, and there is no obvious

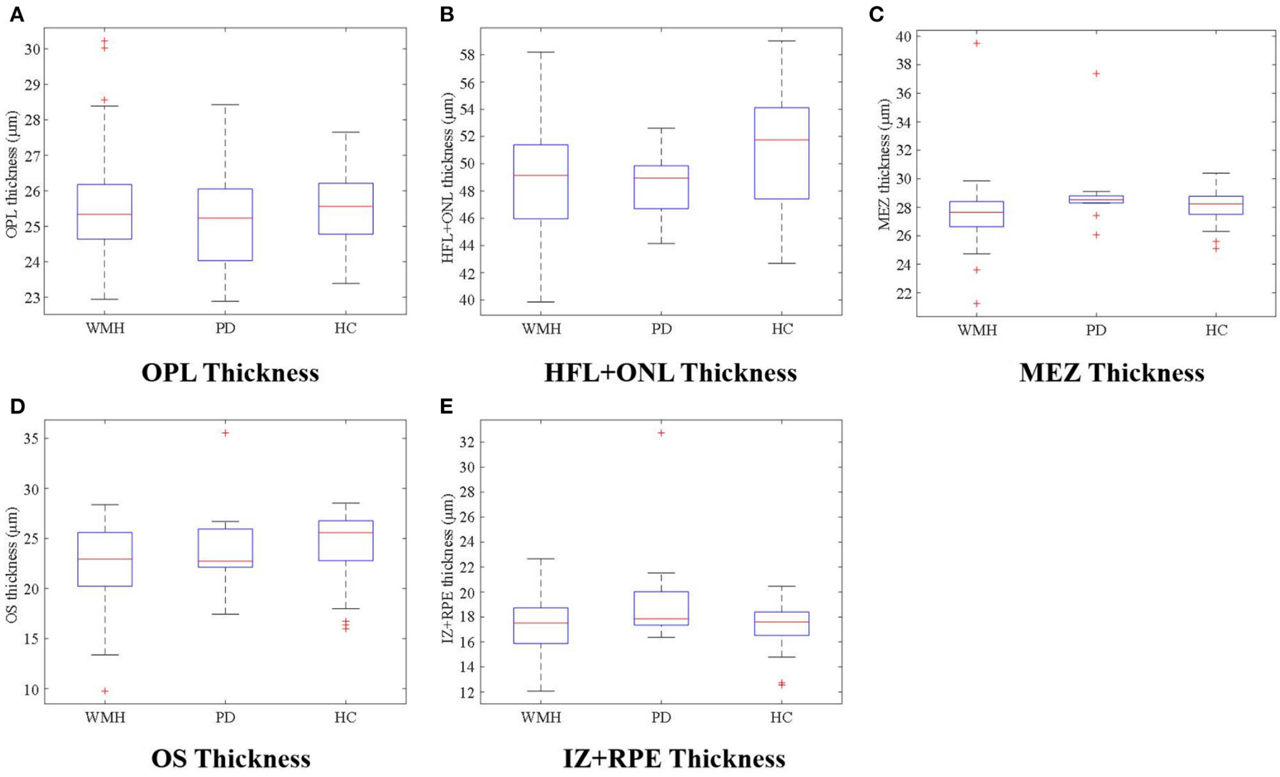

FIGURE 3 | (A–E) illustrate thickness differences in the outer retina sublayers between the WMH, PD, and HC groups.

significance in the nonparametric test. In **Figure 4**, we present the thickness differences between outer retinal layers of 3 cases from different groups.

2.5.2. Logistic Regression Analysis

Some studies concluded that the outer retinal thickness was significantly correlated with age and sex. However, in our study we could not find a significant collinear relationship between these variables. Therefore, we took age, gender and thickness as independent variables, and took the HC group as the reference group for multiple logistic regression analysis with the PD and WMH groups, respectively. Considering the reliability of multivariate logistic regression over a small sample size, the demographic data was selected before enrolled as independent variables. Demographic variables with $p < 0.2$ in the univariate logistic regression were selected for adjustment in the multivariate logistic regression if the number of variables was more than one-tenth of the sample size. The results are shown in **Table 3**. Excluding the interference of age and gender, the thickness of the HFL+OPL and the OS layers in WMH patients were significantly reduced when compared to the HC group ($p = 0.031$ and $p = 0.005$, respectively). However, there was no significant difference in the thickness of the OPL, MEZ and IZ+RPE layer between these two groups. For the PD and HC groups, there was no statistically significant difference ($p > 0.05$) between PD patients and healthy people in the outer retinal layers.

TABLE 2 | Thickness comparison among WMH, PD, and HC (μm).

Outer retinal layer	WMH (*n* = 56)	PD (*n* = 11)	HC (*n* = 58)	*p*
OPL	25.542 ± 1.479	25.179 ± 1.578	25.553 ± 1.031	0.669
HFL+ONL	49.282 ± 4.689	48.474 ± 2.425	51.178 ± 4.213	**0.031**
MEZ	27.575 ± 2.224	29.607 ± 2.884	28.091 ± 1.116	**0.042**
OS	22.354 ± 4.059	24.096 ± 4.580	24.550 ± 3.190	**0.008**
IZ+RPE	17.290 ± 2.228	**19.619 ± 4.626**	17.434 ± 1.664	0.268*

p-value was obtained by ANOVA, and P represents the result of a nonparametric test (Kruskal Wallis test) applied when the sample variance was non-homogeneous. Bold values indicate statistical significance of P < 0.05.*

3. DISCUSSION

The retina is an extension of the brain and central nervous system. Some lesions in the brain will produce corresponding changes in some areas of the retina. Therefore, the retina is an ideal place to study Parkinson's Disease, Alzheimer's Disease, stroke and other brain diseases. Identifying early, non-invasive and inexpensive biomarkers for proxy outcome measurement has important clinical significance for the diagnosis of brain diseases. We evaluated the thickness of the outer retina in different groups,

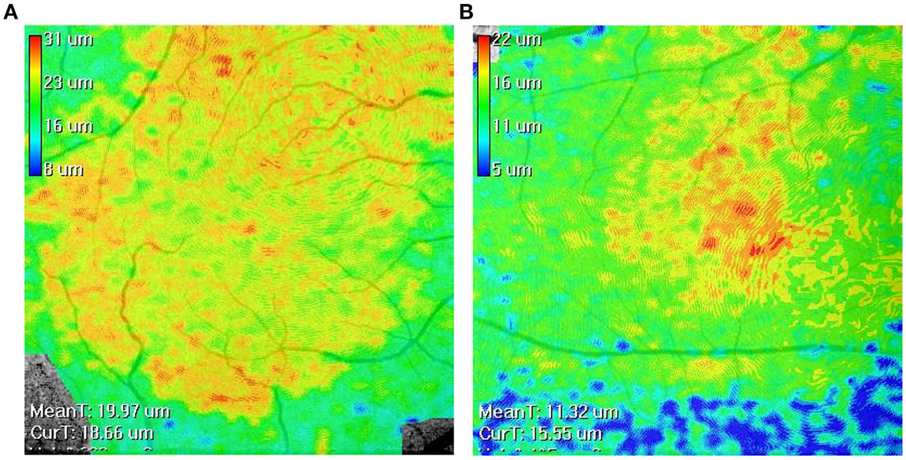

OS thickness of an HC case

OS thickness of a WMH case

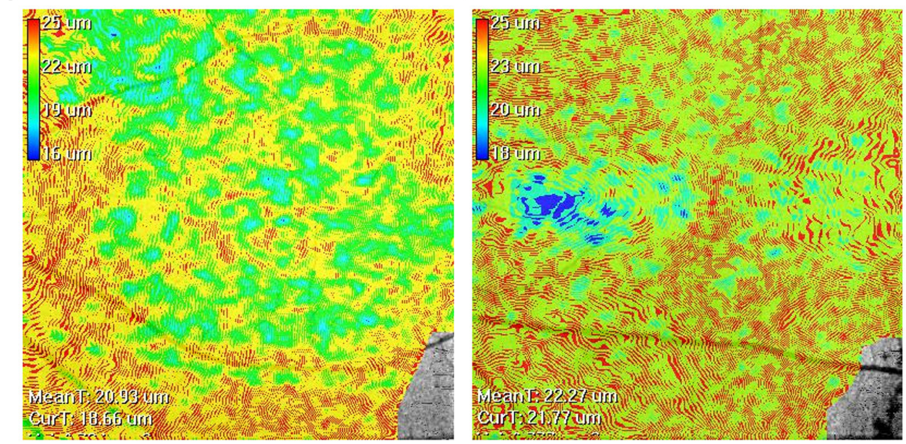

IZ+RPE thickness of an HC case

IZ+RPE thickness of a PD case

FIGURE 4 | The en-face retinal layer thickness maps of four cases from the WMH, PD and HC groups, respectively. **(A,B)** show the thickness distribution difference of the OS layer between the HC and WMH groups. **(C,D)** show the thickness distribution difference of the IZ+RPE layer between the HC and PD groups.

and found some sublayer thickness differences in the PD and WMH groups when compared with the HC group.

3.1. Parkinson's Disease and the IZ+RPE Layer of the Retina

Degeneration of dopaminergic neurons in substantia nigra is an important feature of Parkinson's Disease, and dopamine is the key neurotransmitter of motor function. Earlier studies showed that dopamine-containing neurons are found in the retina, particularly in the interamacrine cell of the inner plexiform layer and in the flexor cells of the inner and outer plexiform layers (Frederick et al., 1982). Almost all types of retinal neurons have dopamine receptors, whether in synaptic contact or not (Djamgoz et al., 1997). Most patients with PD experience symptoms of impaired vision during the course of their illness (Bodis-Wollner, 2013). In addition, dopamine was reported to induce axial eye elongation, which suggests that dopamine can prevent myopia (Papastergiou et al., 1998). These studies indicated that PD may contribute to structural and functional retinal changes on account of abnormalities in retinal dopamine.

Some prior studies have focused on changes in outer retinal layer thickness in brain-related diseases. Spund et al. (2013) found that there was no statistical difference in photoreceptor thickness in the central fovea between PD and HC groups. Roth et al. (2014) concluded that combined ONL and photoreceptor layer thickness were significantly decreased in PD patients compared to HC. Altintaş et al. (2008) reported that, compared with the control group, the mean retinal nerve fiber layer (RNFL) thickness was significantly reduced in Parkinson's disease patients.

In our study, however, some of the obtained results were inconsistent with previous studies. For instance, we found that the thickness of the IZ+RPE layer increases in the PD group ($p = 0.052$), while the thickness of the HFL+ONL/MEZ/OS layer shows no statistical difference between the PD and HC groups. On one hand, a relatively small number of samples is one of the major issues for inconsistency. On the other hand,

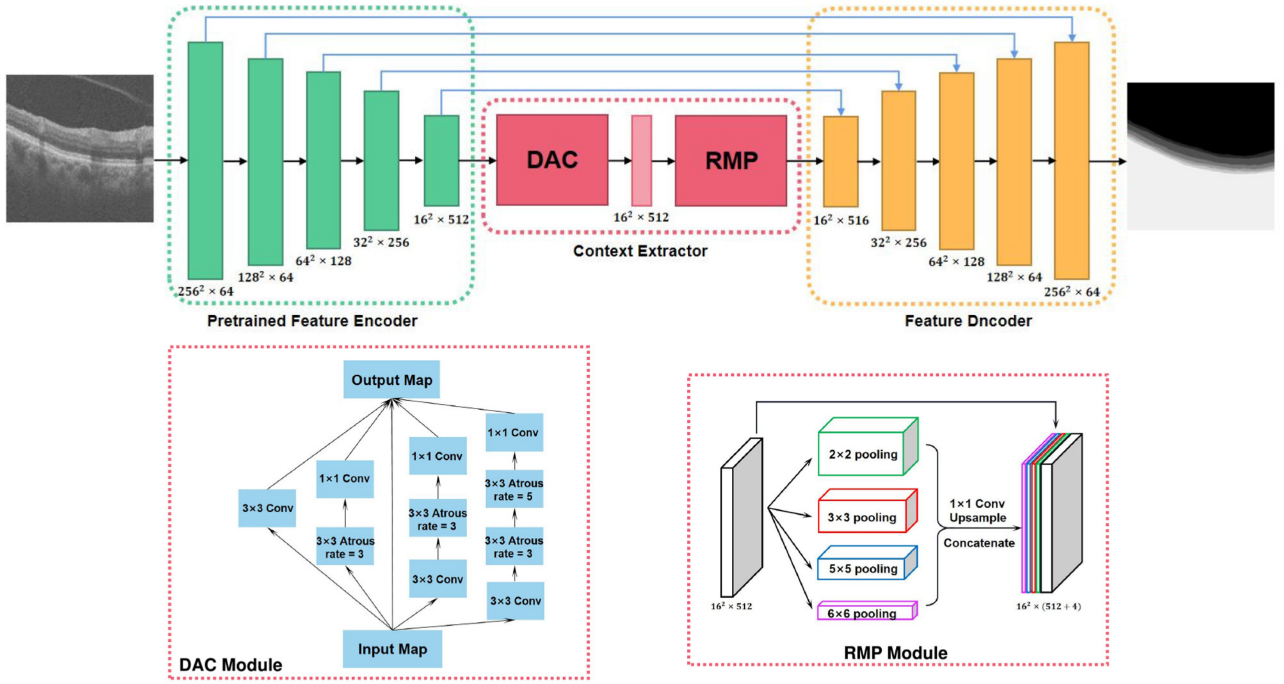

FIGURE 5 | Overview of the context encoder network (CE-Net) (Gu et al., 2019).

TABLE 3 | Results of multivariate logistic regression for demographic data.

Outer retinal layer	**WMH**			**PD**		
	OR	**95% CI**	**P_1**	**OR**	**95% CI**	**P_2**
OPL	1.022	0.758–1.380	0.885	0.791	0.452–1.385	0.412
HFL+ONL	0.897	0.813–0.990	**0.031**	0.868	0.738–1.020	0.085
MEZ	0.847	0.668–1.073	0.169	1.229	0.912–1.657	0.176
OS	0.851	0.759–0.953	**0.005**	0.964	0.791–1.175	0.715
IZ+RPE	0.921	0.753–1.126	0.422	1.681	1.149–2.461	0.052

P_1 and P_2 were calculated by multivariate logistic regression analysis between WMH and HC, PD and HC groups, respectively.
OR represents the odd ratio and 95% CI denotes the 95% confidence interval.

and we also consider the differences in the instruments and embedded software used may cause inconsistencies between different studies. For example, The data used in study (Roth et al., 2014) was captured by spectral domain OCT (Cirrus HD-OCT Version 5.0, Carl Zeiss Meditec, Dublin, CA, USA), and the retinal thickness measured by commercially available OCT Model 3000 unit (Model 3000, software version A1.1, Carl Zeiss Meditec, Inc., Dublin, California, USA) in study (Altintaş et al., 2008), while the data we studied was acquired by RTVue XR Avanti SD-OCT system (Optovue Inc., Fremont, California, USA), and different imaging devices may lead to the heterogeneity in imaging retinal tissue and image quality.

RPE is the outermost cell layer of the retina whose function is to nourish the retinal visual cells. As it is reported that the RPE layer can produce levodopa, a precursor to dopamine. The RPE transplantation into the striatum might be a promising prospect in clinical treatment of PD (McKay et al., 2006; Ming et al., 2009). The increasing of RPE layer in PD is likely to be a kind of compensation mechanism in response to the shortage of dopamine. Nevertheless, further study is required for confirmation.

3.2. White Matter Hyperintensities and the ONL+HFL/OS Layer of the Retina

White matter hyperintensity, one of the imaging features of Cerebral Small Vessel Disease (CVD), is a clinically important marker of several common brain diseases, such as dementia and stroke. White matter is the site where nerve fibers gather in the brain, and is mainly composed of the dendrites and axons of brain neurons. Previous studies have explored the relationship between ganglion cells and white matter (Ong et al., 2015; Mutlu et al., 2017; Tak et al., 2018). Ganglion cells are located in the inner layer of the retina: nerve fiber layer (NFL), ganglion cell layer (GCL) and inner plexiform layer (IPL) together forming the ganglion cell complex. The NFL and IPL are composed of axons and dendrites respectively, and they are more likely to reflect the condition of the white matter as a whole. The GCL is composed of cell bodies, and it is more likely to be related to gray matter (Mutlu et al., 2017). Qu et al. (2020) has also recently reported that the thickness of the NFL and GCL+IPL were associated with WMH, and deteriorate with the severity of lesions.

To the best of our knowledge, no effort has been made to unveil any correlation between outer retinal layer thickness measurements between WMH and HC groups. In our study, we found that the INL+HFL and OS thickness of the WMH group was significantly thinner than in the HC group. Interestingly, the INL+HFL contains bundles of unmyelinated cone and rod photoreceptor axons (Lujan et al., 2011), whereas the OS is equivalent to the dendritic part of a photoreceptor cell. The decrease of the thickness of these two layers is consistent with the findings of a prior study of ganglion cells, in which the sublayer of axons and dendrites became thinner (Qu et al., 2020). This provides new evidence for a correlation between the neurites of retinal cells and white matter.

We speculate that the concentration of amyloid beta protein(Aβ) may lead to changes in the neurite layer of retinal neurons. Aβ is one of the important causes of Alzheimer's disease, and it is also related to WMH (Osborn et al., 2018). Animal experiments have shown that the concentration of Aβ is positively related to synaptic activity. Thus, it is reasonable to speculate that Aβ deposition may lead to the degeneration of different nerve cells in the retina, resulting in the thinning of the related sublayers. Unfortunately, our data did not record the amyloid beta protein content of patients and the control group, but this provides a specific idea for follow-up research.

3.3. Limitations

Our study still has some limitations. On one hand, this study lacks longitudinal follow-up. Our WMH group might contain a mixture of AD patients, dementia subjects with Lewy bodies, and stroke participants. It should be split up into several subgroups to better understand the different clinical relationship. On the other hand, our present study is also limited by the relatively small sample size of the PD group. Hence, expansion of the dataset pool is desirable.

4. CONCLUSION

In conclusion, we used a state-of-the-art deep learning-based method to segment the outer retinal layers, and further measure the thickness of the sublayers. We found that retinal degeneration in the ONL+HFL and OS were independently associated with the WMH, and that the thickness of the IZ+RPE in the PD group was significantly greater than in the HC group, providing new evidence that some brain diseases may cause changes in the retina. Finally, we recommend that future studies should expand the sample size and employ longitudinal designs to further elucidate the relationship between the WMH/PD and outer retinal thickness.

DATA AVAILABILITY STATEMENT

The raw data supporting the conclusions of this article will be made available by the authors, without undue reservation.

ETHICS STATEMENT

The studies involving human participants were reviewed and approved by Ningbo Institute of Materials Technology and Engineering, Chinese Academy of Sciences. The patients/participants provided their written informed consent to participate in this study.

AUTHOR CONTRIBUTIONS

YZ and JinZ were involved in data analysis and interpretation and drafting and revising the manuscript. BC, JG, JX, QY, and YM were involved in data analysis. YW was involved in data interpretation. YG, JioZ, and JL were involved in study conceptualization, supervision, and revising the manuscript. All authors contributed to the article and approved the submitted version.

FUNDING

This work was supported in part by the Shenzhen Natural Science Fund (JCYJ20200109140820699 and the Stable Support Plan Program 20200925174052004), Zhejiang Provincial Natural Science Foundation of China (LZ19F010001), in part by the Youth Innovation Promotion Association CAS (2021298), in part by the Key Research and Development Program of Zhejiang Province (2020C03036), and in part by the Ningbo 2025 S&T Megaprojects (2019B10033 and 2019B1006).

SUPPLEMENTARY MATERIAL

The Supplementary Material for this article can be found online at: https://www.frontiersin.org/articles/10.3389/fnins.2021.741651/full#supplementary-material

REFERENCES

Altintaş, Ö., Işeri, P., Özkan, B., and Çağlar, Y. (2008). Correlation between retinal morphological and functional findings and clinical severity in parkinson's disease. *Doc. Ophthalmol.* 116, 137–146. doi: 10.1007/s10633-007-9091-8

Baker, M. L., Hand, P. J., Wang, J. J., and Wong, T. Y. (2008). Retinal signs and stroke: revisiting the link between the eye and brain. *Stroke* 39, 1371–1379. doi: 10.1161/STROKEAHA.107.496091

Balakrishnan, R., Hernández, M. d. C. V., and Farrall, A. J. (2021). Automatic segmentation of white matter hyperintensities from brain magnetic resonance images in the era of deep learning and big data-a systematic review. *Comput. Med. Imaging Graph.* 88:101867. doi: 10.1016/j.compmedimag.2021.101867

Bodis-Wollner, I. (2013). Foveal vision is impaired in parkinson's disease. *Parkinsonism Relat. Disord.* 19, 1–14. doi: 10.1016/j.parkreldis.2012.07.012

Bulut, M., Kurtuluş, F., Gözkaya, O., Erol, M. K., Cengiz, A., Akıdan, M., et al. (2018). Evaluation of optical coherence tomography angiographic findings in alzheimer's type dementia. *Br. J. Ophthalmol.* 102, 233–237. doi: 10.1136/bjophthalmol-2017-310476

Cheung, C. Y., Chan, V. T., Mok, V. C., Chen, C., and Wong, T. Y. (2019). Potential retinal biomarkers for dementia: what is new? *Curr. Opin. Neurol.* 32, 82–91. doi: 10.1097/WCO.0000000000000645

Chrysou, A., Jansonius, N. M., and van Laar, T. (2019). Retinal layers in parkinson's disease: a meta-analysis of spectral-domain optical coherence tomography studies. *Parkinsonism Relat. Disord.* 64, 40–49. doi: 10.1016/j.parkreldis.2019.04.023

Crum, W. R., Camara, O., and Hill, D. L. (2006). Generalized overlap measures for evaluation and validation in medical image analysis. *IEEE Trans. Med. Imaging* 25, 1451–1461. doi: 10.1109/TMI.2006.880587

Djamgoz, M., Hankins, M., Hirano, J., and Archer, S. (1997). Neurobiology of retinal dopamine in relation to degenerative states of the tissue. *Vision Res*. 37, 3509–3529. doi: 10.1016/S0042-6989(97)00129-6

Etherton, M. R., Wu, O., Cougo, P., Giese, A.-K., Cloonan, L., Fitzpatrick, K. M., et al. (2017). Integrity of normal-appearing white matter and functional outcomes after acute ischemic stroke. *Neurology* 88, 1701–1708. doi: 10.1212/WNL.0000000000003890

Etherton, M. R., Wu, O., Giese, A.-K., Lauer, A., Boulouis, G., Mills, B., et al. (2019). White matter integrity and early outcomes after acute ischemic stroke. *Transl. Stroke Res*. 10, 630–638. doi: 10.1007/s12975-019-0689-4

Fazekas, F., Chawluk, J. B., Alavi, A., Hurtig, H. I., and Zimmerman, R. A. (1987). Mr signal abnormalities at 1.5 t in alzheimer's dementia and normal aging. *Am. J. Roentgenol*. 149, 351–356. doi: 10.2214/ajr.149.2.351

Frederick, J. M., Rayborn, M. E., Laties, A. M., Lam, D. M., and Hollyfield, J. G. (1982). Dopaminergic neurons in the human retina. *J. Compar. Neurol*. 210, 65–79. doi: 10.1002/cne.902100108

Fyfe, I. (2018). Retinal nerve fibre layer thickness–a biomarker of early dementia? *Nat. Rev. Neurol*. 14, 449–449. doi: 10.1038/s41582-018-0044-5

Gu, Z., Cheng, J., Fu, H., Zhou, K., Hao, H., Zhao, Y., et al. (2019). Ce-net: context encoder network for 2d medical image segmentation. *IEEE Trans. Med. Imaging* 38, 2281–2292. doi: 10.1109/TMI.2019.2903562

Hughes, A. J., Daniel, S. E., Kilford, L., and Lees, A. J. (1992). Accuracy of clinical diagnosis of idiopathic parkinson's disease: a clinico-pathological study of 100 cases. *J. Neurol. Neurosurg. Psychiatry* 55, 181–184. doi: 10.1136/jnnp.55.3.181

Lindley, R. I., Wang, J. J., Wong, M.-C., Mitchell, P., Liew, G., Hand, P., et al. (2009). Retinal microvasculature in acute lacunar stroke: a cross-sectional study. *Lancet Neurol*. 8, 628–634. doi: 10.1016/S1474-4422(09)70131-0

Lujan, B. J., Roorda, A., Knighton, R. W., and Carroll, J. (2011). Revealing henle's fiber layer using spectral domain optical coherence tomography. *Invest. Ophthalmol. Vis. Sci*. 52, 1486–1492. doi: 10.1167/iovs.10-5946

Ma, L.-J., Xu, L.-L., Mao, C.-,j., Fu, Y.-T., Ji, X.-Y., Shen, Y., et al. (2018). Progressive changes in the retinal structure of patients with Parkinson's disease. *J. Parkinsons Dis*. 8, 85–92. doi: 10.3233/JPD-171184

Ma, Y., Hao, H., Xie, J., Fu, H., Zhang, J., Yang, J., et al. (2021). Rose: a retinal oct-angiography vessel segmentation dataset and new model. *IEEE Trans. Med. Imaging* 40, 928–939. doi: 10.1109/TMI.2020.3042802

Matlach, J., Wagner, M., Malzahn, U., Schmidtmann, I., Steigerwald, F., Musacchio, T., et al. (2018). Retinal changes in parkinson's disease and glaucoma. *Parkinsonism Relat. Disord*. 56, 41–46. doi: 10.1016/j.parkreldis.2018.06.016

McKay, B. S., Goodman, B., Falk, T., and Sherman, S. J. (2006). Retinal pigment epithelial cell transplantation could provide trophic support in Parkinson's disease: results from an *in vitro* model system. *Exp. Neurol*. 201, 234–243. doi: 10.1016/j.expneurol.2006.04.016

Ming, M., Li, X., Fan, X., Yang, D., Li, L., Chen, S., et al. (2009). Retinal pigment epithelial cells secrete neurotrophic factors and synthesize dopamine: possible contribution to therapeutic effects of rpe cell transplantation in Parkinson's disease. *J. Transl. Med*. 7, 1–9. doi: 10.1186/1479-5876-7-53

Moreno-Ramos, T., Benito-León, J., Villarejo, A., and Bermejo-Pareja, F. (2013). Retinal nerve fiber layer thinning in dementia associated with parkinson's disease, dementia with lewy bodies, and alzheimer's disease. *J. Alzheimers Dis*. 34, 659–664. doi: 10.3233/JAD-121975

Mutlu, U., Bonnemaijer, P. W., Ikram, M. A., Colijn, J. M., Cremers, L. G., Buitendijk, G. H., et al. (2017). Retinal neurodegeneration and brain mri markers: the rotterdam study. *Neurobiol. Aging* 60, 183–191. doi: 10.1016/j.neurobiolaging.2017.09.003

Oh, S. L., Hagiwara, Y., Raghavendra, U., Yuvaraj, R., Arunkumar, N., Murugappan, M., et al. (2018). A deep learning approach for parkinson's disease diagnosis from eeg signals. *Neural Comput. Appl*. 32, 10927–10933. doi: 10.1007/s00521-018-3689-5

Ong, Y.-T., Hilal, S., Cheung, C. Y., Venketasubramanian, N., Niessen, W. J., Vrooman, H., et al. (2015). Retinal neurodegeneration on optical coherence tomography and cerebral atrophy. *Neurosci. Lett*. 584, 12–16. doi: 10.1016/j.neulet.2014.10.010

Osborn, K. E., Liu, D., Samuels, L. R., Moore, E. E., Cambronero, F. E., Acosta, L. M. Y., et al. (2018). Cerebrospinal fluid β-amyloid42 and neurofilament light relate to white matter hyperintensities. *Neurobiol. Aging* 68, 18–25. doi: 10.1016/j.neurobiolaging.2018.03.028

Papastergiou, G. I., Schmid, G. F., Laties, A. M., Pendrak, K., Lin, T., and Stone, R. A. (1998). Induction of axial eye elongation and myopic refractive shift in one-year-old chickens. *Vision Res*. 38, 1883–1888. doi: 10.1016/S0042-6989(97)00347-7

Qu, M., Kwapong, W. R., Peng, C., Cao, Y., Lu, F., Shen, M., et al. (2020). Retinal sublayer defect is independently associated with the severity of hypertensive white matter hyperintensity. *Brain Behav*. 10, e01521. doi: 10.1002/brb3.1521

Roth, N. M., Saidha, S., Zimmermann, H., Brandt, A. U., Isensee, J., Benkhellouf-Rutkowska, A., et al. (2014). Photoreceptor layer thinning in idiopathic parkinson's disease. *Mov. Disord*. 29, 1163–1170. doi: 10.1002/mds.25896

Shen, T., Yue, Y., Zhao, S., Xie, J., Chen, Y., Tian, J., et al. (2021). The role of brain perivascular space burden in early-stage parkinson's disease. *npj Parkinsons Dis*. 7, 1–9. doi: 10.1038/s41531-021-00155-0

Song, J., Kim, K.-,h., Jeon, P., Kim, Y.-W., Kim, D.-I., Park, Y.-J., et al. (2021). White matter hyperintensity determines ischemic stroke severity in symptomatic carotid artery stenosis. *Neurol. Sci*. 42, 3367–3374. doi: 10.1007/s10072-020-04958-6

Spund, B., Ding, Y., Liu, T., Selesnick, I., Glazman, S., Shrier, E., et al. (2013). Remodeling of the fovea in parkinson disease. *J. Neural Trans*. 120, 745–753. doi: 10.1007/s00702-012-0909-5

Tak, A. Z. A., Sengul, Y., and Bilak, Ş. (2018). Evaluation of white matter hyperintensities and retinal fiber layer, ganglion cell layer, inner-plexiform layer, and choroidal layer in migraine patients. *Neurol. Sci*. 39, 489–496. doi: 10.1007/s10072-017-3234-9

Thomson, K. L., Yeo, J. M., Waddell, B., Cameron, J. R., and Pal, S. (2015). A systematic review and meta-analysis of retinal nerve fiber layer change in dementia, using optical coherence tomography. *Alzheimers Dementia* 1, 136–143. doi: 10.1016/j.dadm.2015.03.001

Van Dalen, J., Mutsaerts, H., Nederveen, A., Vrenken, H., Steenwijk, M., Caan, M., et al. (2016). White matter hyperintensity volume and cerebral perfusion in older individuals with hypertension using arterial spin-labeling. *Am. J. Neuroradiol*. 37, 1824–1830. doi: 10.3174/ajnr.A4828

Wang, D., Li, Y., Wang, C., Xu, L., You, Q. S., Wang, Y. X., et al. (2014). Localized retinal nerve fiber layer defects and stroke. *Stroke* 45, 1651–1656. doi: 10.1161/STROKEAHA.113.004629

Wardlaw, J. M., Smith, E. E., Biessels, G. J., Cordonnier, C., Fazekas, F., Frayne, R., et al. (2013). Neuroimaging standards for research into small vessel disease and its contribution to ageing and neurodegeneration. *Lancet Neurol*. 12, 822–838. doi: 10.1016/S1474-4422(13)70124-8

Yan, Q., Chen, B., Hu, Y., Cheng, J., Gong, Y., Yang, J., et al. (2020). Speckle reduction of oct via super resolution reconstruction and its application on retinal layer segmentation. *Artif. Intell. Med*. 106, 101871. doi: 10.1016/j.artmed.2020.101871

Zhuang, Y., Zeng, X., Wang, B., Huang, M., Gong, H., and Zhou, F. (2017). Cortical surface thickness in the middle-aged brain with white matter hyperintense lesions. *Front. Aging Neurosci*. 9:225. doi: 10.3389/fnagi.2017.00225

Conflict of Interest: The authors declare that the research was conducted in the absence of any commercial or financial relationships that could be construed as a potential conflict of interest.

frontiers in Neuroscience

ORIGINAL RESEARCH
published: 08 October 2021
doi: 10.3389/fnins.2021.743769

MF-Net: Multi-Scale Information Fusion Network for CNV Segmentation in Retinal OCT Images

Qingquan Meng, Lianyu Wang, Tingting Wang, Meng Wang, Weifang Zhu, Fei Shi, Zhongyue Chen and Xinjian Chen*

School of Electronics and Information Engineering, Soochow University, Jiangsu, China

Choroid neovascularization (CNV) is one of the blinding ophthalmologic diseases. It is mainly caused by new blood vessels growing in choroid and penetrating Bruch's membrane. Accurate segmentation of CNV is essential for ophthalmologists to analyze the condition of the patient and specify treatment plan. Although many deep learning-based methods have achieved promising results in many medical image segmentation tasks, CNV segmentation in retinal optical coherence tomography (OCT) images is still very challenging as the blur boundary of CNV, large morphological differences, speckle noise, and other similar diseases interference. In addition, the lack of pixel-level annotation data is also one of the factors that affect the further improvement of CNV segmentation accuracy. To improve the accuracy of CNV segmentation, a novel multi-scale information fusion network (MF-Net) based on U-Shape architecture is proposed for CNV segmentation in retinal OCT images. A novel multi-scale adaptive-aware deformation module (MAD) is designed and inserted into the top of the encoder path, aiming at guiding the model to focus on multi-scale deformation of the targets, and aggregates the contextual information. Meanwhile, to improve the ability of the network to learn to supplement low-level local high-resolution semantic information to high-level feature maps, a novel semantics-details aggregation module (SDA) between encoder and decoder is proposed. In addition, to leverage unlabeled data to further improve the CNV segmentation, a semi-supervised version of MF-Net is designed based on pseudo-label data augmentation strategy, which can leverage unlabeled data to further improve CNV segmentation accuracy. Finally, comprehensive experiments are conducted to validate the performance of the proposed MF-Net and SemiMF-Net. The experiment results show that both proposed MF-Net and SemiMF-Net outperforms other state-of-the-art algorithms.

Keywords: choroid neovascularization, OCT images, multi-scale information fusion network, segmentation, convolutional neural networks

Edited by:
Jian Zheng,
Suzhou Institute of Biomedical Engineering and Technology (CAS), China

Reviewed by:
Lingjiao Pan,
Jiangsu University of Technology, China
Yakang Dai,
Suzhou Institute of Biomedical Engineering and Technology (CAS), China

****Correspondence:***
Xinjian Chen
xjchen@suda.edu.cn

Specialty section:
This article was submitted to Perception Science, a section of the journal Frontiers in Neuroscience

Received: *19 July 2021*
Accepted: *23 August 2021*
Published: *08 October 2021*

Citation:
Meng Q, Wang L, Wang T, Wang M, Zhu W, Shi F, Chen Z and Chen X (2021) MF-Net: Multi-Scale Information Fusion Network for CNV Segmentation in Retinal OCT Images. Front. Neurosci. 15:743769. doi: 10.3389/fnins.2021.743769

INTRODUCTION

Choroidal neovascularization (CNV), also known as subretinal neovascularization, is a basic pathological change of various intraocular diseases such as age-related macular degeneration, central exudative chorioretinopathy, idiopathic choroidal neovascularization, pathological myopic macular degeneration, and ocular histoplasmosis syndrome (DeWan et al., 2006; Abdelmoula et al., 2013; Jia et al., 2014; Liu et al., 2015; Zhu et al., 2017). It often involves the macula, causing serious damage to the central vision. In the early stage of CNV, there are usually no abnormal symptoms. Along with the gradual expansion of neovascular leakage and rupture, it may cause vision loss, visual distortion, or central scotoma (Freund et al., 1993; Grossniklaus and Green, 2004). CNV can persist for months or years and then gradually become steady (Zhu et al., 2017). The macula of the patients with recurrent symptoms are seriously damaged, which may cause permanent visual impairment. Optical coherence tomography (OCT) is a non-invasive imaging technology proposed by Huang et al. (1991), which can capture high-resolution cross-sectional retinal structure. It plays an important role in the diagnosis and monitoring of retinal diseases (Shi et al., 2014; Chen et al., 2015; Wang et al., 2021a). In addition, fluorescence angiography (FA) and indocyanine green angiography (ICGA) are also important diagnostic imaging modalities for the detection of retinal diseases in clinical practice, and there are many works to analyze CNV based on FA and ICGA (Talisa et al., 2015; Gao et al., 2016; Corvi et al., 2020). However, FA and ICGA can only capture one 2D fundus image, which may cause the loss of internal structure information of CNV (Zhang et al., 2019). Besides, FA and ICGA are invasive and may cause nausea and other allergic reactions due to intravenous injection of dye (Jia et al., 2014). Instead, OCT is non-invasive and can obtain high-resolution cross-sectional images of the retina with a high speed (Talisa et al., 2015; Corvi et al., 2020). Therefore, accurate segmentation of CNV in OCT images is essential for ophthalmologists to analyze the condition of the patient and specify treatment plan. There are also previous studies that have been proposed for CNV segmentation in retinal OCT images (Xi et al., 2019; Zhang et al., 2019). Zhang et al. (2019) designed a multi-scale parallel branch CNN to improve the performance of CNV segmentation in OCT images. Xi et al. (2019) proposed an automated segmentation method for CNV in OCT images using multi-scale CNN with structure prior, in which a structure learning method was innovatively proposed based on sparse representation classification and the local potential function to capture the global spatial structure and local similarity structure prior. However, CNV segmentation in retinal OCT images is still very challenging as the complicated pathological characteristics of CNV, such as blur boundary, large morphological differences, speckle noise, and other similar disease interference. Multi-scale global pyramid feature aggregation module and multi-scale adaptive-aware deformation module are proposed to segment corneal ulcer in slit-lamp image in our previous study (Wang et al., 2021b). Therefore, to tackle these challenges and improve the CNV segmentation accuracy, a novel multi-scale information fusion network (MF-Net) is proposed for CNV segmentation in retinal OCT images. Our main contributions are summarized as follows,

1) A multi-scale adaptive-aware deformation module (MAD) is used and inserted at the top of encoder path to guide the model to focus on multi-scale deformation of the targets and aggregates the contextual information.
2) To improve the ability of the network to learn to supplement low-level local high-resolution semantic information to high-level feature maps, a novel semantics-details aggregation module (SDA) between encoder and decoder is designed.
3) Based on a U-shape architecture, a novel MF-Net integrated MAD module and SDA module are proposed and applied for CNV segmentation tasks. In addition, to leverage unlabeled data to further improve the CNV segmentation accuracy, a semi-supervised version of MF-Net is proposed by combining pseudo-data augmentation strategy named as SemiMF-Net.
4) Extensive experiments are conducted to evaluate the effectiveness of the proposed method. The experimental results show that, compared to state-of-the-art CNN-based methods, the proposed MF-Net achieves higher segmentation accuracy.

RELATED WORK

Recently, deep learning-based method has been proposed for image segmentation and achieved remarkable results. Long et al. (2015) proposed a fully convolutional networks (FCN) for semantic segmentation, which removed the full connection layer and could adapt to any input size. Although FCN has achieved satisfactory performance in semantic segmentation, the capacity of FCN to capture contextual information still needs to be improved as the limitation of convolutional layers. To tackle these problems, there are many methods that use pyramid-based modules or global pooling to aggregate regional or global contextual information (Chen et al., 2017; Zhao et al., 2017). Zhao et al. (2017) proposed a pyramid scene parsing network (PSPNet) based on pyramid pool modules, which aggregated context information from different regions to learn global context information. Chen et al. (2017) further proposed DeepLab v3 for semantic segmentation by introducing atrous convolution and atrous spatial pyramid pooling (ASPP). In addition, many attention mechanism-based methods have been explored to aggregate heterogeneous contextual information (Li et al., 2018; Oktay et al., 2018; Fu et al., 2019). However, these methods are mainly applied to the segmentation tasks with obvious features. In additional, there are also many deep learning-based methods have been proposed for medical image segmentation (Ronneberger et al., 2015; Gu et al., 2019; Feng et al., 2020). Although these methods have achieved impressive results, their performance of CNV segmentation in OCT images with large morphological differences, speckle noise, and other similar disease interference features has been reduced. Therefore, to improve the segmentation accuracy and tackle the challenges of CNV segmentation in retinal OCT images, a novel multi-scale information fusion network (MF-Net) is proposed for CNV segmentation in retinal OCT images.

METHOD

As shown in **Figure 1**, the proposed encoder-decoder structure-based multi-scale information fusion network (MF-Net) consists

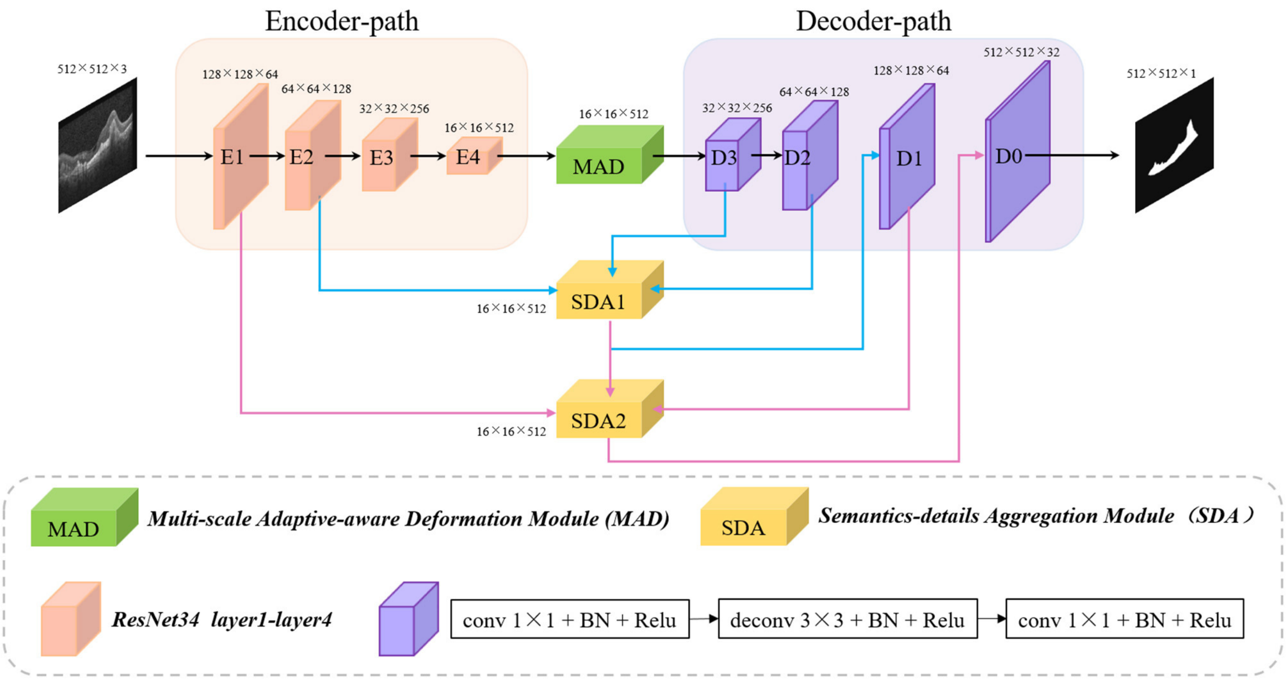

FIGURE 1 | Architecture of the proposed MF-Net.

of three parts: encoder-decoder network, multi-scale adaptive-aware deformation module (MAD), and semantics-details aggregation module (SDA). Specifically, the encoder-decoder network is used as our backbone network. MAD is inserted at the top of the encoder to guide the model to focus on the multi-scale deformation maps and aggregate the contextual information, while SDA is applied as a variant of skip connection of the whole network to fuse multi-level semantic information.

Backbone

Recently, the encoder-decoder structure is proved to be an efficient architecture for pixel-wised semantic segmentation. Most of the state-of-the-art segmentation networks are based on encoder-decoder structures, including AttUNet (Oktay et al., 2018), CE-Net (Gu et al., 2019), and PSPNet (Zhao et al., 2017) that have achieved remarkable performances in medical image segmentation. The encoder-path is mainly used to extract rich semantic information and global features from the input image and down sample the feature maps layer by layer, while the decoder-path aims to up sample the feature maps with strong semantic information from higher level stage, and restore the spatial resolution layer by layer.

To maximize the use of the information provided by the original image, the same encoder-decoder path is used as our backbone network. Unlike CE-Net, which send, the output of the encoder-path to dense atrous convolution (DAC) followed by residual multi-kernel pooling (RMP), the output is directly sent to the decoder-path. In addition, the skip-connection between the same level of encoder and decoder in CE-Net is also deleted in our backbone network.

Multi-Scale Adaptive-Aware Deformation Module (MAD)

It has been demonstrated that the multi-scale feature can improve the CNV segmentation accuracy in Zhang et al. (2019) and Xi et al. (2019). Therefore, to tackle the problems of large morphological differences of CNV in retinal OCT images, a MAD module is embedded at the top of the encoder-path to guide the model to focus on multi-scale deformation of the targets and aggregate the contextual information. As can be seen from **Figure 2** that the MAD module contains four parts: parallel and deformable convolution module, multiple global spatial attention module, multiple global channel attention module, and adaptive residual module as shown in **Figure 2**.

Parallel and Deformable Convolution Module

After features are encoded by Encoder 4 (E4), they are fed into parallel and deformable convolution module to augment the spatial sampling locations in the modules by additional offsets of kernel size in horizontal and vertical direction. As shown in **Figure 2**, the output of Encoder 4 (E4) is simultaneously fed into four 1×1 convolutional layers. Four dilation convolutions with rate 1, 3, 5, and 7 are, respectively, further used after the four parallel layers to squeeze the channel and to extract global context information from different levels of feature maps, and then, the feature maps are concatenated and fed into a deformable convolution to compute $B \in R^{c\times h\times w}$. Finally, $B \in R^{c\times h\times w}$ are fed into the parallel-linked multiple global spatial attention module, multiple global channel attention module, and adaptive residual module, respectively. The parallel and deformable convolution

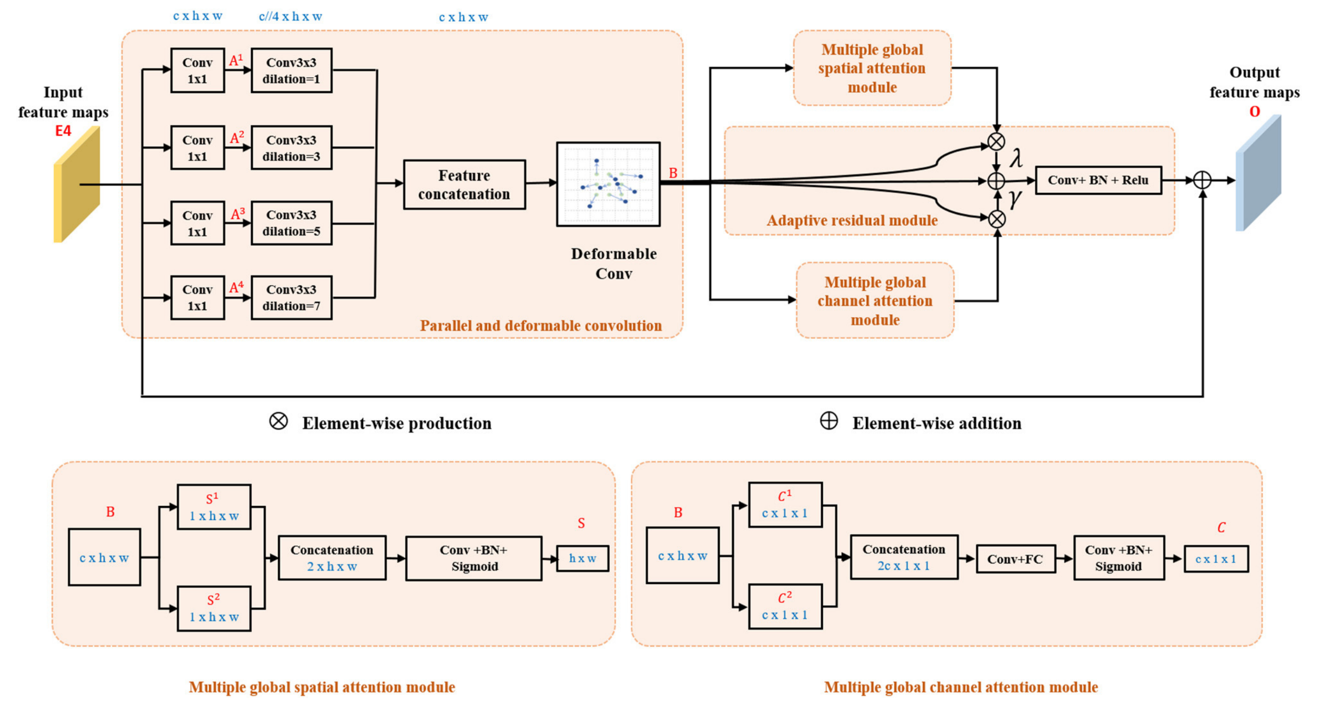

FIGURE 2 | Architecture of the proposed multi-scale adaptive-aware deformation module (MAD).

module can be summarized as

$$B = Conv_{deform} concat_{k=1}^{4}\left(conv_{dilation@2k-1}\left(A^{k}\right)\right), \tag{1}$$

where $A^k \in R^{c\times h\times w}$ denotes the output of 1×1 convolutional layers in k-th parallel branch, and $@_{2k-1}$ represents the convolution with a dilation rate of $2k-1$.

Multiple Global Spatial Attention Module

Max-pooling and average pooling are commonly used operations in convolutional neural networks, since they can reduce the sizes of feature maps and keep significant spatial response information in each channel; nevertheless, noise may also be kept due to the different sizes and shapes of the lesion. To reduce the influence of the irrelevant significant spatial response information in all channels, average pooling can be used to compute the mean value of all channels in the corresponding position in the input feature maps. Therefore, 2D average-pooling and max-pooling are performed simultaneously in our multiple global spatial attention module to get the most significant spatial response information in all channels and suppress noise interference. B are fed to the maximum map branch and the mean map branch in parallel to generate attention map $S^1 \in R^{1\times h\times w}$ and $S^2 \in R^{1\times h\times w}$, respectively, and then are concatenated in channel dimension. Then, a convolutional operation is applied to squeeze the channel of concatenated maps. Finally, a sigmoid function is used to generate the final attention feature map $S \in R^{1\times h\times w}$,

$$S = sigmoid\left(conv\left(concat\left(S^1, S^2\right)\right)\right). \tag{2}$$

This module can get the response of each feature map in all channels and suppress noise interference.

Multiple Global Channel Attention Module

Two parallel branches with global pooling are also constructed. The feature maps B are fed into a global max-pooling operation to obtain global channel maximum value maps $C^1 \in R^{c\times 1\times 1}$, while B are also fed into a global average-pooling operation to obtain global channel mean value maps $C^2 \in R^{c\times 1\times 1}$. Then, C^1 and C^2 are concatenated and fed into a convolution layer to smooth and squeeze the feature maps. Finally, the results are reshaped and fed into a fully connected layer followed by a sigmoid function to obtain the final feature map $C \in R^{c\times 1\times 1}$,

$$C = sigmoid\left(FC\left(conv\left(concat\left(C^1, C^2\right)\right)\right)\right). \tag{3}$$

This module can get the response of each feature map in all channels and suppress noise interference.

Adaptive Residual Module

The output of parallel and deformable convolution module $B \in R^{c\times h\times w}$ is multiplied by feature maps from multiple global spatial attention module $S \in R^{1\times h\times w}$ spatial-wisely and feature maps from multiple global channel attention module $C \in R^{c\times 1\times 1}$ channel-wisely, respectively. Then, pixel-wise addition operation followed by a convolutional layer is applied as

$$O = B \oplus conv\left(\left(\lambda B \otimes_{spatial}(S)\right) \oplus \left(\gamma B \otimes_{channel}(C)\right)\right), \tag{4}$$

where $\otimes_{spatial}$ and $\otimes_{channel}$ denote spatial-wise and channel-wise multiple, respectively. $O \in R^{c\times h\times w}$ represents the output of the adaptive residual module. $\oplus$ represents pixel-wise addition. λ and γ are learnable parameters and are initialized as a non-zero value (1.0 in this study). Finally, pixel-wise addition is used to add the original feature maps to the smoothed feature maps to get the final output of multi-scale adaptive-aware deformation module $O \in R^{c\times h\times w}$ to the decoder-path.

Semantics-Details Aggregation Module (SDA)

Skip-connection can fuse the strong semantic information of the decoder-path with the high-resolution feature of the encoder-path. It is a commonly used structure in encoder-decoder-based network and further promotes the applications of the encoder-decoder structure. However, directly sending the high-resolution features of the encoder to the decoder will introduce irrelevant clutters and result in incorrect segmentation. Therefore, a novel semantics-details aggregation module (SDA) has been proposed as a variant of skip-connection to enhance the information that is conducive to segmentation and suppress invalid information. As can be seen in **Figure 1**, two SDA modules have been introduced between encoders and decoders. The structure of the proposed SDA module is shown in **Figure 3**. In the SDA module, the skip-connection is reconstructed by combining the feature map of encoder, decoder, and upper-level decoder. For example, the left of **Figure 3** shows the structure of SDA 1. First, output feature maps of the Decoder 3 are upsampled followed by 3 × 3 convolutional layers to squeeze the channel. Then, the obtained feature maps and the output of the Encoder 2 are multiplied pixel-wisely to filter the detailed information that is conducive to segmentation. Finally, the filtered feature maps and the output of the Decoder 2 are added pixel-wisely to fuse detailed information and high-level semantic information. Above all, each SDA module in different stages can be summarized as

$$S^k = Conv\left(F^k @_2\right) \otimes E^{3-k} \oplus D^{3-k}, k = 1, 2, \tag{5}$$

where S^k denotes the output of the k-th SDA module, and $@_2$ represents the upsampling operation with rate of 2. E^k and D^k denote the output feature maps of the k-th Encoder and Decoder. F^1 and F^2 represent the output feature maps of the Decoder 3 and SDA 1, respectively. S^k denotes the output of the k-th SDA module. It is worth noting that no skip-connection is introduced after Encoder 3 and Encoder 4, because the detailed information may be gradually weakened when transmitted to the deeper layers, and also, it can save computing resources.

Loss Function

Image segmentation tasks can be analogized to pixel-level classification problems. Therefore, the binary cross-entropy loss L_{BCE}, commonly used in classification tasks, is adopted to guide the optimization of our proposed method. However, L_{BCE} only be adopted to optimize segmentation performance in pixel level, ignoring the integrity of the image level. Therefore, to tackle this problem, the dice loss also be introduced to optimize our proposed method. The joint loss function as

$$L_{Real} = L_{Dice} + L_{BCE}, \tag{6}$$

$$L_{Dice} = 1 - \sum\nolimits_{h,w} \frac{2\,|X \times Y|}{|X| + |Y|}, \tag{7}$$

$$L_{BCE} = -\sum\nolimits_{h,w} \left(Y \log X + (1 - Y) \log (1 - X)\right), \tag{8}$$

where X and Y denote the segmentation results and the corresponding ground truth, and h and w represent the coordinates of the pixel in X and Y.

SemiMF-Net

In medical image segmentation tasks, the lack of pixel-level annotation data has always been one of the important factors that hinder the further improvement of segmentation accuracy, and it is expensive and time-consuming to obtain these label data. Therefore, it has always been an urgent problem in the field of medical image segmentation to use unlabeled data combined with limited labeled data to further improve segmentation performance. To this end, based on the newly proposed MF-Net, a novel SemiMF-Net is further proposed by combining the pseudo-label augmentation strategy to leverage unlabeled data to further improve the CNV segmentation accuracy, as shown in **Figure 4**. It can be seen from **Figure 4** that our proposed

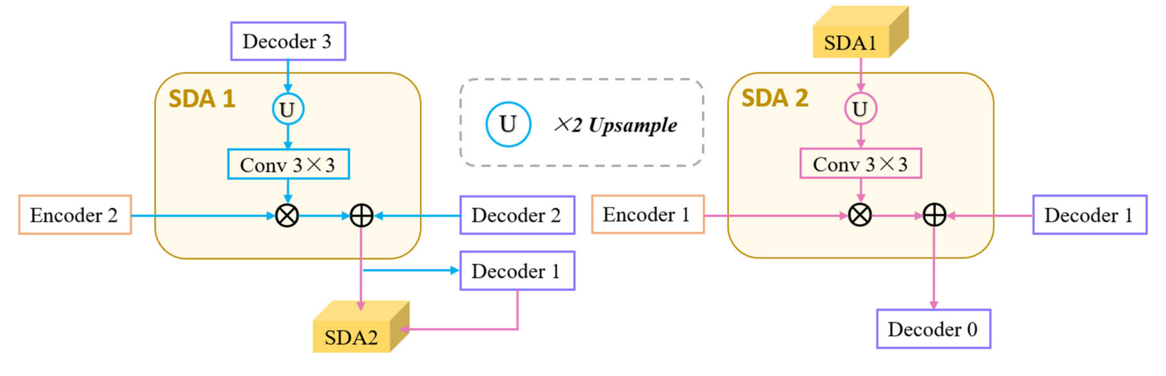

FIGURE 3 | Architecture of the proposed semantics-details aggregation module (SDA).

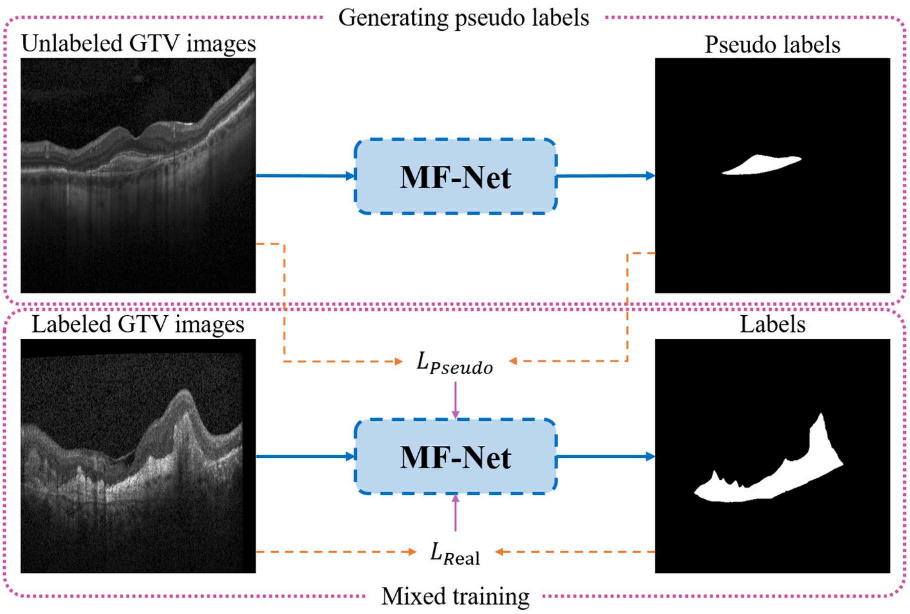

FIGURE 4 | Architecture of the proposed SemiMF-Net.

semi-supervised framework of SemiMF-Net mainly consists of three steps: (1) Limited labeled data are adopted to pre-train MF-Net to segment unlabeled, and these segmentation results are employed as pseudo-labels for unlabeled data. (2) Unlabeled data with pseudo labels and labeled data are mixed to re-train the MF-Net based on the objective function $L_{Pseudo} + \beta L_{Real}$ in a semi-supervised way, where L_{Pseudo} and L_{Real} are the joint loss function as Equation (6), and β is a weight paramter (1.0 in this study). (3) Finally, the SemiMF-Net that can accurately segment CNV in retinal OCT images is obtained.

EXPERIMENTS

Dataset

In order to accurately segment CNV and evaluate the performance of the proposed method, experienced ophthalmologists annotate pixel-level ground truth for the 1,522 OCT images with CNV collected from the UCSD public dataset (Kermany et al., 2018), which collected by the Shiley Eye Institute of the University of California San Diego (UCSD) and all of the images (Spectralis OCT, Heidelberg Engineering, Germany) were selected from retrospective cohorts of adult patients without exclusion criteria based on age, gender, or race. In addition, to evaluate the performance of the proposed method and all comparison algorithms comprehensively and objectively, four-fold cross-validation is performed in all experiments, in which each fold contained 380 OCT images except the fourth fold that had 382 OCT images. In addition, 2,560 retinal OCT images from the remaining 35,683 OCT images are randomly selected as unlabeled data to participate in SemiMF-Net training. The details for data strategies are listed in **Table 1**.

TABLE 1 | The details of data strategies.

	Supervised	Semi-supervised
Training	Retinal OCT images with ground truth from three folds.	Retinal OCT images with ground truth from three folds+2,560 retinal OCT images with pseudo labels.
Testing	Retinal OCT images with ground truth from the remaining one fold.	Retinal OCT images with ground truth from the remaining one fold.

Implementation Details

Binary cross-entropy loss and dice loss are jointly used as the loss function to train the proposed network. The implementation of our proposed MF-Net is based on the public platform Pytorch and NVIDIA Tesla K40 GPU with 12GB memory. Adam is used as the optimizer. Initial learning rate is set to 0.0005, and weight decay is set to 0.0001. The batch size is set as 4 and epoch is 50. To be fair, all experiments adopt the same data preprocessing and training strategy.

Evaluation Metrics

To comprehensively and fairly evaluate the segmentation performance of different methods, three indicators including dice similarity coefficients (DSC), sensitivity (SEN), and Jaccard similarity coefficient (JSC) are adopted to quantitatively analyze the experimental results, among which JSC and DSC are the most commonly used indices in validating the performance of segmentation algorithms (CE-Net, CPFNet, PSPNet, and DeepLabV3). In addition, the SEN is always adopted to evaluate the recall rate of abnormal conditions, which is essential for accurate screening of abnormal subjects and has been applied in many medical segmentation tasks (CE-Net, CPFNet, and AttUNet). The formulas of the three evaluation metrics are as follows

$$Dice = \frac{2TP}{FP + 2TP + FN}, \tag{9}$$

$$SEN = \frac{TP}{TP + FN}, \tag{10}$$

$$JSC = \frac{TP}{FP + TP + FN}, \tag{11}$$

where TP represents the number of true positives, FP represents the number of false positives, and FN represents the number of false negatives.

Results

The proposed MF-Net and SemiMF-Net are compared with state-of-the-art methods, including UNet (Ronneberger et al., 2015), CE-Net (Gu et al., 2019), CPFNet (Feng et al., 2020), AttUNet (Oktay et al., 2018), DeepLab v3 (Li et al., 2018), and PSPNet (Chen et al., 2017), as shown in **Table 2**. Compared to the backbone, CE-Net achieves an increase of 0.21% for the main evaluation metric DSC, due to the combination of dense atrous convolution (DAC) and residual multi-kernel pooling (RMP). The performance of CPFNet is comparable with the proposed MF-Net as for the insertion of global pyramid guidance (GPG) module, which combines multi-stage global context information to reconstruct skip-connection and provide global information guidance flow for the decoder.

It is worth noting that both proposed MF-Net and SemiMF-Net achieves better performance than all of the above methods. As shown in **Table 2**, the DSC, SEN, and JSC of MF-Net achieves 92.90, 93.01, and 86.80%, respectively. Compared to MF-Net, the average values of DSC, SEN, and JSC of the proposed SemiMF-Net have been improved to 93.07, 93.26, and 87.07%, respectively. These experimental results show that our proposed SemiMF-Net can leverage unlabeled data to further improve the segmentation performance.

It can be seen from **Table 2** that our proposed method takes slightly longer time than backbone due to the introduction of MAD and SDA in MF-Net. However, it can still meet the requirement of real-time processing. These experimental results show that compared with other CNN-based methods, our proposed MF-Net and SemiMF-Net can achieve better segmentation performance with similar efficiency.

Furthermore, to demonstrate the effectiveness of the proposed method, the qualitative segmentation results are also given in **Figure 5**. The proposed SemiMF-Net is more accurate and has better robustness in the CNV segmentation task.

Statistical Significance Assessment

We further investigate the statistical significance of the performance improvement for the proposed MF-Net and SemiMF-Net by the paired t-test, and these p-values are listed in **Tables 3**, **4**, respectively.

TABLE 2 | The result of comparison experiments and ablation studies (mean ± SD).

Methods	DSC	SEN	JSC	Time (s)
UNet	92.38 ± 0.31	92.44 ± 0.97	85.92 ± 0.53	0.1158
CE-Net	92.73 ± 0.23	92.82 ± 0.81	86.52 ± 0.41	0.0921
CPFNet	92.77 ± 0.22	92.96 ± 0.52	86.58 ± 0.38	0.1053
AttUNet	92.31 ± 0.14	92.22 ± 0.37	85.81 ± 0.25	0.1289
DeepLabV3	92.73 ± 0.19	92.75 ± 0.25	86.55 ± 0.35	0.1316
PSPNet	92.62 ± 0.37	92.79 ± 0.29	86.32 ± 0.62	0.2237
Backbone	92.46 ± 0.29	92.56 ± 0.44	86.05 ± 0.50	0.0789
Backbone+MAD	92.71 ± 0.28	92.81 ± 0.39	86.48 ± 0.48	0.0842
Backbone+SDA	92.76 ± 0.18	92.69±0.68	86.57 ± 0.33	0.0711
MF-Net	92.90 ± 0.21	93.01 ± 0.50	86.80 ± 0.37	0.0895
SemiMF-Net	93.07 ± 0.18	93.26 ± 0.45	87.07 ± 0.31	0.0895

As shown in **Table 3** that compared with other CNN-based methods, except for the significance compared with PSPNet and DeepLab v3 is not obvious, all the improvements for JSC and DSC of MF-Net are statistically significant with $p < 0.05$. The results further prove the effectiveness of the proposed MF-Net. **Table 4** lists the p-values of the proposed SemiMF-Net compared with MF-Net and other CNN-based methods. All the improvements for JSC and DSC of SemiMF-Net are statistically significant with $p < 0.05$. The results further prove that the proposed SemiMF-Net can leverage unlabeled data to further improve the CNV performance significantly.

Ablation Study

To verify the validity of the proposed MAD module and SDA module, we also conduct ablation experiments. As shown in **Table 2**, the embedding of MAD module (Baseline + MAD) achieves substantial improvement over the backbone in terms of all metric, which proves that multi-scale deformation features and adaptively aggregate contextual information are conducive for segmentation.

Furthermore, numerical results show that, the embedding of SDA (baseline + SDA) also contributes to the performance improvement, suggesting that well-designed skip connections can extract detailed information that is more conducive to segmentation, thereby improving the accuracy of segmentation. Especially, our proposed MAD module and SDA module can be easily introduced into other encoder-decoder network, which is our near future work. Furthermore, the proposed MF-Net achieves the highest DSC, and these results further demonstrate the effectiveness of our proposed method.

CONCLUSION

Choroid neovascularization segmentation is a fundamental task in medical image analysis. In this study, we propose a novel encoder-decoder based multi-scale information fusion network named MF-Net. A multi-scale adaptive-aware deformation module (MAD) and a semantics-details aggregation module (SDA) are integrated to the encoder-decoder structure to fuse

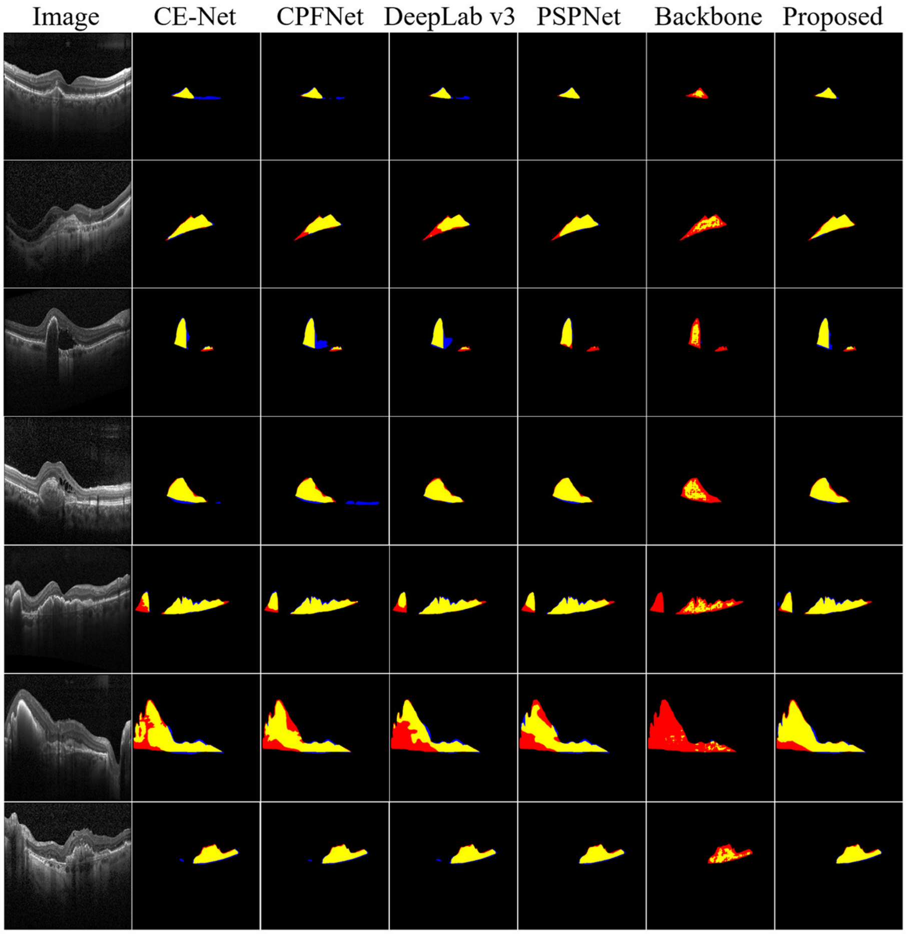

FIGURE 5 | Examples of CNV segmentation. From left to right are original image, CE-Net, CPFNet, DeepLab v3, PSPNet, backbone, and our proposed method SemiMF-Net. Yellow represents the correctly segmented region, while red and blue are the results of false-positive segmentation and false-negative segmentation, respectively.

TABLE 3 | Statistical analysis (*p*-value) of the proposed MF-Net compared with other CNN-based methods.

Method	**JSC**	**DSC**
MF-Net-UNet (Ronneberger et al., 2015)	0.015	0.018
MF-Net-AttUNet (Oktay et al., 2018)	0.001	0.001
MF-Net-CE-Net (Gu et al., 2019)	0.001	<5E-4
MF-Net-PSPNet (Chen et al., 2017)	0.069	0.069
MF-Net-CPFNet (Feng et al., 2020)	0.004	0.003
MF-Net-DeepLab v3 (Li et al., 2018)	0.122	0.118
MF-Net-Backbone	0.002	0.002

TABLE 4 | Statistical analysis (*p*-value) of the proposed SemiMF-Net compared with other CNN-based methods.

Method	**JSC**	**DSC**
SemiMF-Net-UNet (Ronneberger et al., 2015)	0.013	0.014
SemiMF-Net-AttUNet (Oktay et al., 2018)	<5E-4	<5E-4
SemiMF-Net-CE-Net (Gu et al., 2019)	0.011	0.009
SemiMF-Net-PSPNet (Chen et al., 2017)	0.042	0.040
SemiMF-Net-CPFNet (Feng et al., 2020)	0.005	0.004
SemiMF-Net-DeepLab v3 (Li et al., 2018)	0.051	0.041
SemiMF-Net-Backbone	0.007	0.007
SemiMF-Net- MF-Net	0.046	0.038

multi-scale contextual information and multi-level semantic information that is conducive to segmentation and further improve the segmentation performance. Furthermore, to solve the problem of insufficient pixel-level annotation data, based on the newly proposed MF-Net, SemiMF-Net is proposed by introducing semi-supervised learning to leverage unlabeled data to further improve the CNV segmentation accuracy. The comprehensive experimental results show that the segmentation performance of the proposed MF-Net and SemiMF-Net outperforms other state-of-the-art algorithms.

There is still a limitation on this study that the proposed MF-Net is designed based on the encoder-decoder structure, and cannot effectively prove its generalization on different backbone networks. In future work, we will extend the proposed MAD and SDA to various backbones to further prove its stability and versatility, and strive to reduce the number of parameters.

DATA AVAILABILITY STATEMENT

The datasets presented in this study can be found in online repositories. The names of the repository/repositories and accession number(s) can be found below: https://data.mendeley.com/datasets/rscbjbr9sj/2.

ETHICS STATEMENT

The retinal OCT B-scans used in this paper are collected from the UCSD public dataset, it has been mentioned in the paper's section of "Experiments, Dataset". All data in UCSD public dataset, Institutional Review Board (IRB)/Ethics Committee approvals were obtained. The work was conducted in a manner compliant with the United States Health Insurance Portability and Accountability Act (HIPAA) and was adherent to the tenets of the Declaration of Helsinki.

AUTHOR CONTRIBUTIONS

QM conceptualized and designed the study, wrote the first draft of the manuscript, and performed data analysis. LW, TW, MW, FS, WZ, ZC, and XC performed the experiments, collected and analyzed the data, and revised the manuscript. All authors contributed to the article and approved the submitted version.

FUNDING

This study was supported part by the National Key R&D Program of China (2018YFA0701700) and part by the National Nature Science Foundation of China (61971298 and 81871352).

REFERENCES

Abdelmoula, W. M., Shah, S. M., and Fahmy, A. S. (2013). Segmentation of choroidal neovascularization in fundus fluorescein angiograms. *IEEE Trans. Biomed. Eng.* 60, 1439–1445. doi: 10.1109/TBME.2013.2237906

Chen, H., Chen, X., Qiu, Z., Xiang, D., Chen, W., Shi, F., et al. (2015). Quantitative analysis of retinal layers' optical intensities on 3d optical coherence tomography for central retinal artery occlusion. *Sci. Rep.* 5, 1–6. doi: 10.1038/srep09269

Chen, L.-C., Papandreou, G., Schroff, F., and Adam, H. (2017). Rethinking atrous convolution for semantic image segmentation. *arXiv arXiv*:1706.05587.

Corvi, F., Cozzi, M., Barbolini, E., Nizza, D., Belotti, M., Staurenghi, G., et al. (2020). Comparison between several optical coherence tomography angiography devices and indocyanine green angiography of choroidal neovascularization. *Retina* 40, 873–880. doi: 10.1097/IAE.0000000000002471

DeWan, A., Liu, M., Hartman, S., Zhang, S. S.-M., Liu, D. T., Zhao, C., et al. (2006). Htra1 promoter polymorphism in wet age-related macular degeneration. *Science* 314, 989–992. doi: 10.1126/science.1133807

Feng, S., Zhao, H., Shi, F., Cheng, X., Wang, M., Ma, Y., et al. (2020). Cpfnet: context pyramid fusion network for medical image segmentation. *IEEE Trans. Med. Imaging* 39, 3008–3018. doi: 10.1109/TMI.2020.2983721

Freund, K. B., Yannuzzi, L. A., and Sorenson, J. A. (1993). Age-related macular degeneration and choroidal neovascularization. *Am. J. Ophthalmol.* 115, 786–791. doi: 10.1016/S0002-9394(14)73649-9

Fu, J., Liu, J., Tian, H., Li, Y., Bao, Y., Fang, Z., et al. (2019). "Dual attention network for scene segmentation," in *Proceedings of the IEEE/CVF Conference on Computer Vision and Pattern Recognition*, (Long Beach, CA: IEEE), 3146–3154.

Gao, S. S., Liu, L., Bailey, S. T., Flaxel, C. J., Huang, D., Li, D., et al. (2016). Quantification of choroidal neovascularization vessel length using optical coherence tomography angiography. *J. Biomed. Opt.* 21, 076010. doi: 10.1117/1.JBO.21.7.076010

Grossniklaus, H. E., and Green, W. R. (2004). Choroidal neovascularization. *Am. J. Ophthalmol.* 137, 496–503. doi: 10.1016/j.ajo.2003.09.042

Gu, Z., Cheng, J., Fu, H., Zhou, K., Hao, H., Zhao, Y., et al. (2019). Ce-net: Context encoder network for 2d medical image segmentation. *IEEE Trans. Med. Imaging* 38, 2281–2292. doi: 10.1109/TMI.2019.2903562

Huang, D., Swanson, E. A., Lin, C. P., Schuman, J. S., Stinson, W. G., Chang, W., et al. (1991). Optical coherence tomography. *Science* 254, 1178–1181. doi: 10.1126/science.1957169

Jia, Y., Bailey, S. T., Wilson, D. J., Tan, O., Klein, M. L., Flaxel, C. J., et al. (2014). Quantitative optical coherence tomography angiography of choroidal neovascularization in age-related macular degeneration. *Ophthalmology* 121, 1435–1444. doi: 10.1016/j.ophtha.2014.01.034

Kermany, D. S., Goldbaum, M., Cai, W., Valentim, C. C., Liang, H., Baxter, S. L., et al. (2018). Identifying medical diagnoses and treatable diseases by image-based deep learning. *Cell* 172, 1122–1131. doi: 10.1016/j.cell.2018.02.010

Li, H., Xiong, P., An, J., and Wang, L. (2018). Pyramid attention network for semantic segmentation. *arXiv arXiv*:1805.10180.

Liu, L., Gao, S. S., Bailey, S. T., Huang, D., Li, D., and Jia, Y. (2015). Automated choroidal neovascularization detection algorithm for optical coherence tomography angiography. *Biomed. Opt. Express* 6, 3564–3576. doi: 10.1364/BOE.6.003564

Long, J., Shelhamer, E., and Darrell, T. (2015). "Fully convolutional networks for semantic segmentation," in *Proceedings of the IEEE Conference on Computer Vision and Pattern Recognition* (Boston, MA: IEEE), 3431–3440.

Oktay, O., Schlemper, J., Folgoc, L. L., Lee, M., Heinrich, M., Misawa, K., et al. (2018). Attention u-net: learning where to look for the pancreas. *arXiv arXiv*:1804.03999.

Ronneberger, O., Fischer, P., and Brox, T. (2015). "U-net: convolutional networks for biomedical image segmentation," in *International Conference on Medical Image Computing and Computer-Assisted Intervention* (Cham: Springer), 234–241.

Shi, F., Chen, X., Zhao, H., Zhu, W., Xiang, D., Gao, E., et al. (2014). Automated 3-d retinal layer segmentation of macular optical coherence tomography images with serous pigment epithelial detachments. *IEEE Trans. Med. Imaging* 34, 441–452. doi: 10.1109/TMI.2014.2359980

Talisa, E., Bonini Filho, M. A., Chin, A. T., Adhi, M., Ferrara, D., Baumal, C. R., et al. (2015). Spectral-domain optical coherence tomography angiography of choroidal neovascularization. *Ophthalmology* 122, 1228–1238. doi: 10.1016/j.ophtha.2015.01.029

Wang, M., Zhu, W., Yu, K., Chen, Z., Shi, F., Zhou, Y., et al. (2021a). Semi-supervised capsule cgan for speckle noise reduction in retinal oct images. *IEEE Trans. Med. Imaging* 40, 1168–1183. doi: 10.1109/TMI.2020.3048975

Wang, T., Zhu, W., Wang, M., Chen, Z., and Chen, X. (2021b). "Cu-segnet: corneal ulcer segmentation network," In *2021 IEEE 18th International Symposium on Biomedical Imaging (ISBI)* (Nice: IEEE), 1518–1521.

Xi, X., Meng, X., Yang, L., Nie, X., Yang, G., Chen, H., et al. (2019). Automated segmentation of choroidal neovascularization in optical coherence tomography images using multi-scale convolutional neural networks with structure prior. *Multimedia Syst.* 25, 95–102. doi: 10.1007/s00530-017-0582-5

Zhang, Y., Ji, Z., Wang, Y., Niu, S., Fan, W., Yuan, S., et al. (2019). Mpb-cnn: a multi-scale parallel branch cnn for choroidal neovascularization segmentation in sd-oct images. *OSA Continuum* 2, 1011–1027. doi: 10.1364/OSAC.2.001011

Zhao, H., Shi, J., Qi, X., Wang, X., and Jia, J. (2017). "Pyramid scene parsing network," in *Proceedings of the IEEE Conference on Computer Vision and Pattern Recognition* (Honolulu, HI: IEEE), 2881–2890.

Zhu, S., Shi, F., Xiang, D., Zhu, W., Chen, H., and Chen, X. (2017). Choroid neovascularization growth prediction with treatment based on reaction-diffusion model in 3-d oct images. *IEEE J. Biomed. Health Inform*. 21, 1667–1674. doi: 10.1109/JBHI.2017.2702603

Conflict of Interest: The authors declare that the research was conducted in the absence of any commercial or financial relationships that could be construed as a potential conflict of interest.

frontiers
in Neuroscience

ORIGINAL RESEARCH
published: 13 October 2021
doi: 10.3389/fnins.2021.758887

Optimized-Unet: Novel Algorithm for Parapapillary Atrophy Segmentation

Cheng Wan[1], Jiasheng Wu[2], Han Li[1], Zhipeng Yan[3], Chenghu Wang[3], Qin Jiang[3], Guofan Cao[3]*, Yanwu Xu[4]* and Weihua Yang[3]*

[1] College of Electronic and Information Engineering/College of Integrated Circuits, Nanjing University of Aeronautics and Astronautics, Nanjing, China, [2] School of Electronic Information and Communications, Huazhong University of Science and Technology, Wuhan, China, [3] The Affiliated Eye Hospital of Nanjing Medical University, Nanjing, China, [4] Intelligent Healthcare Unit, Baidu, Beijing, China

In recent years, an increasing number of people have myopia in China, especially the younger generation. Common myopia may develop into high myopia. High myopia causes visual impairment and blindness. Parapapillary atrophy (PPA) is a typical retinal pathology related to high myopia, which is also a basic clue for diagnosing high myopia. Therefore, accurate segmentation of the PPA is essential for high myopia diagnosis and treatment. In this study, we propose an optimized Unet (OT-Unet) to solve this important task. OT-Unet uses one of the pre-trained models: Visual Geometry Group (VGG), ResNet, and Res2Net, as a backbone and is combined with edge attention, parallel partial decoder, and reverse attention modules to improve the segmentation accuracy. In general, using the pre-trained models can improve the accuracy with fewer samples. The edge attention module extracts contour information, the parallel partial decoder module combines the multi-scale features, and the reverse attention module integrates high- and low-level features. We also propose an augmented loss function to increase the weight of complex pixels to enable the network to segment more complex lesion areas. Based on a dataset containing 360 images (Including 26 pictures provided by PALM), the proposed OT-Unet achieves a high AUC (Area Under Curve) of 0.9235, indicating a significant improvement over the original Unet (0.7917).

Keywords: medical image segmentation, high myopia, parapapillary atrophy, convolutional neural network, fundus image

OPEN ACCESS

Edited by:
Jian Zheng,
Suzhou Institute of Biomedical Engineering and Technology, Chinese Academy of Sciences (CAS), China

Reviewed by:
Xi Jiang,
University of Electronic Science and Technology of China, China
Weifang Zhu,
Soochow University, China

****Correspondence:***
Guofan Cao
caoguofan587@163.com
Yanwu Xu
ywxu@ieee.org
Weihua Yang
benben0606@139.com

Specialty section:
This article was submitted to Perception Science, a section of the journal Frontiers in Neuroscience

Received: *15 August 2021*
Accepted: *23 September 2021*
Published: *13 October 2021*

Citation:
Wan C, Wu J, Li H, Yan Z, Wang C, Jiang Q, Cao G, Xu Y and Yang W (2021) Optimized-Unet: Novel Algorithm for Parapapillary Atrophy Segmentation. Front. Neurosci. 15:758887. doi: 10.3389/fnins.2021.758887

INTRODUCTION

Myopia is a common eye disease, which refers to the blur of vision when light enters the eye and gathers in front of the human retina (Saw et al., 1996). Some patients experience symptoms such as headache and eye fatigue. Myopia is the main cause of vision loss worldwide (Fredrick, 2002). Vision can be corrected using glasses, contact lenses, and refractive surgery; however, they do not solve the potential defects (Morgan et al., 2012; Dolgin, 2015). In recent years, the global proportion of patients with myopia has been increasing (Holden et al., 2016). Adolescent myopia has become a common phenomenon in East and Southeast Asia (Morgan et al., 2018). The degree of myopia is usually divided by the size of the diopter D, which is divided into mild myopia (−3 D or below), moderate myopia (−3 D to −6 D), and high myopia (−6 D or above)

(Saw et al., 2005). Patients with high myopia are more likely to have retinal detachment, and the probability of suffering from glaucoma is higher. Floating objects and shadows appear in the field of vision in many highly myopic patients. The medical burden of high myopia includes pathological complications such as myopic macular degeneration, choroidal neovascularization, cataracts, and glaucoma (Pan et al., 2012).

Parapapillary atrophy (PPA) often occurs in the fundus of patients with high myopia. The extent and development of PPA are useful medical assessment tools because they are closely related to the severity of several eye diseases and conditions, including glaucomatous optic nerve damage, visual field defects, and myopia (Heijl and Samander, 1985; Park et al., 1996; Uchida et al., 1998; Dai et al., 2013). The size and position of PPA are not fixed. If it progresses to the macular area, patients will find it difficult to see objects close to them. Generally, it is determined whether it is still expanding according to the shrinking edge. A clear edge indicates that the PPA has probably stopped progressing; the fuzzy and irregular edges indicate that it is still progressing.

Currently, convolutional neural networks are widely used in the field of medical diagnosis (Fang et al., 2020; Xia et al., 2020; Yang et al., 2021). This study attempts to use a new type of convolutional neural network (OT-Unet) to automatically segment PPA. The OT-Unet is based on Unet, using three pre-training models: VGG, ResNet, and Res2Net in the convolutional feature extraction stage. The edge attention, parallel partial decoder, and reverse attention modules were added to the network, and the loss function was improved simultaneously. Considering these improvements, the accuracy of the network segmentation has significantly improved.

MATERIALS AND METHODS

Data Acquisition and Processing

There are few datasets of color fundus photos for high myopia, and only 26 images on iChallenge-PALM can be retrieved on the Internet. This cannot meet the needs of segmentation network training. The research team obtained more than 400 datasets from the Affiliated Eye Hospital of Nanjing Medical University. The shooting equipment was a Topcon TRC-NW300 non-mydriatic fundus camera. Preliminary processing of the data was performed. The blurred pictures and pictures with severely deformed fundus were removed, the rectangular pictures were cut into squares, and the size was unified. Finally, 360 color fundus photos of better quality were obtained. **Figure 1** shows color photo of fundus. The labelme tool was used to label the PPA, and the labeling was performed under the guidance of a professional doctor. **Figure 2** shows the relationship between the position of the parapapillary atrophy and optic disc.

The resolution of the color fundus photos used in the experiment was 352 × 352, and the edge truth map was obtained from the real label map using Adobe Illustrator 2019. The dataset was certified by a professional doctor. According to the ratio of 4:1, we divided the data set into 288 training pictures and 72 test pictures. To highlight the PPA while reducing the size of the image, the grayscale fundus photos were obtained. This operation was implemented using Adobe PhotoShop 2019. **Figure 3** shows the original image and its corresponding grayscale map, PPA truth map and PPA edge map.

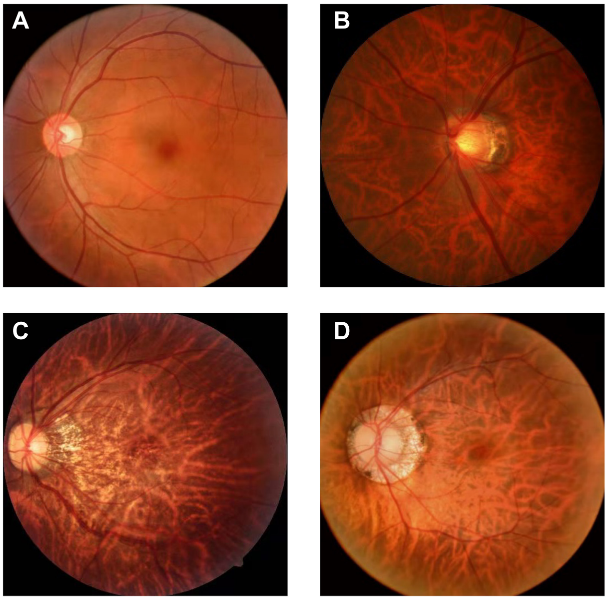

FIGURE 1 | Color photo of fundus: **(A)** fundus of normal eye: It has clear boundary and clear blood vessels, and the overall color is rosy; **(B)** fundus of high myopia: It has blurred boundary, parapapillary atrophy and leopard eye fundus; **(C)** progressive parapapillary atrophy: It has blurred boundary; **(D)** unprogressive parapapillary atrophy: It has clear borders.

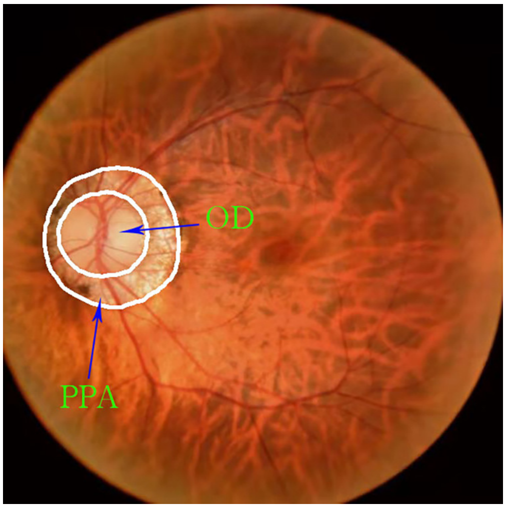

FIGURE 2 | Relationship between the position of the parapapillary atrophy and optic disc: The part inside the white circle in the middle is optic disc, and the ring part between the two white circles is parapapillary atrophy.

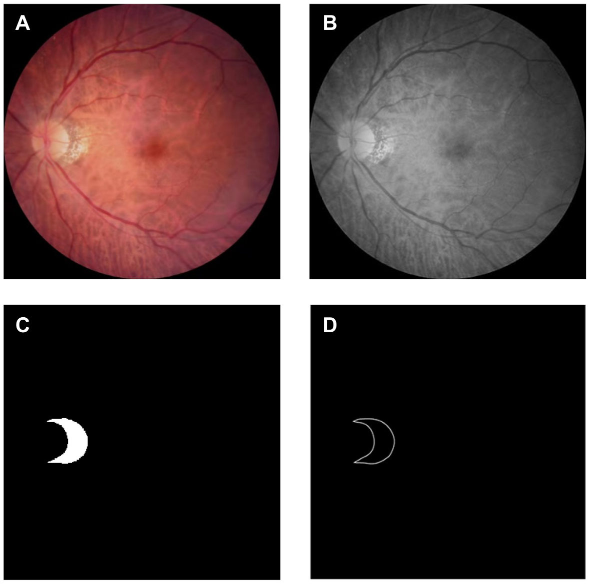

FIGURE 3 | Dataset: **(A)** color photo of the fundus of high myopia: Obtained using Topcon TRC-NW300 non-mydriatic fundus camera; **(B)** grayscale image of the fundus of high myopia: Apply Adobe PhotoShop 2019 to grayscale images; **(C)** gorund truth mask of the parapapillary atrophy: Obtained by labeling the grayscale image using labelme; **(D)** edge map of the parapapillary atrophy: Obtained by processing the real label image using Adobe Illustrator 2019.

Optimized-Unet Overview

The network block diagram of the OT-Unet algorithm proposed in this study is shown in **Figure 4**. The network uses Unet as the backbone network and introduces a pre-training model to generate five convolutional layers. The first two layers $\{f_i, i = 1, 2\}$ are used to extract low-level feature maps that are rich in contextual information, and the high-level feature maps extracted from the last three layers $\{f_i, i = 3, 4, 5\}$ include more local information. An edge attention module is added between the low- and high-level feature convolutional layers to extract the edge feature information of the lesion area. Using the edge feature enhancement module in the second convolutional layer can extract richer local information. Compared with the first convolutional layer, the resolution of the image is lower, which can speed up the calculation. Simultaneously, parallel partial decoders are used to aggregate multi-scale high-level feature information to generate a global map. Since the aggregation of low-level features does not significantly improve the segmentation performance of the network, the network chooses to aggregate three high-level features to obtain richer joint feature information. In addition, the low-level feature map is input to the reverse attention module at all levels under the effect of the global map. These reverse attention modules are cascaded with each other to aggregate the low- and high-level feature information. It can be seen from the figure that the second convolutional layer information, the high-level convolutional layer information, and the aggregated information output by the parallel partial decoder are connected and processed in the reverse attention module. In addition, the use of three reverse attention modules ensures that the network generates sufficiently rich aggregate information. The feature information generated by the last-level inverse attention module is activated by the sigmoid activation function to generate the final lesion area segmentation prediction map. The following will be introduced in detail: the backbone network (Unet), key modules, and improved loss functions.

Backbone Network—Unet

In 2015, Ronneberger et al. (2015) proposed the Unet structure. Unet is a semantic segmentation network based on Fully Convolutional Networks (FCN), which is currently widely used in the field of biomedical image segmentation. The segmentation network system includes contraction (also known as an encoder) and expansion (also known a decoder) paths.

ImageNet's Pre-trained Model

Visual Geometry Group

In 2014, Simonyan and Zisserman (2014) proposed a new network known as the VGG. The image passes through the convolutional layer, and the filter uses a very small receptive field of 3 × 3 (the minimum size to capture the concepts of left/right, up/down, and center).

ResNet

From experience, the depth of the network is critical to the performance of the model. When the number of network layers is increased, the network can extract more complex feature patterns, so theoretically better results can be achieved when the model is deeper. However, when the network reaches a certain level, the depth of the network increases, and the accuracy of the network becomes saturated or even declined. Considering the ResNet (He et al., 2016), the author uses a residual block to avoid this situation.

Res2Net

Most of the existing methods use a hierarchical method to represent multi-scale features; nonetheless, Gao et al. (2021) have constructed hierarchical residual connections in a single residual block in a different way, proposing the Res2Net neural network building block. This module can express particle-level multiscale features and expand the range of receptive fields.

Feature Expression Enhancement Module

Edge Attention Module

The enhancement effect of edge information in segmentation features has been verified in many studies (Zhang et al., 2019; Xing, 2020; Zhao et al., 2020; Zhou, 2020). The resolution of the low-level feature map was higher, and the edge information was richer. The network inputs the feature map obtained by the second- and low-level convolution to the edge attention module, extracts the edge information feature, and obtains the corresponding map. The difference between the generated edge map and edge truth map G_e corresponding to the

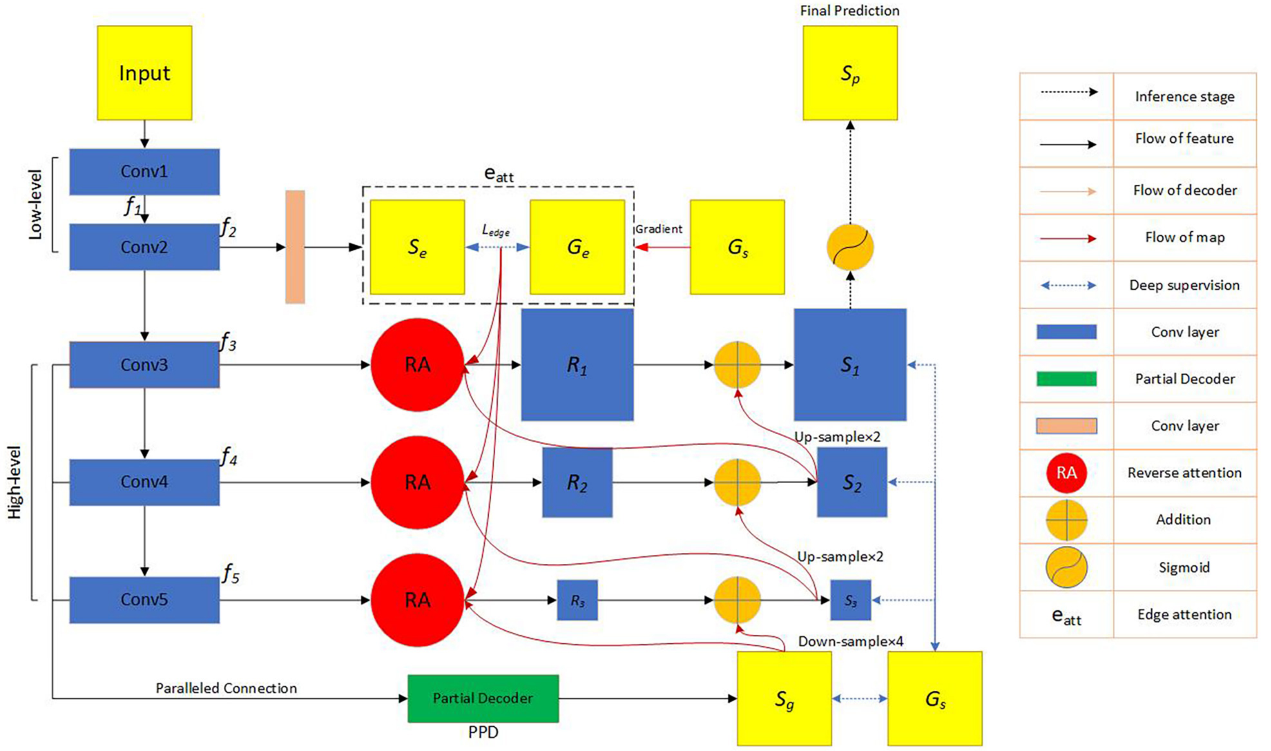

FIGURE 4 | Flow chart of the automatic network segmentation: In the convolutional feature extraction stage, three pre-training models of VGG, ResNet and Res2Net are used, respectively, and the edge attention module, parallel partial decoder module and reverse attention module are added to enhance the feature expression ability. The model also improves the loss function. f_i represents the feature information obtained by the image through the *i*-th convolutional layer. S_e represents the feature information generated by the second convolutional layer information through the edge attention module. G_e represents the edge map obtained by the ground truth map. L_{edge} represents the standard binary cross-entropy loss function. G_S represents the ground truth map. S_g represents the feature information obtained by the parallel partial decoder aggregating high-level convolutional layer information. R_i (i = 1, 2, 3), respectively, represent the feature information output by the three reverse attention modules. S_i (i = 1, 2, 3), respectively, represent the information obtained by the combination of the reverse attention module information and the higher-level information.

true label is calculated using the binary cross entropy (BCE) loss function:

$$L_{edge} = -\sum_{x=1}^{w}\sum_{y=1}^{h}\left[G_e log\left(S_e\right) + \left(1-G_e\right) log\left(1-S_e\right)\right] \quad (1)$$

where (x, y) represent the coordinates of the pixel points in the predicted edge map S_e and the edge truth map G_e. G_e is derived from the real label G_s. w and h represent the width and height of the feature map, respectively.

Parallel Partial Decoder Module

Segmentation through the combined use of high and low feature maps is a common method of medical segmentation (Qian et al., 2015; Zhou et al., 2018; Gu et al., 2019; Fan et al., 2020). However, because of their large size, low-level feature maps require more resources, and the effect on performance improvement is not obvious (Wu et al., 2019). The parallel partial decoder $Pd(\cdot)$ is used to fuse the high-level features to form a prediction map $S_g = Pd\left(f_3, f_4, f_5\right)$, guiding the input of the inverse attention module. **Figure 5** shows parallel partial decoder module frame diagram.

Reverse Attention Module

Inspired by the study of Chen et al. (2018), the network uses the reverse attention module to extract richer information. The inverse attention module uses a progressive framework. Its information comes from the same convolutional layer, and it includes low-level features f_2 and aggregated features from a higher level. This method can obtain more complex feature information and optimize the segmentation performance of the network.

The predicted feature map of the upper layer was expanded after the sigmoid activation, inversion, and smoothing. We multiplied the expanded feature by the high-level output feature (dot multiplication ·) and concatenated it with the edge attention feature $e_{att}\left(f_2\right)$ to obtain the corresponding reverse attention feature output as demonstrated below:

$$R_i = C\left(f_i \cdot A_i, Dow\left(e_{att}\right)\right) \quad (2)$$

where $Dow(\cdot)$ and $C(\cdot)$ are the down-sampling concatenation operations, respectively.

Figure 6 shows frame diagram of the reverse attention module.

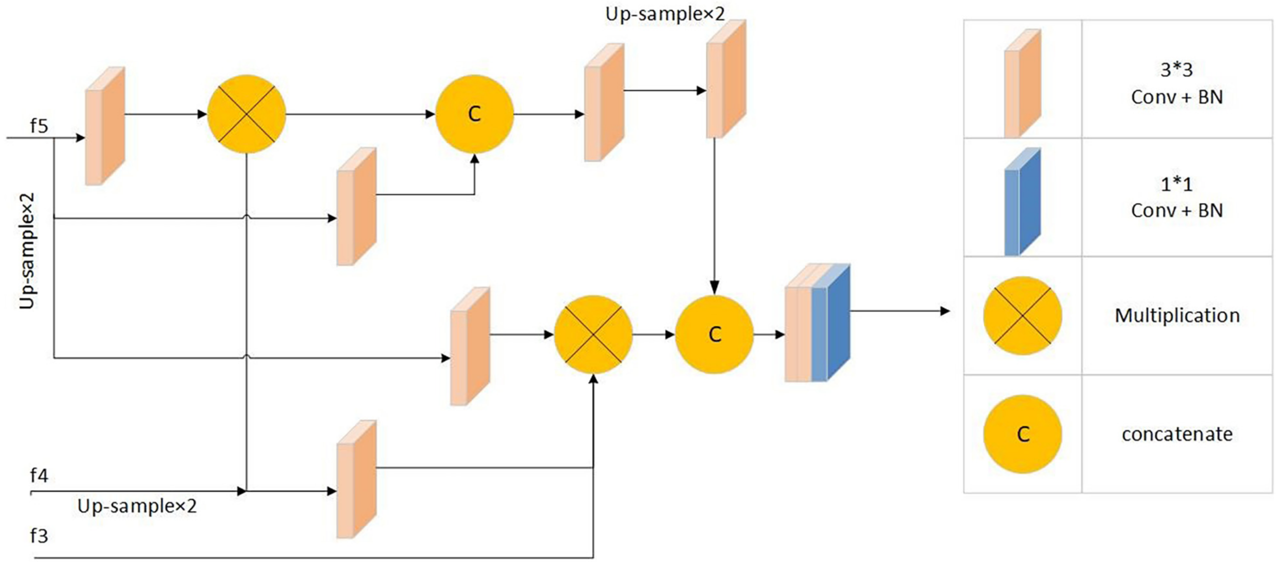

FIGURE 5 | Parallel partial decoder module frame diagram: Including 1*1 convolution + batch normalization processing module, 3*3 convolution + batch normalization processing modules, multiplication operation and concatenate operation.

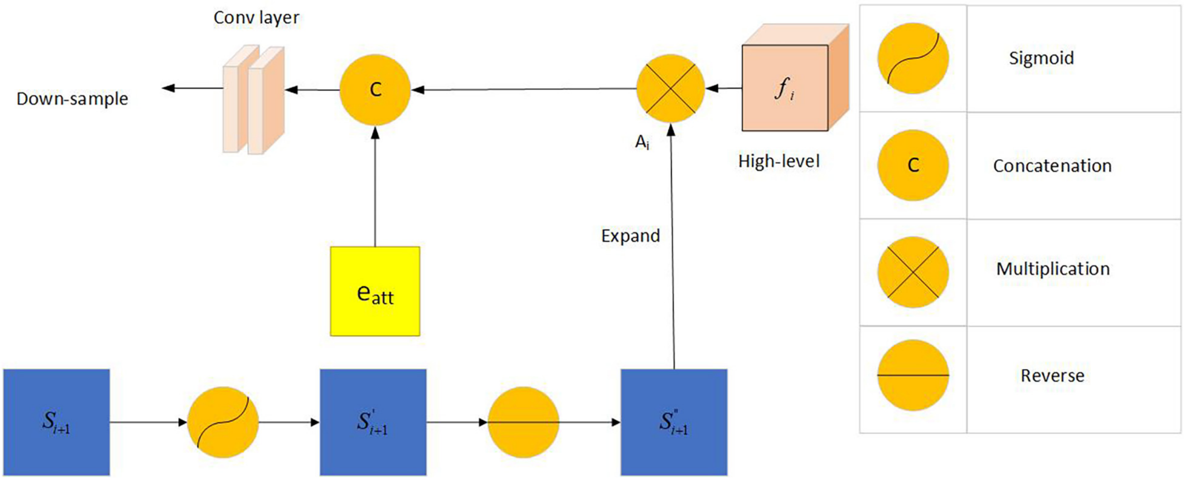

FIGURE 6 | Frame diagram of the reverse attention module: Including Sigmoid activation function, concatenation operation, multiplication operation and reverse operation. f_i (i = 3,4,5) represents the feature information obtained by the picture through the i-th convolutional layer. S_{i+1} (i = 1, 2) represents the information obtained by the combination of the reverse attention module information and the higher-level information. A_i represents the output after S_{i+1} expand.

Loss Function

The standard IoU loss and binary cross-entropy loss functions are the commonly used loss functions. The calculation formulas are as follows:

$$L_{IoU} = 1 - \frac{|A \cap B|}{|A \cup B|} \tag{3}$$

$$L_{BCE} = -\left(ylog\left(p\right) + \left(1{-}y\right) log\left(1{-}p\right)\right) \tag{4}$$

$$weight = 1 + 5\left|AVG(B) - B\right| \tag{5}$$

$$L^{w}_{IoU} = 1 - \frac{(A \cap B) \cdot weight + 1}{|A \cup B| \cdot weight - |A \cap B| \cdot weight + 1} \tag{6}$$

$$L^{w}_{BCE} = \frac{L_{BCE} \cdot weight}{weight} \tag{7}$$

where A represents the predicted map, B represents the true label, y is the true category, and p is the probability of the predicted category. AVG() is a function in the torch library, specifically torch.nn.AvgPool2d(kernel_size, stride = None, padding = 0), kernel size is the size of the window, stride is the stride of the

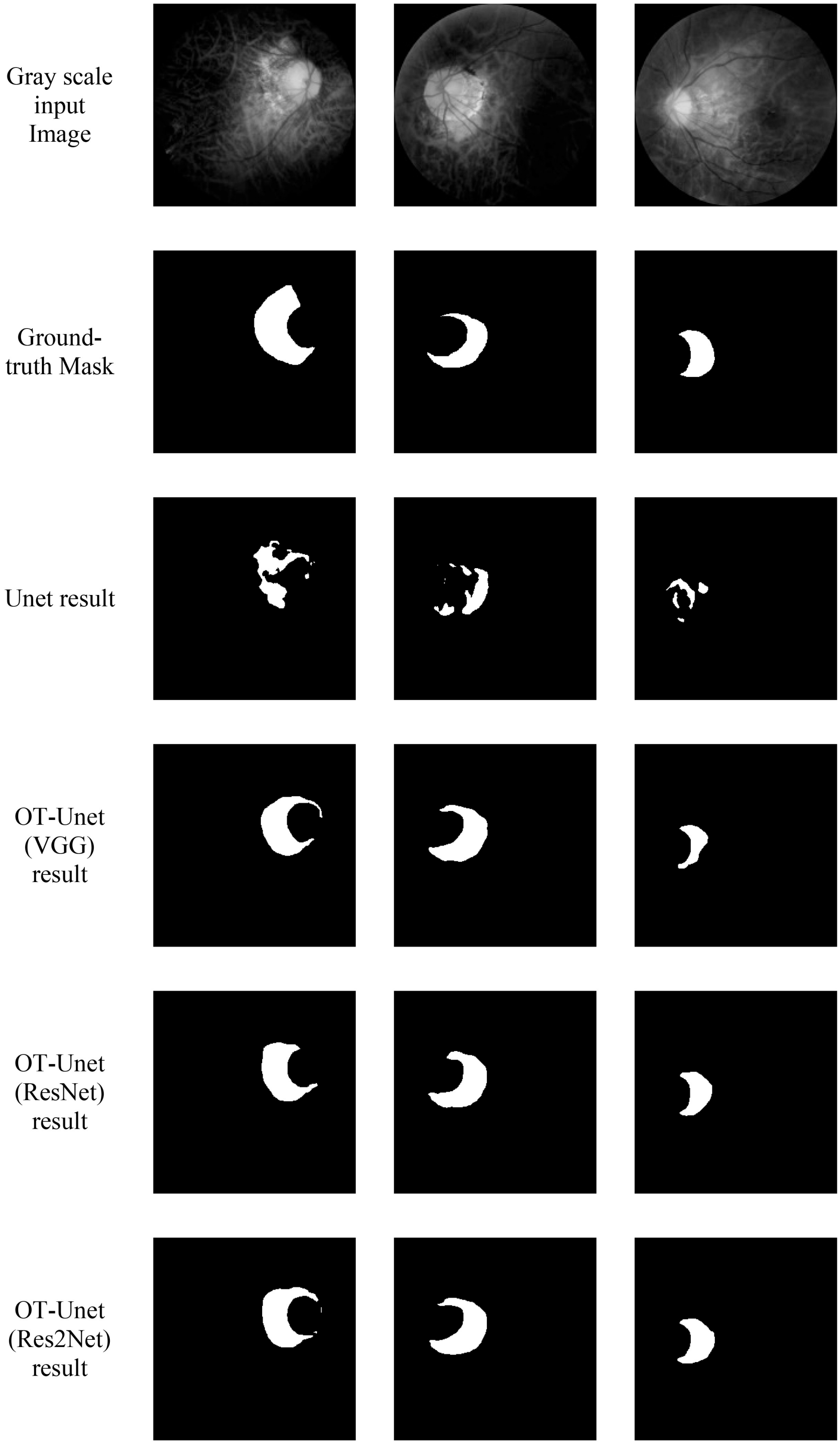

FIGURE 7 | Visualized results of the segmentation of parapapillary atrophy in high myopia: It shows the Gray scale input Image, the Ground-truth Mask, and the segmentation results of Unet, OT-Unet (VGG), OT-Unet (ResNet), and OT-Unet (Res2Net).

TABLE 1 | Comparison of segmentation results of different models.

Methods	Precision	Sensitivity	Specificity	AUC	IoU	DSC
Unet	0.7226	0.8303	0.9879	0.7917	0.4731	0.6413
OT-Unet (VGG)	**0.8227**	0.8225	**0.9963**	0.9134	0.7004	0.8086
OT-Unet (ResNet)	0.7980	0.8398	0.9957	0.9171	0.6877	0.8022
OT-Unet (Res2Net)	0.8020	**0.8450**	0.9958	**0.9235**	**0.7034**	**0.8101**

DSC means Dice similarity coefficient. Bold values indicate that the value is the largest in the same indicator.

TABLE 2 | Comparison of the segmentation results of OT-Unet (Res2Net) in different sizes of lesion areas.

Type of lesion	Precision	Sensitivity	Specificity	AUC	IoU	DSC
Small lesion	0.7479	0.8287	0.9956	0.9076	0.6517	0.7712
Large lesion	**0.9251**	**0.8820**	**0.9962**	**0.9352**	**0.8209**	**0.8986**

Bold values indicate that the value is the largest in the same indicator.

window, and padding is implicit zero padding to be added on both sides.Input(*N,C,Hin,Win*), output(*N,C,Hout,Wout*), where

$$H_{out} = \left\lfloor \frac{H_{in} + 2 \times \text{padding}\,[0] - \text{kernel\_size}\,[0]}{\text{stride}\,[0]} + 1 \right\rfloor \quad (8)$$

$$W_{out} = \left\lfloor \frac{W_{in} + 2 \times \text{padding}\,[1] - \text{kernel\_size}\,[1]}{\text{stride}\,[1]} + 1 \right\rfloor \quad (9)$$

Where *N* stands for quantity, *C* stands for channel, *Hin* stands for input height, *Win* stands for input width, *Hout* stands for output height, and *Wout* stands for output width.

However, the weights assigned to each pixel by the above two loss functions are the same, and they do not focus on the extraction of complex pixel samples. This study combines the weighted IoU and weighted BCE loss functions to obtain a new loss function:

$$L_{seg} = L_{IoU}^{w} + L_{BCE}^{w} \quad (10)$$

To facilitate the calculation, each predicted feature map is restored to its original size through an up-sampling operation (for example, S_3^{up}). Therefore, we rewrite the total loss function as:

$$L_{total} = L_{seg}\left(G_s, S_g^{up}\right) + L_{edge} + \sum_{i=3}^{5} L_{seg}\left(G_s, S_i^{up}\right) \quad (11)$$

RESULTS

Visualization of Segmentation Results

Figure 7 shows the visualized results of high myopia grayscale images, real labels, and the visual segmentation results of the PPA. It can be observed that the OT-Unet segmentation algorithm has a better segmentation effect than the original Unet.

Comparison of Segmentation Results

The following are the experimental segmentation results of the four networks.

Considering **Table 1**, it can be observed that the segmentation network of this study has improved for all the indicators. It can be seen that OT-Unet is significantly better than Unet in all indicators. The three pre-training models of OT-Unet have different performance in various indicators. OT-Unet (VGG) has the best performance on the Precision and Specificity indicators; on the other indicators, OT-Unet (Res2Net) has the best performance. **Figure 8** shows experimental ROC curve diagram of different segmented image networks.

Comparison of the Segmentation Results of Large and Small Lesions

Based on the relationship between the PPA and papilla diameter (PD), we divided the PPA that was less than or equal to one-third of the PD into small lesion areas (50 images), and the rest were large lesion areas (22 images). The best-performing Res2Net pre-training model was used for the segmentation to obtain the visualization and quantification results.

The quantification results of the segmentation of the large and small lesions are shown in **Table 2**. When OT-Unet segmented large lesions, its Precision, Sensitivity, Specificity and AUC scores were higher than those of small lesions. When segmenting a small lesion area, the lesion area is smaller than the optic disc and is more disturbed by it. Other non-lesion regions around the optic disc also interfere with the segmentation.

According to the segmentation results, the segmentation performance of the OT-Unet on a large lesion area is better than that of a small lesion area in all indicators. When segmenting a small lesion area, the model is more susceptible to the influence of other areas around the optic disc, and even an extreme situation where the segmentation area does not match the real label at all occurs as shown in **Figure 9**.

DISCUSSION

As a method of auxiliary diagnosis, automatic segmentation of ophthalmic medical images can help ophthalmologists to understand a patient's fundus more conveniently and clearly, indicating that this study is very valuable. The width of the PPA is positively correlated with the degree of myopia; therefore, early diagnosis is very important for patients with high myopia. Automatic segmentation of medical images can effectively extract and express image features with less preprocessing and reduce labor costs. Considering the introduction of many excellent segmentation network models and rapid improvement in image processor performance, deep learning can achieve higher segmentation accuracy.

Currently, there are few studies on the automatic segmentation of the PPA. The datasets on the Internet are very limited, manual labeling is time-consuming and laborious, and labeling accuracy cannot be guaranteed. In addition, the early PPA was crescent-shaped, which occurred near the optic disc with a small area. The difference between PPA and the brightness of the optic disc is not obvious, making it easy to be affected by the optic disc when splitting the PPA. Meanwhile, patients with high myopia often have a leopard-shaped fundus,

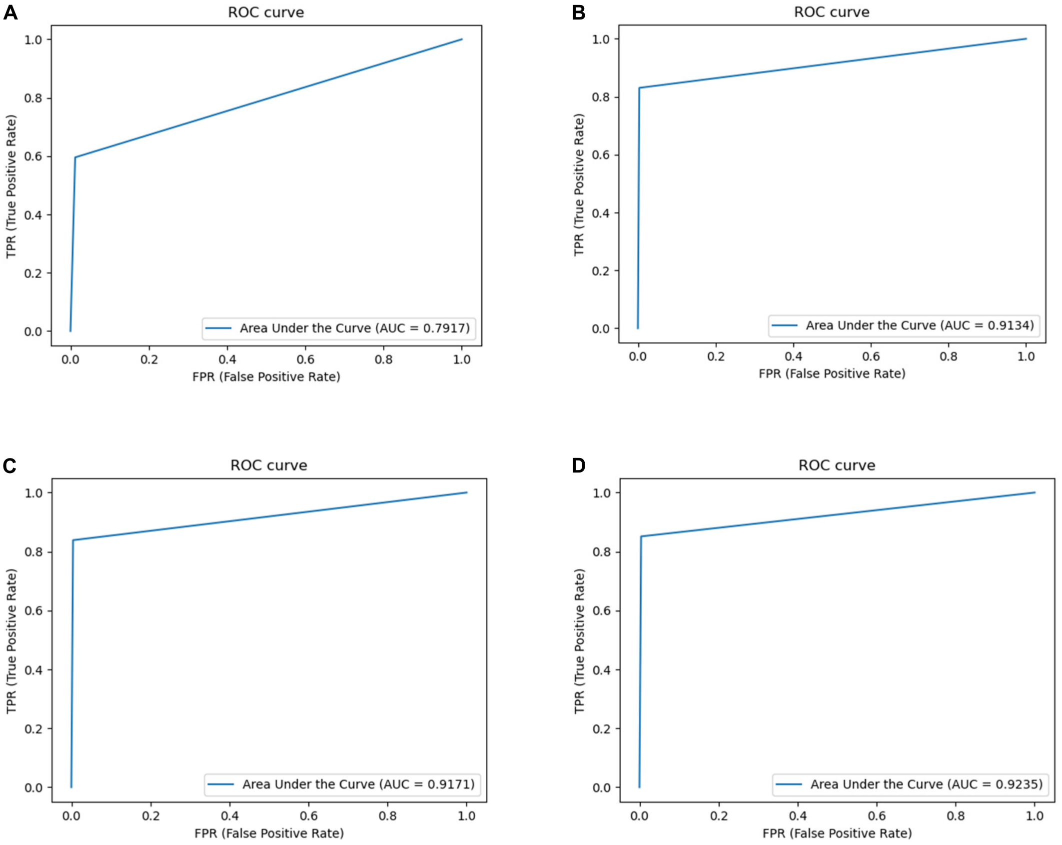

FIGURE 8 | Experimental ROC curve diagram: **(A)** Unet (AUC = 0.7917); **(B)** VGG network (AUC = 0.9134); **(C)** ResNet (AUC = 0.9171); **(D)** Res2Net (AUC = 0.9235).

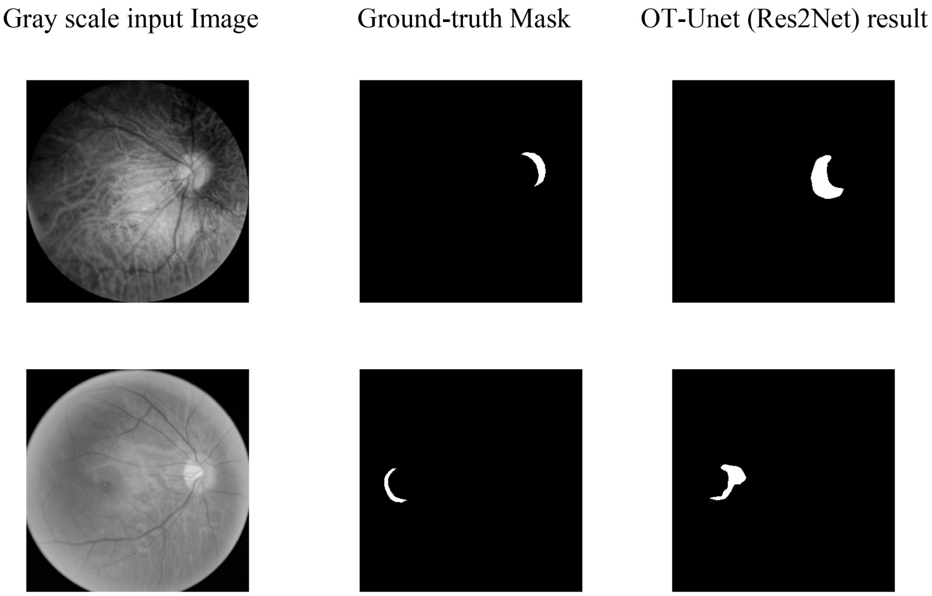

FIGURE 9 | Segmentation of extremely small lesions: It can be seen that the segmentation prediction map does not correspond to the Ground-truth Mask at all.

which is a result of stretching the retina. Visible blood vessels affect the recognition and segmentation of the lesion area and reduce the accuracy of the segmentation. There is no obvious rule for the expansion of the PPA, and the shape and size of the PPA of the fundus in different patients are quite different. There was obvious pigmentation in the PPA, which will also affect the segmentation of PPA. It can be observed that various factors restrict the study of the PPA segmentation network.

The experimental results show that Unet can only segment the approximate outline of the lesion area, which is greatly affected by the optic disc. Also, the prediction map is irregular and has many noises. In the feature extraction stage, OT-Unet uses VGG, ResNet and Res2Net three pre-training models to extract richer feature information. Considering the problem of irregular contours of the lesion, this study adopts the method of adding the edge attention module to extract the contour features of the lesion area during the training phase of feature learning. The trained model can generate a clearer boundary prediction map. Solving the problem of the Unet being severely interfered by the optic disc, this study uses a parallel partial decoder and reverse attention modules to obtain more high-level and low-level fusion features. This helps the network learnt to distinguish between the PPA and optic disc, avoiding splitting the disc. OT-Unet also improved the loss function to get more accurate segmentation results.

However, according to the visualization results, the segmentation result still cannot completely avoid the interference of the optic disc, and the effect is not sufficient when segmenting the small-sized PPA. In the future, the learning ability of the low-level features of the network will be further enhanced to make the network perform better in the segmentation of small lesion areas.

Compared to the original segmentation network (Unet), the improved network has a better effect on lesion segmentation; however, there are still some areas to be improved. Only 288 training images are used in this study, which weakens the generalization ability of the network. Considering high myopia, the size and shape of the PPA at different stages of development are very different, and the use of the same segmentation strategy will reduce the segmentation effect. The improved network makes it difficult to segment small-sized PPA. In the future, it will be necessary to use larger datasets and use data enhancement methods for expansion. Before segmentation, a classification network can be used to classify the PPA according to early, middle, and late stages. Subsequently, based on the characteristics of the para-optical atrophy in the different stages, targeted segmentation strategies can be formulated for segmentation. Regarding the loss function, this study does not systematically study the weight distribution of the weighted IoU and binary cross-entropy loss functions; nonetheless, it simply adds them. In the future, the relationship between these two loss functions can be explored, and a more appropriate weight distribution of the loss functions can be found to improve the segmentation performance of the network.

CONCLUSION

Considering the segmentation task of PPA for high myopia, this study proposes an OT-Unet algorithm network. In this study, three pre-training models (VGG, ResNet, and Res2Net) are used in the Unet for the extraction of convolutional features. Between the high- and low-level convolutions, this study introduces an edge attention module to extract edge feature maps and enrich the network information. Multi-scale high-level feature maps use a parallel partial decoder module to perform feature fusion and obtain global information. The network also uses a reverse attention module which uses a progressive framework to extract high- and low-level feature information. Considering the loss function, the network combines the weighted IoU and binary cross-entropy loss functions to increase the weight of the complex pixels. This shows that the improvement of the network structure and loss function significantly improves the segmentation performance of the network and obtains a better segmentation effect than the Unet in the segmentation of the lesion area. Compared to the Unet, the improved OT-Unet is superior for all the evaluation criteria.

DATA AVAILABILITY STATEMENT

The raw data supporting the conclusions of this article will be made available by the authors, without undue reservation.

AUTHOR CONTRIBUTIONS

CW contributed to the conception of the study and performed the experiments. JW performed the data analyses and wrote the manuscript. HL helped to perform the analysis with constructive discussions. ZY, CHW, and QJ collected the data and directed the writing of the manuscript. GC contributed significantly to analysis and manuscript preparation. YX revised the manuscript. WY supervised the whole study. All authors contributed to the study and approved the submitted version.

FUNDING

This study was supported by the Chinese Postdoctoral Science Foundation (2019M661832), Jiangsu Planned Projects for Postdoctoral Research Funds (2019K226), the Jiangsu Province Advantageous Subject Construction Project, and the Nanjing Enterprise Expert Team Project.

ACKNOWLEDGMENTS

We thank the Affiliated Eye Hospital of Nanjing Medical University for providing the fundus data set.

REFERENCES

Chen, S., Tan, X., Wang, B., Lu, H., Hu, X., Fu, Y., et al. (2018). "Reverse attention for salient object detection," in *Lecture Notes in Computer Science*, eds V. Ferrari, M. Hebert, C. Sminchisescu, and Y. Weiss (Cham: Springer), 236–252. doi: 10.1007/978-3-030-01240-3_15

Dai, Y., Jonas, J. B., Huang, H., Wang, M., and Sun, X. (2013). Microstructure of parapapillary atrophy: beta zone and gamma zone. *Invest. Ophthalmol. Vis. Sci.* 54, 2013–2018. doi: 10.1167/iovs.12-11255

Dolgin, E. (2015). The myopia boom. *Nature* 519, 276–278. doi: 10.1038/519276a

Fan, D. P., Zhou, T., Ji, G.-P., Zhou, Y., Chen, G., Fu, H., et al. (2020). Inf-net: automatic covid-19 lung infection segmentation from ct images. *IEEE Trans. Med. Imaging* 39, 2626–2637. doi: 10.1109/TMI.2020.2996645

Fang, J., Xu, Y., Zhang, X., Hu, Y., and Liu, J. (2020). "Attention-based saliency hashing for ophthalmic image retrieval," in *Proceedings of the IEEE International Conference on Bioinformatics and Biomedicine (BIBM)*, (Piscataway, NJ: Institute of Electrical and Electronics Engineers), 990–995. doi: 10.1109/BIBM49941.2020.9313536

Fredrick, D. R. (2002). Myopia. *BMJ* 324, 1195–1199. doi: 10.1136/bmj.324.7347.1195

Gao, S. H., Cheng, M.-M., Zhao, K., Zhang, X.-Y., Yang, M.-H., and Torr, P. (2021). Res2net: a new multi-scale backbone architecture. *IEEE Trans. Pattern Anal. Mach. Intell.* 43, 652–662. doi: 10.1109/TPAMI.2019.2938758

Gu, Z., Cheng, J., Fu, H., Zhou, K., Hao, H., Zhao, Y., et al. (2019). Ce-net: context encoder network for 2d medical image segmentation. *IEEE Trans. Med. Imaging* 38, 2281–2292. doi: 10.1109/TMI.2019.2903562

He, K., Zhang, X., Ren, S., and Sun, J. (2016). "Deep residual learning for image recognition," in *Proceedings of the 2016 IEEE Conference on Computer Vision and Pattern Recognition (CVPR)*, (Las Vegas, NV: Institute of Electrical and Electronics Engineers), 770–778. doi: 10.1109/CVPR.2016.90

Heijl, A., and Samander, C. (1985). "Peripapillary atrophy and glaucomatous visual field defects," in *Proceedings of the 6th International Visual Field Symposium. Documenta Ophthalmologica Proceedings Series*, eds A. Heijl and E. L. Greve (Dordrecht: Springer), 403–407. doi: 10.1007/978-94-009-5512-7_58

Holden, B. A., Fricke, T. R., Wilson, D. A., Jong, M., Naidoo, K. S., Sankaridurg, P., et al. (2016). Global prevalence of myopia and high myopia and temporal trends from 2000 through 2050. *Ophthalmology* 123, 1036–1042. doi: 10.1016/j.ophtha.2016.01.006

Morgan, I. G., French, A. N., Ashby, R. S., Guo, X., Ding, X., He, M., et al. (2018). The epidemics of myopia: aetiology and prevention. *Prog. Retin. Eye Res.* 62, 134–149. doi: 10.1016/j.preteyeres.2017.09.004

Morgan, I. G., Ohno-Matsui, K., and Saw, S.-M. (2012). Myopia. *Lancet* 379, 1739–1748. doi: 10.1016/S0140-6736(12)60272-4

Pan, C. W., Ramamurthy, D., and Saw, S.-M. (2012). Worldwide prevalence and risk factors for myopia. *Ophthalmic Physiol. Opt.* 32, 3–16. doi: 10.1111/j.1475-1313.2011.00884.x

Park, K. H., Tomita, G., Liou, S. Y., and Kitazawa, Y. (1996). Correlation between peripapillary atrophy and optic nerve damage in normal-tension glaucoma. *Ophthalmology* 103, 1899–1906. doi: 10.1016/S0161-6420(96)30409-0

Qian, S., Hai, C. Z., Lin, M., and Zhang, C. (2015). Saliency detection based on conditional random field and image segmentation. *Acta Autom. Sin.* 41, 711–724.

Ronneberger, O., Fischer, P., and Brox, T. (2015). "U-net: convolutional networks for biomedical image segmentation," in *Proceedings of the International Conference on Medical Image Computing and Computer-Assisted Intervention*, (Cham: Springer), 234–241. doi: 10.1007/978-3-319-24574-4_28

Saw, S. M., Gazzard, G., Shih-Yen, E. C., and Chua, W.-H. (2005). Myopia and associated pathological complications. *Ophthalmic Physiol. Opt.* 25, 381–391. doi: 10.1111/j.1475-1313.2005.00298.x

Saw, S. M., Katz, J., Schein, O. D., Chew, S. J., and Chan, T. K. (1996). Epidemiology of myopia. *Epidemiol. Rev.* 18, 175–187. doi: 10.1093/oxfordjournals.epirev.a017924

Simonyan, K., and Zisserman, A. (2014). Very deep convolutional networks for large-scale image recognition. *Arxiv* [Preprint] ArXiv: 1409.1556,

Uchida, H., Ugurlu, S., and Caprioli, J. (1998). Increasing peripapillary atrophy is associated with progressive glaucoma. *Ophthalmology* 105, 1541–1545. doi: 10.1016/S0161-6420(98)98044-7

Wu, Z., Su, L., and Huang, Q. (2019). "Cascaded partial decoder for fast and accurate salient object detection," in *Proceedings of the IEEE/CVF Conference on Computer Vision and Pattern Recognition (CVPR)*, (Piscataway, NJ: Institute of Electrical and Electronics Engineers), 3907–3916. doi: 10.1109/CVPR.2019.00403

Xia, Z., Yue, G., Xu, Y., Feng, C., Yang, M., Wang, T., et al. (2020). "A novel end-to-end hybrid network for Alzheimer's disease detection using 3D CNN and 3D CLSTM," in *Proceedings of the 17th International Symposium on Biomedical Imaging (ISBI)*, (Iowa City, IA: Institute of Electrical and Electronics Engineers), 1–4. doi: 10.1109/ISBI45749.2020.9098621

Xing, C. S. (2020). *Research on Medical Image Segmentation Method Based on Dual Attention Mechanism*. Changchun: Jilin University.

Yang, P., Zhou, F., Ni, D., Xu, Y., Chen, S., Wang, T., et al. (2021). "Fused sparse network learning for longitudinal analysis of mild cognitive impairment," in *Proceedings of the IEEE Transactions on Cybernetics*, (Piscataway, NJ: Institute of Electrical and Electronics Engineers), 233–246. doi: 10.1109/TCYB.2019.2940526

Zhang, Z., Zhang, Z., Fu, H., Dai, H., Shen, J., Pang, Y., et al. (2019). "Et-net: a generic edge-attention guidance network for medical image segmentation," in *Proceedings of the International Conference on Medical Image Computingand Computer-Assisted Intervention*, (Cham: Springer), 442–450.

Zhao, J., Liu, J. J., Fan, D. P., Cao, Y., Yang, J., and Cheng, M.-M. (2020). "EGNet: edge guidance network for salient object detection," in *Proceedings of the CVF International Conference on Computer Vision (ICCV)*, (Piscataway, NJ: Institute of Electrical and Electronics Engineers).

Zhou, Y. (2020). Saliency detection based on edge effect and attention mechanism. *Comput. Eng. Softw.* 41, 111–116.

Zhou, Z., Rahman Siddiquee, M. M., Tajbakhsh, N., and Liang, J. (2018). "Unet++: a nested u-net architecture for medical image segmentation," in Proceedings of the Deep Learning in Medical Image Analysis and Multimodal Learning for Clinical Decision Support, (Cham: Springer), 3–11.

Conflict of Interest: The authors declare that the research was conducted in the absence of any commercial or financial relationships that could be construed as a potential conflict of interest.

frontiers in Psychology

ORIGINAL RESEARCH
published: 22 October 2021
doi: 10.3389/fpsyg.2021.759229

Implementation and Application of an Intelligent Pterygium Diagnosis System Based on Deep Learning

Wei Xu[1,2†], Ling Jin[3†], Peng-Zhi Zhu[4†], Kai He[5,6], Wei-Hua Yang[3] and Mao-Nian Wu[5,6*]*

[1] Department of Optometry, Jinling Institute of Technology, Nanjing, China, [2] Nanjing Key Laboratory of Optometric Materials and Application Technology, Nanjing, China, [3] Affiliated Eye Hospital of Nanjing Medical University, Nanjing, China, [4] Guangdong Medical Devices Quality Surveillance and Test Institute, Guangzhou, China, [5] School of Information Engineering, Huzhou University, Huzhou, China, [6] Zhejiang Province Key Laboratory of Smart Management & Application of Modern Agricultural Resources, Huzhou, China

Edited by:
Haoyu Chen,
Shantou University & The Chinese University of Hong Kong, China

Reviewed by:
Suho Lim,
Daegu Veterans Health Service Medical Center, South Korea
Aouache Mustapha,
Center for Development of Advanced Technologies (CDTA), Algeria
Kosol Kampitak,
Thammasat University, Thailand

***Correspondence:**
Wei-Hua Yang
benben0606@139.com
Mao-Nian Wu
wmn@zjhu.edu.cn

† These authors share first authorship

Specialty section:
This article was submitted to Perception Science, a section of the journal Frontiers in Psychology

Received: 16 August 2021
Accepted: 04 October 2021
Published: 22 October 2021

Citation:
Xu W, Jin L, Zhu P-Z, He K, Yang W-H and Wu M-N (2021) Implementation and Application of an Intelligent Pterygium Diagnosis System Based on Deep Learning. Front. Psychol. 12:759229. doi: 10.3389/fpsyg.2021.759229

Objective: This study aims to implement and investigate the application of a special intelligent diagnostic system based on deep learning in the diagnosis of pterygium using anterior segment photographs.

Methods: A total of 1,220 anterior segment photographs of normal eyes and pterygium patients were collected for training (using 750 images) and testing (using 470 images) to develop an intelligent pterygium diagnostic model. The images were classified into three categories by the experts and the intelligent pterygium diagnosis system: (i) the normal group, (ii) the observation group of pterygium, and (iii) the operation group of pterygium. The intelligent diagnostic results were compared with those of the expert diagnosis. Indicators including accuracy, sensitivity, specificity, kappa value, the area under the receiver operating characteristic curve (AUC), as well as 95% confidence interval (CI) and F1-score were evaluated.

Results: The accuracy rate of the intelligent diagnosis system on the 470 testing photographs was 94.68%; the diagnostic consistency was high; the kappa values of the three groups were all above 85%. Additionally, the AUC values approached 100% in group 1 and 95% in the other two groups. The best results generated from the proposed system for sensitivity, specificity, and F1-scores were 100, 99.64, and 99.74% in group 1; 90.06, 97.32, and 92.49% in group 2; and 92.73, 95.56, and 89.47% in group 3, respectively.

Conclusion: The intelligent pterygium diagnosis system based on deep learning can not only judge the presence of pterygium but also classify the severity of pterygium. This study is expected to provide a new screening tool for pterygium and benefit patients from areas lacking medical resources.

Keywords: intelligent diagnosis system, pterygium, anterior segment photograph, deep learning, diagnostic model training

INTRODUCTION

Pterygium is a common exterior ocular disease with unknown etiology. It is essentially a chronic conjunctival degeneration more common among people who live near the equator or work outdoors (e.g., fishermen and farmers) and is thought to be an irritative phenomenon due to ultraviolet light, drying, and windy environments (Coroneo, 2011; Delic et al., 2017). A pterygium is clinically divided into two phases: active and stationary. As a horizontal, triangular growth of the bulbar conjunctiva with the head extending toward the cornea, it appears as hypertrophy and hyperemia of the fibrovascular tissue in the active phase, with corneal infiltration. In the stationary phase, it shows no hyperemia, no or less fibrovascular proliferation, a flat head of the pterygium, and transparent cornea. If the pterygium in the active phase enlarges and encroaches on the pupillary area, it may cause vision loss with limited eye movement, pain, congestion, and other symptoms, as well as affect an individual's appearance, and trigger astigmatism and higher-order aberrations (Lin and Stern, 1998; Gumus et al., 2012; Zhou et al., 2018). Currently, surgical resection is the main clinical treatment (Graue-Hernandez et al., 2019). If a patient is diagnosed early and treated with proper adjuvants, such as corticosteroids and mitomycin C, pterygium growth can effectively be controlled, and the recurrence rate could be reduced before and after surgical excision (Kaufman et al., 2013; Chen et al., 2015; Abdani et al., 2020). Early diagnosis helps to alleviate a patient's pain, relieve their economic burden, and improve the quality of their vision.

Traditional screening methods for pterygium mainly depend on slit-lamp microscope observations and anterior segment photographs taken by ophthalmologists (Troutbeck and Hirst, 2001; Gumus et al., 2011). However, due to the lack of primary ophthalmologists, screening for pterygium still faces a huge gap in remote or rural areas with relatively limited medical resources. With the constant improvement of artificial intelligence (AI) theories and technologies, intelligent diagnosis and treatment have been rapidly growing in recent years; thus, many ophthalmologists and intelligent technologists have focused on relevant research. Deep learning was first used by the Google team to diagnose diabetic retinopathy (DR) through fundus images in 2016 (Gulshan et al., 2016). Since then different researchers have used deep learning models to detect DR (Kermany et al., 2018; Raman et al., 2018) and other fundus diseases, such as glaucoma (Li et al., 2018; Medeiros et al., 2020) and age-related macular degeneration (Nagasato et al., 2018; Yim et al., 2020). These studies obtained remarkable results and provided extensive ideas for clinical AI application. Some researchers have attempted using deep learning for ocular surface disease, the common one being pterygium. An iris segmentation method has been proposed to assess ptergium-infected tissues by analyzing anterior segment photographed images (ASPI) using digital image processing (DIP) algorithms (Abdani et al., 2015). Furthermore, a deep learning approach based on fully convolutional neural networks was set up for automatic detection and localization of the pterygium (Zulkifley et al., 2019). If we can utilize these techniques and develop a new intelligent method for consistent pterygium detection and mass screening, it will be beneficial for pterygium diagnoses and treatment. This study aims to investigate the application of a special intelligent diagnostic system, based on deep learning, in the diagnosis of pterygium. As a consequence, we expect that early detection and appropriate interventions could provide great convenience for ophthalmic patients.

MATERIALS AND METHODS

Objects

The images used in this study were acquired from the Affiliated Eye Hospital of Nanjing Medical University. Anterior segment photographs were collected from a total of 1,220 patients (1,220 eyes) with/without pterygium from December 2019 to May 2021. Only one image was selected from each patient. For patients with pterygium, photographs of the worse eye were selected; for those with a normal ocular surface, photographs of a random eye were selected. The photos were selected by an experienced eye-surface specialist, and subsequent diagnoses were conducted by three ophthalmologists. The high-definition images selected in this study contained upper and lower lid margins, bulbar conjunctiva in the palpebral fissure area, and the whole cornea. The anterior segment photographs showed either normal appearance or a pterygium.

The exclusion criteria were as follows: (i) having conjunctivitis, subconjunctival hemorrhage, conjunctival cyst, conjunctival chemosis, conjunctival nevus, pseudopterygium, corneal conjunctival papilloma, and other ocular surface diseases; (ii) having had infectious keratitis, undergone corneal refractive surgery, and other medical histories; (iii) confusing signs like corneal scar or haze that affect the transparency of the cornea; and (iv) bad quality photographs, such as those out of focus or without appropriate light exposure.

This study was approved by the Institutional Research Ethics Committee of the Nanjing Medical University. All photographs were anonymized before inclusion in this study to ensure that they contained no information about the patients other than their diagnoses. These photographs were then randomly allocated into training samples (750 eyes) and the test set (470 eyes), and the training samples were divided into training and validation sets at a 9:1 ratio.

Image Acquisition

All photographs were taken on a digital single-lens reflex camera (EOS 600D, Canon, Tokyo, Japan) that was integrated with a slit-lamp microscope as a digital slit-lamp image acquisition system (SLM-7E, Chongqing Kanghua Ruiming S&T Co., Ltd., Chongqing, China) using diffuse illumination, 10 × magnification, front view, an image resolution of 5,184 × 3,456, and an exposure time of 1/30 s. The operators were trained and qualified in a unified standardized anterior segment photographic technique.

The photographic images were classified into three categories (Lin and Stern, 1998) as follows: (i) normal anterior segment photographs with no obvious congestion or conjunctival proliferation, or corneal transparency (as shown in **Figure 1**);

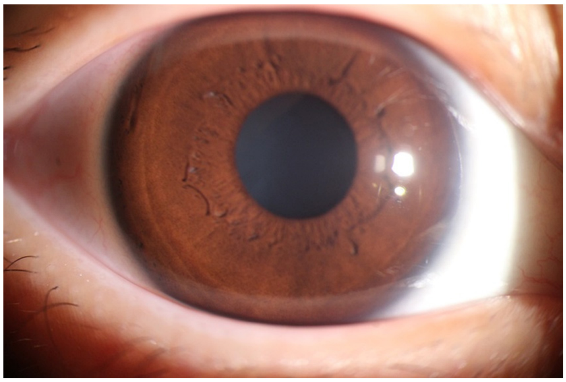

FIGURE 1 | An example of the Normal group.

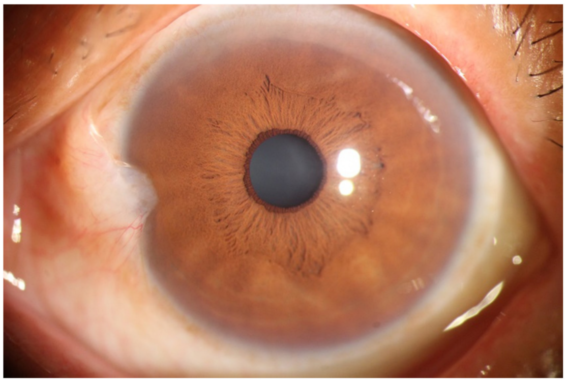

FIGURE 2 | An example of the Observation group (pterygium).

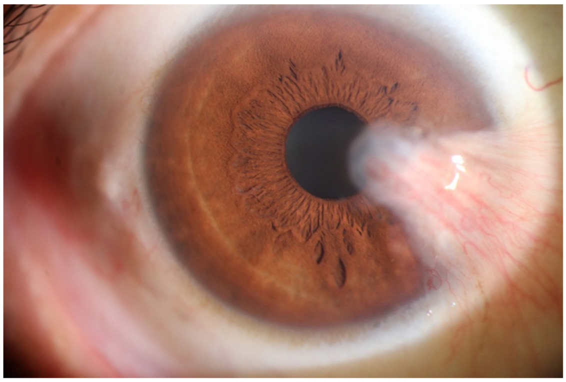

FIGURE 3 | An example of the Operation group (pterygium).

(ii) the observation group (pterygium) with the proliferative head extending beyond the corneal limbus <3 mm by horizontal length (as shown in **Figure 2**); and (iii) the operation group (pterygium) with the head extending beyond the limbus ≥3 mm by horizontal length (as shown in **Figure 3**).

Model Training

This study was based on the deep learning software and hardware platform built by 20 Dawning graphics workstations with Graphic Processing Unit (GPU) M40, using a PyCharm integrated development environment to train a deep learning model. PyCharm is a powerful Python editor and a cross-platform that can improve the efficiency of program development. The 20 Dawning graphics workstations can satisfy the demand for a large amount of data training, which requires the support of a powerful GPU.

Based on EfficientNet-B6 (Tan and Le, 2019), we proposed a computer-aided diagnosis system for pterygium that relied on the anterior segment photography in this study. EfficientNets are a family of models obtained from a new baseline network designed by neural architecture, which uniformly scales all depth, width, and resolution dimensions using a compound coefficient (Tan and Le, 2019). It is an open-source project developed by Google with an Apache-2.0 license. EfficientNet-B0 acquires a better backbone with a neural network search (NAS) than previous algorithmic models. Being a variation from the family, EfficientNets-B6 is 1.8 times wider and 2.6 times deeper than B0, with the original image resolution reduced to 528 (Tan and Le, 2019).

Transfer learning is used to determine the initial parameters for systematic training without structural change in the EfficientNet model. We used parameters that have been trained on ImageNet as the initial parameters and then trained the model using photos collected and marked by our team to get a suitable model for this study.

A total of 750 anterior segment photographs previously diagnosed as normal or pterygium by the expert (250 eyes in each group) were used as training samples and randomly divided into training and validation sets at a ratio of 9:1 to train EfficientNet-B6. The classification criteria were based on the aforementioned methods.

With fewer parameters and efficient results, EfficientNet-B6 mainly includes a stem, seven blocks, and the final layers (as shown in **Figure 4**). The model's batch size was 4, using the stochastic gradient descent method for optimization. A total of 50 epochs were trained, with the initial learning rate set at 0.01. Cosine annealing was used to reduce the learning rate during the training. On the basis of this framework, the parameters were adjusted during the training process.

The other 470 clear, canonical, and standard anterior segment photographs were then uploaded to the computer-aided diagnosis system, EfficientNet-B6, and judged by the artificial intelligence diagnosis technique. The results were obtained as the test set.

Model Evaluation

An intelligent diagnosis was performed according to the photographic images of the anterior segment. The camera captured an anterior segment photograph of the interpalpebral zone, including the upper and lower lid margin and the whole cornea, at a right angle perpendicular to the iris, and uploaded it to the artificial intelligence diagnostic system. The photographs

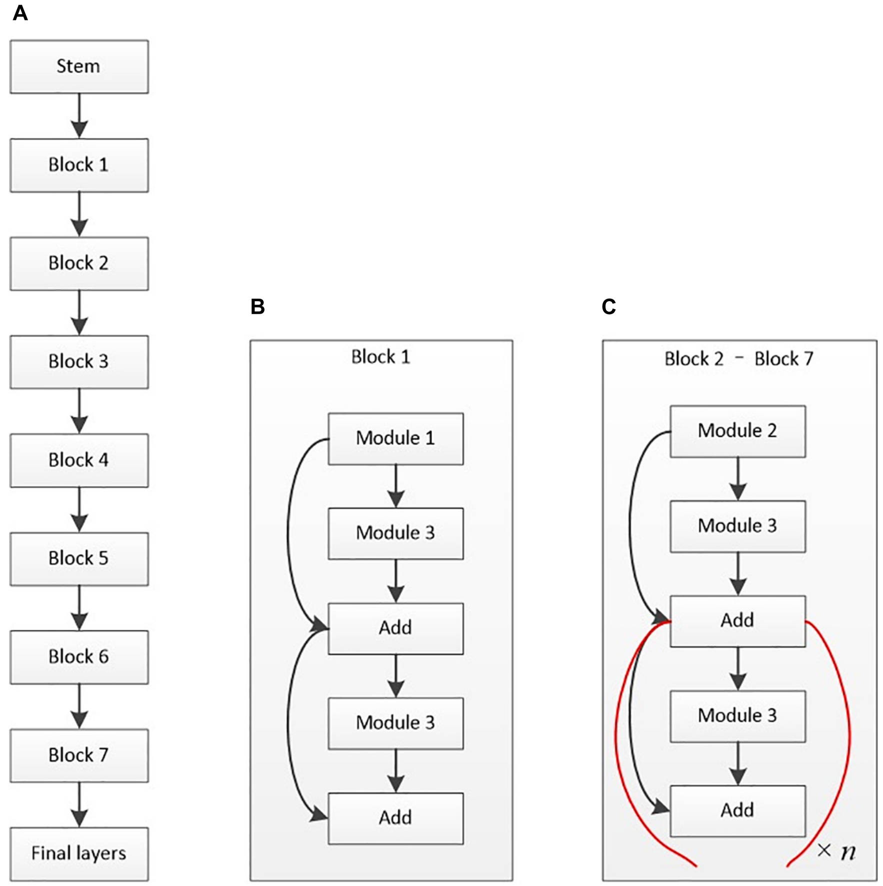

FIGURE 4 | Architectural diagram of EfficientNet-B6. **(A)** Basic architecture. **(B)** Structure of block 1. **(C)** Structure of blocks 2–7. The basic structure of the stem is composed of a data input layer, convolution layer, activation function layer, and other layers. Module 1 mainly contains depth-wise convolution (D-Conv2D), batch normalization, and activation. Module 2 is primarily the connected two modules 1 with zero padding. Module 3 mainly contains global average pooling (GAP), rescaling, and Conv2D. The final layers include Conv2D,batch normalization, and activation layers.

used in the study were in a uniform format without black edge or extra elements, and need no preprocessing. Before input to the model, the obtained photographs were resized to a slightly lower resolution for model and hardware reasons, and flipped horizontally at random during model training. When a photo was judged by the system, the report was obtained as the intelligent diagnosis group. The same photo will also be assessed by three eye-surface specialists independently in a double-blind trial on the same computer screen. The size of the pterygium was measured by the length of the slit light band of the slit lamp, and the grading diagnosis result of the pterygium was obtained according to the clinical diagnosis and treatment guidelines (Chinese Medical Association [CMA], 2007). Two or more identical grading diagnoses were used to create the final clinical diagnostic result. If two ophthalmologists provide unanimous grading diagnoses, that would be taken as the expert diagnosis; if two ophthalmologists provide different grades, a third ophthalmologist's diagnosis would be considered and form the final result of expert diagnosis.

At present, there is no clear expert consensus on the indications for pterygium surgery; however, most ocular surface experts agree that the most important surgical indication is vision loss caused by the invasion of the visual axis (Twelker et al., 2000; Troutbeck and Hirst, 2001; Graue-Hernandez et al., 2019). In this study, a medium or large pterygium (horizontal length of the head extending beyond the corneal limbus ≥3 mm) warrants the recommendation for surgery (Wilson et al., 2008; Gumus et al., 2011). The sensitivity, specificity, kappa value, area under curve (AUC), and other indicators of the AI diagnostic system were calculated by comparing the results of intelligent diagnosis and expert diagnosis.

Statistical Analysis

Statistical analyses were conducted with SPSS 22.0 (IBM Inc., Armonk, NY, United States), using methods for evaluating diagnostic tests, and represented by four grid tables. The enumeration data were represented by the number of images; indicators including accuracy, sensitivity and specificity, as well as F1-score and 95% confidence interval (CI) were expressed as percentages. Receiver operating characteristic (ROC) curves were plotted, and then the areas under the concentration-time curve (AUC) were calculated to measure the performance of the model. The kappa test was performed to evaluate the consistency of the diagnostic test. Taking the results of the expert diagnosis for the ground truth, a kappa value of 0.61–0.80 was considered significantly consistent, while a kappa value higher than 0.80 was considered highly consistent.

RESULTS

In this study, 470 anterior segment photographs were used to test the proposed intelligent diagnosis system for pterygium. According to the expert diagnosis, 189, 171, and 110 images were categorized into the normal, observation, and operation groups, respectively. The intelligent diagnostic system categorized 190, 162, and 118 images into these same groups respectively. The diagnostic results of the expert and intelligent diagnoses are listed in **Table 1**.

Compared with the expert diagnostic result, the true positive rate of the intelligent diagnostic system is almost 100% in the normal group. It also provides a high specificity of 99.64%. For both the observation and operation groups, the specificities of diagnosis for pterygium are above 95%, indicating the systems' low misdiagnosis rates. The sensitivity for pterygium diagnosis is 90.06% in the observation group and 92.73% in the operation group, which is lower than that for the normal eye group. The kappa values for the normal group, the observation group, and the operation group is 0.996, 0.884, and 0.861, respectively. The AUC values of all three groups approaches 90%, with the highest value of 0.998 (for the normal group). Overall, the intelligent diagnostic system provides an average accuracy of 94.68% (**Table 2**). A comparison of the ROC curves of the normal, observation, and operation groups is shown in **Figure 5**.

DISCUSSION

Currently, there is no clear expert consensus regarding the surgical indications of pterygium. A survey conducted by Mexican investigators, covering 199 cornea specialists worldwide, shows that more than 90% of the specialists considered that surgery should be performed when the pterygium blocks up on the visual axis, or when there is pain, redness, eye movement restriction, or induction of astigmatism. In the same study, cosmesis was considered by 41.7% of the participants (Graue-Hernandez et al., 2019). For patients with pterygium in the stationary phase and without vision impairment, observations could be made temporarily without surgery. For pterygium in the active phase with vision loss, surgical resection should be performed. Although surgical treatments of pterygium vary, the indications for different operations are comparable (Troutbeck and Hirst, 2001; Janson and Sikder, 2014). Inappropriate surgical timing may cause unnecessary complications (Anduze and Burnett, 1996; Ti and Tan, 2003; Boui et al., 2020). The selection of medicines or surgical treatments relies on a doctor's subjective judgment. Therefore, the development of an intelligent image processing method based on anterior segment photography, and the implementation of an AI-assisted automatic detection of pterygium, by which surgical indications could be identified through deep learning, will be beneficial for pterygium diagnoses. It not only ensures consistent pterygium detection but also enables mass screening for pterygium; therefore, the subsequent early detection and appropriate interventions will benefit patients.

At present, AI technology is being used more widely for anterior segment diseases, such as keratoconus, infectious keratitis, refractive surgery, corneal transplantation, cataract, angle closure glaucoma, dry eye and pterygium (Wu et al., 2020; Ting et al., 2021). A computer-aided pterygium screening platform developed by Zaki et al. has been used to classify pterygium and non-pterygium cases (Wan Zaki et al., 2018). This system is composed of four modules: the first uses the HSV color space and sigmoid transfer function to enhance the pterygium tissue in the image pre-processing; the second differentiates the pterygium tissue and the corneal region with a segmentation module; the third extracts corneal features with the circularity ratio, Haralick's circulatory, eccentricity, and solidity; and the fourth identifies the presence or absence of pterygium by support vector machines and artificial neural networks. The sensitivity, specificity, and area under the curve of the pterygium screening system were 88.7, 88.3, and 95.6%, respectively. Recently, Zhang et al. have set up a deep learning diagnostic system to make diagnostic recommendations on whether a pterygium patient needs surgery, with a final accuracy of up to 95% (Zhang et al., 2018). Abdani et al. have utilized DeepLab V2 deep learning to increase the pterygium tissue segmentation performance from photographs taken on a mobile phone with an accuracy of 92% (Abdani et al., 2020). These results suggest that AI can classify pterygium based on its appearance.

In contrast to the above research, this study not only judged the presence of a pterygium using AI but also classified the observation and operation groups according to the horizontal length of the head extending beyond the corneal limbus in anterior segment photographs, therefore providing more accurate treatment recommendations. The results of the consistency analysis of the intelligent and expert diagnoses showed a high consistency (accuracy) of 445 eyes (94.68%). Among them, the sensitivity and specificity of the intelligent diagnosis system in the normal group were 100 and 99.64%, respectively. In the observation group, the sensitivity and specificity were 90.06 and 97.32%, respectively. Finally, in the operation group, the sensitivity and specificity were 92.73 and 95.56%, respectively. This study shows high consistency between intelligent and expert diagnoses when judging the presence of pterygium. However, the intelligent diagnosis is slightly less sensitive in grading the pterygium. This study shows high consistency between intelligent and expert diagnoses when judging the presence of pterygium. However, the intelligent diagnosis is slightly less sensitive in grading the pterygium.

Pterygium is one of the most common ocular surface disorders that causes vision loss and affects an individual's appearance. It has a higher prevalence among people who live near the equator or work outdoors, being exposed to ultraviolet radiation, wind and dust. For the vast rural and remote areas where

TABLE 1 | Diagnostic results.

Expert diagnosis	Intelligent diagnosis			Total
	Normal	Observation (pterygium)	Operation (pterygium)	
Normal group	189	0	0	189
Observation group (pterygium)	1	154	16	171
Operation group (pterygium)	0	8	102	110
Total	190	162	118	470

TABLE 2 | Evaluation index results.

	Evaluation indicators						
	Sensitivity	Specificity	F1-score	AUC	95% CI	Kappa	Accuracy
Normal group	100.00%	99.64%	99.74%	0.998	0.994–1	0.996	94.68%
Observation group (pterygium)	90.06%	97.32%	92.49%	0.937	0.909–0.965	0.884	
Operation group (pterygium)	92.73%	95.56%	89.47%	0.941	0.911–0.972	0.861	

AUC, area under the curve; CI, confidence interval.

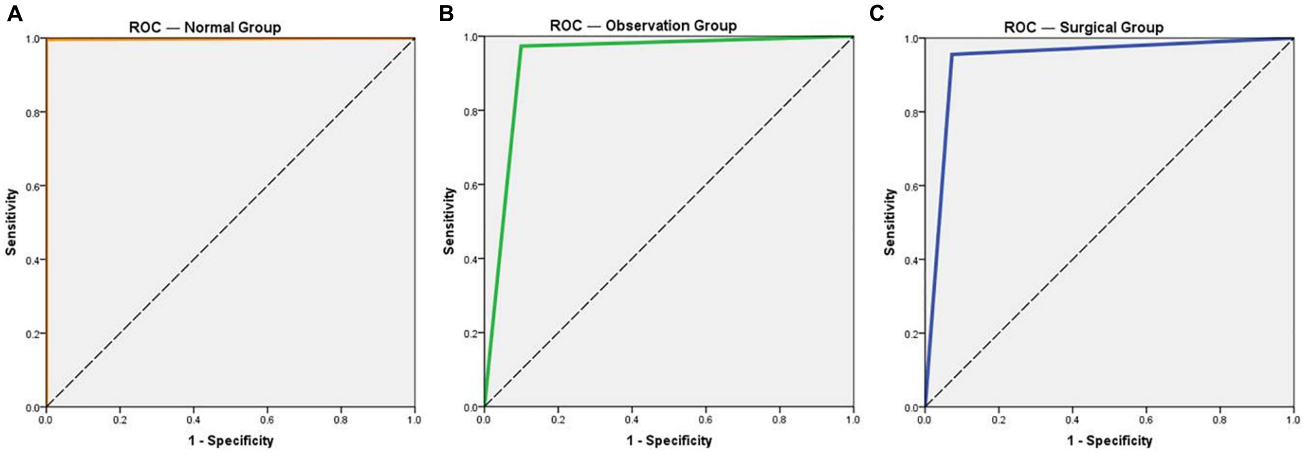

FIGURE 5 | Receiver operating characteristic (ROC) curves of the three groups for normal eye and pterygium. **(A)** ROC curve of the normal group. **(B)** ROC curve of the observation group. **(C)** ROC curve of the operation group.

there is a lack of professional medical resources, especially ophthalmic specialists and products, intelligent diagnostic technology provides a convenient screening method for local patients with pterygium. It also aids communities by decreasing travel to distant county or city hospitals, reducing the economic burdens of the patients, and progressively providing treatment advice and clear further surgical indications. It will also be convenient for the timely referral of patients who need surgery in such situations as the global COVID-19 pandemic and will help facilitate the appropriate allocation of medical resources.

This study has some limitations. As the results suggested that the intelligent diagnosis was slightly less sensitive in grading the pterygium, further investigation and optimization of the diagnostic model are needed. All cases of mismatch in observation and operation groups were middle size pterygia, and the lengths of the proliferative head extending beyond the corneal limbus were between 2.5 and 3.5 mm, close to the critical value of 3 mm. For further research, the number of model training samples should be increased, and the acquisition of anterior segment photographs requires further optimization and screening because the quality of the images is very important for model training and testing. We only focused on the three-group classification of pterygium at this stage, there was no preprocessing of the original image before deep learning; We also continue working on localization of the lesions, involving segmentation and visualization for labeling and rating the image category.

Based on the relevant technical basis of this study, a new mobile terminal pterygium screening and diagnostic system will be developed in our future work, using photographs taken by a mobile phone as the training set. This system is expected to facilitate patients in remote or rural areas without anterior segment photographic facilities so that they can obtain a common eye disease diagnosis and treatment recommendations at home, with the aid of a smartphone.

CONCLUSION

To meet the requirements of intelligent pterygium diagnosis, this study focused on breaking through the core theoretical models and key techniques needed for the initial screening diagnosis by the anterior segment photographs of pterygium. The intelligent pterygium diagnosis system based on deep learning can preferably classify pterygium. Intelligent diagnosis is highly consistent with expert diagnosis, especially in determining the presence or absence of pterygium. As the first study attempting to identify the severity of conjunctival proliferation, this study has made vital contributions by providing a new screening tool for pterygium to make basic diagnosis and treatment suggestions, and benefiting the majority of ordinary patients who lack medical resources. Future studies should aim to increase the number of training sets, constantly improve accuracy and sensitivity, and establish an intelligent pterygium diagnosis system suitable for basic use.

DATA AVAILABILITY STATEMENT

The raw data supporting the conclusions of this article will be made available by the authors, without undue reservation.

ETHICS STATEMENT

This study was approved by the Institutional Research Ethics Committee of the Nanjing Medical University. Written informed consent from the patients/participants was not required to participate in this study in accordance with the national legislation and the institutional requirements.

AUTHOR CONTRIBUTIONS

W-HY and M-NW contributed to conception and design of the study and developed the intelligent system. WX, LJ, and P-ZZ organized the database. KH and M-NW conducted model training and algorithm adjustment. WX and LJ performed the statistical analysis and wrote the first draft of the manuscript. WX, LJ, P-ZZ, W-HY, and M-NW wrote sections of the manuscript. All authors contributed to manuscript revision, read, and approved the submitted version.

FUNDING

This study was supported by the National Natural Science Foundation of China (No. 61906066), the Zhejiang Medical and Health Research Project (2020PY027), the Huzhou Science and Technology Planning Program (2018GY06), and the Nanjing Enterprise Expert Team Project.

REFERENCES

Abdani, S. R., Zaki, W., Mustapha, A., and Hussain, A. (2015). "Iris segmentation method of pterygium anterior segment photographed image," in *Proceeding of the 2015 IEEE Symposium on Computer Applications & Industrial Electronics (ISCAIE)*, (IEEE).

Abdani, S. R., Zulkifley, M. A., and Moubark, A. M. (2020). "Pterygium tissues segmentation using densely connected DeepLab," in *Proceeding for the 10th Symposium on Computer Applications & Industrial Electronics (ISCAIE)*, (IEEE).

Anduze, A. L., and Burnett, J. M. (1996). Indications for and complications of mitomycin-C in pterygium surgery. *Ophthal. Surg. Lasers* 27, 667–673. doi: 10.3928/1542-8877-19960801-05

Boui, H., Mouzari, Y., Boui, M., Al Asri, F., Reda, K., and Oubaaz, A. (2020). Scleral dellen: early complication of pterygium surgery and literature review. *Int. J. Med. Sci. Clin. Invent.* 7, 4845–4847. doi: 10.18535/ijmsci/v7i06.04

Chen, Q., Li, Y., Xu, F., Yan, Y. M., Lu, K. W., Cui, L., et al. (2015). Comparison of inferior and superior conjunctival autograft for primary pterygium. *Curr. Eye Res.* 40, 786–791. doi: 10.3109/02713683.2014.961612

Chinese Medical Association [CMA], (2007). *Clinical Diagnosis and Treatment Guidelines / Ophthalmology Section*. Beijing: People's Medical Publishing House.

Coroneo, M. (2011). Ultraviolet radiation and the anterior eye. *Eye Contact Lens* 37, 214–224. doi: 10.1097/ICL.0b013e318223394e

Delic, N. C., Lyons, J. G., Di Girolamo, N. D., and Halliday, G. M. (2017). Damaging effects of ultraviolet radiation on the cornea. *Photochem. Photobiol.* 93, 920–929. doi: 10.1111/php.12686

Graue-Hernandez, E. O., Córdoba, A., Jimenez-Corona, A., Ramirez-Miranda, A., Navas, A., Serna-Ojeda, J. C., et al. (2019). Practice patterns in the management of primary pterygium: a survey study. *Cornea* 38, 1339–1344. doi: 10.1097/ICO.0000000000002091

Gulshan, V., Peng, L., Coram, M., Stumpe, M. C., Wu, D., Narayanaswamy, A., et al. (2016). Development and validation of a deep learning algorithm for detection of diabetic retinopathy in retinal fundus photographs. *JAMA* 316, 2402–2410. doi: 10.1001/jama.2016.17216

Gumus, K., Erkilic, K., Topaktas, D., and Colin, J. (2011). Effect of pterygia on refractive indices, corneal topography, and ocular aberrations. *Cornea* 30, 24–29. doi: 10.1097/ICO.0b013e3181dc814e

Gumus, K., Topaktas, D., Göktaş, A., Karakucuk, S., Oner, A., and Mirza, G. E. (2012). The change in ocular higher-order aberrations after pterygium excision with conjunctival autograft: a 1-year prospective clinical trial. *Cornea* 31, 1428–1431. doi: 10.1097/ICO.0b013e3182431465

Janson, B. J., and Sikder, S. (2014). Surgical management of pterygium. *Ocul. Surf.* 12, 112–119. doi: 10.1016/j.jtos.2014.01.001

Kaufman, S. C., Jacobs, D. S., Lee, W. B., Deng, S. X., Rosenblatt, M. I., and Shtein, R. M. (2013). Options and adjuvants in surgery for pterygium: a report by the American Academy of Ophthalmology. *Ophthalmology* 120, 201–208. doi: 10.1016/j.ophtha.2012.06.066

Kermany, D. S., Goldbaum, M., Cai, W., Valentim, C. S., Liang, H., Baxter, S. L., et al. (2018). Identifying medical diagnoses and treatable diseases by image-based deep learning. *Cell* 172, 1122–1131. doi: 10.1016/j.cell.2018.02.010

Li, Z., He, Y., Keel, S., Meng, W., Chang, R. T., and He, M. (2018). Efficacy of a deep learning system for detecting glaucomatous optic neuropathy based on color fundus photographs. *Ophthalmology* 125, 1199–1206. doi: 10.1016/j.ophtha.2018.01.023

Lin, A., and Stern, G. (1998). Correlation between pterygium size and induced corneal astigmatism. *Cornea* 17, 28–30. doi: 10.1097/00003226-199801000-00005

Medeiros, F. A., Jammal, A. A., and Mariottoni, E. B. (2020). Detection of progressive glaucomatous optic nerve damage on fundus photographs with deep learning. *Ophthalmology* 128, 383–392. doi: 10.1016/j.ophtha.2020.07.045

Nagasato, D., Tabuchi, H., Ohsugi, H., Masumoto, H., Enno, H., Ishitobi, N., et al. (2018). Deep neural network-based method for detecting central retinal vein occlusion using ultrawide-field fundus ophthalmoscopy. *J. Ophthalmol.* 2018, 1–6. doi: 10.1155/2018/1875431

Raman, R., Srinivasan, S., Virmani, S., Sivaprasad, S., Rao, C., and Rajalakshmi, R. (2018). Fundus photograph-based deep learning algorithms in detecting diabetic retinopathy. *Eye* 33, 97–109. doi: 10.1038/s41433-018-0269-y

Tan, M., and Le, Q. V. (2019). "EfficientNet: rethinking model scaling for convolutional neural networks," in *Proceeding of the International Conference on Machine Learning (ICML) 2019*, (ICML).

Ti, S. E., and Tan, D. T. H. (2003). Tectonic corneal lamellar grafting for severe scleral melting after pterygium surgery. *Ophthalmology* 110, 1126–1136. doi: 10.1016/S0161-6420(03)00260-4

Ting, D. S. J., Foo, V. H. X., Yang, L. W. Y., Sia, J. T., Ang, M., Lin, H. T., et al. (2021). Artificial intelligence for anterior segment diseases: emerging applications in ophthalmology. *Br. J. Ophthalmol.* 105, 158–168. doi: 10.1136/bjophthalmol-2019-315651

Troutbeck, R., and Hirst, L. (2001). Review of treatment of pterygium in Queensland: 10 years after a primary survey. *Clin. Exp. Ophthalmol.* 29, 286–290. doi: 10.1046/j.1442-9071.2001.00435.x

Twelker, J. D., Bailey, I. L., Mannis, M. J., and Satariano, W. A. (2000). Evaluating pterygium severity: a survey of corneal specialists. *Cornea* 19, 292–296. doi: 10.1097/00003226-200005000-00007

Wan Zaki, W. M. D., Mat Daud, M., Abdani, S. R., Hussain, A., and Mutalib, H. A. (2018). Automated pterygium detection method of anterior segment photographed images. *Comput. Methods Programs Biomed.* 154, 71–78. doi: 10.1016/j.cmpb.2017.10.026

Wilson, G., Horner, D., Begley, C., and Page, J. (2008). Ocular discomfort from pterygium in men and women. *Eye Contact Lens* 34, 201–206. doi: 10.1097/ICL.0b013e31815eb0c9

Wu, X., Liu, L., Zhao, L., Guo, C., Li, R., Wang, T., et al. (2020). Application of artificial intelligence in anterior segment ophthalmic diseases: diversity and standardization. *Ann. Transl. Med.* 8:714. doi: 10.21037/atm-20-976

Yim, J., Chopra, R., Spitz, T., Winkens, J., Obika, A., Kelly, C., et al. (2020). Predicting conversion to wet age-related macular degeneration using deep learning. *Nat. Med.* 26, 892–899. doi: 10.1038/s41591-020-0867-7

Zhang, K., Liu, X. Y., Liu, F., He, L., Zhang, L., Yang, Y., et al. (2018). An interpretable and expandable deep learning diagnosis system for multiple ocular diseases: elaborately simulating doctors working. *J. Med. Internet Res.* 20:e11144. doi: 10.2196/11144

Zhou, Z., Wu, R., Yang, Y., and Li, J. (2018). Analysis of the relationship between corneal aberration and the size of pterygium. *J. Clin. Ophthalmol.* 4, 315–317.

Zulkifley, M. A., Abdani, S. R., and Zulkifley, N. H. (2019). Pterygium-Net: a deep learning approach to pterygium detection and localization. *Multimed. Tools Appl.* 78, 34563–34584. doi: 10.1007/s11042-019-08130-x

Conflict of Interest: The authors declare that the research was conducted in the absence of any commercial or financial relationships that could be construed as a potential conflict of interest.

ORIGINAL RESEARCH
published: 14 December 2021
doi: 10.3389/fnins.2021.727998

Correlation Between Retinal Microvascular Abnormalities and Total Magnetic Resonance Imaging Burden of Cerebral Small Vessel Disease in Patients With Type 2 Diabetes

Ying Zhang†, Zhixiang Zhang†, Min Zhang, Yin Cao* and Wenwei Yun**

Department of Neurology, Changzhou Second People's Hospital Affiliated to Nanjing Medical University, Changzhou, China

Background and Purpose: Diabetic retinopathy (DR) is one of the common microvascular complications in diabetes. The total magnetic resonance imaging (MRI) burden of cerebral small vessel disease (CSVD) tends to be increased in diabetic patients and is a marker of microvascular disease; however, the relationship between DR and CSVD is unclear. This study aimed to explore the relationship between retinal microvascular abnormalities and the total MRI burden of CSVD in patients with type 2 diabetes.

Methods: Data were collected from patients with type 2 diabetes who were hospitalized between December 2019 and November 2020 in Changzhou Second People's Hospital affiliated to Nanjing Medical University. All patients underwent retinal photography and cerebral MRI. The central retinal artery equivalent (CRAE), the central retinal venous equivalent (CRVE), and arteriole-to-venule ratio (AVR) were calculated using Image J software to determine the retinal vascular calibers for each patient. The total MRI burden score for CSVD was determined, and the relationship between retinal microvascular abnormalities and the total MRI burden of CSVD was analyzed.

Results: Of the 151 diabetic patients included in the study, 84 (55.6%) had no diabetic retinopathy (NDR), 27 (17.9%) had mild DR, and 40 (26.5%) had moderate, or severe non-proliferative DR (grouped together for this study as "more than mild DR"). In patients with more than mild DR, the proportion of moderate to severe burden of CSVD was 75%, which was higher than in patients with mild DR (48.1%) or NDR (26.2%). Patients with moderate to severe burden of CSVD were more likely than those with mild burden of CSVD to have narrowed retinal arterioles (105.24 ± 8.42 μm vs. 109.45 ± 7.93 μm), widened retinal venules (201.67 ± 16.25 μm vs. 193.95 ± 13.54 μm), and lower arteriole-to-venule ratio (0.52 ± 0.05 vs. 0.57 ± 0.04) ($P < 0.05$ for all). The degree of DR ($r = 0.465$, $P < 0.001$) and CRVE ($r = 0.366$, $P < 0.001$) were positively correlated with the total MRI burden of CSVD. Multivariate logistic regression analysis indicated that, after adjustments were made for age, smoking, alcohol consumption, hypertension, and

Edited by:
Pablo Pérez-Merino,
Ghent University, Belgium

Reviewed by:
Ester Carreño,
University Hospital Fundación
Jiménez Díaz, Spain
Josy Augustine,
Queen's University Belfast,
United Kingdom
Maximilian Gabriel,
Medical University of Graz, Austria

***Correspondence:**
Min Zhang
zhangmin0411@njmu.edu.cn
Yin Cao
czcaoyin@163.com
Wenwei Yun
yunwenwei1266@njmu.edu.cn

†These authors have contributed equally to this work

Specialty section:
This article was submitted to
Perception Science,
a section of the journal
Frontiers in Neuroscience

Received: 20 June 2021
Accepted: 22 November 2021
Published: 14 December 2021

Citation:
Zhang Y, Zhang Z, Zhang M, Cao Y and Yun W (2021) Correlation Between Retinal Microvascular Abnormalities and Total Magnetic Resonance Imaging Burden of Cerebral Small Vessel Disease in Patients With Type 2 Diabetes. Front. Neurosci. 15:727998. doi: 10.3389/fnins.2021.727998

other factors, more than mild DR (OR, 4.383; $P = 0.028$), CRAE (OR, 0.490; $P = 0.031$), and CRVE (OR, 1.475; $P = 0.041$) were independently associated with moderate to severe burden of CSVD.

Conclusion: Retinal microvascular abnormalities in patients with type 2 diabetes are associated with the presence of cerebral small vessel lesions. The degree of DR and retinal vessel changes can be used as predictors of intracranial microcirculation lesions.

Keywords: cerebral small vessel disease, retinal microvascular, diabetic retinopathy, type 2 diabetes, retinal photography

INTRODUCTION

Type 2 diabetes is a strong risk factor for the development of atherosclerosis. Research has shown that type 2 diabetes is associated with a 2.5-fold increased risk of ischemic stroke, a 1.5-fold increased risk of hemorrhagic stroke, and a 1.5-fold increased risk of dementia compared to the risk in the general population (van Sloten et al., 2020). Type 2 diabetes is also a major risk factor for microvascular dysfunction, including dysfunction in the retinal microvascular system. Specifically, the effect of diabetes is reflected not only in subtle abnormalities of retinal vessels but also in the occurrence of diabetic retinopathy (DR) (Stehouwer, 2018; van Sloten et al., 2020). DR is the most common diabetes-related microvascular complication, with a global prevalence of 34.6% (Shahulhameed et al., 2020).

Research has shown that type 2 diabetes may also be associated with an increasing occurrence of cerebral small vessel disease (CSVD) over time (Qiu et al., 2018; van Agtmaal et al., 2018). CSVD is a slowly progressing disease with non-specific symptoms. Magnetic resonance imaging (MRI) features of CSVD can include white matter hyperintensities (WMHs), lacunes, enlarged perivascular spaces (PVS), and cerebral microbleeds (CMBs), all of which may be a manifestation of cerebral microvascular dysfunction. In recent years, numerous studies have demonstrated a significant correlation between CSVD and retinal vascular changes (McGrory et al., 2019; Shu et al., 2020). Sanahuja et al. (2016) also found that the presence of DR is associated with more severe CSVD. In terms of anatomical features, the retinal arterioles, and venules, measuring 100–300 μm in diameter, share similar features with cerebral small blood vessels. The retinal microvasculature is therefore thought to be a "window" to reflect the condition of the cerebral microvasculature (London et al., 2013).

Given the simultaneous occurrence and joint effects of MRI markers of CSVD, the total MRI burden of CSVD could be used to comprehensively evaluate the cumulative effect of various types of CSVD, with total MRI burden of CSVD potentially offering a better overall assessment of the severity and clinical impact of CSVD (Lau et al., 2017). However, previous studies assessing these potential links usually focused on patients who had experienced stroke; patients with type 2 diabetes have rarely been directly studied. In addition, in previous research assessing the relationship between type 2 diabetes and retinal microvascular abnormalities, the fundus has usually been evaluated via either qualitative assessment of retinopathy signs or quantitative assessment of retinal vessel calibers. In this study, we enrolled only patients with type 2 diabetes and we used retinal photography to assess retinopathy and retinal vascular calibers, thus combining qualitative assessment with quantitative assessment to more fully reflect the abnormalities of the retinal microvasculature. With this study design, we aimed to investigate the correlation between retinal microvascular abnormalities and the total MRI burden of CSVD in patients with type 2 diabetes.

MATERIALS AND METHODS

Study Design

We collected and analyzed data from patients with type 2 diabetes who were hospitalized in the Department of Endocrinology at Changzhou Second People's Hospital from December 2019 to November 2020. This cross-sectional observational study was approved by the Ethics Committee of Changzhou Second People's Hospital (2017KY015-01). Informed consent was obtained from patients (or from their family members, if patients were unable to sign the consent form because of illiteracy).

Patient Selection

A total of 170 patients with type 2 diabetes were screened for our study. These patients did not have dementia and had not experienced stroke. Patients were included if they (1) were aged $\geq$ 18 years old; (2) met the diagnostic criteria for type 2 diabetes mellitus (Hemmingsen et al., 2017); (3) had cerebral MR images demonstrating any markers of CSVD; and (4) provided informed consent. Patients were excluded if they (1) were unable to complete the cerebral MRI examination or fundus photography; (2) demonstrated evidence of acute cerebral infarcts on cerebral MRI, even if asymptomatic; (3) had any brain disease affecting fundus vessels (e.g., intracranial tumors, arteriovenous malformations, venous sinus thrombosis); (4) had known eye disease or disease that affected the retinal vessel structure or hindered observation of the fundus (e.g., age-related maculopathy, central serous chorioretinopathy, cataract, retinal pigment epithelial detachment) or had undergone previous ophthalmological treatment (e.g., laser photocoagulation, intravitreal injection); (5) had type 1 diabetes or other types of diabetes; (6) had severe organic or metabolic disease; and (7) had unclear fundus images or incomplete cerebral MRI sequences. Of the 170 patients screened for the study, 8 had unclear fundus images, 5 had cataracts or other fundus diseases, 3 had incomplete MRI sequences, and 3 had asymptomatic acute cerebral infarction. These patients were excluded from the analysis, leaving a total of 151 patients enrolled in the study.

Data Collection

We collected information about patient age, sex, vascular risk factors (including BMI, duration of diabetes, hypertension, smoking, alcohol consumption, previous stroke, coronary heart disease, systolic, and diastolic blood pressure), and laboratory tests such as fasting glucose, glycated hemoglobin (HbA_1c), total cholesterol, triglyceride, low-density lipoprotein cholesterol, high-density lipoprotein cholesterol, serum creatinine, and urinary microalbumin/creatinine ratio. We also performed carotid ultrasound at baseline for each enrolled participant.

Analysis of Retinal Microvascular Abnormalities

Retinal Vascular Assessment

A Topcon (TRC-NW400) non-mydriatic fundus camera was used to perform fundus photographic examination of all enrolled patients. Binocular fundus images were obtained with patients sitting under a slit lamp, and the optic disc was confirmed to be in the center of each image. These fundus images were qualitatively analyzed by 2 experienced ophthalmologists. In addition, the software Image J[1] was used to measure retinal vascular calibers for each patient (**Figure 1**). The measurement process was completed by a well-trained ophthalmology graduate student. First, all photographs were projected at the same magnification. Next, a 0.5–1 disc diameter surrounding the optic disc was circled and the calibers of the largest 6 retinal arteries and venules were measured. The edge of each blood vessel wall was selected to measure the diameter of the blood vessel vertically. Using this method, we obtained the diameter of 6 retinal arteries and venules. Calibration of the retinal vascular calibers was performed based on the standard disc diameter (1,850 μm) as a defined unit of measurement. Using this uniform conversion, we obtained the vascular calibers close to the true value. Finally, the revised Parr-Hubbard formula was used to calculate the retinal vascular caliber. We used an iterative procedure of pairing up the largest vessels with the smallest and repeating this process until we reached a single number that summarized as the central retinal artery equivalent (CRAE), the central retinal venous equivalent (CRVE), and the arteriole-to-venule ratio (AVR). The following formulas were used to obtain these values (Yip et al., 2016):

$$CRAE = 0.88 * (W_1^2 + W_2^2)^{1/2}$$

$$CRVE = 0.95 * (W_1^2 + W_2^2)^{1/2}$$

$$\text{AVR} : CRAE/CRVE$$

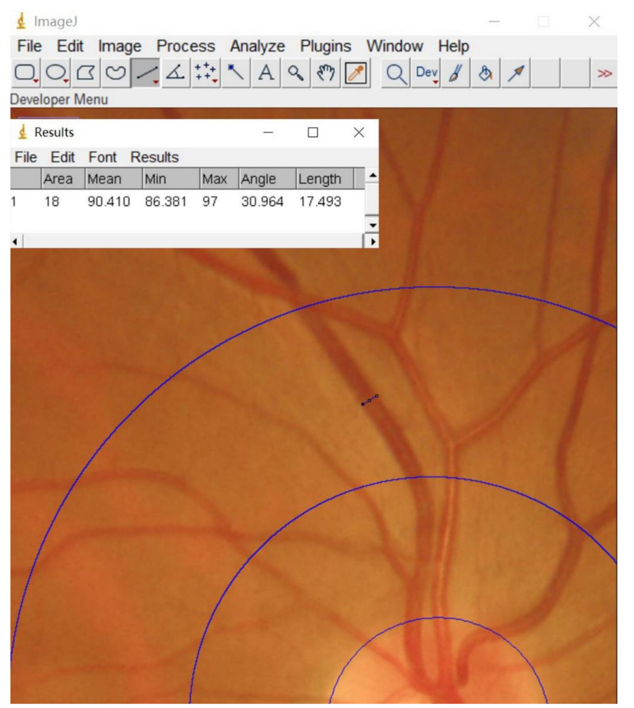

	Area	Mean	Min	Max	Angle	Length
1	18	90.410	86.381	97	30.964	17.493

FIGURE 1 | A screenshot of the Image J interface.

Diabetic Retinopathy Definition and Classification

DR grades (**Figure 2**) were determined by an experienced ophthalmologist who assessed the cases online, and these grades were reviewed by another experienced ophthalmologist at our hospital; both were blinded to all clinical data and other measurements. Based on an international consensus on clinical DR (Solomon et al., 2017), the grades of DR were defined as follows: 1 = non-DR (NDR), diabetic patients without DR; 2 = mild non-proliferative DR, indicated by microaneurysms only; 3 = moderate non-proliferative DR, indicated by more than just microaneurysms but less than severe non-proliferative DR; 4 = severe non-proliferative DR, indicated by > 20 intraretinal hemorrhages in each of 4 quadrants, definite venous beading in 2 or more quadrants, prominent intraretinal microvascular abnormalities in 1 or more quadrants, or no signs of proliferative retinopathy; and 5 = proliferative DR, indicated by neovascularization and/or vitreous/preretinal hemorrhage. There were no cases of PDR in our study population. For this analysis, DR grades 3 and 4 were combined into a group referred to as "more than mild DR."

Analysis of the Total Magnetic Resonance Imaging Burden of Cerebral Small Vessel Disease

Within 7 days after admission, all enrolled patients underwent 3.0T cerebral MRI examination, including T1-weighted imaging (T1WI), T2-weighted imaging (T2WI), fluid attenuation inversion recovery (FLAIR) imaging, diffusion-weighted imaging (DWI), and susceptibility-weighted imaging (SWI).

---

[1] https://imagej.en.softonic.com/

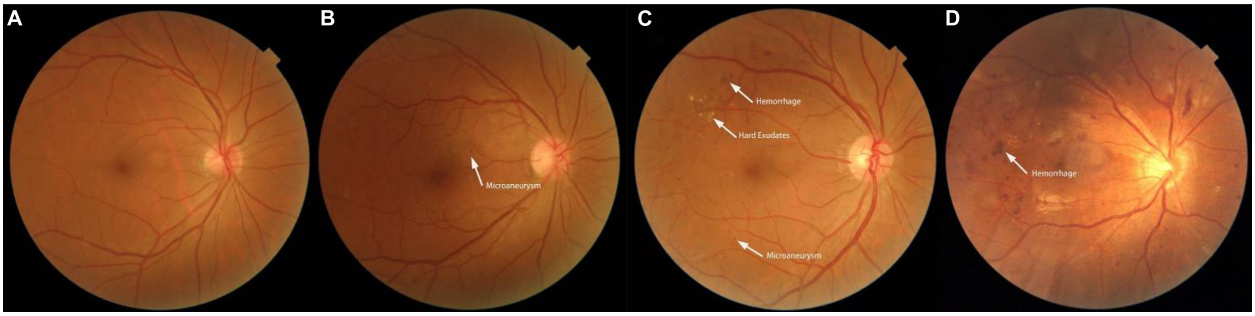

FIGURE 2 | Fundus photographs showing features of a normal fundus and features of the various grades of diabetic retinopathy. **(A)** Photograph of a normal fundus. **(B)** Fundus image showing mild non-proliferative diabetic retinopathy with microaneurysms. **(C)** Fundus image showing moderate non-proliferative diabetic retinopathy with hemorrhages, hard exudates, and microaneurysms. **(D)** Fundus image showing severe non-proliferative diabetic retinopathy.

Two experienced neurologists who were blinded to the clinical information and retinal photography findings independently evaluated all images based on an international consensus (Wardlaw et al., 2013). The total MRI burden scores of CSVD were calculated ranging from 0 to 4 (**Figure 3**) by combining 4 individual CSVD markers, with 1 point allocated to each of the markers. The specific criteria for the markers were as follows:

(1) WMHs: defined as periventricular or deep brain lesions of varying sizes, hyperintense on T2WI or FLAIR imaging, and isointense or hypointense on T1WI with abnormal white matter signals. The severity of WMHs was assessed using the Fazekas scale. A score of 3 points for hyperintensities in periventricular white matter or $\geq$ 2 points for hyperintensities in deep white matter was counted as 1 point.
(2) Lacunes: defined as round or oval cerebrospinal fluid-like signals on T1WI and T2WI, with a surrounding rim of hyperintensities and central cerebrospinal fluid-like hypointensities on FLAIR imaging, with a diameter of 3–15 mm, distributed under the cortex. The presence of $\geq$ 1 lacune was counted as 1 point.
(3) CMBs: defined as round or oval signal loss lesions on SWI, with clear boundaries, mostly 2–5 mm in diameter, located in the cortico-subcortical junction and deep in the cerebral hemispheres. The presence of $\geq$ 1 CMB was counted as 1 point.
(4) PVS: defined as round, oval, or linear lesions that pass-through of gray or white matter, hypointense on T1WI and FLAIR imaging, and hyperintense on T2WI, with a diameter of $<$ 3 mm. A visual quantization method was used to count the number of lesions in the basal ganglia and semioval center. A PVS of level $\geq$ 2 was counted as 1 point (Huijts et al., 2013; Lau et al., 2017).

The total MRI burden of CSVD scores was then categorized into 2 groups based on the simple CSVD score: mild burden (0–1 points) or moderate to severe burden (2–4 points).

Statistical Analysis

All statistical analyses were performed with the Windows SPSS software package (Version 26.0, IBM Corporation, Armonk, NY, United States). Continuous variables with normal distribution were presented as mean ± SD, whereas continuous variables with skewed distribution were summarized as medians and interquartile ranges. Categorical variables were expressed as numbers and percentages. Differences between groups were tested in univariate analyses using independent sample *t*-test, Kruskal-Wallis *H*-test, Mann-Whitney *U*-test, chi-square test, or Fisher's exact test as appropriate. LSD tests and Bonferroni corrections were used in *post hoc* analyses. Variables that demonstrated a degree of significance of $P < 0.1$ in univariate analysis were entered into a multivariate binary logistic regression model to analyze the relationship between retinal microvascular abnormalities and the total MRI burden of CSVD. The correlation between the total MRI burden of CSVD and DR degree and retinal vascular calibers was tested using the Spearman rank method. Significance was defined as $P < 0.05$.

RESULTS

Baseline Characteristics of Diabetic Retinopathy

Among the 151 patients included in the study, the average age was 63.9 ± 8.6 years. There were 84 (55.6%) patients with NDR, 27 (17.9%) patients with mild DR, and 40 (26.5%) patients with moderate, severe, or proliferative DR (more than mild DR). Patients with more than mild DR were older and had a longer duration of diabetes, higher systolic blood pressure, and greater urinary microalbumin excretion than those with NDR (**Table 1**). No significant difference was observed among groups in sex distribution, medication use, or other baseline data.

The proportion of moderate to severe burden of CSVD in the more than mild DR group was 75%, which was higher than that of the mild DR group (48.1%) and the NDR group (26.2%) (**Figure 4**). There was a significant tendency toward retinal arteriolar narrowing and venular widening with increasing degree of DR. The AVR values in patients with mild DR (0.53 ± 0.04) and in those with more than mild DR (0.51 ± 0.04) were smaller than in patients with NDR (0.57 ± 0.04). These

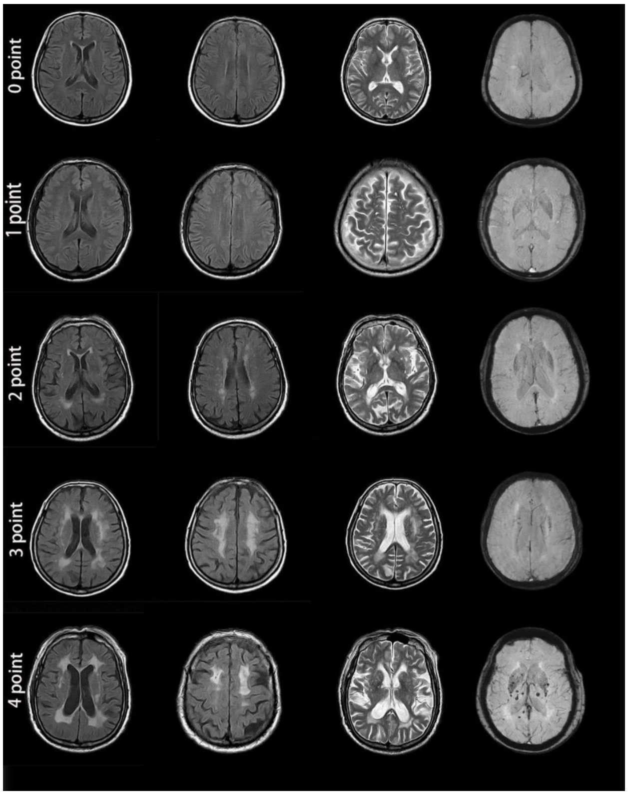

FIGURE 3 | MRI images from patients with different cerebral small vessel disease scores. **Zero points:** This patient was a 46-year-old man with no apparent lesions on MR images. **One point:** This patient was a 56-year-old man. Enlarged perivascular spaces (PVS) (grade 3) could be seen in the brain cortex on T2-weighted imaging. MR images showed no other abnormality. **Two points:** This patient was a 72-year-old woman. MRI demonstrated a lacune in the right basal ganglia, smooth halo-like lesions near the bilateral ventricles (Fazekas 2 for periventricular WMH), confluent white matter hyperintensities (Fazekas 2 for deep WMH) in the deep lobe and enlarged PVS (grade 1) in the bilateral basal ganglia. Susceptibility-weighted imaging showed no abnormality. **Three points:** This patient was a 69-year-old woman. MRI showed irregular white matter lesions in the lateral ventricles extending to the white matter (Fazekas 3 for periventricular WMH), large confluent areas of WMH (Fazekas 3 for deep WMH) in the center of the bilateral semioval and enlarged PVS (grade 3). **Four points:** This patient was a 77-year-old man. There were patchy, irregular white matter lesions extending to the white matter in the lateral ventricle (Fazekas 3 for periventricular WMH), fused WMH (Fazekas 3 for deep WMH), and 2 lacunes in the parietal lobe, enlarged PVS (grade 2) in the bilateral basal ganglia, and cerebral microbleeds at the level of the bilateral ventricles. All 4 MRI markers appeared in the images from this patient.

significant associations remained significant after LSD tests or Bonferroni corrections (**Table 1**).

Association of Retinal Microvascular Abnormalities With Total Magnetic Resonance Imaging Burden of Cerebral Small Vessel Disease

A total of 86 patients demonstrated mild burden of CSVD, and 65 patients demonstrated moderate to severe burden of CSVD. Patients with moderate to severe CSVD burden were more likely than those with mild CSVD burden to have narrowed retinal arterioles (105.24 ± 8.42 μm vs. 109.45 ± 7.93 μm), widened retinal venules (201.67 ± 16.25 μm vs. 193.95 ± 13.54 μm), and lower AVR (0.52 ± 0.05 vs. 0.57 ± 0.04) ($P < 0.05$ for all). Patients with moderate to severe burden of CSVD also demonstrated a higher proportion of more than mild DR (46.2%) than those with mild burden of CSVD (11.6%) (**Table 2**).

Spearman rank correlation analysis demonstrated that the degree of DR ($r = 0.465$, $P < 0.001$) and CRVE ($r = 0.366$, $P < 0.001$) were positively correlated with the total MRI burden of CSVD, whereas CRAE ($r = -0.306$, $P < 0.001$) was negatively correlated with the total MRI burden of CSVD.

Multivariate Logistic Regression Analysis of Total Magnetic Resonance Imaging Burden of Cerebral Small Vessel Disease

Multivariate logistic regression analysis was performed to further evaluate the association between the total MRI burden of CSVD and retinal microvascular abnormalities. After adjustments were made for confounding factors such as age, smoking, alcohol consumption, hypertension, and stroke, more than mild DR (OR, 4.383; 95% CI, 1.179–17.202; $P = 0.028$), CRAE (OR, 0.490; 95% CI, 0.256–0.936; $P = 0.031$), and CRVE (OR, 1.475; 95% CI, 1.016–2.143; $P = 0.041$) were found to be independently associated with moderate to severe burden of CSVD (**Table 3**).

DISCUSSION

This study found that DR was correlated with the total MRI burden of CSVD in patients with type 2 diabetes. More specifically, the degree of DR was associated with more severe CSVD. Further, CRAE, CRVE, and the presence of more than mild DR were independently associated with increased burden of CSVD.

DR has a high incidence in patients with diabetes and is one of the most common microvascular complications in this population. Additionally, as a slowly progressive neuromicrovascular disorder, diabetes is associated with an increased risk of the occurrence of CSVD (van Sloten et al., 2020). Research has shown that retinal microvascular abnormalities can reflect changes in small cerebral arteries caused by vascular risk factors such as diabetes and hypertension (Yip et al., 2016). Previous studies have mostly focused on the relationship between retinal microvascular abnormalities and individual CSVD markers. Mutlu et al. (2016) found that the widening of retinal venules and arteriole stenosis were related to the volume of white matter lesions and that changes in retinal vessels calibers may have predated these lesions. Dumitrascu et al. (2018) found that changes in arteriovenous nicking, focal arteriolar narrowing, and retinal vascular curvature were more common in patients with CSVD than in those without CSVD. The degree of retinal vein dilation and focal arteriolar narrowing was related to the presence of lacunes. In our study, we used a scoring system that included WMHs, lacunes, EPVS, and

TABLE 1 | Clinical characteristics of the study population according to DR status (NDR, mild DR, or more than mild DR).

Variables	NDR (*n* = 84)	Mild DR (*n* = 27)	More than mild DR (*n* = 40)	*P*-value
Age, y; mean ± SD	62.3 ± 8.6	65.5 ± 8.0	66.3 ± 8.2*	0.030
Male, n (%)	44 (52.4)	14 (51.9)	16 (40.0)	0.413
Vascular risk factors at baseline				
Smoking, n (%)	22 (23.8)	11 (40.7)	9 (22.5)	0.178
Alcohol consumption, n (%)	14 (16.7)	6 (22.2)	9 (22.5)	0.675
Hypertension, n (%)	51 (60.7)	18 (66.7)	27 (67.5)	0.714
Duration of diabetes, years, median (IQR)	10 (4, 15)	12 (10, 20)	19.5 (10, 21)*	<0.001
Previous stroke, n (%)	14 (16.7)	5 (18.5)	9 (22.5)	0.737
Coronary heart disease, n (%)	6 (7.1)	2 (7.4)	0 (0)	0.218
Carotid artery plaques, n (%)	51 (60.7)	19 (70.4)	29 (72.5)	0.367
Systolic BP, mmHg, mean ± SD	135 ± 18	129 ± 17	143 ± 21*§	0.009
Diastolic BP, mmHg, mean ± SD	78 ± 10	75 ± 12	78 ± 11	0.314
BMI, kg/m^2, mean ± SD	24.16 ± 3.57	23.58 ± 2.92	23.88 ± 3.11	0.715
Laboratory tests				
Fasting glucose, mmol//L, median (IQR)	8.38 (6.62, 11.30)	8.06 (6.29, 12.09)	8.79 (6.89, 11.70)	0.774
HbA$_1$c, %, median (IQR)	8.40 (7.73, 10.50)	8.40 (7.30, 10.50)	8.45 (7.53, 9.95)	0.880
Total cholesterol, mmol//L, mean ± SD	4.29 ± 1.02	4.60 ± 1.59	4.46 ± 1.34	0.492
Triglycerides, mmol//L, mean ± SD	1.86 ± 1.17	1.81 ± 1.41	1.70 ± 1.02	0.771
LDL-C, mmol//L, mean ± SD	2.42 ± 0.71	2.56 ± 0.90	2.55 ± 0.87	0.605
HDL-C, mmol//L, mean ± SD	1.04 ± 0.29	1.14 ± 0.37	1.10 ± 0.30	0.268
Serum creatinine, μmol/L, mean ± SD	63.26 ± 19.10	67.76 ± 28.84	73.60 ± 34.14	0.112
Urinary microalbumin/creatinine ratio, mg/g, median (IQR)	11.80 (7.15, 28.73)	27.00 (8.40, 58.40)*	20.80 (9.33, 163.65)*	0.012
Medication use				
Insulin treatment, n (%)	25 (29.8)	6 (22.2)	15 (37.5)	0.402
Hypoglycemic agents, n (%)	48 (57.1)	14 (51.9)	20 (50.0)	0.727
Antihypertensive medication, n (%)	30 (35.7)	11 (40.7)	17 (42.5)	0.740
Antiplatelet medication, n (%)	15 (17.9)	8 (29.6)	6 (15.0)	0.294
Lipid-modifying medication, n (%)	28 (33.3)	11 (40.7)	10 (25.0)	0.389
Retinal vessel changes				
CRAE, μm, mean ± SDmean SD	109.15 ± 8.96	106.37 ± 6.70	105.32 ± 7.62*	0.039
CRVE, μm, mean ± SD	191.58 ± 16.47	200.34 ± 9.63*	207.15 ± 8.59*	<0.001
AVR, mean ± SD	0.57 ± 0.04	0.53 ± 0.04*	0.51 ± 0.04*§	<0.001
Total MRI burden score of CSVD				<0.001
Mild burden, n (%)	62 (73.8)	14 (51.9)	10 (25.0)*	
Moderate to severe burden, n (%)	22 (26.2)	13 (48.1)	30 (75.0)*	

DR, diabetic retinopathy; NDR, no diabetic retinopathy; SD, standard deviation; IQR, interquartile range; LDL, low-density lipoprotein; HDL, high-density lipoprotein; CRAE, Central Retinal Arterial Equivalent; CRVE, Central Retinal Venous Equivalent; AVR, arteriole-to-venule ratio; CSVD, cerebral small vessel disease.

**Indicates that the difference was statistically significant compared with the NDR group.*

§Indicates that the difference was statistically significant compared with the mild DR group.

cerebral microhemorrhages in the assessment of CSVD. It is a relatively new scoring system in recent years that can comprehensively evaluate the combined effect of CSVD lesions. The effectiveness and applicability of this scoring system for CSVD have been demonstrated in a growing number of studies (Lau et al., 2017; Yang et al., 2019; Shu et al., 2020).

Previous research has shown that retinal microvascular dysfunction is related to diabetes mellitus; this dysfunction includes not only DR but also subtle abnormalities in the structure and function of retinal microvascular vessels, such as retinal venule dilation or arteriole reduction, and increased fractal dimension (Stehouwer, 2018; van Sloten et al., 2020). In our study, differences in retinal blood vessel calibers were observed among patients with different severities of DR. With the aggravation of DR, CRVE tended to increase, whereas CRAE and AVR tended to decrease. These differences were statistically significant, suggesting that widened retinal venules and narrowed retinal arterioles may be related to the progression of DR. Diabetes is associated with a number of microvascular and macrovascular complications that affect the retina and the brain in parallel, so both retinal blood vessels and cerebrovascular vessels are susceptible to this disease (Pearce et al., 2019). Previous research has shown that retinopathy and retinal microvascular abnormalities are associated with the presence and progression of CSVD in patients with type 2 diabetes (Cheung et al., 2015), some of the findings confirmed by our study. In our study, we

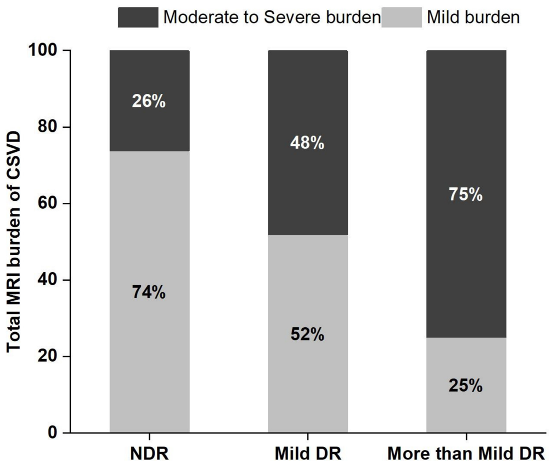

FIGURE 4 | Frequency and severity of cerebral small vessel disease (CSVD) in the 3 study groups. DR, diabetic retinopathy; NDR, no diabetic retinopathy.

found that DR was related to the total MRI burden of CSVD, and the more severe the DR was, the heavier the total MRI burden was.

Hyperglycemia is associated with systemic endothelial dysfunction of the microcirculation, which can cause cerebral hypoperfusion, leading to chronic cerebral ischemia (Sörensen et al., 2016). The changes in cerebral microcirculation in diabetic patients are related to the increased permeability of the blood-brain barrier and changes in cerebral blood flow regulation. The blood-brain barrier is susceptible to oxidative stress, which may be caused by the increased production of reactive oxygen species associated with hyperglycemia and limited antioxidant defenses in the brain. This disruption of the blood-brain barrier in turn leads to vessel wall thickening and disorders of the cerebral microcirculation, resulting in structural brain abnormalities (Bogush et al., 2017; Rhea and Banks, 2019). In our study, we found that patients with narrower retinal arterioles and wider retinal venules show a heavier total MRI burden of CSVD. After adjusting for confounding factors such as age, smoking, alcohol consumption, hypertension, and stroke, we found that CRAE, CRVE, and the presence of more than mild DR were independently associated with moderate to severe burden of CSVD.

Patients with diabetes may also be affected by microvascular complications other than DR, such as diabetic nephropathy and diabetic neuropathy. A systematic review reported that DR is consistently associated with other complications of

TABLE 2 | Clinical characteristics of the study population based on the total MRI burden of CSVD.

Variables	Mild burden (*n* = 86)	Moderate to severe burden (*n* = 65)	*P*-value
Age, y; mean ± SD	61.3 ± 8.7	67.4 ± 7.2	<0.001
Male, n (%)	43 (50.0)	31 (47.7)	0.779
Vascular risk factors at baseline			
Smoking, n (%)	17 (19.8)	23 (35.4)	0.031
Alcohol consumption, n (%)	11 (12.8)	18 (27.7)	0.021
Hypertension, n (%)	44 (51.2)	52 (80.0)	<0.001
Duration of diabetes, years, median (IQR)	10 (6, 17)	12 (6.5, 20.5)	0.113
Previous stroke, n (%)	7 (8.1)	21 (32.3)	<0.001
Coronary heart disease, n (%)	4 (4.7)	4 (6.2)	0.726
Carotid artery plaques, n (%)	47 (54.7)	52 (80.0)	0.001
Systolic BP, mmHg, mean ± SD	133 ± 18	141 ± 21	0.008
Diastolic BP, mmHg, mean ± SD	77 ± 11	78 ± 10	0.741
BMI, kg/m^2, mean ± SD	24.05 ± 3.12	23.90 ± 3.61	0.781
Laboratory test			
Fasting glucose, mmol//L, median (IQR)	7.78 (6.47, 9.89)	9.37 (7.47, 12.77)	0.005
HbA$_1$c, %, median (IQR)	8.10 (7.0, 9.68)	9.40 (8.05, 10.90)	<0.001
Total cholesterol, mmol//L, mean ± SD	4.47 ± 1.17	4.28 ± 1.30	0.350
Triglycerides, mmol//L, mean ± SD	1.83 ± 1.12	1.79 ± 1.25	0.846
LDL-C, mmol//L, mean ± SD	2.48 ± 0.75	2.36 ± 0.83	0.475
HDL-C, mmol//L, mean ± SD	1.11 ± 0.32	1.02 ± 0.28	0.086
Serum creatinine, μmol//L, mean ± SD	60.95 ± 19.46	74.54 ± 30.93	0.001
Urinary microalbumin/creatinine ratio, mg/g, median (IQR)	11.80 (6.60, 27.58)	20.50 (9.10, 97.95)	<0.001
Retinal microvascular abnormalities			
DR			<0.001
NDR, n (%)	62 (72.1)	22 (33.8)	
Mild DR, n (%)	14 (16.3)	13 (20.0)	
More than mild DR, n (%)	10 (11.6)	30 (46.2)	
CRAE, μm, mean ± SD	109.45 ± 7.93	105.24 ± 8.42	0.002
CRVE, μm, mean ± SD	193.95 ± 13.54	201.67 ± 16.25	0.002
AVR, mean ± SD	0.57 ± 0.04	0.52 ± 0.05	<0.001

DR, diabetic retinopathy; NDR, no diabetic retinopathy; SD, standard deviation; IQR, interquartile range; LDL, low-density lipoprotein; HDL, high-density lipoprotein; CRAE, Central Retinal Arterial Equivalent; CRVE, Central Retinal Venous Equivalent; AVR, arteriole-to-venule ratio; CSVD, cerebral small vessel disease.

TABLE 3 | Multivariate logistic regression analysis of the total MRI burden of CSVD.

Variable	OR	95% CI	*P*-value
Age	1.100	1.024∼1.181	0.009
Hypertension	3.531	1.118∼11.148	0.031
HbA_1c	1.601	1.117∼2.294	0.010
More than mild DR	4.383	1.179∼17.202	0.028
CRAE	0.490	0.256∼0.936	0.031
CRVE	1.475	1.016∼2.143	0.041

OR, odds ratio; CI, confident interval; DR, diabetic retinopathy; CRAE, Central Retinal Arterial Equivalent; CRVE, Central Retinal Venous Equivalent; CSVD, cerebral small vessel disease.

diabetes, with the severity of DR contributing to a higher risk of developing other microvascular complications (Pearce et al., 2019). One study found that nephropathy was the only complication of diabetes independently associated with DR, and the presence of retinopathy increased the likelihood of developing nephropathy by 4.37 times (El-Asrar et al., 2001). In our study, we also found that patients with diabetes who have retinopathy, compared with those without retinopathy, had greater urinary albumin excretion. Fewer studies have evaluated the relationship between retinal vascular changes and diabetic neuropathy. One population-based cross-sectional study found that suboptimal arteriolar caliber and DR were associated with peripheral neuropathy (Ding et al., 2012).

This study also found that age and hypertension were independent risk factors for increased total MRI burden of CSVD, which is consistent with the results of previous studies (Hernandez-Diaz et al., 2019; Shu et al., 2020). Nam et al. (2020) found that in patients with no history of cerebrovascular disease, a high triglyceride-glucose index was associated with a higher total burden of CSVD, suggesting that this index may be a convenient and useful predictor of CSVD. In a large population-based study, van Agtmaal et al. (2018) found that persistent hyperglycemia was associated with abnormalities such as WMHs and lacunes. In our study, HbA1c was found to be an independent risk factor for moderate to severe burden of CSVD, which was consistent with the findings of van Agtmaal et al. (2018). However, we observed no significant correlation between triglycerides or fasting blood glucose and the total MRI burden of CSVD; this lack of association may be related to the use of medications to control diabetes, as well as lipid-regulating agents.

This study had several limitations. First, because this was a cross-sectional study, a direct relationship between retinal microangiopathy and CSVD could not be demonstrated. Second, the study included patients with type 2 diabetes but did not include age-matched prediabetic or non-diabetic controls, making it difficult to extrapolate these results to a wider population. Future studies will be needed to assess the relationship between total MRI burden and retinal microvascular lesions in patients with prediabetes and non-vascular factors. The semiquantitative method used in this study to evaluate retinal blood calibers may be inaccurate. In addition, while some studies have adopted quantitative assessment of WMHs, there is no quantitative disease burden evaluation system that truly targets small blood vessels themselves. Further research is needed to establish a more accurate system for evaluating the total MRI burden of CSVD. In future studies, we plan to use a high-resolution, high-quality imaging segmentation method to examine volumetric data for WMH, lacunes, EPVS, recent subcortical infarcts, microbleeds, and global and regional brain volume, with the goal of identifying the global burden of brain changes. Automated image quantification tools are becoming a crucial part of clinical research and practice; thus, a robust and precise MRI segmentation method capable of identifying multiple imaging features of CSVD is needed. Finally, further research is needed regarding quantifying and intelligentizing imaging and symptomatic diagnosis for CSVD.

CONCLUSION

In conclusion, this study found that retinal microvascular abnormalities in diabetic patients are related to the occurrence of CSVD. These retinal microvascular abnormalities can be used to evaluate the severity of CSVD and to predict the occurrence of intracranial microvascular disease.

DATA AVAILABILITY STATEMENT

The original contributions presented in the study are included in the article/supplementary material, further inquiries can be directed to the corresponding author.

ETHICS STATEMENT

This cross-sectional observational study was approved by the Ethics Committee of Changzhou Second People's Hospital (2017KY015-01). Informed consent was obtained from patients or their family members. The patients/participants provided their written informed consent to participate in this study.

AUTHOR CONTRIBUTIONS

YZ, ZZ, and MZ designed the study. YC, ZZ, and WY reviewed clinical MRIs for radiologic grading. YZ carried out data analysis. YZ and ZZ wrote the manuscript. MZ, YC, and WY made the important data analysis suggestions and manuscript revisions. All authors contributed to the article and approved the submitted version.

FUNDING

This study was supported by the General Program of Jiangsu Commission of Health (H2019051) and the Changzhou Health Care Young Talents Training Project (CZQM2020073).

ACKNOWLEDGMENTS

We are indebted to the patients and families for their kind participation in our research and the medical staff of Changzhou

Second People's Hospital affiliated to Nanjing Medical University for their help in conducting medical interviews, acquiring clinical data. We also thank ophthalmologists Yanwen Ja and Ting Pan and ophthalmology graduate student Yaomin Qi, who assessed the retinal microvascular abnormalities. Without them, this study would not have been possible.

REFERENCES

Bogush, M., Heldt, N. A., and Persidsky, Y. (2017). Blood brain barrier injury in diabetes: unrecognized effects on brain and cognition. *J. Neuroimmune Pharmacol.* 12, 593–601. doi: 10.1007/s11481-017-9752-7

Cheung, C. Y., Ikram, M. K., Klein, R., and Wong, T. Y. (2015). The clinical implications of recent studies on the structure and function of the retinal microvasculature in diabetes. *Diabetologia* 58, 871–885. doi: 10.1007/s00125-015-3511-1

Ding, J., Cheung, C. Y., Ikram, M. K., Zheng, Y. F., Cheng, C. Y., Lamoureux, E. L., et al. (2012). Early retinal arteriolar changes and peripheral neuropathy in diabetes. *Diabetes Care* 35, 1098–1104. doi: 10.2337/dc11-1341

Dumitrascu, O. M., Demaerschalk, B. M., Sanchez, C. V., Almader-Douglas, D., O'Carroll, C. B., Aguilar, M. I., et al. (2018). Retinal microvascular abnormalities as surrogate markers of cerebrovascular ischemic disease: a meta-analysis. *J. Stroke Cerebrovasc. Dis.* 27, 1960–1968. doi: 10.1016/j.jstrokecerebrovasdis.2018.02.041

El-Asrar, A., Al-Rubeaan, K., Al-Amro, S., Moharram, O., and Kangave, D. (2001). Retinopathy as a predictor of other diabetic complications. *Int. Ophthalmol.* 24, 1–11. doi: 10.1023/a:1014409829614

Hemmingsen, B., Gimenez-Perez, G., Mauricio, D., Roque, F. M., Metzendorf, M. I., and Richter, B. (2017). Diet, physical activity or both for prevention or delay of type 2 diabetes mellitus and its associated complications in people at increased risk of developing type 2 diabetes mellitus. *Cochrane Database Syst. Rev.* 12:CD003054. doi: 10.1002/14651858.CD003054.pub4

Hernandez-Diaz, Z. M., Pena-Sanchez, M., Gonzalez-Quevedo Monteagudo, A., Gonzalez-Garcia, S., Arias-Cadena, P. A., Brown-Martinez, M., et al. (2019). Cerebral small vessel disease associated with subclinical vascular damage indicators in asymptomatic hypertensive patients. *Behav. Sci.* 9:91. doi: 10.3390/bs9090091

Huijts, M., Duits, A., van Oostenbrugge, R. J., Kroon, A. A., de Leeuw, P. W., and Staals, J. (2013). Accumulation of MRI markers of cerebral small vessel disease is associated with decreased cognitive function. A study in first-ever lacunar stroke and hypertensive patients. *Front. Aging Neurosci.* 5:72. doi: 10.3389/fnagi.2013.00072

Lau, K. K., Li, L., Schulz, U., Simoni, M., Chan, K. H., Ho, S. L., et al. (2017). Total small vessel disease score and risk of recurrent stroke: validation in 2 large cohorts. *Neurology* 88, 2260–2267. doi: 10.1212/WNL.0000000000004042

London, A., Benhar, I., and Schwartz, M. (2013). The retina as a window to the brain-from eye research to CNS disorders. *Nat. Rev. Neurol.* 9, 44–53. doi: 10.1038/nrneurol.2012.227

McGrory, S., Ballerini, L., Doubal, F. N., Staals, J., Allerhand, M., Valdes-Hernandez, M. D., et al. (2019). Retinal microvasculature and cerebral small vessel disease in the Lothian Birth Cohort 1936 and Mild Stroke Study. *Sci. Rep.* 9:6320. doi: 10.1038/s41598-019-42534-x

Mutlu, U., Cremers, L. G. M., de Groot, M., Hofman, A., Niessen, W. J., van der Lugt, A., et al. (2016). Retinal microvasculature and white matter microstructure: the rotterdam study. *Neurology* 87, 1003–1010. doi: 10.1212/wnl.0000000000003080

Nam, K.-W., Kwon, H.-M., Jeong, H.-Y., Park, J.-H., Kwon, H., and Jeong, S.-M. (2020). High triglyceride-glucose index is associated with subclinical cerebral small vessel disease in a healthy population: a cross-sectional study. *Cardiovasc. Diabetol.* 19:53. doi: 10.1186/s12933-020-01031-6

Pearce, I., Simo, R., Lovestam-Adrian, M., Wong, D. T., and Evans, M. (2019). Association between diabetic eye disease and other complications of diabetes: implications for care. A systematic review. *Diabetes Obes. Metab.* 21, 467–478. doi: 10.1111/dom.13550

Qiu, C., Ding, J., Sigurdsson, S., Fisher, D. E., Zhang, Q., Eiriksdottir, G., et al. (2018). Differential associations between retinal signs and CMBs by location: the AGES-reykjavik study. *Neurology* 90, e142–e148. doi: 10.1212/WNL.0000000000004792

Rhea, E. M., and Banks, W. A. (2019). Role of the blood-brain barrier in central nervous system insulin resistance. *Front. Neurosci.* 13:521. doi: 10.3389/fnins.2019.00521

Sanahuja, J., Alonso, N., Diez, J., Ortega, E., Rubinat, E., Traveset, A., et al. (2016). Increased burden of cerebral small vessel disease in patients with type 2 diabetes and retinopathy. *Diabetes Care* 39, 1614–1620. doi: 10.2337/dc15-2671

Shahulhameed, S., Vishwakarma, S., Chhablani, J., Tyagi, M., Pappuru, R. R., Jakati, S., et al. (2020). A systematic investigation on complement pathway activation in diabetic retinopathy. *Front. Immunol.* 11:154. doi: 10.3389/fimmu.2020.00154

Shu, L., Liang, J., Xun, W., Yang, H., and Lu, T. (2020). Prediction for the total MRI burden of cerebral small vessel disease with retinal microvascular abnormalities in ischemic stroke/TIA patients. *Front. Neurol.* 11:268. doi: 10.3389/fneur.2020.00268

Solomon, S. D., Chew, E., Duh, E. J., Sobrin, L., Sun, J. K., VanderBeek, B. L., et al. (2017). Diabetic retinopathy: a position statement by the american diabetes association. *Diabetes Care* 40, 412–418. doi: 10.2337/dc16-2641

Sörensen, B., Houben, A., Berendschot, T., Schouten, J., Kroon, A., van der Kallen, C., et al. (2016). Prediabetes and Type 2 diabetes are associated with generalized microvascular dysfunction: the maastricht study. *Circulation* 134, 1339–1352. doi: 10.1161/circulationaha.116.023446

Stehouwer, C. D. A. (2018). Microvascular dysfunction and hyperglycemia: a vicious cycle with widespread consequences. *Diabetes* 67, 1729–1741. doi: 10.2337/dbi17-0044

van Agtmaal, M. J. M., Houben, A., de Wit, V., Henry, R. M. A., Schaper, N. C., Dagnelie, P. C., et al. (2018). Prediabetes is associated with structural brain abnormalities: the maastricht study. *Diabetes Care* 41, 2535–2543. doi: 10.2337/dc18-1132

van Sloten, T. T., Sedaghat, S., Carnethon, M. R., Launer, L. J., and Stehouwer, C. D. A. (2020). Cerebral microvascular complications of type 2 diabetes: stroke, cognitive dysfunction, and depression. *Lancet Diabetes Endocrinol.* 8, 325–336. doi: 10.1016/s2213-8587(19)30405-x

Wardlaw, J. M., Smith, E. E., Biessels, G. J., Cordonnier, C., Fazekas, F., Frayne, R., et al. (2013). Neuroimaging standards for research into small vessel disease and its contribution to ageing and neurodegeneration. *Lancet Neurol.* 12, 822–838. doi: 10.1016/s1474-4422(13)70124-8

Yang, X., Zhang, S., Dong, Z., Zi, Y., Luo, Y., Jin, Z., et al. (2019). Insulin resistance is a risk factor for overall cerebral small vessel disease burden in old nondiabetic healthy adult population. *Front. Aging Neurosci.* 11:127. doi: 10.3389/fnagi.2019.00127

Yip, W., Tham, Y. C., Hsu, W., Lee, M. L., Klein, R., Klein, B., et al. (2016). Comparison of common retinal vessel caliber measurement software and a conversion algorithm. *Transl. Vis. Sci. Technol.* 5:11. doi: 10.1167/tvst.5.5.11

Conflict of Interest: The authors declare that the research was conducted in the absence of any commercial or financial relationships that could be construed as a potential conflict of interest.

frontiers in Neuroscience

METHODS
published: 24 December 2021
doi: 10.3389/fnins.2021.797166

DW-Net: Dynamic Multi-Hierarchical Weighting Segmentation Network for Joint Segmentation of Retina Layers With Choroid Neovascularization

*Lianyu Wang[1], Meng Wang[1], Tingting Wang[1], Qingquan Meng[1], Yi Zhou[1], Yuanyuan Peng[1], Weifang Zhu[1], Zhongyue Chen[1] and Xinjian Chen[1,2]**

[1] School of Electronics and Information Engineering, Soochow University, Suzhou, China, [2] State Key Laboratory of Radiation Medicine and Protection, Soochow University, Suzhou, China

OPEN ACCESS

Edited by:
Jian Zheng,
Suzhou Institute of Biomedical Engineering and Technology, Chinese Academy of Sciences (CAS), China

Reviewed by:
Shouping Zhu,
Xidian University, China
Xiaopeng Ma,
Shandong University, China

***Correspondence:**
Xinjian Chen
xjchen@suda.edu.cn

Specialty section:
This article was submitted to Perception Science, a section of the journal Frontiers in Neuroscience

Received: *18 October 2021*
Accepted: *22 November 2021*
Published: *24 December 2021*

Citation:
Wang L, Wang M, Wang T, Meng Q, Zhou Y, Peng Y, Zhu W, Chen Z and Chen X (2021) DW-Net: Dynamic Multi-Hierarchical Weighting Segmentation Network for Joint Segmentation of Retina Layers With Choroid Neovascularization. Front. Neurosci. 15:797166. doi: 10.3389/fnins.2021.797166

Choroid neovascularization (CNV) is one of the blinding factors. The early detection and quantitative measurement of CNV are crucial for the establishment of subsequent treatment. Recently, many deep learning-based methods have been proposed for CNV segmentation. However, CNV is difficult to be segmented due to the complex structure of the surrounding retina. In this paper, we propose a novel dynamic multi-hierarchical weighting segmentation network (DW-Net) for the simultaneous segmentation of retinal layers and CNV. Specifically, the proposed network is composed of a residual aggregation encoder path for the selection of informative feature, a multi-hierarchical weighting connection for the fusion of detailed information and abstract information, and a dynamic decoder path. Comprehensive experimental results show that our proposed DW-Net achieves better performance than other state-of-the-art methods.

Keywords: multi-target segmentation, choroid neovascularization, convolutional neural network, optical coherence tomography, medical image processing, attention mechanism

INTRODUCTION

The choroid is an important tissue of the human eye. It is a soft and smooth brown film located between the retina and the sclera (Hageman et al., 1995; Bressler, 2002). Optical coherence tomography (OCT) is a noninvasive, high-resolution biological imaging technology that can be used for *in vivo* measurement of fundus structures such as the retina, retinal nerve fiber layer, macula, and optic disc (Huang et al., 1991; Fercher et al., 1993). In OCT image, the normal retinal structure presents multiple interconnected retinal layers (Srinivasan et al., 2014; Zanet et al., 2019); from the inside to the outside are: the nerve fiber layer (NFL), Ganglion cell layer (GCL), inner plexiform layer (IPL), inner nuclear layer (INL), outer plexiform layer (OPL), outer nuclear layer (ONL), outer photoreceptor segment layer (OPSL), and retinal pigment epithelium (RPE). **Figure 1** shows the OCT image with normal retinal layers.

Choroid neovascularization (CNV), also known as sub-retinal neovascularization, refers to the pathologically proliferating blood vessels that extend from the choroid to the sub-retinal pigment epithelium, the sub-retinal space, or a combination of the above (Lopez et al., 1991; Laud et al., 2006). **Figure 2** shows the OCT image of the retina with CNV. Due to the high permeability of

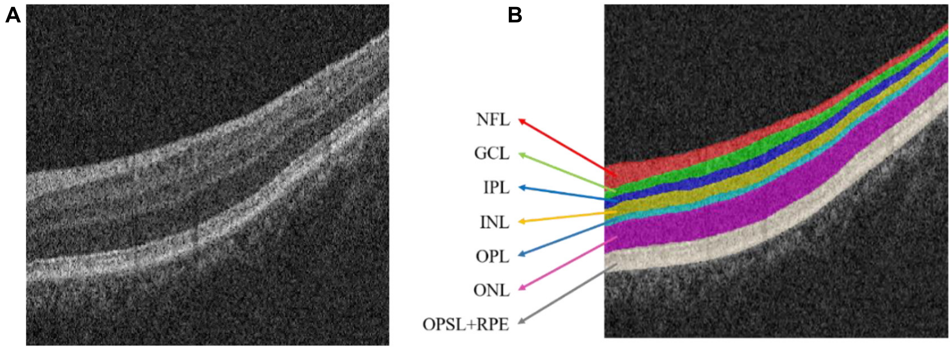

FIGURE 1 | Optical coherence tomography (OCT) image of the normal retinal layer. **(A)** Original image. **(B)** Label. *NFL*, nerve fiber layer; *GCL*, ganglion cell layer; *IPL*, inner plexiform layer; *INL*, inner nuclear layer; OPL, outer plexiform layer; *ONL*, outer nuclear layer; *OPSL*, outer photoreceptor segment layer; *RPE*, retinal pigment epithelium.

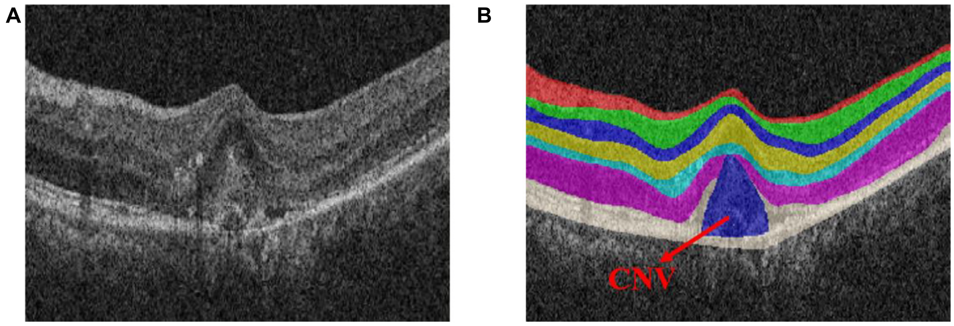

FIGURE 2 | Optical coherence tomography (OCT) image of the normal retinal layer containing choroid neovascularization (CNV). **(A)** Original image. **(B)** Label.

the vascular wall of neovascularization, it may lead to sub-retinal hemorrhage, lipid exudation, detachment of the retinal pigment epithelium and choroid, and the formation of fibrotic scars (Zhang et al., 2017). The main symptoms are visual loss, distortion of vision, and central or para-central dark spots, which eventually lead to blindness (Saxe et al., 1993; Grossniklaus and Green, 2004). Therefore, early detection and quantitative measurement of CNV are crucial for the establishment of subsequent treatment plans.

Medical-aided diagnosis segmentation algorithm based on computer vision can quickly obtain the shape, size, location, and optical density value, which can provide reliable and accurate quantitative information for the diagnosis and treatment of CNV (Chen et al., 2012, 2016; Gao et al., 2015). Therefore, the development of a reliable and automatic OCT-based CNV segmentation method requires further attention.

However, accurate segmentation of CNV still faces great challenges. Firstly, the structure of the retina is complex due to the multiple retinal layers it contains (Garvin et al., 2009; Roy et al., 2017). Secondly, with the existence of CNV or fluid, the adjacent retinal layers will deform greatly, resulting in a decrease in contrast (Shi et al., 2015). Thirdly, some CNVs are small objects that are hard to discriminate, resulting in performance degradation.

Therefore, focusing on these problems, we propose a new dynamic multi-hierarchical weighting segmentation network (DW-Net) for the joint segmentation of CNV and retinal layers in retinal OCT images. To alleviate the increase in the difficulty of CNV segmentation due to the complexity of the retinal layer structure, we developed a joint framework for the simultaneous segmentation of the retinal layers and CNV. To reduce the impact of partial deformation of the retinal layers and improve the segmentation performance on small CNVs, multiple multi-hierarchical connections are introduced in our proposed network, thus making full use of contextual information. Comprehensive experimental results suggest that our proposed DW-Net achieves superior performance in OCT-based segmentation of retinal layers with CNV compared with several state-of-the-art methods.

The major contributions of this paper can be summarized as follows. Firstly, we create an end-to-end deep learning framework for the simultaneous segmentation of the retinal layers and CNV. Secondly, we develop multiple multi-hierarchical connections to extract and fuse the features in a contextual-driven manner. Thirdly, we evaluate the proposed methods on OCT images of the retina, with experimental results suggesting the effectiveness of our methods.

The rest of the paper is organized as follows. We first briefly review related work in section "Related Work." Then, we introduce the proposed dynamic multi-hierarchical weighting segmentation network (DW-Net) in section "Methods". In section "Experiments and Results," we present the experimental settings, experimental results, ablation study, and the materials used in this study. The ablation study and the limitations of our current work are shown in section "Discussion," as well as possible future directions. Finally, we conclude this paper in section "Conclusion."

RELATED WORK

In recent years, several automatic CNV segmentation methods of the retinal layers and CNV have been proposed. Lu et al. (2010) segmented the retinal blood vessel into multiple vascular and non-vascular slices, smoothed and filtered to refine the layer boundary. Song et al. (2013) further used arc-based graph representation, combined extensive prior information through paired energy terms, and calculated the maximum flow in low-order polynomial time. In the same year, Dufour et al. (2013) proposed a graph-based automatic multi-surface segmentation algorithm to add prior information from the learning model and further improved the accuracy of segmentation. Xu et al. (2013) used the Iowa reference algorithm to segment 10 retinal layers, followed by a combined graph search/graph cut method to segment pairs of adjacent retinal layers and any present fluid-associated abnormality detection region in 3D. Xi et al. (2017, 2018) developed a structure prior method based on sparse representation classification and local latent function to capture the global spatial structure and local similarity structure prior, which improved the segmentation robustness of CNVs of different sizes.

At present, deep neural networks have been widely used for the segmentation of retinal images and CNV. Su et al. (2020) proposed a differential amplification block to extract the contrast information of the foreground and background, which is integrated into the U-shaped convolutional neural network for CNV segmentation. Based on density cell-like P systems, Xue et al. (2018) proposed an automatic quantification method of the CNV total lesion area on outer retinal OCT angiograms to improve the accuracy of the segmentation boundaries. To simultaneously segment layers and neovascularization, Xiang et al. (2018) extracted well-designed features to find the coarse surfaces of different OCTs and introduced a constrained graph search algorithm to accurately detect retinal surfaces. Wang et al. (2020) trained two independent convolutional neural networks to classify the input scans according to the presence or absence of CNVs in a complementary manner, forming a powerful CNV description system.

METHODS

Overview

The encoder–decoder structure (Ronneberger et al., 2015; Zhao et al., 2017; Feng et al., 2020) has been proven to be an efficient architecture for pixel-wise semantic segmentation among many deep learning-based methods; therefore, we propose a novel joint segmentation framework to solve the challenges in retinal CNV segmentation based on this. As shown in **Figure 3A**, the proposed DW-Net consists of three parts: residual aggregation encoder path, dynamic multi-hierarchical weighting connection, and dynamic decoder path.

Residual Aggregation Encoder Path

In the conventional encoder path, encoders are composed of stacked convolutional layers and pooling layers, which are used to extract rich semantic information and global features layer by layer. However, continuous convolution and pooling will reduce the resolution of semantic features, which may lead to the loss of some small objects (such as small CNVs). To reduce the loss of resolution and enhance the selectivity of the feature encoder, we utilized the residual module as our encoder in this paper. By fusing the current feature maps with previous feature maps, the residual module can obtain informative feature maps that are more conducive to subsequent segmentation.

As shown in **Figure 3B**, the input data $X \in \mathbb{R}^{H\times W\times C}$ is encoded by a convolutional layer and four encoders, as follows:

$$\begin{cases} X^{i,0} = \mathrm{Conv}(X) & i{=}0 \\ X^{i,0} = ResNet(X^{i-1,0}) & 1 \le i \le 4 \end{cases} \tag{1}$$

where H, W, and C denote the height, width, and channels of the input data, respectively, and $X^{0,0}$ represents the output of the first convolutional layer. $X^{i,0}(1 \le i \le 4)$ denotes the output feature maps of four encoders, with channel numbers of 64, 128, 256, and 512, respectively. To improve the feature extraction ability and save computing resources, we used the pre-trained model of layers 1–4 in ResNet18 (He et al., 2016) to initialize the parameters of the encoders.

Dynamic Multi-Hierarchical Weighting Connection

Encoders of different hierarchies can extract features of different levels. The local features extracted by the low-level encoder are relatively simple and are more inclined to the basic components of images such as points, lines, and contours, while the high-level encoder is able to extract more complex features, such as abstract globe information. As for the semantic segmentation tasks, abstract global features can improve the overall positioning ability of the object, while fine local features can refine the edges of the segmented object.

To make full use of the feature maps in multilevel encoders, as in **Figure 4** (Zhou et al., 2018) developed UNet++. They concatenated the features of encoders in order layer by layer directly (gray dotted line in **Figure 4**), thus improving the performance of the segmentation network. However, the output feature map of the encoder usually contains interference information such as background and noise, which need to be selected and filtered. Also, the output features of each level have different contributions to the segmentation task; therefore, direct concatenation cannot highlight the importance of each part. In addition, concatenation in each hierarchy will greatly increase the

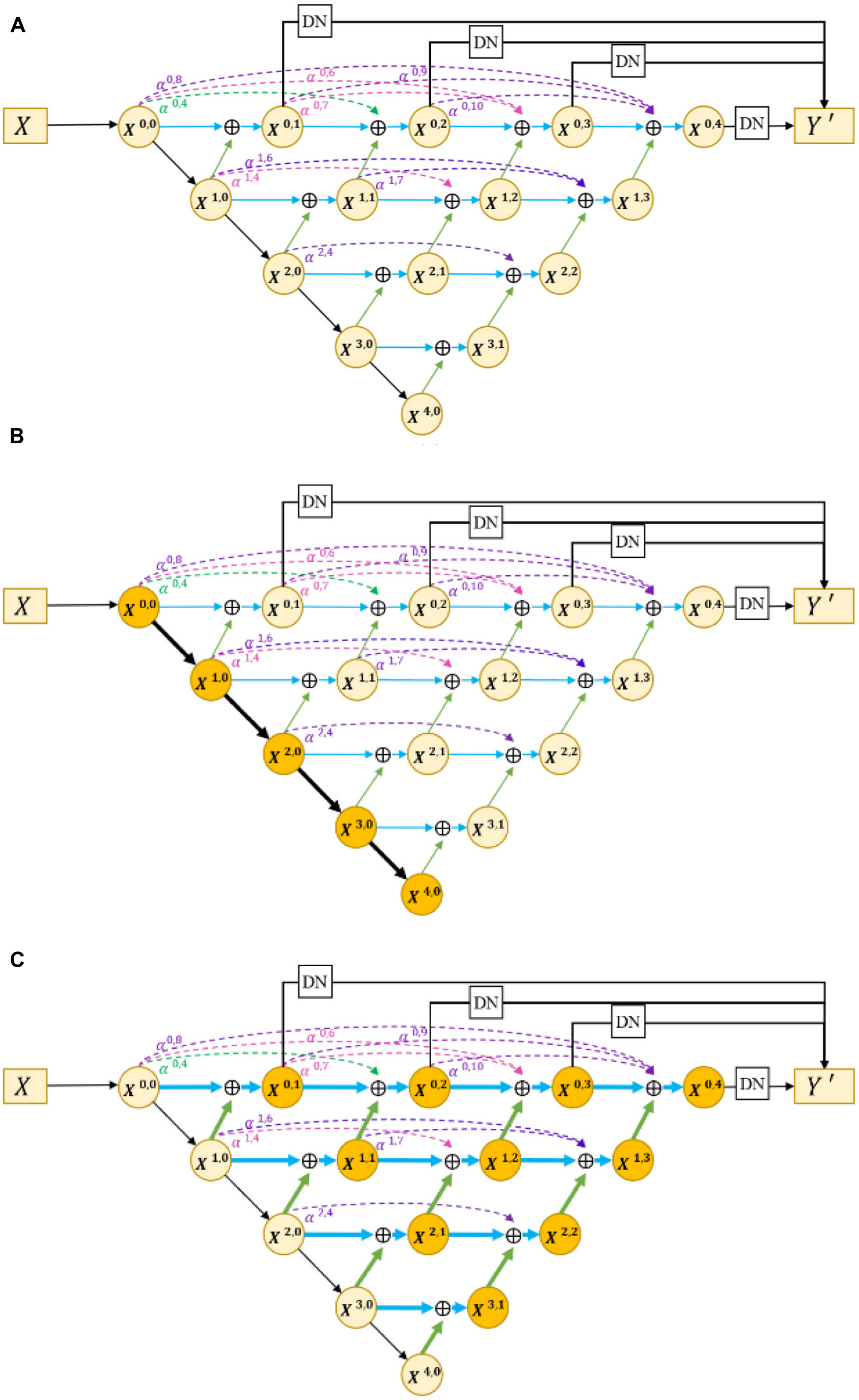

FIGURE 3 | (A) Architecture of the proposed dynamic multi-hierarchical weighting segmentation network (DW-Net). The *dark yellow* part in **(B,C)** indicate the residual aggregation encoder path and the dynamic multi-hierarchical weighting connection, respectively.

parameters of the network, which may reduce the training and increase the risk of overfitting.

In response to the above problems, we proposed a dynamic multi-hierarchical weighting connection, which aims to take full advantage of the multi-scale extracted features that are conducive to segmentation in a contextual-driven manner and to filter irrelevant information. **Figure 3C** shows the structure of our proposed dynamic multi-hierarchical weighting connection, and

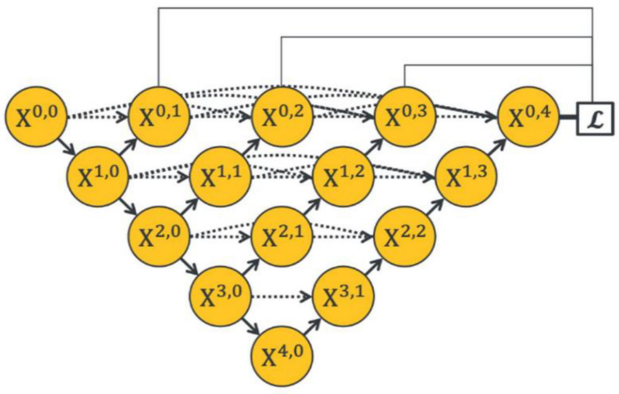

FIGURE 4 | Architecture of the UNet++ by Zhou et al. (2018).

its calculation process is as follows:

$$X^{i,j} = \mathrm{Conv}(X^{i,0} + DB(X^{x+1,j-1})) \quad 0 \le i \le 3, \quad j = 1 \tag{2}$$

$$X^{i,j} = \mathrm{Conv}(\sum_{k=0}^{j-2} \alpha^{i,2j+k} * X^{i,k} + X^{i,j-1} + DB(X^{x+1,j-1})) \qquad 0 \le i \le 4-j, \; 2 \le j \le 4 \tag{3}$$

where i and j denote the layer index and column index of the feature map $X^{i,j}$, respectively, and DB represents a decode module composed of a 3 × 3 convolutional layer and an upsampling layer. $\alpha^{i,2j+k}$ is a learnable parameter, which is optimized through multiple iterations. To make full advantage of the known detailed information and abstract information at all hierarchies, we performed pixel addition on all higher-level feature maps and current-level feature maps according to their weight, thereby dynamically enhancing the segmentation ability of the current-level decoder.

Dynamic Decoder Path

The dynamic decoder path contains four decoders, and the channels of the output feature map $X^{4-i,i} (0 \le i \le 3)$ are 256, 128, 64, and 32, respectively. The decoder path is composed of stacked convolutional layers and upsampling layers, which aims to upsample the feature maps with strong semantic information from a high level and restore the spatial resolution layer by layer. Zhou et al. (2018), conducted pixel-wise averaging on the output feature map of the decoder path and output feature maps at the same hierarchy (the black straight line in the upper part of **Figure 4**), as follows:

$$Y^{'} = \mathrm{soft\,max}\left(\frac{1}{4}\sum_{j=1}^{4} \mathrm{Conv}\left(X^{0,j}\right)\right) \tag{4}$$

where $Conv$ is a simple 1 × 1 convolutional layer for compressing the output feature channel. This strategy directly merges different feature maps without considering their depths. However, in convolutional neural networks, segmentation tasks are sensitive to the depth of the network; thus, a reasonable design of its depth will improve the performance (Simonyan and Zisserman, 2014). For this consideration, we modified the decoder path of UNet++ (Zhou et al., 2018) to extract more informative prediction results.

$$Y^{'} = \mathrm{soft\,max}\left(\frac{1}{4}\sum_{j=1}^{4} DN\left(X^{0,j}\right)\right) \tag{5}$$

where DN is a dynamic fusion module consisting of a bilinear upsampling layer used to restore the input spatial resolution and two 1 × 1 convolutional layers followed by a normalization layer and a Relu nonlinear activation layer. Then, the 1 × 1 convolutional layer is applied for channel compression. Finally, we performed pixel-wise averaging on the output of DN, followed by a softmax layer. $Y^{'}$ represents the predicted probability map.

Loss Function

In the task of semantic segmentation of medical images, the pixel-by-pixel cross-entropy loss, $\mathcal{L}_{CE}$, is a commonly used loss function that compares the predicted probability map with the gold standard (GT) in order according to the spatial position.

$$Y^{'} = \mathrm{soft\,max}\left(\frac{1}{4}\sum_{j=1}^{4} DN\left(X^{0,j}\right)\right) \tag{6}$$

where k denotes the number of objects and Y represents the gold standard.

TABLE 1 | Mean segmentation results (in percent) of the contrast experiments and ablation studies (mean ± SD).

Methods	DSC	IoU	Acc	Sen	Pre
UNet	94.01 ± 1.34	88.89 ± 2.27	99.23 ± 0.17	94.10 ± 1.30	94.03 ± 1.32
AttUNet	93.19 ± 0.38	87.48 ± 0.67	99.13 ± 0.07	93.27 ± 0.49	93.25 ± 0.33
CE-Net	94.98 ± 0.32	90.55 ± 0.57	99.36 ± 0.03	95.19 ± 0.17	94.84 ± 0.45
Multi-ResUNet	94.41 ± 0.31	89.57 ± 0.54	99.28 ± 0.04	94.42 ± 0.25	94.49 ± 0.38
R2UNet	88.19 ± 1.10	79.48 ± 1.61	98.49 ± 0.11	88.38 ± 1.29	88.67 ± 0.87
DeepLab v3	95.05 ± 0.10	90.69 ± 0.18	99.38 ± 0.01	95.26 ± 0.19	94.90 ± 0.10
Backbone	93.54 ± 0.39	88.07 ± 0.68	99.17 ± 0.08	93.69 ± 0.32	93.50 ± 0.51
DW-Net	**95.38 ± 0.22**	**91.26 ± 0.40**	**99.41 ± 0.02**	**95.44 ± 0.22**	**95.36 ± 0.23**

Values in bold indicate the best performance. DSC, dice similarity coefficient; IoU, intersection-over-union; Acc, accuracy; Sen, sensitivity; Pre, precision.

TABLE 2 | Choroid neovascularization (CNV) segmentation results (in percent) of the contrast experiments and ablation studies (mean ± SD).

Methods	DSC	IoU	Acc	Sen	Pre
UNet	92.80 ± 2.17	87.15 ± 3.46	99.73 ± 0.08	93.12 ± 2.25	93.10 ± 1.72
AttUNet	91.27 ± 0.86	84.67 ± 1.31	99.68 ± 0.06	91.68 ± 1.73	91.75 ± 1.23
CE-Net	94.53 ± 0.92	90.00 ± 1.63	99.80 ± 0.04	**95.61** ± **0.95**	93.86 ± 2.17
Multi-ResUNet	93.70 ± 0.80	88.66 ± 1.26	99.77 ± 0.03	93.25 ± 0.88	94.72 ± 0.68
R2UNet	85.00 ± 3.48	75.64 ± 4.68	99.39 ± 0.02	89.52 ± 4.71	83.26 ± 3.17
DeepLab v3	93.74 ± 0.73	88.62 ± 1.23	99.77 ± 0.04	95.11 ± 0.76	92.77 ± 1.58
Backbone	92.51 ± 0.54	86.65 ± 0.85	99.72 ± 0.06	92.67 ± 0.94	92.99 ± 0.28
DW-Net	**94.84** ± **0.80**	**90.48** ± **1.38**	**99.81** ± **0.02**	95.13 ± 0.92	**94.81** ± **0.78**

Values in bold indicate the best performance. DSC, dice similarity coefficient; IoU, intersection-over-union; Acc, accuracy; Sen, sensitivity; Pre, precision.

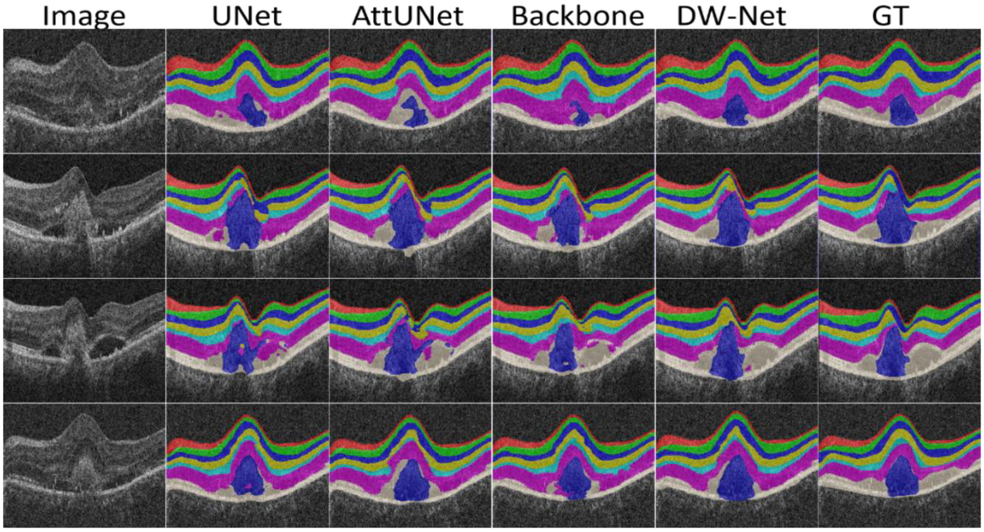

FIGURE 5 | Visualization results of the different methods.

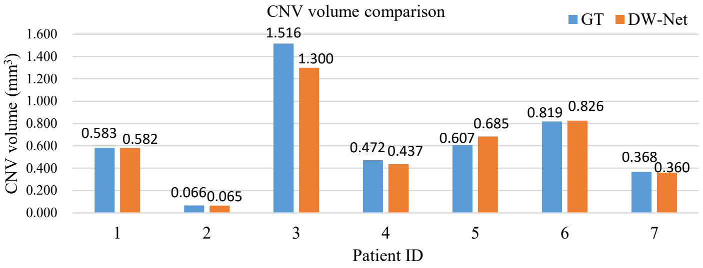

FIGURE 6 | Histogram of choroid neovascularization (CNV) volume comparison.

Dice loss, $\mathcal{L}_{Dice}$, is another widely used loss function (Milletari et al., 2016) that aims to measure the overlap ratio of two samples, and its value ranges from 0 to 1.

$$\mathcal{L}_{Dice} = 1 - \frac{1}{k}\sum_{c=0}^{k-1}\frac{2YY^{'} + \xi}{Y + Y^{'} + \xi} \tag{7}$$

where ξ is set to a very small constant to ensure that the divisor is not equal to 0. The final loss function we used is as follows:

$$\mathcal{L} = \mathcal{L}_{Dice} + \mathcal{L}_{CE} \tag{8}$$

EXPERIMENTS AND RESULTS

Dataset and Implementation

Dataset

To evaluate the effectiveness of the proposed method, we conducted comprehensive experiments. The dataset we used in the experiment was collected by the Joint Shantou International Eye Center of Shantou University and The Chinese University of Hong Kong. The acquisition process lasted 13 months, and 6,016 retinal OCT images from 47 three-dimensional retinal

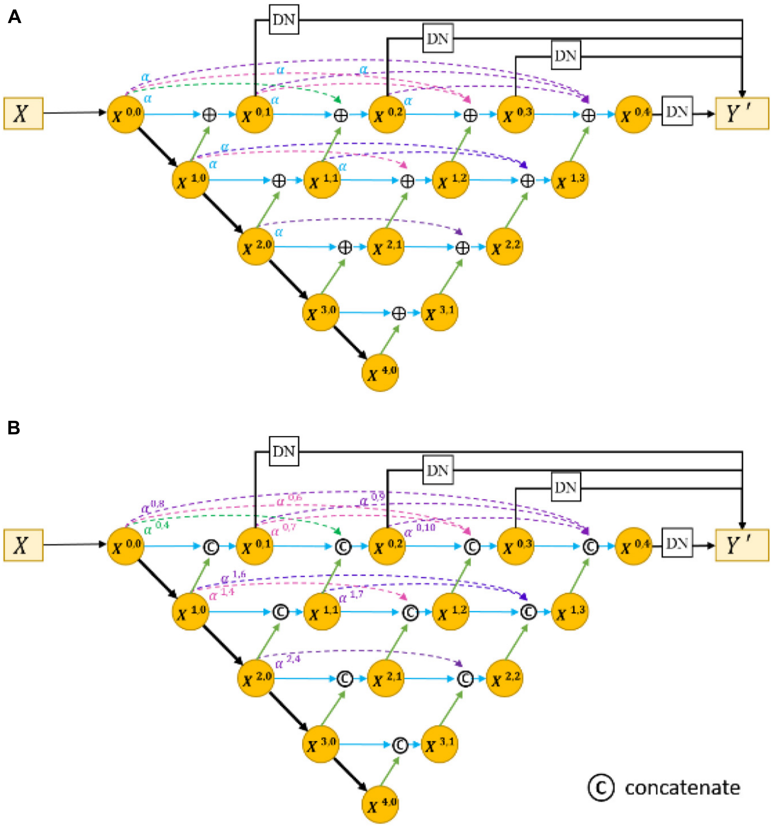

FIGURE 7 | Architecture of Res18UNet++ **(A)** and AdaptiveUNet++ **(B)**.

OCT volumes with CNV were completely acquired through the Zeiss canner. The size of the actual scanning area is 6 mm × 2 mm × 6 mm ($X \times Y \times Z$), and the number of voxels is 512 × 1,024 × 128. Pixel-level annotations of NFL, GCL, IPL, INL, OPL, ONL, OPSL+RPE, and CNV were provided by senior ophthalmologists.

Implementation Details

The implementation of our proposed DW-Net is based on the public platform Pytorch 1.8.0 with CUDA 11.0 parallel computing library and GeForce RTX 3090 GPU with 24-GB memory.

To save computing resources and increase network receptivity, each slice was resized to 512 × 512 by bilinear interpolation. We divided the 6,016 retinal OCT images into four groups, with the slice number as balanced as possible. Fourfold cross-validation was conducted on the divided dataset (1,664, 1,792, 1,280, and 1,280). The Adam optimizer with a learning rate of 1e-4 was adopted as our optimizer. The batch size and epoch were set to 4 and 100, respectively. For fair comparison, we used the same training strategy in all experiments.

Evaluation Metrics

Five metrics including dice similarity coefficients (DSCs), intersection-over-union (IoU), accuracy (Acc), sensitivity (Sen), and precision (Pre) (Garcia-Garcia et al., 2017) were used to fully and fairly evaluate the performance, where TN, TP, FN, and FP represent true negative, true positive, false negative, and false positive, respectively.

$$\mathrm{DSC} = \frac{2\mathrm{TP}}{2\mathrm{TP} + \mathrm{FP} + \mathrm{FN}} \tag{9}$$

$$\mathrm{IoU} = \frac{\mathrm{TP}}{\mathrm{TP} + \mathrm{FP} + \mathrm{FN}} \tag{10}$$

$$\mathrm{Acc} = \frac{\mathrm{TP} + \mathrm{TN}}{\mathrm{TP} + \mathrm{FP} + \mathrm{TN} + \mathrm{FN}} \tag{11}$$

$$\mathrm{Sen} = \frac{\mathrm{TP}}{\mathrm{TP} + \mathrm{FN}} \tag{12}$$

$$\mathrm{Pr\,e} = \frac{\mathrm{TP}}{\mathrm{TP} + \mathrm{FP}} \tag{13}$$

Results

We first compared our proposed DW-Net with other excellent convolutional neural network (CNN)-based methods, including UNet (Ronneberger et al., 2015), AttUNet (Oktay et al., 2018), CE-Net (Gu et al., 2019), Multi-ResUNet

TABLE 3 | Ablation experiments (mean ± SD).

Methods	DSC	IoU	Acc	Sen	Pre
Backbone	92.51 ± 0.54	86.65 ± 0.85	99.72 ± 0.06	92.67 ± 0.94	92.99 ± 0.28
Res18UNet++	94.64 ± 0.60	90.21 ± 0.91	99.80 ± 0.03	94.65 ± 0.83	**95.02 ± 0.23**
AdaptiveUNet++	92.76 ± 0.60	87.06 ± 0.94	99.73 ± 0.05	92.96 ± 1.16	93.15 ± 0.75
DW-Net	**94.84 ± 0.80**	**90.48 ± 1.38**	**99.81 ± 0.02**	**95.13 ± 0.92**	94.81 ± 0.78

Values in bold indicate the best performance. DSC, dice similarity coefficient; IoU, intersection-over-union; Acc, accuracy; Sen, sensitivity; Pre, precision.

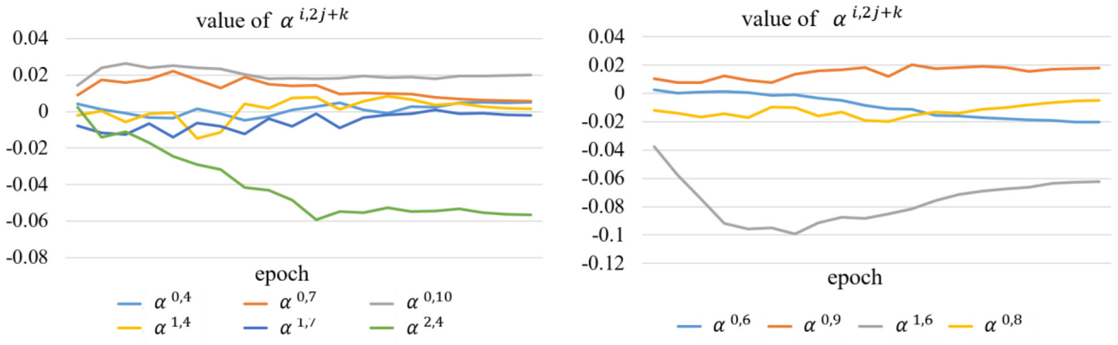

FIGURE 8 | Value of the learnable parameter $\alpha^{i,2j+k}$ during training.

TABLE 4 | Choroid neovascularization (CNV) segmentation experiments without retinal layers (mean ± SD).

Methods	DSC	IoU	Acc	Sen	Pre
DW-Net-2	90.06 ± 0.62	82.98 ± 0.90	99.63 ± 0.07	89.93 ± 0.50	91.52 ± 0.90
DW-Net	**94.84 ± 0.80**	**90.48 ± 1.38**	**99.81 ± 0.02**	**95.13 ± 0.92**	**94.81 ± 0.78**

Values in bold indicate the best performance. DSC, dice similarity coefficient; IoU, intersection-over-union; Acc, accuracy; Sen, sensitivity; Pre, precision.

(Ibtehaz and Rahman, 2020), R2UNet (Alom et al., 2018), and DeepLab v3 (Chen et al., 2017). In addition, UNet++ (Zhou et al., 2018) was applied as our backbone. **Tables 1**, **2** show the mean joint segmentation results of the 7 retinal layers containing CNV and the joint segmentation results of CNV, respectively.

From **Table 1**, it is worth noting that the proposed DW-Net achieves better performance than all of the above methods, with DSC, IoU, Acc, Sen, and Pre of 95.38, 91.26, 99.41, 95.44, and 95.36%, respectively. As for CNV, the performance of our proposed joint segmentation realized 2.52, 4.42, 0.09, 2.65, and 1.96% improvements in terms of DSC, IoU, Acc, Sen, and Pre, respectively, over the backbone, as shown in **Table 2**.

The performance of CE-Net (Gu et al., 2019) was comparable to that of the proposed DW-Net for CNV Sen, while being slightly lower in other metrics. In **Figure 5**, we plotted the visualization results of the different methods, where the red, green, dark blue, yellow, light blue, purple, white, and navy blue areas represent NFL, GCL, IPL, INL, OPL, ONL, OPSL+RPE, and CNV, respectively. It can be seen that our proposed DW-Net can accurately segment each retinal layer and CNV, which is closer to the GT compared with the other methods.

Furthermore, we carried out a quantitative analysis of the experimental results. **Figure 6** shows a histogram of the comparison between the size of the actual CNV and the segmented CNV using DW-Net, which are represented by blue and orange bars, respectively. It can be seen from the qualitative and quantitative results in the figure that the volume difference between the prediction of DW-Net and GT is generally small, which further proves the effectiveness and stability of the joint segmentation network and suggest promising clinical value and application prospects.

DISCUSSION

In this section, we first conduct a series of ablation experiments. Then, we study the contribution of the information on the retinal layers to the CNV segmentation task. Finally, we introduce the limitations of this work and possible future research directions.

Ablation Experiments for Residual Aggregation Encoder Path

To evaluate the effectiveness of the residual aggregation encoder path, we further compared the backbone with its counterparts (called Res18UNet++). Specifically, Res18UNet++ directly applies residual aggregation encoder path based on UNet++ (Zhou et al., 2018) and replaces concatenation by pixel addition, as shown in **Figure 7A**, where α is a constant that is fixed to 1. **Table 3** reports the segmentation results.

It can be seen that our proposed Res18UNet++ achieves better performance over the backbone on all metrics, which suggests that the residual aggregation encoder path can retain more effective features as possible to alleviate the resolution loss caused by network deepening.

Ablation Experiments for Dynamic Multi-Hierarchical Weighting Connection

We also compared the backbone with another counterpart (called AdaptiveUNet++), as shown in **Figure 7B**. Here, $\alpha^{i,2j+k}$ is a learnable parameter that is multiplied with the output feature map of the corresponding encoder. Its value during the training process is shown in **Figure 8**.

We can conclude from **Table 3** and **Figure 8** that our proposed AdaptiveUNet++ enables the encoders to utilize multi-scale context information and filter irrelevant information. In addition, residual aggregation encoder path and dynamic multi-hierarchical weighting connection can influence and promote each other, thereby further improving the overall joint segmentation performance of the network, as shown in the results of DW-Net in **Table 3**.

Ablation Experiments for Retinal Layer Information

All the experiments above were based on the assumption that the introduction of complex retinal layer information is conducive to improving the performance of CNV segmentation. Therefore, we performed joint segmentation of the retinal layers and CNV. In this section, we set out to verify the assumption.

Pre-processing

We considered CNV as the foreground, and the corresponding spatial label was set to 1, then the remaining area including the retinal layers was regarded as background, with the label of 0. Here, the joint segmentation was transformed into a foreground–background segmentation. A variant of DW-Net, named DW-Net-2, was applied for a single CNV segmentation, where the last layer of the network was modified to sigmoid function, and the number of output channels was set to 1. **Table 4** shows the segmentation results of DW-Net-2 and DW-Net.

It can be clearly seen that the performance of DW-Net is superior, which proves that the introduction of retinal layer information is conducive to distinguishing the features of background, retinal layers, and CNV, thereby improving the segmentation performance of CNV.

Limitations and Future Work

The current work still has many limitations. Our proposed DW-Net contains many learnable parameters, which will increase the computational burden; therefore, further compression is needed in practical applications. The dataset used in our experiment needs further expansion, which is also one of our future works. We will conduct experiments on more datasets to verify the effectiveness and generalization of the proposed DW-Net.

CONCLUSION

CNV segmentation is a fundamental task in medical image analysis. In this paper, we proposed a novel end-to-end dynamic multi-hierarchical weighting segmentation network (DW-Net) for the simultaneous segmentation of the retinal layers and CNV. Specifically, the proposed network is composed of a residual aggregation encoder path for the selection of informative feature, a multi-hierarchical weighting connection for the fusion of detailed information and abstract information, and a dynamic decoder path. Comprehensive experimental results show the effectiveness and stability of our proposed DW-Net and suggest promising clinical value and application prospects.

DATA AVAILABILITY STATEMENT

The datasets presented in this article are not readily available because constrained by ethics and patient privacy. Requests to access the datasets should be directed to corresponding author and LW, lywang12@126.com.

ETHICS STATEMENT

The studies involving human participants were reviewed and approved by the Soochow University. Written informed consent for participation was not required for this study in accordance with the national legislation and the institutional requirements.

AUTHOR CONTRIBUTIONS

LW conceptualized and designed the study, wrote the first draft of the manuscript, and performed data analysis. MW, TW, QM, YZ, YP, ZC, and XC performed the experiments, collected and analyzed the data, and revised the manuscript. All authors contributed to the article and approved the submitted version.

FUNDING

This study was supported by the National Key R&D Program of China (2018YFA0701700).

REFERENCES

Alom, M. Z., Hasan, M., Yakopcic, C., Taha, T. M., and Asari, V. K. (2018). Recurrent residual convolutional neural network based on U-Net (R2U-Net) for medical image segmentation. *arXiv* [Preprint]. arXiv:1802.06955.

Bressler, N. M. (2002). Verteporfin therapy of subfoveal choroidal neovascularization in age-related macular degeneration-Reply. *Am. J. Ophthalmol.* 133, 857–859. doi: 10.1016/s0002-9394(02)01423-x

Chen, H., Xia, H., Qiu, Z., Chen, W., and Chen, X. (2016). Correlation of optical intensity on optical coherence tomography and visual outcome in central retinal artery occlusion. *Retina* 36, 1964–1970. doi: 10.1097/IAE.0000000000001017

Chen, L.-C., Papandreou, G., Schroff, F., and Adam, H. (2017). Rethinking atrous convolution for semantic image segmentation. *arXiv* [Preprint]. arXiv:1706.05587.

Chen, X., Zhang, L., Sohn, E. H., Lee, K., Niemeijer, M., Chen, J., et al. (2012). Quantification of external limiting membrane disruption caused by diabetic macular edema from SD-OCT. *Invest. Ophthalmol. Vis. Sci.* 53, 8042–8048. doi: 10.1167/iovs.12-10083

Dufour, P. A., Ceklic, L., Abdillahi, H., Schröder, S., De Dzanet, S., Wolf-Schnurrbusch, U., et al. (2013). Graph-based multi-surface segmentation of OCT data using trained hard and soft constraints". *IEEE Trans. Med. Imag.* 32, 531–543. doi: 10.1109/TMI.2012.2225152

Feng, S., Zhao, H., Shi, F., Cheng, X., Wang, M., Ma, Y., et al. (2020). CPFNet: context pyramid fusion network for medical image segmentation. *IEEE Trans. Med. Imaging* 39, 3008–3018. doi: 10.1109/TMI.2020.2983721

Fercher, A. F., Hitzenberger, C. K., Drexler, W., Kamp, G., and Sattmann, H. (1993). In vivo optical coherence tomography in ophthalmology. *Am. J. Ophthalmol.* 116, 113–115.

Gao, E., Chen, B., Yang, J., Shi, F., Zhu, W., Xiang, D., et al. (2015). Comparison of retinal thickness measurements between the topcon algorithm and a graph-based algorithm in normal and glaucoma eyes. *PLoS One* 10:e0128925. doi: 10.1371/journal.pone.0128925

Garcia-Garcia, A., Orts-Escolano, S., Oprea, S., Villena-Martinez, V., and Garcia-Rodriguez, J. (2017). A review on deep learning techniques applied to semantic segmentation. *arXiv* [Preprint]. arXiv:1704.06857.

Garvin, M. K., Abramoff, M. D., Wu, X., Russell, S. R., Burns, T. L., and Sonka, M. (2009). Automated 3-D intraretinal layer segmentation of macular spectral-domain optical coherence tomography images. *IEEE Trans. Med. Imag.* 28, 1436–1447. doi: 10.1109/TMI.2009.2016958

Grossniklaus, H. E., and Green, W. R. (2004). Choroidal neovascularization. *Am. J. Ophthalmol.* 137, 0–503.

Gu, Z., Cheng, J., Fu, H., Zhou, K., Hao, H., Zhao, Y., et al. (2019). CE-Net: context encoder network for 2D medical image segmentation. *IEEE Trans. Med. Imaging* 38, 2281–2292. doi: 10.1109/TMI.2019.2903562

Hageman, G. S., Gehrs, K., Johnson, L. V., and Anderson, D. (1995). "Age-related macular degeneration (AMD)," in *The Orianization of the Retina and Visual System* (Salt Lake City, UT: University of Utah Health Sciences Center).

He, K., Zhang, X., Ren, S., and Sun, J. (2016). "Deep residual learning for image recognition," in *Proceedings of the IEEE Conference on Computer Vision and Pattern Recognition* (Las Vegas, NV), 770–778.

Huang, D., Swanson, E. A., Lin, C. P., Schuman, J. S., Stinson, W. G., Chang, W., et al. (1991). Optical coherence tomography. *Science* 254, 1178–1181.

Ibtehaz, N., and Rahman, M. S. (2020). MultiResUNet: rethinking the U-Net architecture for multimodal biomedical image segmentation. *Neural Netw.* 121, 74–87. doi: 10.1016/j.neunet.2019.08.025

Laud, K., Spaide, P. F., and Freund, K. B. (2006). Treatment of choroidal neovascularization in pathologic myopia with intravitreal bevacizumab. *Ratina* 26, 960. doi: 10.1097/01.iae.0000240121.28034.c3

Lopez, P. F., Grossniklaus, H. E., Lambert, H. M., Aaberg, T. M., Capone, A., Sternberg, P., et al. (1991). Pathologic features of surgically-excised subretinal neovascular membranes in age-related macular degeneration. *Am. J. Ophthalmol.* 112, 647–656. doi: 10.1016/s0002-9394(14)77270-8

Lu, S., Cheung, C. Y.-L., Liu, J., Lim, J. H., Leung, C. K.-S., and Wong, T. Y. (2010). Automated layer segmentation of optical coherence tomography images. *IEEE Trans. Biomed. Eng.* 57, 2605–2608.

Milletari, F., Navab, N., and Ahmadi, S. (2016). "V-net: fully convolutional neural networks for volumetric medical image segmentation," in *Proceedings of the 2016 Fourth International Conference on 3D Vision (3DV)*, Stanford, CA.

Oktay, O., Schlemper, J., Le Folgoc, L., Lee, M., Heinrich, M., Misawa, K., et al. (2018). Attention U-Net: learning where to look for the pancreas. *arXiv* [Preprint]. arXiv:1804.03999.

Ronneberger, O., Fischer, P., and Brox, T. (2015). "U-net: convolutional networks for biomedical image segmentation," in *International Conference on Medical Image Computing and Computer-Assisted Intervention*, eds N. Navab, J. Hornegger, W. Wells, and A. Frangi (Cham: Springer), 234–241.

Roy, A. G., Conjeti, S., Karri, S. P. K., Sheet, D., Katouzian, A., Wachinger, C., et al. (2017). ReLayNet: retinal layer and fluid segmentation of macular optical coherence tomography using fully convolutional networks. *Biomed. Optics Exp.* 8, 3627–3642. doi: 10.1364/BOE.8.003627

Saxe, S. J., Grossniklaus, H. E., Lopez, P. F., Sternberg, P., and L'Hernault, N. (1993). Ultrastructural features of surgically-excised subretinal neovascular membranes in the ocular histoplasmosis syndrome. *Arch. Ophthalmol.* 111, 88–95. doi: 10.1001/archopht.1993.01090010092033

Shi, F., Chen, X., Zhao, H., Zhu, W., Xiang, D., Gao, E., et al. (2015). Automated 3-D retinal layer segmentation of macular optical coherence tomography images with serous pigment epithelial detachments. *IEEE Trans. Med. Imag.* 34, 441–452. doi: 10.1109/TMI.2014.2359980

Simonyan, K., and Zisserman, A. (2014). Very deep convolutional networks for large-scale image recognition. *arXiv* [Preprint]. arXiv: 1409.1556.

Song, Q., Bai, J., Garvin, M. K., Sonka, M., Buatti, J. M., and Wu, X. (2013). Optimal multiple surface segmentation with shape and context priors. *IEEE Trans. Med. Imag.* 32, 376–386. doi: 10.1109/TMI.2012.2227120

Srinivasan, P. P., Heflin, S. J., Izatt, J. A., Arshavsky, V. Y., and Farsiu, S. (2014). Automatic segmentation of up to ten layer boundaries in SD-OCT images of the mouse retina with and without missing layers due to pathology. *Biomed. Optics Exp.* 5, 348–365. doi: 10.1364/BOE.5.000348

Su, J., Chen, X., Ma, Y., Zhu, W., and Shi, F. (2020). Segmentation of choroid neovascularization in OCT images based on convolutional neural network with differential amplification blocks. *SPIE Med. Imaging 2020 Image Process.*

Wang, J., Hormel, T. T., Gao, L., Zang, P., Guo, Y., Wang, X., et al. (2020). Automated diagnosis and segmentation of choroidal neovascularization in OCT angiography using deep learning. *Biomed. Optics Exp.* 11, 927–944. doi: 10.1364/BOE.379977

Xi, X., Meng, X., Yang, L., Nie, X., Yin, Y., and Chen, X. (2017). Learned local similarity prior embedded active contour model for choroidal neovascularization segmentation in optical coherence tomography images. *Sci. China Inform. Sci.*

Xi, X., Meng, X., YangX, L., Nie, X., Yin, Y., and Chen, X. (2018). Automated segmentation of choroidal neovascularization in optical coherence tomography images using multi-scale convolutional neural networks with structure prior. *Multimedia Syst.* 25, 1–8. doi: 10.1117/1.jmi.6.2.024009

Xiang, D., Tian, H., Yang, X., Shi, F., Zhu, W., Chen, H., et al. (2018). Automatic segmentation of retinal layer in OCT images with choroidal neovascularization. *IEEE Trans. Image Process.* 25, 5880–5891. doi: 10.1109/TIP.2018.2860255

Xu, X., Zhang, L., Lee, K., Wahle, A., Chen, X., Wu, X., et al. (2013). Automated choroidal neovascularization associated abnormality detection and quantitative analysis from clinical SD-OCT. *Invest. Ophthalmol. Visual Sci.* 54:5510.

Xue, J., Camino, A., Bailey, S. T., Liu, X., Li, D., and Jia, Y. (2018). Automatic quantification of choroidal neovascularization lesion area on OCT angiography based on density cell-like P systems with active membranes. *Biomed. Opt. Exp.* 9, 3208–3219. doi: 10.1364/BOE.9.003208

Zanet, S. D., Ciller, C., Apostolopoulos, S., Wolf, S., and Sznitman, R. (2019). "Pathological OCT retinal layer segmentation using branch residual u-shape networks," in *Proceedings of the International Conference on Medical Image Computing and Computer-Assisted Intervention* (Cham: Springer) 2017: 294–301.

Zhang, Q., Chen, C. L., Chu, Z., Zheng, F., Miller, A., Roisman, L., et al. (2017). Automated quantitation of choroidal neovascularization: a comparison study between spectral-domain and sweptsource OCT angiograms. *Invest. Ophthalmol. Vis. Sci.* 58, 1506–1513. doi: 10.1167/iovs.16-20977

Zhao, H., Shi, J., Qi, X., Wang, X., and Jia, J. (2017). "Pyramid scene parsing network," in *Proceedings of the IEEE Conference on Computer Vision and Pattern Recognition* (Piscataway, NJ: IEEE), 2881–2890.

Zhou, Z., Siddiquee, M. M. R., Tajbakhsh, N., and Liang, J. (2018). "UNet++: a nested U-Net architecture for medical image segmentation," in *Deep Learningin Medical Image Analysis and Multimodal Learning for Clinical DecisionSupport*, ed. D. Stoyanov (Cham: Springer), 3–11. doi: 10.1007/978-3-030-00889-5

Conflict of Interest: The authors declare that the research was conducted in the absence of any commercial or financial relationships that could be construed as a potential conflict of interest.

frontiers in Neuroscience

METHODS
published: 04 January 2022
doi: 10.3389/fnins.2021.793377

Semi-MsST-GAN: A Semi-Supervised Segmentation Method for Corneal Ulcer Segmentation in Slit-Lamp Images

Tingting Wang[1], Meng Wang[1], Weifang Zhu[1], Lianyu Wang[1], Zhongyue Chen[1], Yuanyuan Peng[1], Fei Shi[1], Yi Zhou[1], Chenpu Yao[1] and Xinjian Chen[1,2]*

[1] Medical Image Processing, Analysis and Visualization (MIPAV) Laboratory, The School of Electronics and Information Engineering, Soochow University, Suzhou, China, [2] The State Key Laboratory of Radiation Medicine and Protection, Soochow University, Suzhou, China

Edited by:
Jian Zheng,
Suzhou Institute of Biomedical Engineering and Technology, Chinese Academy of Sciences (CAS), China

Reviewed by:
Huiguang He,
Institute of Automation, Chinese Academy of Sciences (CAS), China
Bin Lv,
Ping An Technology Co., Ltd., China

***Correspondence:**
Xinjian Chen
xjchen@suda.edu.cn

Specialty section:
This article was submitted to Perception Science, a section of the journal Frontiers in Neuroscience

Received: 12 October 2021
Accepted: 22 November 2021
Published: 04 January 2022

Citation:
Wang T, Wang M, Zhu W, Wang L, Chen Z, Peng Y, Shi F, Zhou Y, Yao C and Chen X (2022) Semi-MsST-GAN: A Semi-Supervised Segmentation Method for Corneal Ulcer Segmentation in Slit-Lamp Images. Front. Neurosci. 15:793377. doi: 10.3389/fnins.2021.793377

Corneal ulcer is a common leading cause of corneal blindness. It is difficult to accurately segment corneal ulcers due to the following problems: large differences in the pathological shapes between point-flaky and flaky corneal ulcers, blurred boundary, noise interference, and the lack of sufficient slit-lamp images with ground truth. To address these problems, in this paper, we proposed a novel semi-supervised multi-scale self-transformer generative adversarial network (Semi-MsST-GAN) that can leverage unlabeled images to improve the performance of corneal ulcer segmentation in fluorescein staining of slit-lamp images. Firstly, to improve the performance of segmenting the corneal ulcer regions with complex pathological features, we proposed a novel multi-scale self-transformer network (MsSTNet) as the MsST-GAN generator, which can guide the model to aggregate the low-level weak semantic features with the high-level strong semantic information and adaptively learn the spatial correlation in feature maps. Then, to further improve the segmentation performance by leveraging unlabeled data, the semi-supervised approach based on the proposed MsST-GAN was explored to solve the problem of the lack of slit-lamp images with corresponding ground truth. The proposed Semi-MsST-GAN was comprehensively evaluated on the public SUSTech-SYSU dataset, which contains 354 labeled and 358 unlabeled fluorescein staining slit-lamp images. The results showed that, compared with other state-of-the-art methods, our proposed method achieves better performance with comparable efficiency.

Keywords: corneal ulcer, GAN, slit-lamp image, semi-supervision, deep learning

INTRODUCTION

The cornea is a transparent membrane located at the front of the eyeball and is directly exposed to the air. Therefore, it is more likely to be infected with bacteria, resulting in several frequently occurring ophthalmic symptoms such as corneal ulcer. Corneal ulcer is an inflammatory or, more seriously, infective condition of the cornea involving disruption of its stromal–epithelial layers

(Bron et al., 2007; Chen and Yuan, 2010). Late or inappropriate treatment may induce irreversible damages to vision acuity (Cohen et al., 1987; Diamond et al., 1999).

Fluorescein staining is the most widely used diagnostic technology in optometry and ophthalmology to assess the integrity of the ocular surface, particularly the integrity of the cornea (Morgan and Carole, 2009; Zhang et al., 2018). With the development of staining techniques, doctors can quantitatively evaluate the size and severity of corneal ulcers by fluorescein staining of slit-lamp images.

Accurate segmentation of the ulcer region is essential for assessing the severity of corneal ulcer and formulating a treatment plan. As shown in **Figure 1**, corneal ulcer can be classified into point-like corneal ulcer, point-flaky mixed corneal ulcer, and flaky corneal ulcer according to the pathological characteristics and distribution. Although the ulcer region can be marked manually by experienced ophthalmologists *via* some professional software, this task is time-consuming and subjective. Therefore, it is significant to explore a method that can automatically and accurately segment the corneal ulcer area.

There are some segmentation methods (Pritchard et al., 2003; Wolffsohn and Purslow, 2003; Peterson and Wolffsohn, 2009) designed for separate point-like corneal ulcers rather than for the point-flaky or flaky types. Later, methods for the segmentation of corneal ulcers with more complex shapes were proposed and achieved good results (Chun et al., 2014; Sun et al., 2017; Deng et al., 2018a,b; Liu et al., 2019). Chun et al. (2014) proposed an objective digital image analysis system to evaluate the corneal staining using RGB (red–green–blue) and the hue–saturation–value (HSV) technique with 100 images. Deng et al. (2018a) presented an automatic ulcer segmentation method by utilizing *k*-means clustering followed by morphological operations and region growing. Then, in Deng et al. (2018b), a simple linear iterative clustering (SLIC) super-pixel-based pipeline was proposed for automatic flaky corneal ulcer area extraction with 150 images. Liu et al. (2019) segmented the ulcer area by employing a joint method of Otsu and Gaussian mixture model (GMM) with 150 images. Sun et al. (2017) proposed a patch-based deep convolutional neural network (CNN) for corneal ulcer segmentation with 48 images. The methods mentioned above are traditional algorithms mostly based on around 100 images and are only designed for certain types of corneal ulcer, therefore not suitable for all types of segmentation.

Recently, several CNNs have been proposed for medical image segmentation, such as UNet (Ronneberger et al., 2015), CE-Net (Gu et al., 2019), Att-UNet (Oktay et al., 2018), and CPFNet (Feng et al., 2020). Most of them are based on the encoder–decoder architecture (Ronneberger et al., 2015) due to its good performance. The encoder can extract the context information and reduce the spatial dimension of feature maps. The decoder can recover the spatial dimension and details of the targets. The skip connections help to recover the full spatial resolution at the network output, making the network suitable for semantic segmentation (Zhou et al., 2018). However, the original skip connections in the U-shaped network will introduce irrelevant clutters and have semantic gaps due to the mismatch of the receptive fields (Feng et al., 2020). To improve the performance of the original U-Net, methods such as attention U-Net (Att-UNet) (Oktay et al., 2018) and CPFNet (Feng et al., 2020) have introduced an attention mechanism, whose core idea is to change the global focus to key and local region focus. The attention mechanism tries to focus the attention of the network on the relationship of the channels, gather spatial information to focus on the correlated features, and suppress the irrelevant regions in the feature map. It is beneficial to utilize attention mechanism to capture more rich details of objects instead of the direct concatenation of feature maps from the encoder and decoder. Although these CNN-based methods have achieved good performance (Ronneberger et al., 2015; Oktay et al., 2018; Gu et al., 2019; Feng et al., 2020), a few CNN-based methods have been proposed for corneal ulcer segmentation in slit-lamp images. There are still two problems that need to be solved in order to improve the accuracy of corneal ulcer segmentation in slit-lamp images: (1) the interferences caused by complicated pathological features of corneal ulcers in slit-lamp images, such as the large differences in the pathological shapes between point-like, point-flaky, and flaky corneal ulcers, blurred boundary, and noise interference, and (2) how to leverage the large amount of unlabeled data to further improve the segmentation accuracy. In this paper, we propose a novel semi-supervised algorithm based on adversarial learning to solve the current dilemma. Our main contributions are summarized as follows:

(1) To improve the segmentation performance of the corneal ulcer regions with complex pathological features, a novel multi-scale self-transformer network (MsSTNet) is proposed for corneal ulcer segmentation, which can improve the ability of the model to capture the global long-range dependencies of multi-scale features from different layers.
(2) To leverage unlabeled samples for the further performance improvement, a novel semi-supervised multi-scale self-transformer generative adversarial network (Semi-MsST-GAN) is explored.
(3) Comprehensive experiments based on the SUSTech-SYSU dataset have been conducted to demonstrate the effectiveness of our proposed methods. The results show that, compared with other state-of-the-art algorithms, our proposed method not only achieves higher segmentation accuracy but also can leverage unlabeled data to further improve segmentation performance.

METHODS

We adopted the adversarial framework as the architecture of our proposed method, which contains a generator network and a discriminator referred to Mirza and Osindero (2014) and Isola et al. (2017). The following provides a detailed description and functional interpretation of the proposed method.

Semi-MsST-GAN

In recent years, generative adversarial networks (GANs) (Goodfellow et al., 2014) and their variations (Chen et al., 2016;

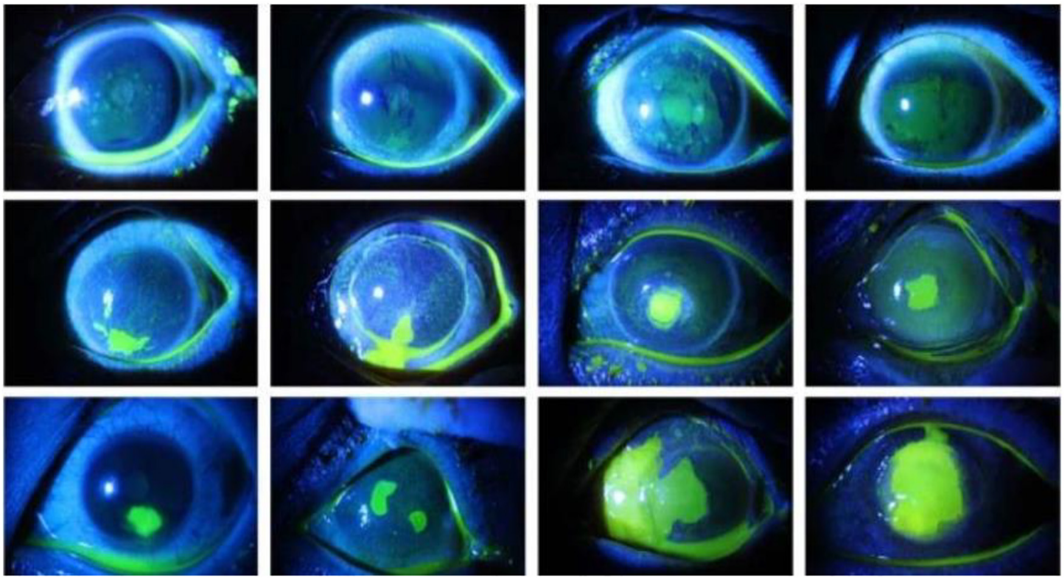

FIGURE 1 | Comparison of the three types of corneal ulcers, with the *top row* representing point-like corneal ulcers, the *middle row* representing point-flaky mixed corneal ulcers, and the *bottom row* representing flaky corneal ulcers.

Ma et al., 2018; Wang T.-C. et al., 2018; Jiang et al., 2019) have been widely used in several domains (Li and Wand, 2016; Pathak et al., 2016; Salimans et al., 2016; Vondrick et al., 2016; Wu et al., 2016; Zhu et al., 2016, 2017; Zha et al., 2019), especially in image processing applications, such as image generation (Zha et al., 2019), image editing (Zhu et al., 2016), representation learning (Salimans et al., 2016), image inpainting (Pathak et al., 2016), style transfer (Li and Wand, 2016), and image-to-image translation (Zhu et al., 2017), with significant performances. Different from the original GAN that generates images based on random noise, conditional GAN (cGAN) generates images based on specified conditional inputs (Mirza and Osindero, 2014). Moreover, the GAN architecture is also widely used in semi-supervision-based methods (Sricharan et al., 2017; Hung et al., 2018; Wang et al., 2021). Therefore, to improve the ability of the model to learn the complex pathological features and leverage unlabeled data in order to further improve the segmentation performance, we proposed a novel semi-supervised MsST-GAN based on cGAN architecture for corneal ulcer segmentation.

As shown in **Figure 2**, similar to general GAN methods (Mirza and Osindero, 2014; Isola et al., 2017), our proposed Semi-MsST-GAN mainly consists of two networks of generator and discriminator. The generator network aims to accurately segment the region of the lesion to confuse the discriminator, while the discriminator aims to discriminate whether its input paired is real or fake. It can be seen from **Figure 2** that MsSTNet is employed as the generator of MsST-GAN. The Semi-MsST-GAN is trained based on the data composed of labeled images and unlabeled images:

(1) For the data with ground truth: MsSTNet is trained to segment the corneal ulcer region as close to the corresponding ground truth as possible based on the guidance of objective function of L_{joint}. Then, the segmentation result of MsSTNet is concatenated with the original data (fake pair) and fed into the discriminator. At the same time, the ground truth is concatenated with the original data (real pair). They are all fed into the discriminator to discriminate whether the input pair is real or fake based on the objective function of L_{D}.

(2) For the data without ground truth: MsSTNet is trained to segment the corneal ulcer region to confuse the discriminator to predict fake results based on the objective function of L_{adv}. Then, the segmentation result of MsSTNet is concatenated with the original data and fed into the discriminator. The discriminator is trained to discriminate whether the input pair is real or fake based on the objective function of L_{D}.

It should be noted that the optimization of Semi-MsST-GAN is an end-to-end training process based on mixed data composed of labeled data and unlabeled data.

Multi-Scale Self-Transformer Network

Recently, researchers have proposed several variant networks based on the encoder–decoder architecture for semantic segmentation tasks, such as SE-Net (Hu et al., 2018), CE-Net (Gu et al., 2019), Attention U-Net (Oktay et al., 2018), U-Net++ (Zhou et al., 2018), and CPFNet (Feng et al., 2020). Most of them introduced an attention mechanism to capture more rich details of objects instead of the direct concatenation of feature maps from the encoder and decoder. However, such attention-based feature extraction method still learns feature relationships in limited receptive fields, which cannot capture the long-range feature dependencies in the entire feature map.

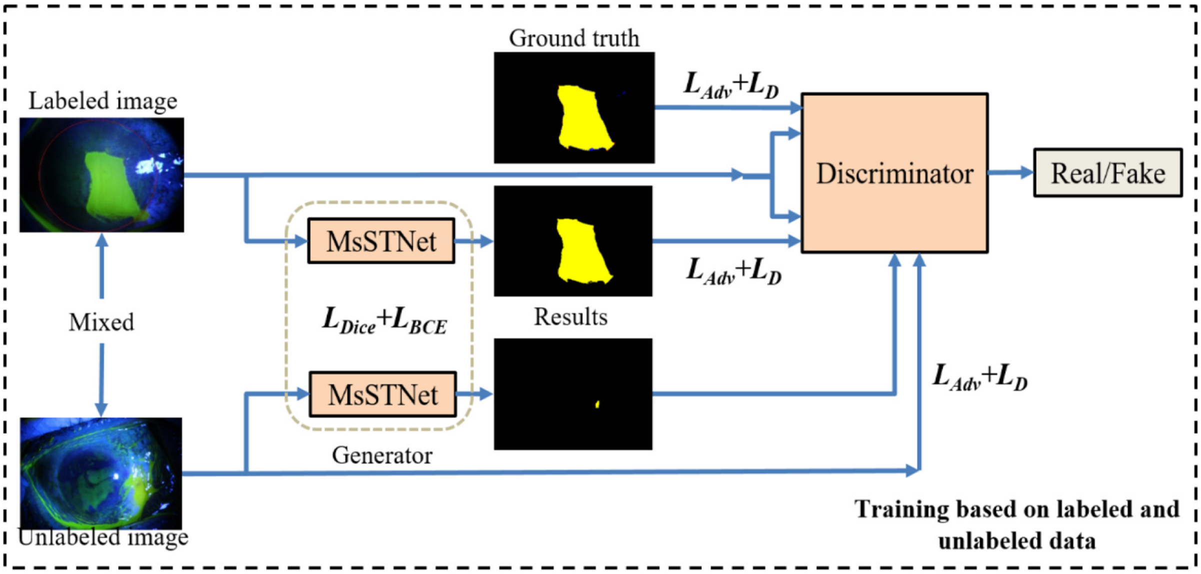

FIGURE 2 | Framework of the proposed semi-supervised multi-scale self-transformer generative adversarial network (Semi-MsST-GAN). In the semi-supervised training process based on labeled and unlabeled images, for the data with ground truth, the multi-scale self-transformer network (MsSTNet) is trained to segment the corneal ulcer region as close to the corresponding ground truth as possible based on the guidance of the objective function of L_{joint}. Then, the segmentation result of MsSTNet is concatenated with the original data and fed into the discriminator. At the same time, the ground truth is concatenated with the original data. They are all fed into the discriminator to discriminate whether the input pair is real or fake based on the objective function of L_{D}. For the data without ground truth, MsSTNet is trained to segment the corneal ulcer region to confuse the discriminator to predict fake results based on the objective function of L_{adv}. Then, the segmentation result of MsSTNet is concatenated with the original data and fed into the discriminator. The discriminator is trained to discriminate whether the input pair is real or fake based on the objective function of L_{D}.

In Lazebnik et al. (2006), Springenberg et al. (2014), He et al. (2015), and Long et al. (2015), contexts were encoded in the gradually larger receptive fields, which can model long-range dependencies. Long-range dependencies play a vital role in image analysis tasks based on deep neural networks (Fukushima and Miyake, 1982; LeCun et al., 1989; Yu and Koltun, 2015). Fukushima and Miyake (1982) and Yu and Koltun (2015) captured the long-range dependency features contained in the feature map by constructing a larger receptive field. LeCun et al. (1989) proposed a novel non-local neural network based on a self-attention mechanism to capture long-range dependencies. However, there is still the problem of non-local spatial interactions that are not cross scales (LeCun et al., 1989; Wang X. et al., 2018). Thus, these methods cannot capture the non-local context of objects with different scales (Zhang et al., 2020), especially for medical image segmentation tasks with complex pathological features (Chen et al., 2017; Zhao et al., 2017). Considering the loss of point-flaky mixed corneal ulcer in high-level feature maps resulting from the continuous downsampling operation, the feature maps from different levels were adopted to supplement long-range dependencies. Therefore, to fully utilize the feature interaction between the local context and the global context, which contains long-range dependencies and spatial correlations from different levels, we developed a novel MsSTNet as the segmentor of MsST-GAN. As shown in **Figure 3**, it adopts a pyramid architecture and self-attention layers to fuse feature maps cross spatial and scales. **Figure 3** also shows that, in MsSTNet, the encoder–decoder architecture was also employed as our framework, in which the pre-trained ResNet-18 was adopted as the encoder path and simple upsampling and deconvolution constituted the decoder path. Especially, to reduce the semantic gap and avoid irrelevant clutters, a novel multi-scale self-transformer (MsST) module was proposed and embedded into the MsSTNet to enhance the ability of the model to extract multi-scale and multi-semantic features, which can improve the segmentation performance.

Figure 3 shows that the proposed novel MsST module was embedded into the top of the encoder path. Firstly, feature maps from stage 2 (F_1), stage 3 (F_2), and stage 4 (F_3) were fed into a downsampling normalized module, which consists of a bilinear downsampling operation, followed by a 3 × 3 convolution layer to match the features of stage 5 in the channels and size. Then, the feature maps with different scales and semantic information were fused by the addition of elements. Finally, the fused feature maps with rich multi-scale and multi-semantic information and the feature maps of the top layer with global feature information were fed into self-attention (often called scaled-dot attention in natural language processing, NLP), which has three branches: query, key, and value (Shaw et al., 2018). As shown in **Figure 3**, to further extract rich features with complex pathological characteristics and suppress the interference from irrelevant features, we employed the fused feature maps with rich multi-scale and multi-semantic features as the input of branch query. The feature maps with rich global features, which are from the encoder's top layer, were adopted as the input of branch key and value. In this way, it guides the model to learn salient global

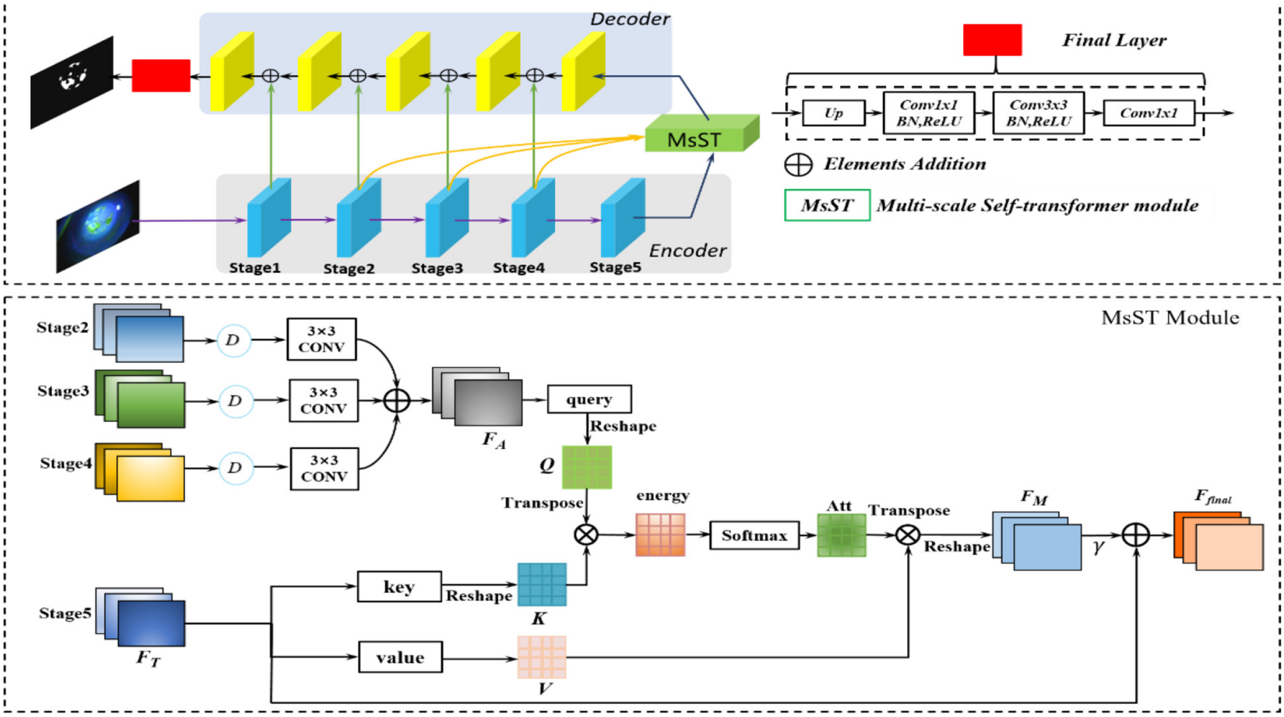

FIGURE 3 | Overview of the proposed multi-scale self-transformer network (MsSTNet). The original image is fed into the encoder path composed of a pre-trained ResNet-18 to obtain the high-level features. Then, the feature maps from stages 2, 3, 4, 5 are fed into the MsST module to fuse multi-scale and multi-semantic information. Subsequently, the features are recovered by the decoder path. Finally, the predicted images are obtained.

features and suppress the interference of unrelated local features. As can be seen from **Figure 3**, our proposed MsST module mainly consists of four steps:

(1) We adopted 1 × 1 convolution to encode the feature map F_A to query (Q) and encode F_T to key (K) and value (V), respectively.

$$Q = \text{Conv}\,1 \times 1\,(F_A) \in R^{B,C/8,W,H} \tag{1}$$

$$K = \text{Conv}\,1 \times 1\,(F_T) \in R^{B,C/8,W,H} \tag{2}$$

$$V = \text{Conv}\,1 \times 1\,(F_T) \in R^{B,C,W,H} \tag{3}$$

(2) Calculate the similarity between query and key to obtain the non-local spatial feature correlation weight guided by global information. ° represents the pixel-wise multiple, as follows:

$$Q = \text{Reshape}\,(Q) \in R^{B,C/8,W\times H} \tag{4}$$

$$K = \text{Reshape}\,(K) \in R^{B,C/8,W\times H} \tag{5}$$

$$\text{energy} = Q^{T\circ}K \in R^{B,W\times H,W\times H} \tag{6}$$

$$Att = \text{Softmax}\,(\text{energy}) \in R^{B,W\times H,W\times H} \tag{7}$$

3) The attention map Att and the corresponding V were weighted and summed to obtain the final spatial response F_{M} with a multi-scale and multi-semantic feature.

$$F_{\text{M}} = \text{Reshape}\left(V^{\circ}\text{Att}^{T}\right) \in R^{B,C,W,H} \tag{8}$$

4) Finally, we multiplied F_{M} by a scale parameter, γ, and performed an element-wise summation operation with the feature map F_{T} to obtain the final output.

$$F_{\text{final}} = F_T + \gamma \times F_M \in R^{B,C,W,H} \tag{9}$$

where γ is initialized as 0 and gradually learns to assign more weight. It can also be seen from Eq. 9 that the final feature map, F_{final}, is the weighted sum of the multi-scale, multi-semantic, and strong semantic global features. Therefore, it not only has a global contextual view but can also selectively aggregate contextual information with multi-scale and multi-semantic features.

Discriminator

The ordinary GAN discriminator maps the input into a real number between 0 and 1, which represents the probability that the input sample is true or fake. It is not suitable for medical image segmentation, which requires high-resolution and high-definition details. Therefore, in this paper, the discriminator of patchGAN (Isola et al., 2017) was employed as the discriminator of MsST-GAN to solve these problems. It could classify whether each $N \times N$ patch from the input image is real or fake. This operation encourages the model to pay more attention to the structure in local patches, which is in favor of modeling high frequencies. The discriminator performs convolution operations on the input images, followed by averaging all responses to provide the ultimate discrimination of the output image. In this paper, N was set as 70.

Loss Function

Given an input image $\boldsymbol{X}$, the segmentor and discriminator were denoted as MsSTNet and D, respectively. The segmentation results from MsSTNet were represented as MsSTNet ($\boldsymbol{X}$). The input of D was defined as X_{D}, which contains two forms: the original image combined with the ground truth (X_{DT}) and the original image combined with the segmentation result (X_{DF}), representing the pairs as True or Fake.

Loss for Discriminator

The spatial binary cross entropy loss L_{D}, as follows, was adopted to optimize the discriminator:

$$L_{\mathrm{D}} = \sum\nolimits_{h,w} (1-y) \log \left(1 - D\left(\mathrm{MsSTNET}\left(X\right)\right)^{h,w}\right) + y \log \left(D\left(y\right)^{h,w}\right) \tag{10}$$

where $y = 0$ if the patch was from MsSTNet prediction and $y = 1$ if the patch was from the ground truth. $D(\mathrm{MsSTNet}(\boldsymbol{X}))^{h,w}$ denotes the probability map of MsSTNet($\boldsymbol{X}$) at location (h,w), and $D(y)^{h,w}$ is the probability map of y at location (h,w).

Loss for MsSTNet

To improve the segmentation accuracy of MsSTNet, we proposed a novel joint loss function to optimize the model, as follows:

$$L_{\mathrm{joint}} = L_{\mathrm{BCE}} + L_{\mathrm{Dice}} + L_{\mathrm{Adv}} \tag{11}$$

It can be seen from Eq. 11 that the joint loss function mainly contains three components: adversarial loss function, L_{Adv}, which helps the segmentor generate prediction as close to the ground truth as possible; spatial cross entropy loss function, L_{BCE}, which was mainly adopted to evaluate the gap between the segmentation result and the ground truth pixel-wise; and the dice loss, L_{Dice}, which was employed to evaluate the segmentation performance in images.

$$L_{\mathrm{Adv}} = -\sum\nolimits_{h,w} \log \left(D\left(\mathrm{MsSTNet}\left(X\right)\right)^{h,w}\right) \tag{12}$$

$$L_{\mathrm{BCE}} = -\sum\nolimits_{h,w} (1-y) \log \left(1-\hat{y}\right)^{h,w} + y \log \left(\hat{y}\right) \tag{13}$$

$$L_{\mathrm{Dice}} = 1 - \frac{2\left(y \cap \hat{y}\right)}{y \cup \hat{y}} \tag{14}$$

where $\hat{y}$ denotes the segmentation result of MsSTNet.

Objective Function for Semi-Supervised Learning

In semi-supervised learning, the loss function often contains two components: supervised loss and unsupervised loss. Supervised loss was adopted to optimize the model based on the data with ground truth. Unsupervised loss was employed to evaluate the segmentation results, optimizing the model to accurately segment the data without ground truth. In this paper, the supervised and unsupervised losses were defined as follows:

$$L_{\mathrm{supervised}} = L_{\mathrm{joint}} + L_{\mathrm{D}} \tag{15}$$

$$L_{\mathrm{unsuperivised}} = L_{\mathrm{Adv}} \tag{16}$$

The semi-supervised loss function was finally defined as follows:

$$L_{\mathrm{semi}} = L_{\mathrm{supervised}} + L_{\mathrm{unsuperivised}} \tag{17}$$

DATASET

To evaluate the performance of the proposed method, comprehensive experiments have been conducted on the SUSTech-SYSU public slit-lamp fluorescein staining image dataset (Deng et al., 2020), which was released to develop and evaluate automatic corneal ulcer segmentation algorithms. As far as we know, this is the first time the semi-supervised-based method has been explored for corneal ulcer segmentation task based on the SUSTech-SYSU dataset. It has 354 point-flaky mixed and flaky corneal ulcer slit-lamp fluorescein staining images with ground truth annotated pixel-wise by ophthalmologists and 358 point-like corneal ulcer images without ground truth, in which the lesions were too small to annotate. Each RGB image with a resolution of 2,592 × 1,728 pixels contains only one corneal area, which is located in the middle of the field of view. In order to achieve a balance between the computational efficiency and avoid the loss of lesions with small size, the original images and their ground truths were resized to 512 × 512 by bilinear interpolation. In order to fully demonstrate the effectiveness of our proposed method, the dataset was randomly divided into fourfolds. The data strategies are listed in **Table 1** to train and evaluate all models. Besides, we also adopted online data augmentation, including rotations from −10 to 10 degrees, horizontal flipping, vertical flipping, Gaussian noise addition, and affine transformation to prevent overfitting and improve the robust ability of the model.

EXPERIMENTS AND RESULTS

Evaluation Metrics

To fully and fairly evaluate the segmentation performance of the different methods, four metrics were employed: dice coefficient (Dsc), Jaccard index (Jac), sensitivity (Sen), and Pearson's product-moment correlation coefficient (PPMCC).

TABLE 1 | Experimental data strategies.

Supervision approach	Data distribution
Supervised	All 354 labeled slit-lamp images were randomly divided into fourfold for cross-validation. Except for the 4th fold, which only had 84 images, each fold contained 90 slit-lamp images.
Semi-supervised	All 354 labeled slit-lamp images were randomly divided into fourfold for cross-validation. Except for the 4th fold, which only had 84 images, each fold contained 90 slit-lamp images. The 358 unlabeled point-like corneal ulcer images in the SUSTech-SYSU dataset were mixed with the labeled images to train the semi-supervised method.

PPMCC, with a value between −1 and 1, is often adopted to measure the correlation (linear correlation) between two variables. The four indicators were calculated as follows:

$$\mathrm{Dsc} = \frac{2 \times \mathrm{TP}}{2 \times \mathrm{TP} + \mathrm{TN} + \mathrm{FP}} \tag{18}$$

$$\mathrm{Sen} = \frac{\mathrm{TP}}{\mathrm{TP} + \mathrm{FN}} \tag{19}$$

$$\mathrm{Acc} = \frac{\mathrm{TP} + \mathrm{FN}}{\mathrm{TP} + \mathrm{FP} + \mathrm{FN}} \tag{20}$$

$$\mathrm{PPMCC} = \frac{\mathrm{Cov}\,(\mathrm{X, Y})}{\sigma_X \sigma_Y} \tag{21}$$

where TN, TP, FN, and FP represent true negative, true positive, false negative, and false positive, respectively. X and Y denote the segmentation result and corresponding ground truth, respectively. $Cov(.)$ represents the covariance between X and Y. σ_X and σ_Y are the standard deviations of X and Y, respectively.

Implementation Details

The proposed network was performed on the public platform Pytorch and a Tesla K40 GPU (12 GB). Adam was used as the optimizer. The initial learning rate was set to 0.0005, and weight decay was set to 0.0001. The batch size was set to be 4 and epoch was 100.

The segmentation performance of our proposed network was compared with other excellent networks, such as Attention U-Net (Oktay et al., 2018), R2U-Net (Alom et al., 2018), CE-Net (Gu et al., 2019), ResU-Net (He et al., 2016), PSPNet (Zhao et al., 2017), DeepLabv3+(Chen et al., 2018), U-Net++ (Zhou et al., 2018), and CPFNet (Feng et al., 2020). Aside from these CNN-based networks, the proposed network was also compared with other GANs, such as cGAN (Mirza and Osindero, 2014), PIX2PIX (Isola et al., 2017), and Cycle GAN (Zhu et al., 2017). Besides, several semi-supervised methods were also compared, such as Semi-cGAN, Semi-PIX2PIX, and Semi-Cycle GAN. All the networks were trained with the same parameters. It should be noted that all experiments based on supervised learning adopted the same data processing strategy and loss function of $L_{\mathrm{BCE}} + L_{\mathrm{Dice}}$. Moreover, the code for Semi-MsST-GAN will be released in https://github.com/TingtingWang12/MsST-GAN.

Experimental Results

Based on the data strategy listed in **Table 1**, we conducted comprehensive experiments to evaluate the effectiveness of our proposed MsST-GAN and Semi-MsST-GAN. MsST-GAN was compared with other CNN-based methods and GAN methods, with 354 labeled images under the supervised condition. Then, 358 unlabeled images were introduced to conduct the semi-supervised strategy. The proposed Semi-MsST-GAN was compared with Semi-cGAN, Semi-PIX2PIX, and Semi-Cycle GAN. Besides, we also conducted a series of ablation experiments to verify the validity of the proposed MsSTNet and loss function. For convenience, we used UNet (Ronneberger et al., 2015) as the baseline. The mean and standard deviation values of the four evaluation metrics and the efficiency for all methods are listed in **Table 2**.

It can be seen from **Table 2** that both supervised MsSTNet and MsST-GAN outperformed other state-of-the-art supervised methods. Cycle GAN achieved the worst results with 82.76% for Dsc as it tended to model collapse, which may be caused by corneal ulcers with complex pathological features. Although the efficiency of our proposed MsST-GAN was slightly lower than that of the baseline (U-Net), the Dsc and Jac indices of MsST-GAN were improved by 3.00 and 4.60%, respectively, compared with U-Net. Moreover, compared with the latest excellent models such as CE-Net (Gu et al., 2019) and CPFNet (Feng et al., 2020), which have been adopted for various medical image segmentation tasks, the Dsc values of MsST-GAN were improved by 1.67 and 0.58%, respectively. Besides, the efficiency of the proposed method was also improved by 52 and 128% compared to CE-Net and CPFNet, respectively. These results show that our proposed method can improve the performance of segmenting corneal ulcers and satisfy real-time requirements by adopting non-local convolution and self-attention rather than the traditional attention mechanism.

The performance of our proposed Semi-MsST-GAN was further improved by introducing 358 unlabeled images obviously. Compared with MsST-GAN, the Dsc, Sen, Jac, and PPMCC of Semi-MsST-GAN were increased from 89.90, 91.03, 82.36, and 89.89% to 90.93, 91.93, 83.79, and 90.77%, by 1.03, 0.9, 1.43, and 0.88%, respectively. On the contrary, the evaluation metrics declined when cGAN and PIX2PIX introduced the semi-supervised strategy. It was mainly caused by the poor ability of cGAN and PIX2PIX to learn the complex pathological features of point-like lesions. These results show that the proposed Semi-MsST-GAN can improve the performance of segmentation by leveraging unlabeled images. Three examples of segmentation results with different methods are shown in **Figure 4**, where yellow represents the correctly segmented region while red and blue are the results of false-positive and false-negative segmentation, respectively. It can be seen from **Figure 4** that our proposed method achieved the best segmentation results. The false-positive and false-negative segmentation results of the proposed Semi-MsST-GAN were obviously less than those of other methods. The results of U-Net (Ronneberger et al., 2015), Att-UNet (Oktay et al., 2018), CE-Net (Gu et al., 2019), and PSPNet (Zhao et al., 2017) had the problem of incorrect segmentation (shown in the bottom line of **Figure 4**). Compared with CE-Net (Gu et al., 2019), PSPNet (Zhao et al., 2017), and CPFNet (Feng et al., 2020), our proposed method cannot only accurately segment the lesion with small sizes but also maintain good regional continuity in segmenting large targets.

Statistical Significance Assessment

We further investigated the statistical significance of the performance improvement for the proposed MsST-GAN and Semi-MsST-GAN using the paired t-test. The p-values are listed in **Tables 3**, **4**, respectively. To avoid confusion, we renamed MsST-GAN as “MsSTGAN” and Semi-MsST-GAN as “Semi MsSTGAN” in both tables. As shown in **Table 3**, compared with the other supervised learning-based methods, the proposed MsST-GAN achieved significant improvement in terms of the main evaluation metrics (Dsc and Jac), with p-values less

TABLE 2 | Evaluation indices for different methods.

Strategy	Methods	Dsc (%)	Sen (%)	Jac (%)	PPMCC (%)	Efficiency (s)
Supervised	U-Net (Ronneberger et al., 2015)	87.28 ± 5.38	88.54 ± 3.71	78.74 ± 8.13	87.40 ± 5.23	0.0015
	CE-Net (Gu et al., 2019)	88.43 ± 4.85	88.45 ± 4.31	80.38 ± 7.16	88.48 ± 4.53	0.0038
	Att-UNet (Oktay et al., 2018)	86.41 ± 6.17	88.05 ± 3.28	77.65 ± 9.05	86.59 ± 6.03	0.0026
	R2U-Net (Alom et al., 2018)	80.76 ± 9.26	82.56 ± 5.78	70.50 ± 11.71	81.29 ± 8.67	0.0042
	ResU-Net (He et al., 2016)	88.64 ± 4.73	89.02 ± 3.90	80.79 ± 7.33	88.71 ± 4.61	0.0029
	PSPNet (Zhao et al., 2017)	89.09 ± 4.64	90.20 ± 3.34	81.28 ± 7.25	89.08 ± 4.56	0.0030
	DeepLabv3+ (Chen et al., 2018)	88.29 ± 5.41	89.19 ± 4.90	80.32 ± 8.04	88.33 ± 5.27	0.0057
	U-Net++ (Zhou et al., 2018)	86.93 ± 4.66	87.31 ± 2.45	78.24 ± 6.97	87.05 ± 4.59	0.0022
	CPFNet (Feng et al., 2020)	89.38 ± 4.30	89.97 ± 2.50	81.76 ± 6.78	89.37 ± 4.23	0.0057
	cGAN (Mirza and Osindero, 2014)	85.22 ± 6.82	86.26 ± 3.37	75.25 ± 9.65	85.17 ± 6.51	0.0015
	PIX2PIX (Isola et al., 2017)	87.49 ± 5.31	87.81 ± 3.67	78.81 ± 7.92	87.55 ± 5.06	**0.0015**
	Cycle GAN (Zhu et al., 2017)	82.76 ± 9.40	80.35 ± 13.4	72.08 ± 13.28	82.98 ± 8.88	**0.0015**
Ablation supervised	Baseline (Ronneberger et al., 2015)	87.28 ± 5.38	88.54 ± 3.71	78.74 ± 8.13	87.40 ± 5.23	**0.0015**
	UNet+MsST	88.24 ± 4.63	90.03 ± 3.21	80.09 ± 7.20	87.85 ± 5.67	0.0022
	UNet+ResNet18	89.11 ± 4.56	90.02 ± 2.95	81.42 ± 7.08	89.11 ± 4.49	0.0021
	MsSTNet (UNet+ResNet18+MsST)	89.41 ± 4.36	90.04 ± 3.70	81.85 ± 6.87	89.41 ± 4.29	0.0025
	MsST-GAN ($L_{adv} + L_D$)	89.21 ± 4.62	90.02 ± 2.98	81.36 ± 6.99	89.25 ± 4.37	0.0025
	MsST-GAN ($L_{adv} + L_D + L_{BCE}$)	89.31 ± 4.52	91.23 ± 2.39	81.44 ± 6.89	89.27 ± 4.33	0.0025
	MsST-GAN ($L_{adv} + L_D + L_{Dice}$)	89.64 ± 4.58	90.57 ± 2.75	82.11 ± 6.98	89.62 ± 4.38	0.0025
	MsST-GAN	89.90 ± 4.31	91.03 ± 1.88	82.36 ± 6.77	89.89 ± 4.12	0.0025
Semi-supervised	Semi-cGAN	83.87 ± 10.98	92.07 ± 4.40	73.89 ± 14.52	80.01 ± 18.07	**0.0015**
	Semi-PIX2PIX	87.28 ± 5.54	87.40 ± 4.11	78.58 ± 7.99	87.29 ± 5.34	**0.0015**
	Semi-Cycle GAN	82.35 ± 3.11	83.39 ± 6.87	70.79 ± 4.19	84.75 ± 5.71	**0.0015**
	Semi-MsST-GAN	**90.93 ± 4.19**	**91.93** ± **3.16**	**83.79 ± 6.72**	**90.77 ± 4.13**	0.0025

Dsc, dice similarity coefficient; Sen, sensitivity; Jac, Jaccard index; PPMCC, Pearson's product-moment correlation coefficient; cGAN, conditional generative adversarial network; MsSTNet, multi-scale self-transformer network; MsST-GAN, multi-scale self-transformer GAN. Values in bold indicate the best performance.

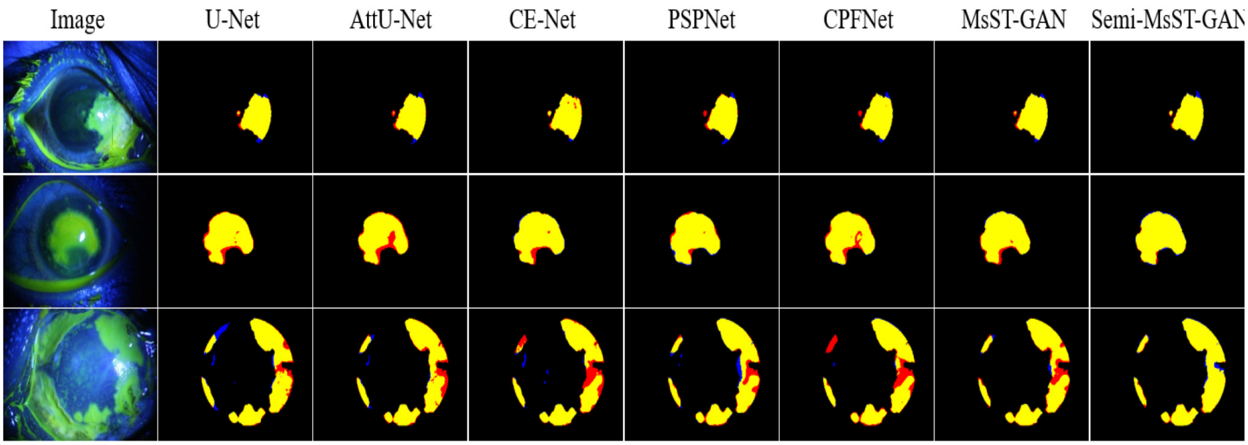

FIGURE 4 | Examples of corneal ulcer segmentation. From *left* to *right*: original image, U-Net, Attention U-Net, CE-Net, PSPNet, CPFNet, MsST-GAN, and the proposed method. *Yellow* represents the correctly segmented region, while *red* and blue are the results of false-positive segmentation and false-negative segmentation, respectively.

than 0.05. **Table 4** shows the p-values of the Semi-MsST-GAN compared with MsST-GAN and other CNN-based methods. All the improvements for the Jac and Dsc values of Semi-MsST-GAN were statistically significant, with $p < 0.05$, except for the Dsc of Cycle GAN ($p = 0.052$, slightly higher than 0.05). **Tables 3**, **4** further proved the effectiveness of the proposed MsST-GAN and Semi-MsST-GAN. Compared with those of the other CNN-based methods, the segmentation accuracies of both MsST-GAN and Semi-MsST-GAN have been significantly improved.

Ablation Experiment for MsSTNet

As shown in **Table 2**, an ablation experiment was conducted to evaluate the proposed MsST module and the ResNet18 encoder path. Compared with the baseline model, our proposed MsSTNet

TABLE 3 | Statistical analysis (*p*-value) of the proposed MsST-GAN compared with other convolutional neural network (CNN)-based methods.

Methods	Dsc	Jac
MsSTGAN–UNet (Ronneberger et al., 2015)	0.025	0.010
MsSTGAN–CENet (Gu et al., 2019)	0.040	0.008
MsSTGAN–Att-UNet (Oktay et al., 2018)	0.003	0.006
MsSTGAN–R2UNet (Alom et al., 2018)	0.038	0.036
MsSTGAN–ResUNet (He et al., 2016)	0.028	0.006
MsSTGAN–PSPNet (Zhao et al., 2017)	0.010	0.001
MsSTGAN–DeepLabv3+ (Chen et al., 2018)	0.014	0.014
MsSTGAN–UNet++ (Zhou et al., 2018)	0.015	0.008
MsSTGAN–CPFNet (Feng et al., 2020)	0.016	0.007
MsSTGAN–cGAN (Mirza and Osindero, 2014)	0.005	0.003
MsSTGAN–PIX2PIX (Isola et al., 2017)	0.005	0.001
MsSTGAN–Cycle GAN (Zhu et al., 2017)	0.049	0.045

Dsc, dice coefficient; Jac, Jaccard index; cGAN, conditional generative adversarial network; MsST-GAN, multi-scale self-transformer GAN.

TABLE 4 | Statistical analysis (*p*-value) of the proposed Semi-MsST-GAN compared with MsST-GAN and other CNN-based methods.

Methods	Dsc	Jac
Semi MsSTGAN–UNet (Ronneberger et al., 2015)	0.013	0.026
Semi MsSTGAN–CENet (Gu et al., 2019)	0.016	0.017
Semi MsSTGAN–Att-UNet (Oktay et al., 2018)	0.005	0.001
Semi MsSTGAN–R2UNet (Alom et al., 2018)	0.043	0.020
Semi MsSTGAN–ResUNet (He et al., 2016)	0.010	0.017
Semi MsSTGAN–PSPNet (Zhao et al., 2017)	0.001	0.004
Semi MsSTGAN–DeepLabv3+ (Chen et al., 2018)	0.025	0.020
Semi MsSTGAN–UNet++ (Zhou et al., 2018)	0.025	0.026
Semi MsSTGAN–CPFNet (Feng et al., 2020)	0.006	0.010
Semi MsSTGAN–cGAN (Mirza and Osindero, 2014)	0.006	0.006
Semi MsSTGAN–PIX2PIX (Isola et al., 2017)	0.001	0.005
Semi MsSTGAN–Cycle GAN (Zhu et al., 2017)	0.052	0.043
Semi MsSTGAN–MsSTGAN	0.029	0.005
Semi MsSTGAN–Semi-cGAN	0.027	0.023
Semi MsSTGAN–Semi-PIX2PIX	0.001	0.001
Semi MsSTGAN–Semi-Cycle GAN	0.005	0.009

Dsc, dice coefficient; Jac, Jaccard index; cGAN, conditional generative adversarial network; Semi MsSTGAN, semi-supervised multi-scale self-transformer GAN.

(Baseline+MsST+ResNet18) achieved improvement in terms of all four evaluation metrics (2.13% for Dsc, 1.5% for Sen, 3.11% for Jac, and 2.01% for PPMCC). In order to demonstrate the performance improvement of the proposed MsST module and the ResNet18 encoder path, we also conducted the experiments of UNet+MsST and UNet+ResNet18. Compared with that of the baseline (UNet), the Dsc of UNet+MsST was improved from 87.28 to 88.24% and that of UNet+ResNet18 was improved from 87.28 to 89.11%, which benefits from the fact that the MsST module can guide the aggregation of low-level weak semantic information with the high-level strong semantic information and adaptively learn the spatial correlation in feature maps and the ResNet18 encoder path can extract feature effectively. These experimental results proved the effectiveness of the proposed MsST module and the ResNet18 encoder path.

Ablation Study for Loss Function

We also conducted experiments to demonstrate the effectiveness of our proposed loss function. It can be seen from **Table 2** that, compared with MsST-GAN with only the generative adversarial loss function $L_{\text{Adv}} + L_{\text{D}}$, both MsST-GAN with $L_{\text{Adv}} + L_{\text{D}} + L_{\text{BCE}}$ and with $L_{\text{Adv}} + L_{\text{D}} + L_{\text{Dice}}$ achieved higher values in all four evaluation metrics. Especially, the average Dsc of MsST-GAN with $L_{\text{Adv}} + L_{\text{D}} + L_{\text{BCE}}$ increased from 89.21 to 89.31%, while MsST-GAN with $L_{\text{Adv}} + L_{\text{D}} + \mathrm{L}_{\text{Dice}}$ increased from 89.21 to 89.64%. These results indicated that the effectiveness of L_{BCE} works at the pixel level and L_{Dice} works at the image level. Finally, the results of our proposed loss function $L_{\text{supervised}}$ were compared with all the ablation experimental results. It can be seen from **Table 2** that MsST-GAN with $L_{\text{supervised}}$ achieved the best results in terms of Dsc, Acc, Jac, and PPMCC, except for Sen, which was slightly lower than that of the MsST-GAN with $L_{\text{Adv}} + L_{\text{D}} + L_{\text{BCE}}$. Especially, the Dsc and PPMCC of MsST-GAN with $L_{\text{supervised}}$ were improved by 0.77 and 1.23% and reached 89.90 and 89.89% compared with the results of $L_{\text{Adv}} + L_{\text{D}}$, respectively.

CONCLUSION AND DISCUSSION

In this paper, we proposed a novel Semi-MsST-GAN for semi-supervised corneal ulcer segmentation, which mainly focused on solving two problems: (1) the interferences caused by large pathological differences between point-like, point-flaky, and flaky corneal ulcers, blurred boundary, and noise interference, and (2) how to improve the segmentation accuracy of the network by leveraging the data without ground truth. This is the first time the semi-supervision-based method has been introduced into the task of corneal ulcer segmentation, which achieved good results. Compared with other state-of-the-art supervised CNN-based methods, the newly proposed MsST-GAN achieved better segmentation performance with comparable efficiency. In addition, our proposed semi-supervision-based method can further improve the performance by leveraging the data without ground truth. Comprehensive experiments have been conducted to evaluate the effectiveness and robustness of the proposed method. The experimental results showed that, compared with that of the other state-of-the-art algorithms, the segmentation performance of our proposed semi-supervision-based method has been improved obviously.

There is still a limitation in this study. All the compared algorithms and the proposed semi-supervision-based method were trained and evaluated based on the limited data from the SUSTech-SYSU dataset. Although the proposed semi-supervision method has achieved better performance, we believe that if more data can be collected, the performance of the proposed method will be further improved. Therefore, it is one of our future works to collect more data and further improve the accuracy of segmentation.

DATA AVAILABILITY STATEMENT

The datasets presented in this study can be found in online repositories. The names of the repository/repositories and accession number(s) can be found below: https://github.com/CRazorback/The-SUSTech-SYSU-dataset-for-automatically-segmenting-and-classifying-corneal-ulcers.

ETHICS STATEMENT

The studies involving human participants were reviewed and approved by the Zhongshan Ophthalmic Centre ethics committee of Sun Yat-sen University. The patients/participants provided their written informed consent to participate in this study. Written informed consent was obtained from the individual(s) for the publication of any potentially identifiable images or data included in this article.

AUTHOR CONTRIBUTIONS

TW conceptualized and designed the study, wrote the first draft of the manuscript, and performed data analysis. MW, WZ, LW, ZC, YP, FS, YZ, CY, and XC performed the experiments, collected, and analyzed the data. All authors contributed to the article and approved the submitted version.

FUNDING

This study was supported in part by the National Key R&D Program of China (2018YFA0701700) and in part by the National Nature Science Foundation of China (U20A20170 and 61622114).

REFERENCES

Alom, M. Z., Hasan, M., Yakopcic, C., Taha, T. M., and Asari, V. K. (2018). Recurrent residual convolutional neural network based on U-Net (R2U-Net) for medical image segmentation. *arXiv* [Preprint]. arXiv:1802.06955, doi: 10.1109/NAECON.2018.8556686

Bron, A. J., Janine, A., and Calonge, M. (2007). Methodologies to diagnose and monitor dry eye disease: report of the Diagnostic Methodology Subcommittee of the International Dry Eye WorkShop (2007). *Ocul. Surf.* 5, 108–152. doi: 10.1016/s1542-0124(12)70083-6

Chen, J. Q., and Yuan, J. (2010). Strengthen the study of the ocular surface recon struction. *Chin. J. Ophthalmol.* 46, 3–5.

Chen, L.-C., Papandreou, G., Schroff, F., and Adam, H. (2017). Rethinking atrous convolution for semantic image segmentation. *arXiv* [Preprint]. arXiv:1706.05587,

Chen, L. C., Zhu, Y., Papandreou, G., Schroff, F., and Adam, H. (2018). "Encoder-decoder with atrous separable convolution for semantic image segmentation," in *Lecture Notes in Computer Science*, eds V. Ferrari, M. Hebert, C. Sminchisescu, and Y. Weiss (Cham: Springer) doi: 10.1007/978-3-030-01234-2_49

Chen, X., Duan, Y., Houthooft, R., Schulman, J., Sutskever, I., and Abbeel, P. (2016). InfoGAN: interpreTABLE representation learning by information maximizing Generative Adversarial Nets. *arXiv*[Preprint]. arXiv:1606.03657.

Chun, Y. S., Yoon, W. B., Kim, K. G., and Park, I. K. (2014). Objective assessment of corneal staining using digital image analysis. *Invest. Ophthalmol. Vis. Sci.* 55, 7896–7903. doi: 10.1167/iovs.14-15618

Cohen, E. J., Laibson, P. R., Arentsen, J. J., and Clemons, C. S. (1987). Corneal ulcers associated with cosmetic extended wear soft contact lenses. *Ophthalmology* 94, 109–114. doi: 10.1016/s0161-6420(87)33491-8

Deng, L., Huang, H., Yuan, J., and Tang, X. (2018a). "Automatic segmentation of corneal ulcer area based on ocular staining images," in *Proceedings of the Medical Imaging 2018: Biomedical Applications in Molecular, Structural, and Functional Imaging* (Bellingham, WA: International Society for Optics and Photonics), 10578D–105781D. doi: 10.1117/12.2293270

Deng, L., Huang, H., Yuan, J., and Tang, X. (2018b). "Superpixel based automatic segmentation of corneal ulcers from ocular staining images," in *Proceedings of the 23rd International Conference on Digital Signal Processing (DSP)* (Shanghai: IEEE), 1–5. doi: 10.1117/1.jei.26.6.061608

Deng, L., Lyu, J., Huang, H., Deng, Y., Yuan, J., and Tang, X. (2020). The SUSTech-SYSU dataset for automatically segmenting and classifying corneal ulcers. *Sci. Data* 7, 1–7. doi: 10.1038/s41597-020-0360-7

Diamond, J., Leeming, J., Coombs, G., Pearman, J., Sharma, A., Illingworth, C., et al. (1999). Corneal biopsy with tissue micro homogenisation for isolation of organisms in bacterial keratitis. *Eye* 13, 545–549. doi: 10.1038/eye.1999.135

Feng, S., Zhao, H., Shi, F., Cheng, X., Wang, M., Ma, Y., et al. (2020). CPFNet: context pyramid fusion network for medical image segmentation. *IEEE Trans. Med. Imaging* 39, 3008–3018. doi: 10.1109/TMI.2020.2983721

Fukushima, K., and Miyake, S. (1982). "Neocognitron: a self-organizing neural network model for a mechanism of visual pattern recognition," in *Competition and Cooperation in Neural Nets*, eds S. Amari, and M. A. Arbib (Berlin: Springer), 267–285. doi: 10.1007/978-3-642-46466-9_18

Goodfellow, I. J., Pouget-Abadie, J., Mirza, M., Xu, B., Warde-Farley, D., Ozair, S., et al. (2014). "Generative adversarial nets," in *Proceedings of Advances in Neural Information Processing Systems* (Montreal, QC), 2672–2680.

Gu, Z., Cheng, J., Fu, H., Zhou, K., Hao, H., Zhao, Y., et al. (2019). Ce-net: context encoder network for 2d medical image segmentation. *IEEE Trans. Med. Imaging* 38, 2281–2292. doi: 10.1109/TMI.2019.2903562

He, K., Zhang, X., Ren, S., and Sun, J. (2015). Spatial pyramid pooling in deep convolutional networks for visual recognition. *IEEE Trans. Pattern Anal. Mach. Intell.* 37, 1904–1916. doi: 10.1109/TPAMI.2015.2389824

He, K., Zhang, X., Ren, S., and Sun, J. (2016). "Deep residual learning for image recognition," in *Proceedings of the IEEE Conference on Computer Vision and Pattern Recognition* (Las Vegas, NV: IEEE), 770–778. doi: 10.1109/CVPR.2016.90

Hu, J., Shen, L., and Sun, G. (2018). "Squeeze-and-excitation networks," in *Proceedings of the IEEE Conference on Computer Vision and Pattern Recognition* (Salt Lake City, UT: IEEE), 7132–7141. doi: 10.1109/CVPR.2018.00745

Hung, W.-C., Tsai, Y.-H., Liou, Y.-T., Lin, Y.-Y., and Yang, M.-H. (2018). Adversarial learning for semi-supervised semantic segmentation. *arXiv* [Preprint]. arXiv:1802.07934,

Isola, P., Zhu, J. Y., Zhou, T., and Efros, A. A. (2017). "Image-to-image translation with conditional adversarial network," in *Proceedings of the IEEE Conference on Computer Vision and Pattern Recognition* (Honolulu, HI: IEEE), 1125–1134. doi: 10.1109/CVPR.2017.632

Jiang, H., Chen, X., Shi, F., Ma, Y., Xiang, D., Ye, L., et al. (2019). Improved cGAN based linear lesion segmentation in high myopia ICGA images. *Biomed. Opt. Express* 10, 2355–2366. doi: 10.1364/BOE.10.002355

Lazebnik, S., Schmid, C., and Ponce, J. (2006). "Beyond bags of features: spatial pyramid matching for recognizing natural scene categories," in *Proceedings of the IEEE Computer Society Conference on Computer Vision and Pattern Recognition* (New York, NY: IEEE), 2169–2178.

LeCun, Y., Boser, B., Denker, J. S., Henderson, D., Howard, R. E., Hubbard, W., et al. (1989). Backpropagation applied to handwritten zip code recognition. *Neural Comput.* 1, 541–551. doi: 10.1162/neco.1989.1.4.541

Li, C., and Wand, M. (2016). "Precomputed real-time texture synthesis with markovian generative adversarial networks," in *Proceedings of the European Conference on Computer Vision*, eds B. Leibe, J. Matas, N. Sebe, and M. Welling (Cham: Springer), 702–716. doi: 10.1007/978-3-319-46487-9_43

Liu, Z., Shi, Y., Zhan, P., Zhang, Y., Gong, Y., and Tang, X. (2019). "Automatic corneal ulcer segmentation combining Gaussian mixture modeling and Otsu method," in *Proceedings of the 2019 41st Annual International Conference of the IEEE Engineering in Medicine and Biology Society (EMBC)* (Berlin: IEEE), 6298–6301. doi: 10.1109/EMBC.2019.8857522

Long, J., Shelhamer, E., and Darrell, T. (2015). "Fully convolutional networks for semantic segmentation," in *2015 IEEE Conference on Computer Vision and*

Pattern Recognition (CVPR) (Boston, MA: IEEE). doi: 10.1109/CVPR.2015.7298965

Ma, Y., Chen, X., Zhu, W., Cheng, X., Xiang, D., Shi, F., et al. (2018). Speckle noise reduction in optical coherence tomography images based on edge-sensitive cGAN. *Biomed. Opt. Express* 9, 5129–5146. doi: 10.1364/BOE.9.005129

Mirza, M., and Osindero, S. (2014). Conditional generative adversarial nets. *arXiv*[Preprint]. arXiv:1411.1784,

Morgan, P. B., and Carole, M. C. (2009). Corneal staining: do we really understand what we are seeing. *Cont. Lens Anterior Eye* 32, 48–54. doi: 10.1016/j.clae.2008.09.004

Oktay, O., Schlemper, J., Folgoc, L., Lee, M., Misawa, K., Mori, K., et al. (2018). Attention u-net: learning where to look for the pancreas. *arXiv* [Preprint]. arXiv:1804.03999,

Pathak, D., Krahenbuhl, P., Donahue, J., Darrell, T., and Efros, A. A. (2016). "Context encoders: feature learning by inpainting," in *Proceedings of the IEEE Conference on Computer Vision and Pattern Recognition* (Las Vegas, NV: IEEE), 2536–2544.

Peterson, R. C., and Wolffsohn, J. S. (2009). Objective grading of the anterior eye. *Optom. Vis. Sci.* 86, 273–278. doi: 10.1097/opx.0b013e3181981976

Pritchard, N., Young, G., Coleman, S., and Hunt, C. (2003). Subjective and objective measures of corneal staining related to multipurpose care systems. *Cont. Lens Anterior Eye* 26, 3–9. doi: 10.1016/S1367-0484(02)00083-8

Ronneberger, O., Fischer, P., and Brox, T. (2015). "U-net: convolutional networks for biomedical image segmentation," in *Proceedings of the International Conference on Medical Image Computing and Computer-Assisted Intervention* (Cham: Springer), 234–241.

Salimans, T., Goodfellow, I., Zaremba, W., Cheung, V., Radford, A., and Chen, X. (2016). Improved techniques for training gans. *arXiv* [Preprint]. arXiv:1606.03498.

Shaw, P., Uszkoreit, J., and Vaswani, A. (2018). Self-attention with relative position representations. *arXiv* [Preprint]. arXiv:1803.02155,

Springenberg, J. T., Dosovitskiy, A., Brox, T., and Riedmiller, M. (2014). Striving for simplicity: the all convolutional net. *arXiv* [Preprint]. arXiv:1412.6806,

Sricharan, K., Bala, R., Shreve, M., Ding, H., Saketh, K., and Sun, J. (2017). Semi-supervised conditional gans. *arXiv*[Preprint]. arXiv:1708.05789,

Sun, Q., Deng, L., Liu, J., Huang, H., Yuan, J., and Tang, X. (2017). "Patch-based deep convolutional neural network for corneal ulcer area segmentation," in *Fetal, Infant and Ophthalmic Medical Image Analysis*, eds M. Jorge Cardoso, T. Arbel, A. Melbourne, H. Bogunovic, P. Moeskops, and X. Chen (Cham: Springer), 101–108. doi: 10.1007/978-3-319-67561-9_11

Vondrick, C., Pirsiavash, H., and Torralba, A. (2016). Generating videos with scene dynamics. *arXiv* [Preprint]. arXiv:1609.02612,

Wang, M., Zhu, W., Yu, K., Chen, Z., Shi, F., Zhou, Y., et al. (2021). Semi-supervised capsule cGAN for speckle noise reduction in retinal OCT images. *IEEE Trans. Med. Imaging* 40, 1168–1183. doi: 10.1109/TMI.2020.3048975

Wang, T.-C., Liu, M.-Y., Zhu, J.-Y., Tao, A., Kautz, J., and Catanzaro, B. (2018). "High-resolution image synthesis and semantic manipulation with conditional gans," in *Proceedings of the IEEE Conference on Computer Vision and Pattern Recognition* (Berkeley, CA: IEEE), 8798–8807. doi: 10.1109/CVPR.2018.00917

Wang, X., Girshick, R., Gupta, A., and He, K. (2018). "Non-local neural networks," in *Proceedings of the IEEE Conference on Computer Vision and Pattern Recognition*, Salt Lake City, UT, 7794–7803. doi: 10.1109/CVPR.2018.00813

Wolffsohn, J. S., and Purslow, C. (2003). Clinical monitoring of ocular physiology using digital image analysis. *Cont. Lens Anterior Eye* 26, 27–35. doi: 10.1016/S1367-0484(02)00062-0

Wu, J., Zhang, C., Xue, T., Freeman, W. T., and Tenenbaum, J. B. (2016). Learning a probabilistic latent space of object shapes via 3d generative-adversarial modeling. *arXiv* [Preprint]. arXiv:1610.07584.

Yu, F., and Koltun, V. (2015). Multi-scale context aggregation by dilated convolutions. *arXiv* [Preprint]. arXiv:1511.07122,

Zha, X., Shi, F., Ma, Y., Zhu, W., and Chenl, X. (2019). "Generation of retinal OCT images with diseases based on cGAN," in *Proceedings of the Medical Imaging 2019: Image Processing* (Bellingham, WA: International Society for Optics and Photonics). doi: 10.1117/12.2510967

Zhang, D., Zhang, H., Tang, J., Wang, M., Hua, X., and Sun, Q. (2020). "Feature pyramid transformer," in *Proceedings of the European Conference on Computer Vision* (Cham: Springer), 323–339. doi: 10.1109/EMBC46164.2021.9629523

Zhang, Y., Chen, P., Di, G., Qi, X., and Gao, H. (2018). Netrin-1 promotes diabetic corneal wound healing through molecular mechanisms mediated via the adenosine 2b receptor. *Sci. Rep.* 8:5994. doi: 10.1038/s41598-018-24506-9

Zhao, H., Shi, J., Qi, X., Wang, X., and Jia, J. (2017). "Pyramid scene parsing network," in *Proceedings of the IEEE Conference on Computer Vision and Pattern Recognition* (Honolulu, HI: IEEE), 2881–2890. doi: 10.1109/CVPR.2017.660

Zhou, Z., Siddiquee, M. M. R., Tajbakhsh, N., and Liang, J. (2018). "Unet++: a nested u-net architecture for medical image segmentation," in *Deep Learning in Medical Image Analysis and Multimodal Learning for Clinical Decision Support*, ed. D. Stoyanov (Cham: Springer), 3–11. doi: 10.1007/978-3-030-00889-5_1

Zhu, J. Y., Krähenbühl, P., Shechtman, E., and Efros, A. A. (2016). "Generative visual manipulation on the natural image manifold," in *Proceedings of the European Conference on Computer Vision*, eds B. Leibe, J. Matas, N. Sebe, and M. Welling (Cham: Springer), 597–613. doi: 10.1167/18.11.20

Zhu, J.-Y., Park, T., Isola, P., and Efros, A. A. (2017). "Unpaired image-to-image translation using cycle-consistent adversarial networks," in *Proceedings of the IEEE International Conference on Computer Vision* (Venice: IEEE), 2223–2232.

Conflict of Interest: The authors declare that the research was conducted in the absence of any commercial or financial relationships that could be construed as a potential conflict of interest.

frontiers
in Neuroscience

ORIGINAL RESEARCH
published: 31 January 2022
doi: 10.3389/fnins.2021.804273

Dissecting the Profile of Corneal Thickness With Keratoconus Progression Based on Anterior Segment Optical Coherence Tomography

Yanling Dong[1,2], Dongfang Li[1,2], Zhen Guo[1,2], Yang Liu[3], Ping Lin[1,2], Bin Lv[3], Chuanfeng Lv[3], Guotong Xie[3,4,5] and Lixin Xie[1,2]**

[1] Qingdao Eye Hospital of Shandong First Medical University, Qingdao, China, [2] State Key Laboratory Cultivation Base, Shandong Provincial Key Laboratory of Ophthalmology, Eye Institute of Shandong First Medical University, Qingdao, China, [3] Ping An Technology (Shenzhen) Co. Ltd., Shenzhen, China, [4] Ping An Health Cloud Co. Ltd., Shenzhen, China, [5] Ping An International Smart City Technology Co. Ltd., Shenzhen, China

Edited by:
Vishal Jhanji,
University of Pittsburgh, United States

Reviewed by:
Jiaxing Wang,
Emory University, United States
Mo Ziaei,
The University of Auckland,
New Zealand

***Correspondence:**
Guotong Xie
xieguotong@pingan.com.cn
Lixin Xie
lixin_xie@hotmail.com

Specialty section:
This article was submitted to
Perception Science,
a section of the journal
Frontiers in Neuroscience

Received: *29 October 2021*
Accepted: *23 December 2021*
Published: *31 January 2022*

Citation:
Dong Y, Li D, Guo Z, Liu Y, Lin P, Lv B, Lv C, Xie G and Xie L (2022) Dissecting the Profile of Corneal Thickness With Keratoconus Progression Based on Anterior Segment Optical Coherence Tomography.
Front. Neurosci. 15:804273.
doi: 10.3389/fnins.2021.804273

Purpose: To characterize the corneal and epithelial thickness at different stages of keratoconus (KC), using a deep learning based corneal segmentation algorithm for anterior segment optical coherence tomography (AS-OCT).

Methods: An AS-OCT dataset was constructed in this study with 1,430 images from 715 eyes, which included 118 normal eyes, 134 mild KC, 239 moderate KC, 153 severe KC, and 71 scarring KC. A deep learning based corneal segmentation algorithm was applied to isolate the epithelial and corneal tissues from the background. Based on the segmentation results, the thickness of epithelial and corneal tissues was automatically measured in the center 6 mm area. One-way ANOVA and linear regression were performed in 20 equally divided zones to explore the trend of the thickness changes at different locations with the KC progression. The 95% confidence intervals (CI) of epithelial thickness and corneal thickness in a specific zone were calculated to reveal the difference of thickness distribution among different groups.

Results: Our data showed that the deep learning based corneal segmentation algorithm can achieve accurate tissue segmentation and the error range of measured thickness was less than 4 μm between our method and the results from clinical experts, which is approximately one image pixel. Statistical analyses revealed significant corneal thickness differences in all the divided zones ($P < 0.05$). The entire corneal thickness grew gradually thinner with the progression of the KC, and their trends were more pronounced around the pupil center with a slight shift toward the temporal and inferior side. Especially the epithelial thicknesses were thinner gradually from a normal eye to severe KC. Due to the formation of the corneal scarring, epithelial thickness had irregular fluctuations in the scarring KC.

Conclusion: Our study demonstrates that our deep learning method based on AS-OCT images could accurately delineate the corneal tissues and further successfully characterize the epithelial and corneal thickness changes at different stages of the KC progression.

Keywords: keratoconus, corneal thickness, anterior segment optical coherence tomography, deep learning, segmentation

INTRODUCTION

Keratoconus (KC) is a non-inflammatory, chronic, and progressive corneal disease which is characterized by apical thinning and cone-like protrusion of the central cornea, and usually leads to irregular astigmatism and myopia (Kennedy et al., 1986; Hashemi et al., 2020). Reports have shown an incidence of KC to be as high as 1.38/1,000 in the general population (Hashemi et al., 2020). Whereas diagnostic criteria such as CLEK guidelines (Zadnik et al., 1998) and Amsler–Krumeich classification (Krumeich et al., 1998) have been used to grade the severity of KC, the profiles of the corneal thickness along with KC progression are yet to be defined. Corneal thickness including epithelial thickness has been considered as one of the most important morphological features that aids in the characterization of KC progression (Li et al., 2012; Xu et al., 2016; Morishige et al., 2019; Yang et al., 2020; Toprak et al., 2021). Thus, characterizing the corneal thickness at different stages of KC might complement the existing diagnostic criteria.

With its ability for high-resolution non-invasive imaging in cross-sectional biological systems, anterior segment optical coherence tomography (AS-OCT) is an effective tool in observing the whole corneal thickness as well as individual layers such as the epithelium in normal or KC eyes (Chen et al., 2012; Corre-Perez et al., 2012; Li et al., 2012; Xu et al., 2016; Ang et al., 2018; Morishige et al., 2019; Yang et al., 2020; Toprak et al., 2021). Compared with the normal eyes, KC eyes have thinner apical corneal epithelial thickness but thicker epithelial layer superonasally, which is similar to the total corneal thickness pattern (Li et al., 2012). Eyes with forme fruste keratoconus seem to have increased central epithelium/stroma ratio and asymmetric superior-nasal epithelial thinning (Toprak et al., 2021). Besides, some epithelial thickness-based variables and corneal thickness-based variables have been developed for detecting KC (Li et al., 2012; Yang et al., 2020; Toprak et al., 2021). With ultra-high-resolution OCT, vertical thickness profiles of the epithelial and Bowman's layers have been shown to provide valuable diagnostic references for sub-clinical KC (Xu et al., 2016). Recent studies have investigated corneal deformation with the presence of stromal scarring in KC patients and demonstrated a correlation between the progression of KC and a reduction in corneal thickness and volume, as well as stromal scar formation (Morishige et al., 2019). These studies provided useful insights into the potential use of corneal thickness in understanding underlying mechanisms of KC. However, there is no study on the quantification of the characteristics of corneal and epithelial thickness at the different stages of KC development (Zadnik et al., 1998; Morishige et al., 2019).

One of the important premises for obtaining corneal thickness is accurate segmentation of corneal tissue interfaces from the AS-OCT images. Currently, the corneal tissue segmentation often performed through either manual labeling or some traditional image processing algorithms (Larocca et al., 2011; Li et al., 2012; Xu et al., 2016; Ang et al., 2018; Morishige et al., 2019; Yang et al., 2020; Toprak et al., 2021). Whereas manual labeling is time-consuming and has poor repeatability, the traditional image processing methods are less robust to deal with pathological corneas (Larocca et al., 2011; Williams et al., 2015; Ang et al., 2018; Elsawy et al., 2019). Recent studies have explored the feasibility of using deep learning-based methods for corneal tissue segmentation with AS-OCT images (Mathai et al., 2019; Ouyang et al., 2019; Santos et al., 2019). We have also proposed a hierarchy-constrained network, which robustly improves the segmentation performance of the corneal tissue interfaces in both normal and KC eyes (Liu et al., 2020). By taking advantage of this automated method, the profiles of the corneal thickness could be conveniently determined from the AS-OCT images.

In this study, we aimed to investigate the corneal and epithelial thickness profiles along the vertical and horizontal meridians in the KC eyes at different stages. The corneal tissue interfaces were delineated using our previously developed hierarchy-constrained method (Liu et al., 2020), and the thickness was automatically measured from the segmented AS-OCT images. Then one-way ANOVA and linear regression analyses were performed to explore the trends of the thickness changes against the KC progression.

MATERIALS AND METHODS

Dataset

This retrospective study was conducted based on the tenets of the Declaration of Helsinki and was approved by the institutional review board of Qingdao Eye Hospital of Shandong First Medical University. A total of 1,430 images from 715 eyes were selected from a large clinical database of the hospital between January 2009 and July 2021. The 715 eyes included both normal and KC patients. We excluded participants with any type of prior ocular surgery or trauma, associated corneal pathologic features, and those who had undergone collagen cross-linking, corneal rings, or keratoplasty. All AS-OCT images were acquired by Optovue RTVUE 100 (Optovue, Inc., United States), using a line scan mode. Each eye acquired two scans along with the horizontal and vertical meridians. The pupil center was treated as the focus point during scanning. The acquired images had a resolution of 1,019 × 640 pixels and covered an area of 8 mm × 1.933 mm. All the images were unified to 1,024 × 640 pixels by padding zeros on the left and right sides, and then resizing to 2,648 × 640 pixels for isotropy. Consequently, each pixel represented approximately 3 μm in corneal tissue, both horizontally and vertically.

The KC eyes were categorized into four different stages based on both CLEK guidelines (Zadnik et al., 1998) and additional clinical criteria (Morishige et al., 2019). According to the CLEK guidelines (Zadnik et al., 1998), we first identified three stages including mild KC (corneal curvature is less than 45 D), moderate KC (corneal curvature is between 45 D and 52 D), and severe KC (corneal curvature is more than 52 D). Then the scarring KC was classified based on the existence of stromal scarring (Morishige et al., 2019). All patients with scarring have resolved hydrops. In particular, the cornea, which appears as Descemet's membrane rupture with dilacerations of collagen lamellae, large fluid-filled intra-stromal cysts, was excluded from the scarring stage. In total, there were 118 normal eyes, 134 mild KC eyes, 239 moderate KC eyes, 153 severe KC eyes, and 71 scarring KC eyes. The demographic information is shown in **Table 1**.

Deep Learning Based Corneal Segmentation

To measure the corneal layers' thickness, we first performed corneal tissue segmentation using our proposed hierarchy-constrained network (Liu et al., 2020). The network adopted the U-Net architecture (Ronneberger et al., 2015) and consisted of a progressive feature-extraction module (PFEM) and a multi-level prediction fusion module (MPFM) (Liu et al., 2020). The PFEM added side paths to each level of decoder to achieve deep supervision for obtaining correct image features. On the other hand, the MPFM leveraged semantic information in various resolutions by concatenating reconstructed features from each level of the decoder. In addition, we extracted the boundaries of layers to calculate edge loss as additional constraints. Our previous report has shown that such a deep learning-based method improves the performance of corneal tissue segmentation (Liu et al., 2020). The main code is available at https://github.com/sie163/ASOCT_KC.

Before applying the segmentation method to the entire dataset, we evaluated its accuracy on a partial subset. Specifically, 236 normal images (from 118 normal eyes) were numbered, and 150 numbers were randomly generated from 1 to 236 and the images corresponding to the numbers were extracted to form a subset. The same rule was applied to KC images. Finally, we randomly selected 150 normal images and 160 KC images from the AS-OCT dataset, and manually labeled the semantic masks. The boundaries of the cornea and epithelial layer were outlined with customized labeling software by 3 ophthalmologists. Before formal labeling, we verified the labeling consistency of 3 ophthalmologists on 10 AS-OCT images covering different KC stages. Paired comparison of the labeled results showed that the dice values of corneal segmentation all reached 0.99 and the dice values of epithelial segmentation all reached 0.95. It showed that the labels of 3 ophthalmologists were basically the same. In addition, all 310 images were labeled, about 1/3 for each ophthalmologist. Thereafter, a senior expert reviewed the labeled semantic masks and discussed with 3 ophthalmologists to revise the questionable masks. Finally, all 310 AS-OCT images with labeled masks were used to evaluate the performance of our proposed deep learning method.

Measurement of the Corneal Thickness

To automatically measure the corneal thickness, the pupil center in the anterior corneal surface was first defined as a reference point after corneal segmentation. A Region of Interest (ROI) was then derived by cutting off 3 mm sections on either side of the reference point. Thus, an ROI containing 6 mm of the studied corneal section was created. Locating the reference point and corresponding ROI was essential because it serves to map the corneal tissues for further analysis of the corneal layers' thickness. To calculate the thickness of the cornea and epithelium, we then set 40 sampled points in the ROI, which were measured after every 0.15 mm horizontally or vertically. The distance between the sampled points on the anterior surface of the cornea and the intersection points of its incident normal as well as the boundary of epithelial and posterior surface of the cornea were defined as the thickness of the cornea and epithelial layer, respectively (**Figure 1F**). The visualization was implemented using Python (Oliphant, 2007).

Segmentation Evaluation and Statistical Analysis of Corneal Thickness Profiles

The performance of the corneal segmentation was assessed by direct and indirect evaluation metrics. The direct metrics included dice coefficient, IoU, sensitivity, and specificity (Liu et al., 2020), while the indirect metric was only the thickness error. Dice coefficient and IoU represented the overlap between the segmented and the labeled areas by the clinician, which reflects the overall segmentation precision. Sensitivity and specificity were the auxiliary metrics for proper segmentation. Whereas sensitivity calculated the proportion of positive pixels that are correctly segmented, specificity calculated the proportion

TABLE 1 | Demographic information for five groups in KCTD.

	Normal	Mild KC	Moderate KC	Severe KC	Scarring KC
Eyes	118	134	239	153	71
Images	236	268	478	306	142
Sex (M:F)	93:25	112:22	178:61	129:24	58:13
Age (mean ± std)	24.39 ± 6.69	21.01 ± 4.87	20.62 ± 4.43	22.58 ± 5.91	20.73 ± 5.54

KC, Keratoconus; KCTD, KC corneal thickness dataset.

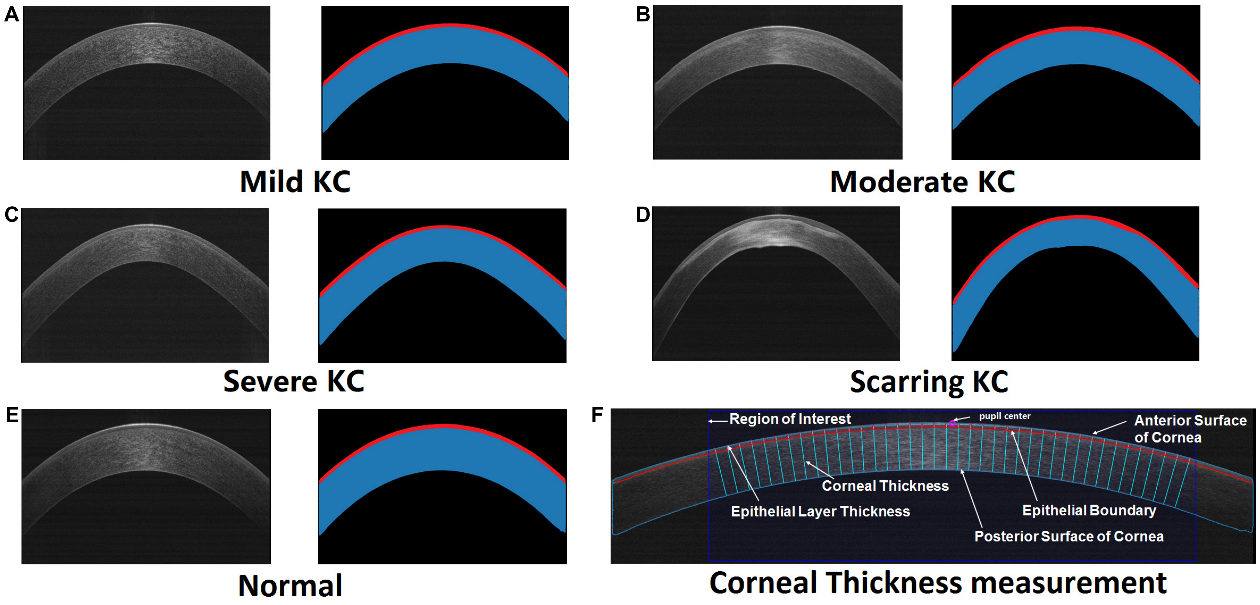

FIGURE 1 | The original AS-OCT images and their corresponding segmented maps generated by our trained deep learning networks. Red masks illustrate the segmented epithelial layers, while masks with red and blue are the segmented corneas. The representative cases included mild KC **(A)**, moderate KC **(B)**, severe KC **(C)**, scarring KC **(D)**, and normal eye **(E)**, respectively. **(F)** An example of the automatic corneal thickness measurement on resized AS-OCT image. The purple circle denotes the pupil center on the cornea. The dark blue rectangle stands for the studied region of interest. The sky-blue and red curves draw the anterior and posterior boundaries of the cornea including the epithelial layer. The normal lines of the corneal anterior surface represent the measurement of the epithelial layer thickness and corneal thickness.

of negative pixels that are properly segmented. We calculated these metrics for the segmentation of the whole cornea and epithelium. Besides, we measured the corneal and epithelial thickness based on the segmented maps and the labeled maps, respectively, and then calculated the average values of their differences as an indirect evaluation metric.

In addition, the thickness profiles in the horizontal and vertical meridians were compared between the normal eyes and the different KC stages. To unify the direction, the horizontal scan of the right eye was mirrored to the left eye during comparison. Each thickness line was divided equally into 20 zones, and the mean values and 95% confidence intervals (CI) were calculated. We applied one-way ANOVA to investigate group effect for mean epithelial thickness and corneal thickness in each zone. On the other hand, a two-sample t-test was used to determine the statistical significance of between-group differences. A $P < 0.05$ was considered as statistically significant. Besides, we applied ordinary least square linear regression to investigate the trend of corneal and epithelial thickness along with the progression of the KC in each zone. To test the diagnostic values of the epithelial and corneal thickness profiles, four thickness ectasia indices, including epithelium ectasia index of the vertical meridian (EEI_V), cornea ectasia index of the vertical meridian (CEI_V), epithelium ectasia index of the horizontal meridian (EEI_H), and cornea ectasia index of the horizontal meridian (CEI_H), were built to quantify the different change patterns at the different KC stages. Thickness ectasia index is defined as the ratio of maximum thickness to minimum thickness. Moreover, then linear discriminant analysis was applied to build discriminant functions with four indices. The predictive accuracies of differentiating the groups with different KC stages from the normal group were determined by receiver operating characteristic (ROC) curves and the area under the curves (AUC). All statistical analyses were performed with SciPy library in Python (Oliphant, 2007).

RESULTS

Evaluation of the Corneal Segmentation Algorithm

Our experiment demonstrated successful segmentation of the different stages of the KC and normal eyes (**Figure 1**). Our designed hierarchy-constrained network enhanced the capability of identifying corneal layers' boundaries from indiscernible images, such as having some degree of scarring around the boundary as shown in **Figure 1D**.

The quantitative evaluation of the segmentation performance was performed based on 310 labeled AS-OCT images. Using our model, there was high consistency of the segmented results with tissue masks labeled by clinical experts for both the whole cornea and epithelial layers in normal and KC eyes (**Table 2**). Besides, whereas dice coefficient, IoU, sensitivity, and specificity were slightly lower in the KC eyes compared with the normal eyes, their values significantly improved to 0.989, 0.978, 0.991, and 0.995 for the whole cornea, and 0.925, 0.860, 0.932, and 0.997 for the epithelium, respectively. The thickness error (T_error) between the segmented and labeled maps was 2.220 μm for the

TABLE 2 | Quantitative evaluation for corneal tissue segmentation and thickness measurement between our model and clinicians.

	Dice	IoU	Sensitivity	Specificity	T_error (μm)
Epithelium					
Normal	0.951	0.906	0.954	0.998	2.220
KC	0.925	0.860	0.932	0.997	3.858
Cornea					
Normal	0.995	0.990	0.996	0.997	1.788
KC	0.989	0.978	0.991	0.995	3.462

epithelial thickness and 1.788 μm for the corneal thickness in the normal eyes. On the other hand, the T_error between the segmented and labeled maps was 3.858 μm for the epithelial thickness and 3.462 μm for the corneal thickness in the KC eyes. The error range of thickness was, therefore, just about one pixel, because each image pixel represented around 3 μm both horizontally and vertically.

Statistical Analysis of the Thickness Changes

The profiles of the corneal and epithelial thickness in the horizontal and vertical meridians were then investigated based on all 1,430 AS-OCT images (**Figure 2**). For the epithelial thickness, there were minimal differences and fluctuations between the normal and mild KC eyes both in the horizontal and vertical meridians. With the progressing of the KC, the central epithelial layer grew thinner, thus the severe KC eyes had the thinnest central epithelial thickness. The epithelial thickness was thicker in the scarring KC stage and was accompanied by irregular fluctuations in both the horizontal and the vertical meridians. For the corneal thickness, the average changes of the thickness profiles were very regular, which were characterized by gradual thinning with KC progression. The thinnest parts were in the temporal and the inferior side next to the pupil center for the horizontal and the vertical meridians, respectively.

In addition, one-way ANOVA revealed significant thickness differences in all the divided zones in the horizontal and vertical meridians ($P < 0.05$). We also assessed the trends of thickness changes in each zone in the normal and KC eyes in different stages (**Figure 3**). The fitted slopes showed similar curve shapes for corneal thickness. The values were all less than zero, which demonstrated that the corneal thickness grew thinner with the KC progression. The lowest slopes occurred at zone 9 both in the horizontal and vertical meridians. However, the slope curves were relatively complex for the epithelial thickness. There were some positive values in the peripheral region of both sides, including zone 1, 2, 18, 19, and 20 for the horizontal meridian, and zone 1, 2, 17, 18, 19, and 20 for the vertical meridian. The lowest slopes occurred at zone 11 and zone 12 for the horizontal and the vertical meridians, respectively. In particular, there were obvious fluctuations around zone 8 for the horizontal meridian and zone 9 for the vertical meridian.

Furthermore, we provided the 95% confidence intervals (CI) for the thickness values (**Table 3**) and their corresponding regression curves for the typical zones (**Figure 3**). The selected zones included epithelial thickness in zone 8 of the horizontal meridian (ET_Z8_H) and the corneal thickness in zone 9 of the horizontal meridian (CT_Z9_H) as well as the epithelial thickness (ET_Z9_V) and the corneal thickness (CT_Z9_V) in zone 9 of the vertical meridian. Two sample *t*-tests revealed that most comparisons of the corneal thickness were statistically different among each group in both meridians (CT_Z9_H and CT_Z9_V). Most of the differences had a significance of $P < 0.001$, except between the normal and mild KC eyes in zone 9 of the horizontal meridian ($P = 0.07$). For the epithelial thickness, most comparisons reached a $P < 0.05$. Besides, due to irregular changes of the epithelial thickness in scarring KC, there were no significant differences between the normal eyes and

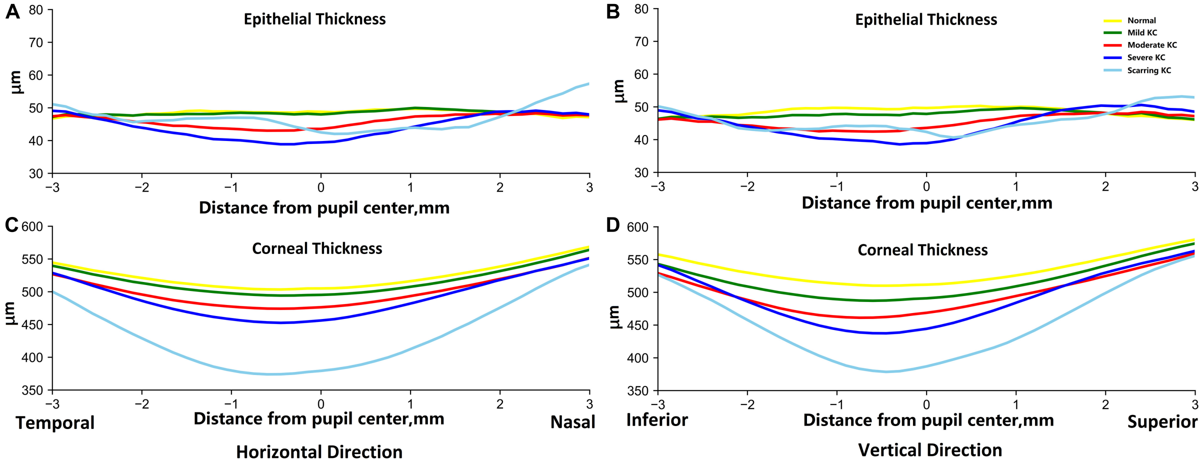

FIGURE 2 | The average epithelial and corneal thickness profiles in the horizontal **(A,C)** and vertical **(B,D)** meridians between the normal and KC eyes in different stages. The reference origin is the pupil center in the scanned AS-OCT image. The horizontal direction is from temporal to nasal, and the vertical direction is from inferior to superior. The yellow lines are for normal groups, and the green, red, dark blue, and sky-blue lines are for mild KC, moderate KC, severe KC, and scarring KC, respectively.

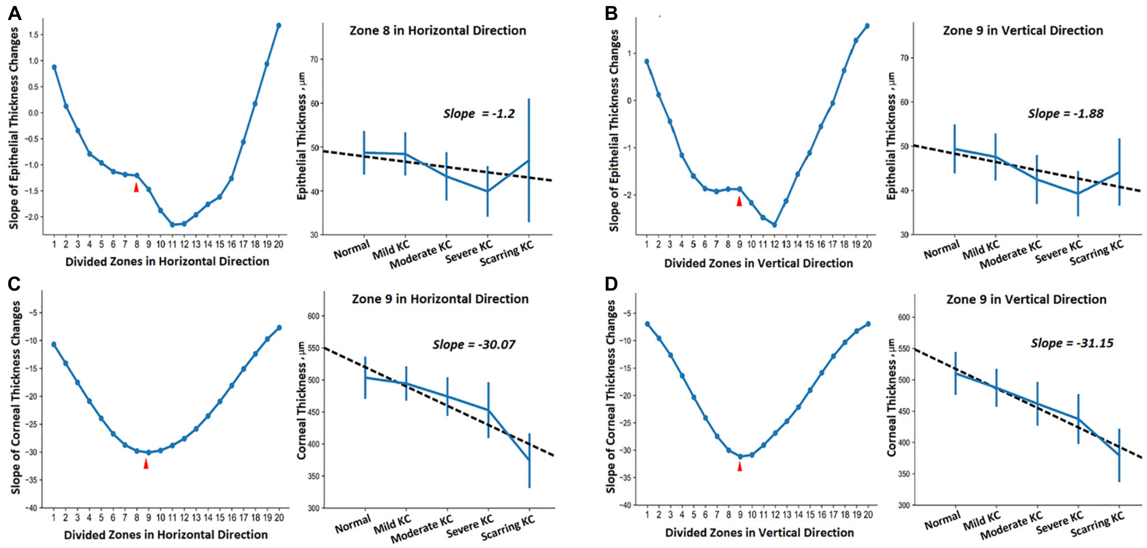

FIGURE 3 | The trends of the thickness change in different zones of the horizontal **(A,C)** and vertical **(B,D)** meridians between the normal and KC eyes in different stages. **(A,B)** Show epithelial thickness changes, while **(C,D)** show the corneal thickness changes. Each subgraph includes the fitted slopes in all divided zones and the detailed regression curve in one of the selected zones.

mild KC (P = 0.37), or between scarring KC and normal eyes (P = 0.28), mild KC (P = 0.47), and moderate KC (P = 0.08) in zone 8 of the horizontal meridian (ET_Z8_H). In addition, there were no significant differences between scarring and moderate KC (P = 0.29) in zone 9 of the vertical meridian (ET_Z9_V).

In **Figure 4**, the ROC curves for each discriminant function illustrated the discriminative abilities of mild KC, moderate KC, severe KC, and scarring KC from normal eyes. The output values of the discriminant functions showed different abilities to discriminate mild KC (AUC = 0.693), moderate KC (AUC = 0.840), severe KC (AUC = 0.918), and scarring KC (AUC = 0.998) from normal eyes, respectively. The more severe keratoconus, the higher the diagnostic accuracy.

DISCUSSION

As described in the global consensus on KC (Hashemi et al., 2020), the existing staging standards of KC [CLEK guidelines (Zadnik et al., 1998) and Amsler–Krumeich classification (Krumeich et al., 1998)] are relatively limited and outdated. For instance, the protocols do not fully consider the variation trend of various parameters such as the anterior and the posterior corneal surface height, the cornea thickness, and cornea curvature (Hashemi et al., 2020). Interestingly, corneal thickness variation is one of the most important characteristics of KC progression. To better guide clinicians in staging of the KC, there is need for accurate measurement of the corneal thickness and analysis of the corneal thickness distribution in patients with KC at different stages. AS-OCT provides cross-sectional information critical in the generation of thickness maps of both the whole cornea and individual layers (Shan et al., 2019; Yip and Chan, 2019). The main obstacle to accurate evaluation of the thickness is precise outlining of the corneal tissue boundaries. Besides the manual segmentation or semi-automated traditional methods (Chen et al., 2012; Corre-Perez et al., 2012; Li et al., 2012; Xu et al., 2016; Ang et al., 2018; Morishige et al., 2019; Yang et al., 2020; Toprak et al., 2021), deep learning-based methods have been proposed for corneal tissue interface segmentation (Mathai et al., 2019; Ouyang et al., 2019; Santos et al., 2019). In our previous studies, we compared these methods with our proposed hierarchy-constrained segmentation network (Liu et al., 2020) and validated the effectiveness of our network architecture and boundary constraint. Here, we further demonstrated that our method could achieve accurate corneal segmentation for measuring corneal and epithelial thickness in both normal and KC eyes. Our experiment demonstrated high segmentation accuracy as evaluated by dice coefficient, IoU, sensitivity, and specificity (**Table 2**). In addition, the error ranges of the corneal thickness were less than 4 μm between our automatic method and the results by clinical experts, which was just about one image pixel.

Although the corneal thickness profiles including the epithelial layer have been investigated based on AS-OCT images

TABLE 3 | A 95% CI of epithelial thickness and corneal thickness in selected zones.

Group	ET_Z8_H (μm)	ET_Z9_V (μm)	CT_Z9_H (μm)	CT_Z9_V (μm)
Normal	47.84–49.93	48.37–50.84	497.28–511.68	503.88–519.23
Mild KC	47.19–49.26	46.73–48.72	490.2–501.83	482.10–493.82
Moderate KC	42.87–44.56	41.79–43.30	470.94–480.41	456.58–466.42
Severe KC	39.20–41.47	38.86–40.81	447.38–463.22	432.33–447.57
Scarring KC	43.34–50.46	41.17–47.16	363.07–389.10	369.19–402.14

CI, confidence intervals; ET_Z8_H, epithelial thickness in zone 8 of horizontal meridian; ET_Z9_V, epithelial thickness in zone 9 of vertical meridian; CT_Z9_H, corneal thickness in zone 9 of horizontal meridian; CT_Z9_V, corneal thickness in zone 9 of vertical meridian.

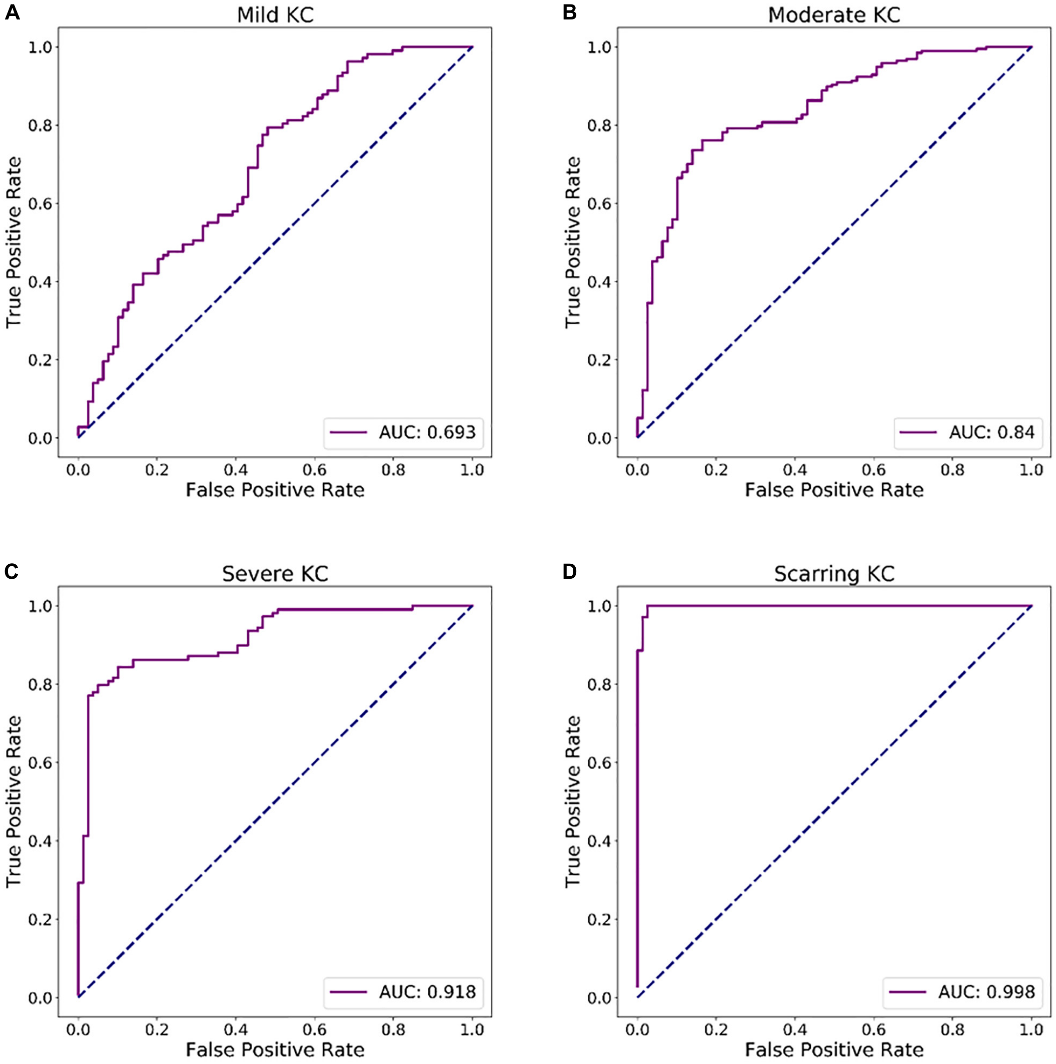

FIGURE 4 | ROC curves of discriminant functions in differentiating the groups with different KC stages from the normal group. **(A)** ROC curve of discriminant function for mild KC vs. the normal group. **(B)** ROC curve of discriminant function for moderate KC vs. the normal group. **(C)** ROC curve of discriminant function for severe KC vs. the normal group. **(D)** ROC curve of a discriminant function for scarring KC vs. the normal group.

(Chen et al., 2012; Corre-Perez et al., 2012; Li et al., 2012; Wu et al., 2014; Ma et al., 2016; Xu et al., 2016; Ang et al., 2018; Mathai et al., 2019; Morishige et al., 2019; Ouyang et al., 2019; Santos et al., 2019; Wang et al., 2019; Yang et al., 2020; Toprak et al., 2021), none of them was able to successfully classify the KC into different stages based on the CLEK guidelines (Zadnik et al., 1998). Often, all the KC eyes are considered as a group when compared with normal eyes. Only two recent studies classified sub-clinical KC (Xu et al., 2016) and scarring KC (Morishige et al., 2019). In this study, we collected KC eyes at four different stages: mild, moderate, severe, and scarring KC. The thickness profiles were revealed within ± 3 mm from the pupil center along with the horizontal and vertical meridians. For the corneal thickness, the overall distribution showed that the cornea was thinner in the central part but thicker on the peripheral sides. The thinnest points were located around 0.5 mm temporal side (CT_Z9_H) and 0.5 mm inferior side (CT_Z9_V) from the pupil center. The thinning phenomenon in the middle became more pronounced with the progression of the KC. On the other hand, for the epithelial thickness, the biggest change happened in the scarring KC with irregular thinning or thickening. Descemet's layer might break spontaneously to produce corneal edema in the late stage of the KC. Thereafter, the scar tissues were formed after corneal edema was repaired, which undoubtedly caused the irregular changes of epithelial thickness in the scarring KC. Since the thickness profiles in some stages of KC had never been investigated based on the AS-OCT, the findings not only supported the previous studies (Li et al., 2012; Ma et al., 2016; Xu et al., 2016; Morishige et al., 2019; Wang et al., 2019; Yang et al., 2020; Toprak et al., 2021), but also provided new evidence for the KC features at different stages. Furthermore, our experimental results with the linear discriminant analysis revealed that the measured thickness indices could be used to differentiate the groups of different KC stages from normal eyes.

Some limitations should be considered and need to be strengthened. First, previous studies have investigated the consistency of the corneal thickness measurement with AS-OCT, ultrasound pachymetry, and Scheimpflug imaging (Chen et al., 2012; Dutta et al., 2013; Huang et al., 2013; Kiraly et al., 2017). To prove the effectiveness of our proposed method, there is a need to perform more comparison studies with other devices or methods in the future. Second, besides the CLEK guidelines, there are more relevant KC grading systems such as topographical keratoconus classification (TKC) (Issarti et al., 2019). Further work includes grading the data with the TKC system and applying our purposed method to characterize the thickness changes along with the TKC system. Third, our study only obtained two AS-OCT images along with the horizontal and vertical meridians. A recent study that scanned 16 AS-OCT images for each eye to form a three-dimensional corneal shape (Morishige et al., 2019). Thus, we could scan more intensive images and detect the KC at different stages based on the AS-OCT derived corneal thickness.

Taken together, with our proposed segmentation network, we could successfully quantify the epithelial and corneal thickness profiles in the horizontal and vertical meridians for the normal and KC eyes at different stages. The entire corneal thicknesses became thinner with the progression of the KC, and their trends were deepened especially around the pupil center with a slight shift to the temporal and inferior side. Besides, the epithelial thickness had more irregular fluctuations due to more complex corneal tissue changes in the scarring KC. These findings therefore provide more quantitative information to investigate the underlying mechanism of KC at different stages.

DATA AVAILABILITY STATEMENT

The original contributions presented in the study are included in the article/supplementary material, further inquiries can be directed to the corresponding authors.

ETHICS STATEMENT

The studies involving human participants were reviewed and approved by the Institutional Review Board of Qingdao Eye Hospital of Shandong First Medical University. Written informed consent to participate in this study was provided by the participants' legal guardian/next of kin. Written informed consent was obtained from the individual(s), and minor(s)' legal guardian/next of kin, for the publication of any potentially identifiable images or data included in this article.

AUTHOR CONTRIBUTIONS

YD, DL, YL, and BL carried out the entire procedure including the literature search, data extraction, method development, statistical analysis, and writing the manuscript. PL and ZG finished the experimental design and clinical interpretation. YL, BL, and CL oversaw method development, statistical analysis, and revision of the manuscript. GX and LX conceived of the study and revised the manuscript. All authors read and approved the final manuscript.

FUNDING

This work has been supported by the Qingdao Science and Technology Demonstration and Guidance Project, under Fund No. 20-3-4-45-nsh.

ACKNOWLEDGMENTS

We would like to thank Yan Guo and Chengfen Zhang for their data labeling and statistical analysis during the experiment and thank the editor and reviewers for the valuable comments and suggestions.

REFERENCES

Ang, M., Baskaran, M., Werkmeister, R. M., Chua, J., Schmidl, D., Santos, V. A. D., et al. (2018). Anterior segment optical coherence tomography. *Prog. Retin. Eye Res.* 66, 132–156. doi: 10.1016/j.preteyeres.2018.04.002

Chen, S., Huang, J., Wen, D., Chen, W., Huang, D., and Wang, Q. (2012). Measurement of central corneal thickness by high-resolution scheimpflug imaging, fourier-domain optical coherence tomography and ultrasound pachymetry. *Acta Ophthalmol.* 90, 449–455. doi: 10.1111/j.1755-3768.2010.01947.x

Corre-Perez, M. E., Lopez-Miguel, A., Miranda-Anta, S., Iglesias-Cortinas, D., Alio, J. L., and Maldonado, M. J. (2012). Precision of high definition spectral-domain optical coherence tomography for measuring central corneal thickness. *Invest. Ophthalmol. Vis. Sci.* 53, 1752–1757. doi: 10.1167/iovs.11-9033

Dutta, D., Rao, H. L., Addepalli, U. K., and Vaddavalli, P. K. (2013). Corneal thickness in keratoconus: comparing optical, ultrasound, and optical coherence tomography pachymetry. *Ophthalmology* 120, 457–463. doi: 10.1016/j.ophtha.2012.08.036

Elsawy, A., Abdel-Mottaleb, M., Sayed, I. O., and Wen, D. (2019). Automatic segmentation of corneal microlayers on optical coherence tomography images. *Transl. Vis. Sci. Technol.* 8:39. doi: 10.1167/tvst.8.3.39

Hashemi, H., Heydarian, S., Hooshmand, E., Saatchi, M., and Khabazkhoob, M. (2020). The prevalence and risk factors for keratoconus: a systematic review and meta-analysis. *Cornea* 39, 263–270. doi: 10.1097/ICO.0000000000002150

Huang, J., Ding, X., Savini, G., Pan, C., Feng, Y., Cheng, D., et al. (2013). A comparison between scheimpflug imaging and optical coherence tomography in measuring corneal thickness. *Ophthalmology* 120, 1951–1958. doi: 10.1016/j.ophtha.2013.02.022

Issarti, I., Consejo, A., Jiménez-García, M., Hershko, S., Koppen, C., and Rozema, J. J. (2019). Computer aided diagnosis for suspect keratoconus detection. *Comput. Biol. Med.* 109, 33–42. doi: 10.1016/j.compbiomed.2019.04.024

Kennedy, R. H., Bourne, W. M., and Dyer, J. A. (1986). A 48-Year clinical and epidemiologic study of keratoconus. *Am. J. Ophthalmol.* 101, 267–273. doi: 10.1016/0002-9394(86)90817-2

Kiraly, L., Stange, J., Kunert, K., and Sel, S. (2017). Repeatability and agreement of central corneal thickness and keratometry measurements between four different devices. *J. Ophthalmol.* 2017:6181405. doi: 10.1155/2017/6181405

Krumeich, J. H., Daniel, J., and Knulle, A. (1998). Live-epikeratophakia for keratoconus. *J. Cataract Refract. Surg.* 24, 456–463. doi: 10.1016/s0886-3350(98)80284-8

Larocca, F., Chiu, S. J., Mcnabb, R. P., Kuo, A. N., Izatt, J. A., and Farsiu, S. (2011). Robust automatic segmentation of corneal layer boundaries in SDOCT images using graph theory and dynamic programming. *Biomed. Opt. Express* 2, 1524–1538. doi: 10.1364/BOE.2.001524

Li, Y., Tan, O., Brass, R., Jack, L. W., and David, H. (2012). Corneal epithelial thickness mapping by fourier-domain optical coherence tomography in normal and keratoconic eyes. *Ophthalmology* 119, 2425–2433. doi: 10.1016/j.ophtha.2012.06.023

Liu, Y., Li, D., Guo, Y., Zhou, X., and Lv, B. (2020). *Hierarchy-Constrained Network for Corneal Tissue Segmentation Based on Anterior Segment OCT Images*. Iowa City: IEEE, 1579–1582.

Ma, Y., He, X., Zhu, X., Lu, L., and Zou, H. (2016). Corneal epithelium thickness profile in 614 normal Chinese children aged 7–15 years old. *Sci. Rep.* 6:23482. doi: 10.1038/srep23482

Mathai, T. S., Lathrop, K. L., and Galeotti, J. (2019). *Learning to Segment Corneal Tissue Interfaces in OCT Images*. Venice: IEEE, 1432–1436.

Morishige, N., Magome, K., Ueno, A., Matsui, T., and Nishida, T. (2019). Relations among corneal curvature, thickness, and volume in keratoconus as evaluated by anterior segment optical coherence tomography. *Invest. Ophthalmol. Vis. Sci.* 60, 3794–3802. doi: 10.1167/iovs.19-27619

Oliphant, T. E. (2007). Python for scientific computing. *Comput. Sci. Eng*. 9, 10–20. doi: 10.1109/MCSE.2007.58

Ouyang, J., Mathai, T. S., Lathrop, K., and Galeotti, J. (2019). Accurate tissue interface segmentation via adversarial pre-segmentation of anterior segment OCT images. *Biomed. Opt. Express* 10, 5291–5324. doi: 10.1364/BOE.10.005291

Ronneberger, O., Fischer, P., and Brox, T. (2015). "U-Net: Convolutional Networks for Biomedical Image Segmentation." in Medical Image Computing and Computer-Assisted Intervention – MICCAI 2015. MICCAI 2015 (eds) Navab N., Hornegger J., Wells W., Frangi A. Springer, Cham: Lecture Notes in Computer Science, vol 9351.

Santos, V. D., Schmetterer, L., Stegmann, H., Pfister, M., Messner, A., Schmidinger, G., et al. (2019). CorneaNet: fast segmentation of cornea OCT scans of healthy and keratoconic eyes using deep learning. *Biomed. Opt. Express* 10, 622–641. doi: 10.1364/BOE.10.000622

Shan, J., Deboer, C., and Xu, B. Y. (2019). Anterior segment optical coherence tomography: applications for clinical care and scientific research. *Asia Pac. J. Ophthalmol.* 8, 146–157. doi: 10.22608/APO.201910

Toprak, I., Vega, A., Barrio, J., Espla, E., Cavas, F., and Alio, J. (2021). Diagnostic value of corneal epithelial and stromal thickness distribution profiles in forme fruste keratoconus and subclinical keratoconus. *Cornea* 40, 61–72. doi: 10.1097/ICO.0000000000002435

Wang, Q., Lim, L., Lim, S. W. Y., and Htoon, H. M. (2019). Comparison of corneal epithelial and stromal thickness between keratoconic and normal eyes in an Asian population. *Ophthalmic Res.* 62, 134–140. doi: 10.1159/000500313

Williams, D., Zheng, Y., Bao, F., and Elsheikh, A. (2015). Fast segmentation of anterior segment optical coherence tomography images using graph cut. *Eye Vis.* 2:1. doi: 10.1186/s40662-015-0011-9

Wu, S., Tao, A., Hong, J., Zhe, X., Perez, V., and Wang, J. (2014). Vertical and horizontal corneal epithelial thickness profile using ultra-high resolution and long scan depth optical coherence tomography. *PLoS One* 9:e97962. doi: 10.1371/journal.pone.0097962

Xu, Z., Jiang, J., Yang, C., Huang, S., Peng, M., Li, W., et al. (2016). Value of corneal epithelial and Bowman's layer vertical thickness profiles generated by UHR-OCT for sub-clinical keratoconus diagnosis. *Sci. Rep.* 6:31550. doi: 10.1038/srep31550

Yang, Y., Pavlatos, E., Chamberlain, W., Huang, D., and Li, Y. (2020). Keratoconus detection using OCT corneal and epithelial thickness map parameters and patterns. *J. Cataract Refract. Surg.* 47, 759–766. doi: 10.1097/j.jcrs.0000000000000498

Yip, H., and Chan, E. (2019). Optical coherence tomography imaging in keratoconus. *Clin. Exp. Optom.* 102, 218–223. doi: 10.1111/cxo.12874

Zadnik, K., Barr, J. T., Edrington, T. B., Everett, D. F., Jameson, M., McMahon, T. T., et al. (1998). Baseline findings in the collaborative longitudinal evaluation of keratoconus (CLEK) study. *Invest. Ophthalmol. Vis. Sci.* 39, 2537–2546. doi: 10.1097/00004397-199803810-00020

Conflict of Interest: YL, BL, CL, and GX were employed by Ping An Technology (Shenzhen) Co. Ltd.

The remaining authors declare that the research was conducted in the absence of any commercial or financial relationships that could be construed as a potential conflict of interest.

frontiers | Frontiers in Neuroscience

ORIGINAL RESEARCH
published: 08 April 2022
doi: 10.3389/fnins.2022.818530

Reduced Radial Peripapillary Capillary in Pathological Myopia Is Correlated With Visual Acuity

Jie Ye, Jue Lin, Meixiao Shen, Wen Chen, Riyan Zhang, Fan Lu and Yilei Shao**

School of Ophthalmology and Optometry, Wenzhou Medical University, Wenzhou, China

Purpose: To quantify the radial peripapillary capillary (RPC) density and the peripapillary retinal nerve fiber layer (pRNFL) thickness in pathological myopia and examine associations among these factors and best-corrected visual acuity (BCVA).

Methods: The cohort was composed of 41 eyes as control and 79 eyes with high myopia (59 simple high myopia, 20 pathological myopia). Optical coherence tomography angiography was done to obtain RPC density and pRNFL thickness, superficial retinal capillary plexus (SRCP), and deep retinal capillary plexus (DRCP) density. The axial length (AL) was measured. Correlations among BCVA, RPC density, pRNFL thickness, AL, and other parameters were determined.

Results: For pathological myopia, the densities of RPC, SRCP, and DRCP were significantly less than those of the control and simple high myopia groups ($p \leq 0.005$). There was no statistical difference in pRNFL thickness between pathological myopia and simple high myopia ($p = 0.063$), whereas there was significant difference in global pRNFL thickness between pathological myopia and control ($p = 0.008$). The global RPC density showed the greatest area under the curve (AUC = 0.962, sensitivity = 94.74%, specificity = 90.00%, cutoff value = 47.8%) for pathological myopia, whereas the AUC of pRNFL thickness, SRCP, and DRCP were only 0.675, 0.824, and 0.865, respectively. The univariate and multiple linear regression models showed that RPC density, SRCP density, and AL were correlated with BCVA (All $p < 0.05$). In the final BCVA model with multiple generalized estimating equation analysis, AL, RPC density and interaction between RPC and AL were shown (all $p < 0.03$). For an eye with AL $\geq$ 27.94 mm, global RPC density was predicted to be less than 48.77% with a high risk of visual impairment.

Conclusion: Peripapillary alterations, both the decreasing RPC density and pRNFL thickness, occurred in pathological myopia compared with the control. The RPC density was associated with BCVA, and this relationship was affected by AL.

Keywords: optical coherence tomography angiography, visual acuity, pathological myopia, radial peripapillary capillary, axial length

Edited by:
Haoyu Chen,
The Chinese University of Hong Kong,
Hong Kong SAR, China

Reviewed by:
Jiaxing Wang,
Emory University, United States
Kai Guo,
University of Illinois at Chicago,
United States

****Correspondence:***
Fan Lu
lufan62@mail.eye.ac.cn
Yilei Shao
magic_shao@163.com

Specialty section:
This article was submitted to
Perception Science,
a section of the journal
Frontiers in Neuroscience

Received: *19 November 2021*
Accepted: *28 February 2022*
Published: *08 April 2022*

Citation:
Ye J, Lin J, Shen M, Chen W,
Zhang R, Lu F and Shao Y (2022)
Reduced Radial Peripapillary Capillary
in Pathological Myopia Is Correlated
With Visual Acuity.
Front. Neurosci. 16:818530.
doi: 10.3389/fnins.2022.818530

INTRODUCTION

High myopia, defined as a spherical equivalent (SE) worse than −6.0 diopter (D) or axial length (AL) greater than 26.5 mm, is not uncommon around the world (Holden et al., 2016; Wong et al., 2017). Holden et al. (2016) predicted that by 2050 there would be 938 million people with high myopia worldwide. With the progression of high myopia, pathological changes often accumulate over time. It was estimated that nearly 40.6% of cases develop pathological myopia, characterized by the presence of myopic maculopathy (Hayashi et al., 2010; Ohno-Matsui et al., 2015). Of the patients with pathological myopia, approximately one of three had a best-corrected visual acuity (BCVA) of less than 20/60 (Liu et al., 2010). Pathological myopia is considered to be one of the major causes of visual impairment. Thus, to develop possible preventative and therapeutic methods, it is necessary to understand the risk factors and pathogenesis associated with it.

In the early stage of pathological myopia, changes in the fundus commonly occur around the optic disc. With the continued axial elongation and progression of high myopia, some peripapillary alterations occur, such as the appearance of peripapillary diffuse atrophy and the tilt of optic disc (Shimada et al., 2007; Nakazawa et al., 2008; Jonas et al., 2016, 2018). Often, in patients with long-term follow-up, early evidence of myopic maculopathy is indicated by the presence of peripapillary diffuse atrophy (Tokoro, 1998; Fang et al., 2018). The reduced peripapillary microvasculature and structure are always considered to be associated with the characteristic of the peripapillary diffuse atrophy. Disease progression then usually includes macular chorioretinal atrophy radiating out from the peripapillary area (Fang et al., 2018). The related macular microvascular and structural alteration in pathological myopia had been reported in our previous studies (Ye et al., 2019, 2020). We hypothesized that peripapillary alterations (especially peripapillary microvasculature and structure) are likely to result in pathological myopia and visual impairment. However, regional differences in peripapillary microvasculature and structure, and the relationship of those alterations to visual function have seldom been studied in quantitative detail. The early detection of the peripapillary microvasculature and structure changes in pathological myopia and differentiating it from the simple high myopia would be important to develop new preventive strategies and prevent further fundus degeneration and the occurrence of visual impairment.

In this study, the changes in the global and sector-specific radial peripapillary microvasculature and structure in pathological myopia would be investigated. We then correlated these sector-specific changes with visual impairment. This new information regarding the peripapillary microvasculature and structure alterations that occur in pathological myopia and visual impairment can help develop new therapeutic approaches to prevent further progression of this disease.

MATERIALS AND METHODS

Subjects and Clinical Examinations

All myopia patients and control subjects were from the Eye Hospital of Wenzhou Medical University, Wenzhou, Zhejiang, China. The control subjects had no vision problems and were present only in the clinic for ocular health screenings. This project was executed in consonance with the tenets of the Declaration of Helsinki and was approved by the Ethics Committee of Wenzhou Medical University. All participants agreed to participate in the project and signed the informed consent.

All subjects were given a clinical examination, including refractive error with BCVA measured as the log minimum angle of resolution (logMAR), slit-lamp biomicroscopy, fundus photography with a 45° retinal camera (Canon EOS 10D SLR backing; Canon, Inc., Tokyo, Japan), AL measurement with the IOL Master (Carl Zeiss, Jena, Germany), and intraocular pressure (IOP) measurement with the Auto Tonometer TX-F (Topcon, Tokyo, Japan).

After the clinical examinations, all subjects were separated into three groups: (1) control subjects for whom the SE varied from -1.5 D to $+ 0.5$ D; (2) simple high myopia patients with SE worse than -6.0 D or AL greater than 26.5 mm, without pathological fundus alteration; and (3) pathological myopia patients with SE worse than -6.0 D or AL greater than 26.5 mm, with pathological fundus alteration. Patients having a fundus with diffuse or severe atrophy were considered to have pathological myopia based on the meta-analysis for pathologic myopia (META-PM) classification (Ohno-Matsui et al., 2015). The diagnosis and classification of the three groups were determined by two ophthalmologists from the Eye Hospital of Wenzhou Medical University. In cases where the two could not reach an agreement, another senior ophthalmologist made the final decision. Exclusion criteria included any of the following: patients with IOP $>$ 21 mm Hg, history of the optic disc and peripapillary disease, visual field defects, pathological myopia-related complications, history of intraocular surgery, or related systemic diseases.

Peripapillary and Macular Image Acquisition

Peripapillary and macular images for all subjects were acquired by optical coherence tomography angiography (OCT-A, Optovue RTVue XR Avanti; Optovue, Inc., Fremont, CA, United States; software version 2017.1.0.155) using the angio disc scan protocol (4.5 × 4.5 mm) and angioretinal macular scan protocol (3 × 3 mm), respectively.

The global peripapillary area was defined as a ring with a 2-mm inner diameter and a 4-mm outer diameter centered on the optic disc. The radial peripapillary capillary (RPC) slab was imaged from the internal limiting membrane to the retinal nerve fiber layer (RNFL). After angio disc scanning, the software automatically segmented the global peripapillary area into eight sectors based on the Garway-Heath grid map (Garway-Heath et al., 2000), that is, nasal-superior, nasal-inferior, inferior-nasal, inferior-temporal, temporal-inferior, temporal-superior, superior-temporal, and superior-nasal. The peripapillary RNFL (pRNFL) thickness and RPC density of the same global peripapillary area and eight sectors were calculated by built-in software. The RPC density was defined as the ratio between the area occupied by the capillary vessels and the whole target area analyzed in the OCT-A image. The angio disc scan also calculated the optic cup-to-disc ratio.

The global analyzed macular area was defined as a ring with a 1-mm inner diameter and 3-mm outer diameter centered on the macular fovea. The superficial retinal capillary plexus (SRCP) slab was imaged from the internal limiting membrane to 10 μm above the inner plexiform layer, and deep retinal capillary plexus (DRCP) slab was imaged from 10 μm above the inner plexiform layer to the 10 μm below the outer plexiform layer. After angioretinal macular scanning, the software automatically segmented the global macular area into four sectors, that is, nasal, inferior, temporal, and superior. The SRCP and DRCP density of the global macular area and four sectors were calculated by built-in software. The density was defined as the ratio between the area occupied by the capillary vessels and the whole target area analyzed in the OCT-A image.

A masked reader reviewed all OCT-A images. Scans with a signal strength index (assessed by the machine itself) less than 4/10, an RPC/SRCP/DRCP slab segmentation error, an obvious motion artifact, a Bruch membrane opening distance at optic disc larger than 2 mm, and without vessels in the target analyzed area were excluded.

Statistical Analyses

Only the right eye of each subject was included for data analysis in this study. All continuous data were analyzed as means ± standard deviations and were calculated by SPSS software (version 22.0; SPSS, Inc., Chicago, IL, United States). The SE was analyzed as the spherical dioptric power plus half of the cylindrical dioptric power. Differences in gender frequencies among the three groups were calculated by the χ^2-test. Differences of other parameters among the three groups were analyzed by one-way analysis of variance (ANOVA). The receiver operating characteristic (ROC) curve was used to determine the diagnostic accuracy of the peripapillary parameters and macular retinal microvascular density to differentiate pathological myopia and the AL cutoff value to the visual impairment. Pearson correlation, partial correlation, and simple and multiple linear regression were used to assess the correlations among the peripapillary parameters, macular retinal microvascular density, BCVA, and AL. To avoid confounding factors, the generalized estimating equations (GEE) were further used to analyze the associations and interactions of the above parameters with the BCVA. Non-linear regression was used to explore the relationship between the AL and RPC density. p-values less than 0.05 were considered to be statistically significant.

RESULTS

Subjects Basic Characteristics

The study population included 41 control, 59 simple high myopia, and 20 pathological myopia eyes (**Table 1**). There were no significant differences in age, gender ratios, IOPs, or optic cup-to-disc ratios among the three groups (p = 0.729, 0.868, 0.852, and 0.606, respectively, **Table 1**). Compared with the control and simple high myopia eyes, the eyes with pathological myopia had worse myopic refraction error, worse BCVA, and longer AL (all $p < 0.001$; **Table 1**).

The Difference of Radial Peripapillary Capillary Density, Peripapillary Retinal Nerve Fiber Layer Thickness, and Macular Retinal Microvascular Density Among the Three Groups

Representative fundus photography and OCT-A images of the control, simple high myopia, and pathological myopia are shown in **Figure 1**. There were significant differences in RPC density for the global area and the respective eight sectors (ANOVA, all $p < 0.001$; **Table 2**). When compared with the control group, the global RPC density in simple high myopia was smaller (p = 0.013; **Table 2**), although none of the eight sectors were significantly different between the control group and the simple high myopia group (**Table 2**). For the pathological myopia group, the RPC densities in not only the global area but also all eight sectors were significantly less than those of the control and simple high myopia groups ($p < 0.01$; **Table 2**).

Although there was a significant difference in pRNFL thickness in the global area among the three groups (ANOVA, p = 0.030; **Table 3**), there was no statistical difference between the simple high myopia and the control group (p = 0.217; **Table 3**). The pRNFL of the simple high myopia and pathological myopia in inferior-nasal and superior-nasal sectors were thinner, and that in the tempo-inferior sector was thicker when compared with the control group ($p < 0.02$; **Table 3**). The pRNFL showed the insignificant difference between the simple high myopia and pathological myopia in the global and respective eight sectors (p = 0.063–1.000; **Table 3**).

There were significant differences in SRCP and DRCP density for the global area and the respective four sectors (ANOVA, all $p < 0.001$; **Table 4**). The global SRCP density in simple high myopia was smaller (p = 0.017; **Table 4**), although nasal, inferior, and superior sectors did not show significant differences when compared with the control group (**Table 4**). When compared with the control group, the global DRCP density in simple high myopia was smaller (p = 0.027; **Table 4**), although the nasal sector was not shown a significant difference (**Table 4**). For the pathological myopia group, the SRCP and DRCP density in not only the global area but also all four sectors were significantly less than those of the control and simple high myopia groups ($p < 0.003$; **Table 4**).

Receiver Operating Characteristic Curve for Discriminating Analysis

The ROC curves were used to show the discriminating power of RPC density, pRNFL thickness, and macular retinal microvascular density for pathological myopia. The global RPC density showed the greatest area under the curve (AUC = 0.962, sensitivity = 94.74%, specificity = 90.00%; **Figure 2A**) with the cutoff global RPC density value as 47.8%, whereas the AUC of pRNFL thickness, SRCP density, and DRCP density were only 0.675, 0.824, and 0.865, respectively (**Figure 2A**). For the respective eight sectors, the AUCs of the RPC density in the tempo-inferior, tempo-superior, and superior-tempo sectors were

TABLE 1 | The basic characteristic information of the control group, simple high myopia, and pathological myopia.

	Control	Simple high myopia	Pathological myopia	p^*	p_1	p_2	p_3
Patients, n	41	59	20	—	—	—	—
Eyes, n	41	59	20	—	—	—	—
Age, year	31 ± 11	31 ± 8	33 ± 9	0.729	0.732	0.622	0.430
Gender, M:F	16: 25	20: 39	7: 13	0.868	0.599	0.761	0.928
SE, diopter	−0.88 ± 1.07	−8.32 ± 2.72	−14.6 ± 3.85	**<0.001**	**<0.001**	**<0.001**	**<0.001**
BCVA, logMAR	−0.0 ± 0.06	0.00 ± 0.03	0.22 ± 0.18	**<0.001**	0.131	**<0.001**	**<0.001**
AL, mm	23.79 ± 0.97	26.71 ± 1.19	29.11 ± 1.66	**<0.001**	**<0.001**	**<0.001**	**<0.001**
IOP, mm Hg	13.67 ± 3.67	14.11 ± 3.44	14.27 ± 3.50	0.852	0.637	0.618	0.891
Optic cup-to-disc ratio	0.30 ± 0.15	0.27 ± 0.14	0.26 ± 0.14	0.606	0.410	0.406	0.772

M, male; F, female; SE, Spherical Equivalent; BCVA, best corrected visual acuity; AL, axial length; p^*, p-value of ANOVA among the three groups; p_1, p-value between the control group and simple high myopia; p_2, p-value between the control group and pathological myopia; p_3, p-value between the simple high myopia and pathological myopia. The bold values just means the P-value less than 0.05.

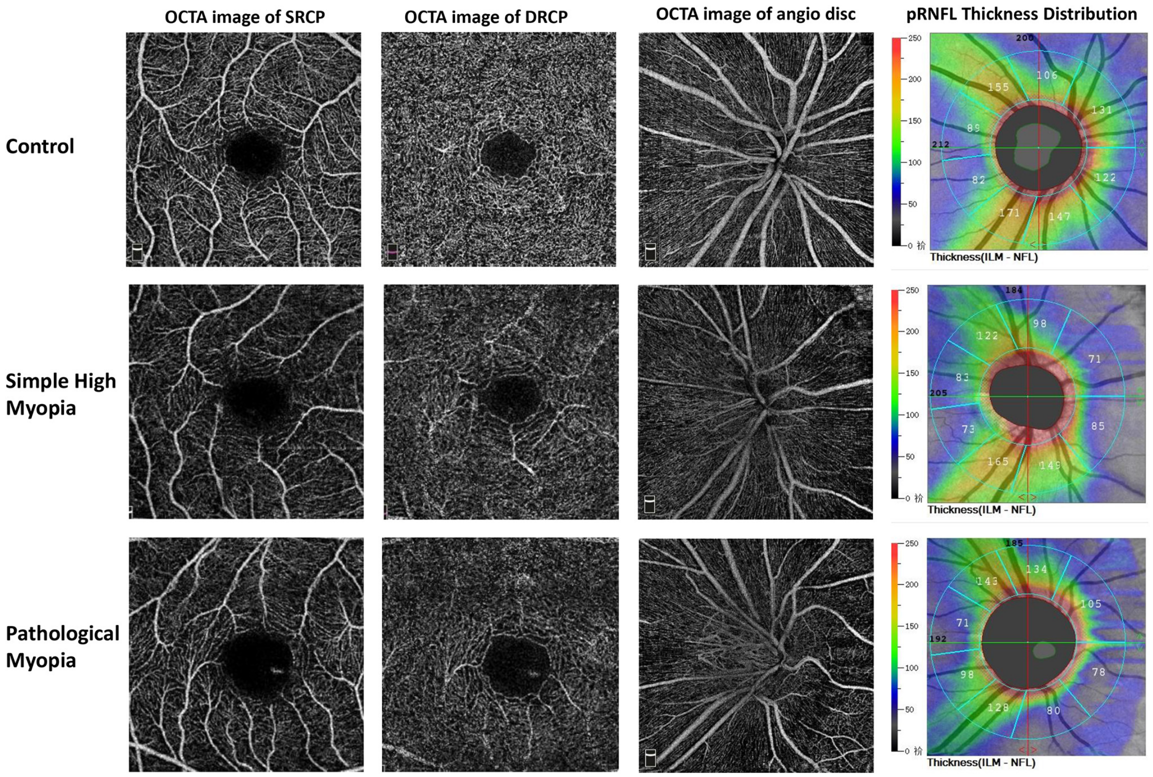

FIGURE 1 | Representative OCT-A images of the control, simple high myopia, and pathological myopia. OCT-A, optical coherence tomography angiography; SRCP, superficial retinal capillary plexus; DRCP, deep retinal capillary plexus; pRNFL, peripapillary retinal nerve fiber layer.

greater than 0.800, while AUCs of RPC density in other five sectors were less than 0.800 (**Figure 2B,C**).

Association of Radial Peripapillary Capillary Density, Peripapillary Retinal Nerve Fiber Layer Thickness, and Macular Retinal Microvascular Density With Best-Corrected Visual Acuity

While doing the associated analysis, we included only the global data instead of data from the respective eight (or four) sectors. In univariate regression with the BCVA as the outcome, the eyes with less RPC density ($p < 0.001$), thinner pRNFL ($p < 0.001$), less SRCP and DRCP density (both $p < 0.001$), and longer AL ($p < 0.001$) would show worse BCVA (**Table 5**). The parameters with p-values less than 0.05 in univariate regression (**Table 5**) would be further included for the multivariate regression analysis. As a result, worse BCVA was associated with less RPC density (standardized coefficient = −0.211, $p = 0.026$), less SRCP density (standardized coefficient = −0.191, $p = 0.043$), and longer AL (standardized coefficient = 0.341, $p = 0.001$; **Table 5**).

TABLE 2 | The radial peripapillary capillary (RPC) density (%) among the control, simple high myopia, and pathological myopia.

	Control	Simple high myopia	Pathological myopia	p^*	p_1	p_2	p_3
Global	52.60 ± 2.42	51.03 ± 3.47	44.15 ± 2.86	**<0.001**	**0.013**	**<0.001**	**<0.001**
Nasal-superior	49.22 ± 3.81	46.81 ± 5.75	41.97 ± 6.98	**<0.001**	0.089	**<0.001**	**0.003**
Nasal-inferior	47.39 ± 4.50	45.61 ± 6.20	41.08 ± 5.68	**<0.001**	0.120	**<0.001**	**0.003**
Inferior-nasal	51.70 ± 4.23	49.41 ± 5.19	44.96 ± 7.18	**<0.001**	0.100	**<0.001**	**0.005**
Inferior-tempo	56.71 ± 3.98	55.20 ± 6.92	48.46 ± 8.39	**<0.001**	0.245	**<0.001**	**<0.001**
Tempo-inferior	54.26 ± 3.63	54.53 ± 4.68	45.04 ± 7.67	**<0.001**	0.786	**<0.001**	**<0.001**
Tempo-superior	57.60 ± 3.15	56.20 ± 6.22	44.24 ± 10.43	**<0.001**	0.282	**<0.001**	**<0.001**
Superior-tempo	55.62 ± 3.41	55.53 ± 4.23	47.33 ± 7.05	**<0.001**	0.921	**<0.001**	**<0.001**
Superior-nasal	51.33 ± 4.14	49.69 ± 5.72	44.65 ± 5.85	**<0.001**	0.127	**<0.001**	**<0.001**

p^*, p-value of ANOVA among the three groups; p_1, p-value between the control group and simple high myopia; p_2, p-value between the control group and pathological myopia; p_3, p-value between the simple high myopia and pathological myopia. The bold values just means the P-value less than 0.05.

TABLE 3 | The peripapillary retinal nerve fiber layer (pRNFL) thickness (μm) among the control, simple high myopia, and pathological myopia.

	Control	Simple high myopia	Pathological myopia	p^*	p_1	p_2	P_3
Global	121.7 ± 12.9	117.7 ± 16.6	109.8 ± 19.3	**0.030**	0.217	**0.008**	0.063
Nasal-superior	114.3 ± 18.0	111.2 ± 30.7	102.1 ± 36.5	0.297	0.891	0.452	0.711
Nasal-inferior	95.46 ± 20.2	94.83 ± 31.0	94.21 ± 33.6	0.986	0.913	0.874	0.934
Inferior-nasal	154.8 ± 25.8	130.7 ± 24.2	117.9 ± 37.7	**<0.001**	**<0.001**	**0.002**	0.443
Inferior-tempo	154.1 ± 21.1	153.4 ± 26.2	140.0 ± 42.5	0.151	0.998	0.456	0.506
Tempo-inferior	76.7 ± 13.7	90.9 ± 19.0	97.7 ± 46.8	**0.003**	**0.017**	**0.008**	0.930
Tempo-superior	85.9 ± 15.8	92.0 ± 14.9	91.2 ± 34.1	0.300	0.167	0.899	1.000
Superior-tempo	151.0 ± 19.8	147.5 ± 22.8	136.4 ± 36.2	0.093	0.798	0.279	0.505
Superior-nasal	149.3 ± 29.6	127.9 ± 26.7	112.6 ± 37.1	**<0.001**	**0.002**	**<0.001**	0.143

p^*, p-value of ANOVA among the three groups; p_1, p-value between the control group and simple high myopia; p_2, p-value between the control group and pathological myopia; p_3, p-value between the simple high myopia and pathological myopia. The bold values just means the P-value less than 0.05.

TABLE 4 | The macular retinal microvascular density (%) among the control, simple high myopia, and pathological myopia.

	Control	Simple high myopia	Pathological myopia	p^*	p_1	p_2	p_3
SRCP							
Global	51.5 ± 4.2	48.9 ± 4.2	43.4 ± 6.4	**<0.001**	**0.017**	**<0.001**	**<0.001**
Nasal	50.5 ± 5.3	47.8 ± 5.1	41.0 ± 8.6	**<0.001**	0.070	**<0.001**	**<0.001**
Inferior	50.8 ± 5.3	48.8 ± 4.5	44.0 ± 5.4	**<0.001**	0.152	**<0.001**	**0.002**
Tempo	51.9 ± 3.7	48.4 ± 4.5	42.8 ± 7.1	**<0.001**	**0.002**	**<0.001**	**<0.001**
Superior	53.0 ± 4.0	50.6 ± 4.1	45.8 ± 8.6	**<0.001**	0.069	**<0.001**	**0.002**
DRCP							
Global	55.3 ± 4.5	52.8 ± 4.3	46.5 ± 5.8	**<0.001**	**0.027**	**<0.001**	**<0.001**
Nasal	56.2 ± 4.1	54.9 ± 4.1	47.9 ± 7.1	**<0.001**	0.584	**<0.001**	**<0.001**
Inferior	53.7 ± 5.3	50.2 ± 6.0	43.1 ± 6.8	**<0.001**	**0.017**	**<0.001**	**<0.001**
Tempo	56.6 ± 4.0	54.4 ± 4.1	49.4 ± 6.7	**<0.001**	**0.045**	**<0.001**	**<0.001**
Superior	54.4 ± 5.4	51.7 ± 4.8	45.7 ± 5.3	**<0.001**	**0.022**	**<0.001**	**<0.001**

SRCP, superficial retinal capillary plexus; DRCP, deep retinal capillary plexus. p^*, p-value of ANOVA among the three groups; p_1, p-value between the control group and simple high myopia; p_2, p-value between the control group and pathological myopia; p_3, p-value between the simple high myopia and pathological myopia. The bold values just means the P-value less than 0.05.

Considering the RPC density, AL, and SRCP density might be influenced by each other in the multivariate regression result, the further multiple GEE was used to form the BCVA model. In the final BCVA model, the AL (coefficient = 0.249, $p < 0.001$), RPC density (coefficient = 0.108, $p = 0.021$), and interaction between the RPC and AL (coefficient = −0.003, $p = 0.016$) were shown (**Table 6**). Further, before the adjustment for the AL, the RPC was correlated with the BCVA ($r = -0.443$, $p < 0.001$). Even after the adjustment for the AL, the RPC was still correlated with the BCVA ($r = -0.241$, $p = 0.010$, **Figure 3**). For the respective eight sectors with the AL adjustment, the significant correlations between the RPC density and BCVA were found in tempo-inferior, tempo-superior, superior-tempo, and superior-nasal sectors ($r = -0.265$ to -0.194, $p = 0.007 \sim 0.049$).

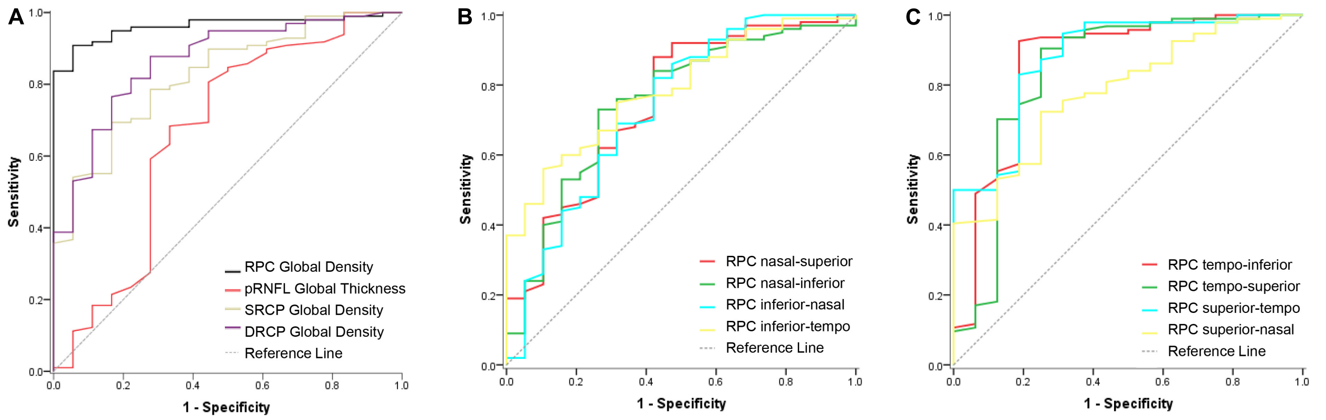

FIGURE 2 | ROC curve of the RPC density, pRNFL thickness, and macular retinal microvascular density for discriminating the pathological myopia. **(A)** The ROC curves of the RPC density, pRNFL thickness, SRCP, and DRCP density in the global area for discriminating the pathological myopia. The AUC values were 0.962, 0.675, 0.824, and 0.865, respectively. **(B)** The ROC curves of the RPC density in the four respective sectors (nasal-superior, nasal-inferior, inferior-nasal, and inferior-tempo) for discriminating the pathological myopia. The AUC values were 0.748, 0.749, 0.735, and 0.786, respectively. **(C)** The ROC curves of the RPC density in the four respective sectors (tempo-inferior, tempo-superior, superior-tempo, and superior-nasal) for discriminating the pathological myopia. The AUC values were 0.861, 0.850, 0.852, and 0.772, respectively. RPC, radial peripapillary capillary; pRNFL, peripapillary retinal nerve fiber layer; SRCP, superficial retinal capillary plexus; DRCP, deep retinal capillary plexus.

TABLE 5 | Linear regression analysis based on the BCVA as the outcome.

Parameters	Univariate regression			Multivariate regression		
	Unstandardized coefficient	Standardized coefficient	*p*	Unstandardized coefficient	Standardized coefficient	*P*
RPC	−0.014	−0.495	**<0.001**	−0.006	−0.211	**0.026**
pRNFL	−0.003	−0.382	**<0.001**	–	–	–
Optic cup-to-disc ratio	−0.132	−0.165	0.098	–	–	–
SRCP	−0.010	−0.471	**<0.001**	−0.004	−0.191	**0.043**
DRCP	−0.008	−0.361	**<0.001**	–	–	–
AL	0.033	0.592	**<0.001**	0.018	0.341	**0.001**
Age	0.002	0.164	0.073	–	–	–
Gender, male	0.002	0.009	0.926	–	–	–

RPC, radial peripapillary capillary; pRNFL, peripapillary retinal nerve fiber layer; SRCP, superficial retinal capillary plexus; DRCP, deep retinal capillary plexus; AL, axial length; BCVA, best corrected visual acuity. The bold values just means the P-value less than 0.05.

Relationship Between Radial Peripapillary Capillary Density and Axial Length

The visual impairment in the current study was determined as BCVA (logMAR) $\geq$ 0.1. The ROC curve here was used to calculate the AL cutoff value determining visual impairment. The AL cutoff value was 27.94 mm with an area under the ROC curve of 0.875.

As shown in **Figure 4A** with non-linear regression, the relationship between AL and global RPC density could be separated into two parts: for AL $<$ 25.01 mm, the global RPC density ranged from 49.20 to 57.80% with 52.76% as average; for AL $\geq$ 25.01 mm, there would be a negative correlation ($r = -0.517$, $p < 0.001$). With such non-linear regression, for an eye with an AL of 27.94 mm (the AL cutoff value for the visual impairment), the global RPC density was predicted to be approximately 48.77%. When analyzing the correlation between the AL and RPC density for the respective eight sectors with non-linear regression, the AL turning points are shown in **Figures 4B–I**.

TABLE 6 | Multivariate GEE analysis based on the BCVA as the outcome.

Parameters	Coefficient	Std. error	95% Confidence interval		*p*
			Lower	Upper	
AL	0.249	0.0705	0.111	0.388	**<0.001**
SRCP	0.076	0.0478	−0.018	0.169	0.113
RPC	0.108	0.0468	0.016	0.200	**0.021**
RPC × AL	−0.003	0.0012	−0.005	0.001	**0.016**
SRCP × AL	−0.002	0.0010	−0.004	0.0003	0.099
RPC × SRCP	−0.001	0.0005	−0.002	0.0003	0.182

AL, axial length; SRCP, superficial retinal capillary plexus; RPC, radial peripapillary capillary; BCVA, best corrected visual acuity; GEE, generalized estimating equations. The bold values just means the P-value less than 0.05.

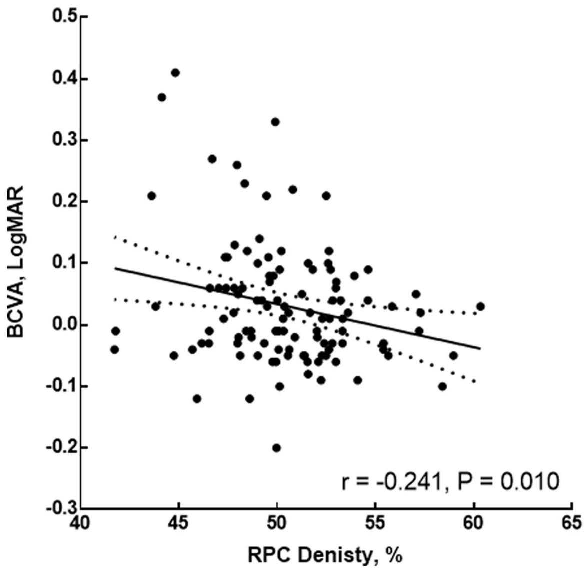

FIGURE 3 | Correlation of the RPC density and BCVA after adjustment for the AL. RPC, radial peripapillary capillary; AL, axial length; BCVA, best-corrected visual acuity.

TABLE 7 | The correlation between the macular retinal microvascular density and radial peripapillary capillary (RPC) density.

	SRCP		DRCP	
	r	***p***	***r***	***p***
Global	0.426	**<0.001**	0.418	**<0.001**
Nasal-superior	0.293	**0.001**	0.286	**0.002**
Nasal-inferior	0.267	**0.004**	0.280	**0.002**
Inferior-nasal	0.052	0.580	0.100	0.284
Inferior-tempo	0.290	**0.002**	0.292	**0.001**
Tempo-inferior	0.353	**<0.001**	0.327	**0.001**
Tempo-superior	0.413	**<0.001**	0.319	**0.001**
Superior-tempo	0.356	**<0.001**	0.342	**<0.001**
Superior-nasal	0.205	**0.027**	0.257	**0.005**

SRCP, superficial retinal capillary plexus; DRCP, deep retinal capillary plexus. The bold values just means the P-value less than 0.05.

Relationship Between Radial Peripapillary Capillary Density and Macular Retinal Microvascular Density

When analyzing the relation between the RPC density and macular retinal microvascular density, the significant correlation was found for the global parameters (SRCP, $r = 0.426$, $p < 0.001$; DRCP, $r = 0.418$, $p < 0.001$; **Table 7**). For eight respective sectors, the highest correlation coefficients between RPC density and macular retinal microvascular density were shown in tempo-inferior, tempo-superior, and superior-tempo sectors (SRCP, $r = 0.353–0.413$, $p < 0.001$; DRCP, $r = 0.319–0.342$, $p < 0.002$; **Table 7**).

DISCUSSION

In the current study, we used OCT-A to evaluate the RPC density and pRNFL thickness in pathological myopia. Previously reported peripapillary alterations in myopia were mostly consistent with our results (**Table 8**). However, most of the previous articles focused only on simple high myopia and did not include pathological myopia. The current study investigated

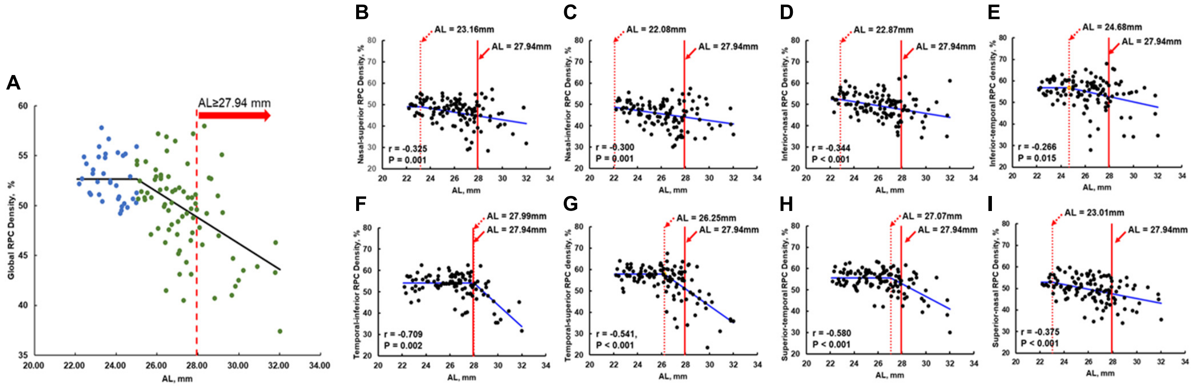

FIGURE 4 | Non-linear regression of the RPC density and the AL in global and all eight sectors. The solid red line in **(A–I)** was the AL cutoff (27.94 mm) for the visual impairment. The dashed red line in **(B–I)** indicates the RPC density flexion point along with the AL. To the left of the dashed red line, the RPC density was stable and not correlated with AL. To the right of the dashed red line, decreases in RPC density were significantly correlated with AL elongation (corresponding *r* and *p*-values were shown in the respective panels). To the right of the solid red line, the eyes were at high risk of visual impairment. **(A)** Non-linear regression of the global RPC density and the AL. **(B)** Nasal-superior RPC density vs. AL with AL flexion point as 23.16 mm. **(C)** Nasal-inferior RPC density vs. AL with AL flexion point as 22.08 mm. **(D)** Inferior-nasal RPC density vs. AL with AL flexion point as 22.87 mm. **(E)** Inferior-temporal RPC density vs. AL with AL flexion point as 24.68 mm. **(F)** Temporal-inferior RPC density vs. AL with AL flexion point as 27.99 mm. **(G)** Temporal-superior RPC density vs. AL with AL flexion point as 26.25 mm. **(H)** Superior-temporal RPC density vs. AL with AL flexion point as 27.07 mm. **(I)** Superior-nasal RPC density vs. AL with AL flexion point as 23.01 mm. RPC, radial peripapillary capillary; AL, axial length.

TABLE 8 | Summary of previous article on peripapillary alteration in myopia.

Authors	Subjects	Conclusions
Current study	Control, simple high myopia, and pathological myopia	The significant difference of the global RPC density and pRNFL thickness among the three groups
Yang et al. (2020)	Mild myopia, moderate myopia, and severe myopia with BCVA of 20/20 or better	The significant difference of the global RPC density and pRNFL thickness among the three groups
Sung et al. (2018)	Control and high myopia without pathologic alteration	No significant alteration of the pRNFL thickness but the significant alteration of RPC density was found
He et al. (2019)	Emmetropia, mild myopia, moderate myopia, and high myopia with BCVA of 20/25 or better	No significant alteration of the pRNFL thickness but the significant alteration of RPC density among the four groups was found.
Wang et al. (2016)	Emmetropia, mild myopia, moderate myopia, and high myopia without any sign of pathological myopia	The significant alteration of the pRNFL thickness and RPC density among the four groups was found
Suwan et al. (2018)	Control and myopia without glaucoma	The decreasing of the RPC density in myopia subjects but without significance.
Sung et al. (2017)	Non-high myopia and high myopia without pathological fundus	The significant difference in the RPC density between the two groups
Mo et al. (2017)	Control, simple high myopia, and pathological myopia	The significant difference of the global RPC density among the three groups

RPC, radial peripapillary capillary; pRNFL, peripapillary retinal nerve fiber layer; BCVA, best corrected visual acuity.

the alteration of peripapillary vascular density and structural thickness simultaneously in pathological myopia and analyzed their correlations with the central visual function. The reduced RPC density of pathological myopia in the current study was found as Mo et al. (2017) had reported, whereas we found that the relationship between the RPC density and AL was not as simple as Mo et al. (2017) reported and further showed the significant correlation between RPC density and BCVA. The RPC density, as peripapillary capillary density, might be more sensitive to indicate the alteration of pathological myopia and related to the central visual impairment than pRNFL thickness, especially in the temporal sectors, which was also affected by the AL. Awareness of the RPC density alteration and preventing its further decrease should be the important clinic goals for pathological myopia.

The peripapillary alterations in pathological myopia were found in our current research, especially the RPC density. The RPC density was decreased in eyes with either simple high myopia or pathological myopia eyes compared with normal eyes; moreover, the RPC density in the eyes with pathological myopia was significantly lower than in eyes with simple high myopia. Myopic eyes have less retrobulbar peripapillary blood flow and smaller vessel diameters than normal eyes (Patton et al., 2005; Benavente-Pérez et al., 2010; La Spina et al., 2016). These suggested that the RPC density may gradually decrease during the progression of normal to simple high myopia and then to pathological myopia. In addition, in eyes with pathological myopia, the RPC density was decreased in all eight sectors, demonstrating that the peripapillary perfusion was widely affected compared with isolated local alterations in different sectors.

From the ROC results of discriminating power for pathological myopia, we hypothesized that the RPC density was sensitive to indicate pathological myopia. As the straight and long vessels without frequent anastomoses, the RPC might even be affected more easily by the pathological progression than macular degeneration (Henkind, 1967). Moreover, it was described that peripapillary retinal perfusion was decreased in some high myopia without the parafoveal perfusion alteration, and pathological myopia always started from the alteration in the temporal peripapillary sector (Tokoro, 1998; Wang et al., 2016). Temporal peripapillary sectors (temporal-inferior, temporal-superior, and superior-tempo sectors) had the highest AUC when compared with other sectors. The reason might be that RPC was more around the arcuate fiber region located in the temporal peripapillary sector. To compensate for the peripapillary ischemia in pathological myopia, we speculated the vascular constriction seriously in RPC. The RPC in these sectors would be sensitive to adjust for the occurrence of pathological myopia. In addition, these temporal sectors were more related to the macular retinal microvasculature in our current study. So, the early detection of the RPC density in these sectors would be important to indicate pathological myopia.

To investigate the peripapillary alteration in pathological myopia would provide clues to the further macular degeneration and vision-threatening alteration in pathological myopia. Within the eye, loss of RPC density was related to degeneration of the retinal pigment epithelium (Tan et al., 2014). Our previous article had reported that retinal pigment epithelium thinning was correlated with the central visual function (Ye et al., 2019). It might be one of the reasons that decreasing RPC density was significantly correlated to central visual impairment. The decreasing RPC density was also associated with the macular microvascular density as well. Large blood vessels in the peripapillary region send branches to the macular region, and then reductions in RPC density would be associated with changes in macular microvascular density that could impair vision (Jonas et al., 2017; Lee et al., 2018). As we have known, the outer retina and the peripapillary area were both mainly supplied by the branches of the posterior ciliary arteries, so pull-back of the optic disc may not only result in the RPC density decreasing but also had an influence on the macular vasculature, which would explain the correlation between the RPC density and visual impairment in pathological myopia. Furthermore, because the RPC consists of straight and long vessels without frequent anastomoses, it might be affected more easily than macular vessels by the pathological progression (Henkind, 1967; Wang et al., 2016).

Axial elongation had long been considered to be the main factor for peripapillary alteration during the progression of pathological myopia. Differently, we found that the relationship between the RPC density and AL was not as simple as the previous article reported (Mo et al., 2017). In the current study, the interaction of the AL and RPC density was shown significantly in the final BCVA model. Actually, for the AL less than 25.01 mm, the axial elongation did not influence the RPC density too much from our current study. On the contrary, the patient with AL longer than 27.94 mm might have serious RPC density decreasing with visual impairment. The eyes with AL ranging from 25.01 to 27.94 mm would be at high risk of visual impairment if their AL elongated furthermore. During our daily clinic, we should pay attention to these cutoff values for pathological myopia to intervene early and avoid a worse visual prognosis. When considering the respective eight sectors, only in the temporal sectors rather than nasal sectors, the RPC density was drastically decreased with extreme axial elongation. We hypothesized that temporal RPC might be a great protective mechanism to visual impairment at the early stage of axial elongation. There might be the condition that only when up to extremely axial elongation in pathological myopia the temporal RPC density would alter significantly with serious visual impairment. Moreover, we found there was still a correlation between the RPC density and BCVA even after adjustment for the AL. It might support the idea that the alterations of the pathological myopic fundus also resulted from progressive deterioration, but not only depending on the axial elongation (Kobayashi et al., 2005).

We acknowledged some limitations in the current study. First, the sample size, especially for the pathological myopic group, was small. We intend to include more subjects in the future. In the current study, we did not correct the AL-dependent image magnification before analyzing the pRNFL thickness and RPC density. Although previous articles had found that correction of AL or not may not significantly influence the peripapillary parameters, we still intend to develop software for image magnification correction to confirm the peripapillary alteration and visual function (Moghimi et al., 2012; Liu et al., 2015). To try our best to avoid the influence of the AL in the analysis, we also adjusted the AL when doing some analysis of the correlation in the current study. Moreover, we did not do the repeatability of these parameters when doing this research. In our previous articles, we had certified the high repeatability of the macular microvascular density and structural thickness in pathological myopia with the OCT-A/OCT images, and Wang et al. (2016) had reported that the peripapillary parameters from the OCT-A images showed higher repeatability than macula (Ye et al., 2019, 2020). Based on these, we thought that there would be good repeatability of the peripapillary parameters in pathological myopia with the OCT-A images. The posterior staphylomas might be a key factor for the visual impairment in pathological myopia as well, we would like to further analyze these details in the future.

CONCLUSION

In conclusion, the current study showed peripapillary alterations in pathological myopia compared with the controls, especially the decreasing diffused RPC density and pRNFL thickness. The current results indicate that RPC density had greater discriminating power to assess pathological myopia, which might play an important role in the further macular alteration and central visual function in these pathological myopic patients. Moreover, the RPC density was associated with BCVA, and this relationship was affected by AL. Quantitative analysis of the peripapillary microvasculature would help clarify the potential pathophysiological mechanism of progression in pathological myopia.

DATA AVAILABILITY STATEMENT

The raw data supporting the conclusions of this article will be made available by the authors, without undue reservation.

ETHICS STATEMENT

The studies involving human participants were reviewed and approved by the Ethics Committee of Wenzhou Medical University. The patients/participants provided their written informed consent to participate in this study.

AUTHOR CONTRIBUTIONS

JY, FL, and YS conceived and designed the study. JY, JL, and WC performed the experiments. JY, MS, and RZ wrote and modified the manuscript. All authors read and approved the manuscript.

FUNDING

This study was supported by the Natural Science Foundation of Zhejiang Province (Grant No. LQ21H120007).

REFERENCES

Benavente-Pérez, A., Hosking, S. L., Logan, N. S., and Broadway, D. C. (2010). Ocular blood flow measurements in healthy human myopic eyes. *Graefes Arch. Clin. Exp. Ophthalmol.* 248, 1587–1594. doi: 10.1007/s00417-010-1407-9

Fang, Y., Yokoi, T., Nagaoka, N., Shinohara, K., Onishi, Y., Ishida, T., et al. (2018). Progression of myopic maculopathy during 18-Year Follow-up. *Ophthalmology* 125, 863–877. doi: 10.1016/j.ophtha.2017.12.005

Garway-Heath, D. F., Poinoosawmy, D., Fitzke, F. W., and Hitchings, R. A. (2000). Mapping the visual field to the optic disc in normal tension glaucoma eyes. *Ophthalmology* 107, 1809–1815. doi: 10.1016/s0161-6420(00)00284-0

Hayashi, K., Ohno-Matsui, K., Shimada, N., Moriyama, M., Kojima, A., Hayashi, W., et al. (2010). Long-term pattern of progression of myopic maculopathy: a natural history study. *Ophthalmology* 117, 1595–1611, 1611.e1–4. doi: 10.1016/j.ophtha.2009.11.003

He, J., Chen, Q., Yin, Y., Zhou, H., Fan, Y., Zhu, J., et al. (2019). Association between retinal microvasculature and optic disc alterations in high myopia. *Eye (Lond.)* 33, 1494–1503. doi: 10.1038/s41433-019-0438-7

Henkind, P. (1967). Symposium on glaucoma: joint meeting with the National society for the prevention of blindness. New observations on the radial peripapillary capillaries. *Invest. Ophthalmol.* 6, 103–108.

Holden, B. A., Fricke, T. R., Wilson, D. A., Jong, M., Naidoo, K. S., Sankaridurg, P., et al. (2016). Global prevalence of myopia and high myopia and temporal trends from 2000 through 2050. *Ophthalmology* 123, 1036–1042. doi: 10.1016/j.ophtha.2016.01.006

Jonas, J. B., Fang, Y., Weber, P., and Ohno-Matsui, K. (2018). Parapapillary gamma and delta zones in high myopia. *Retina* 38, 931–938. doi: 10.1097/IAE.0000000000001650

Jonas, J. B., Ohno-Matsui, K., Jiang, W. J., and Panda-Jonas, S. (2017). Bruch membrane and the mechanism of myopization: a new theory. *Retina* 37, 1428–1440. doi: 10.1097/IAE.0000000000001464

Jonas, J. B., Wang, Y. X., Zhang, Q., Fan, Y. Y., Xu, L., Wei, W. B., et al. (2016). Parapapillary gamma zone and axial elongation-associated optic disc rotation: the Beijing Eye Study. *Invest. Ophthalmol. Vis. Sci.* 57, 396–402. doi: 10.1167/iovs.15-18263

Kobayashi, K., Ohno-Matsui, K., Kojima, A., Shimada, N., Yasuzumi, K., Yoshida, T., et al. (2005). Fundus characteristics of high myopia in children. *Jpn. J. Ophthalmol.* 49, 306–311. doi: 10.1007/s10384-004-0204-6

La Spina, C., Corvi, F., Bandello, F., and Querques, G. (2016). Static characteristics and dynamic functionality of retinal vessels in longer eyes with or without pathologic myopia. *Graefes Arch. Clin. Exp. Ophthalmol.* 254, 827–834.

Lee, K. M., Choung, H. K., Kim, M., Oh, S., and Kim, S. H. (2018). Positional change of optic nerve head vasculature during axial elongation as evidence of lamina cribrosa shifting: boramae myopia cohort study report 2. *Ophthalmology* 125, 1224–1233. doi: 10.1016/j.ophtha.2018.02.002

Liu, H. H., Xu, L., Wang, Y. X., Wang, S., You, Q. S., and Jonas, J. B. (2010). Prevalence and progression of myopic retinopathy in Chinese adults: the Beijing Eye Study. *Ophthalmology* 117, 1763–1768. doi: 10.1016/j.ophtha.2010.01.020

Liu, X., Shen, M., Yuan, Y., Huang, S., Zhu, D., and Ma, Q. (2015). Macular thickness profiles of intraretinal layers in myopia evaluated by ultrahigh-resolution optical coherence tomography. *Am. J. Ophthalmol.* 160, 53–61.e2. doi: 10.1016/j.ajo.2015.03.012

Mo, J., Duan, A., Chan, S., Wang, X., and Wei, W. (2017). Vascular flow density in pathological myopia: an optical coherence tomography angiography study. *BMJ Open* 7:e013571. doi: 10.1136/bmjopen-2016-013571

Moghimi, S., Hosseini, H., Riddle, J., Lee, G. Y., Bitrian, E., Giaconi, J., et al. (2012). Measurement of optic disc size and rim area with spectral-domain OCT and scanning laser ophthalmoscopy. *Invest. Ophthalmol. Vis. Sci.* 53, 4519–4530. doi: 10.1167/iovs.11-8362

Nakazawa, M., Kurotaki, J., and Ruike, H. (2008). Longterm findings in peripapillary crescent formation in eyes with mild or moderate myopia. *Acta Ophthalmol.* 86, 626–629. doi: 10.1111/j.1600-0420.2007.01139.x

Ohno-Matsui, K., Kawasaki, R., Jonas, J. B., Cheung, C. M., Saw, S. M., Verhoeven, V. J., et al. (2015). International photographic classification and grading system for myopic maculopathy. *Am. J. Ophthalmol.* 159, 877–883.e7. doi: 10.1016/j.ajo.2015.01.022

Patton, N., Maini, R., Macgillivary, T., Aslam, T. M., Deary, I. J., and Dhillon, B. (2005). Effect of axial length on retinal vascular network geometry. *Am. J. Ophthalmol.* 140, 648–653. doi: 10.1016/j.ajo.2005.04.040

Shimada, N., Ohno-Matsui, K., Nishimuta, A., Tokoro, T., and Mochizuki, M. (2007). Peripapillary changes detected by optical coherence tomography in eyes with high myopia. *Ophthalmology* 114, 2070–2076.

Sung, M. S., Lee, T. H., Heo, H., and Park, S. W. (2017). Clinical features of superficial and deep peripapillary microvascular density in healthy myopic eyes. *PLoS One* 12:e0187160. doi: 10.1371/journal.pone.0187160

Sung, M. S., Lee, T. H., Heo, H., and Park, S. W. (2018). Association between optic nerve head deformation and retinal microvasculature in high myopia. *Am J Ophthalmol.* 188, 81–90.

Suwan, Y., Fard, M. A., Geyman, L. S., Tantraworasin, A., Chui, T. Y., Rosen, R. B., et al. (2018). Association of myopia with peripapillary perfused capillary density in patients with glaucoma: an optical coherence tomography angiography study. *JAMA Ophthalmol.* 136, 507–513. doi: 10.1001/jamaophthalmol.2018.0776

Tan, C. S., Cheong, K. X., Lim, L. W., and Li, K. Z. (2014). Topographic variation of choroidal and retinal thicknesses at the macula in healthy adults. *Br. J. Ophthalmol.* 98, 339–344.

Tokoro, T. (1998). "*Explanatory factors of Chorioretinal atrophy*," in *Atlas of Posterior Fundus Changes in Pathologic Myopia*, ed. T. Tokoro (Tokyo: Springer).

Wang, X., Kong, X., Jiang, C., Li, M., Yu, J., and Sun, X. (2016). Is the peripapillary retinal perfusion related to myopia in healthy eyes? A prospective comparative study. *BMJ Open* 6:e010791. doi: 10.1136/bmjopen-2015-010791

Wong, C. W., Phua, V., Lee, S. Y., Wong, T. Y., and Cheung, C. M. (2017). Is choroidal or scleral thickness related to myopic macular degeneration? *Invest. Ophthalmol. Vis. Sci.* 58, 907–913. doi: 10.1167/iovs.16-20742

Yang, D., Cao, D., Zhang, L., Yang, C., Lan, J., Zhang, Y., et al. (2020). Macular and peripapillary vessel density in myopic eyes of young Chinese adults. *Clin. Exp. Optom.* 103, 830–837. doi: 10.1111/cxo.13047

Ye, J., Shen, M., Huang, S., Fan, Y., Yao, A., Pan, C., et al. (2019). Visual acuity in pathological myopia is correlated with the photoreceptor myoid and ellipsoid zone thickness and affected by choroid thickness. *Invest. Ophthalmol. Vis. Sci.* 60, 1714–1723. doi: 10.1167/iovs.18-26086

Ye, J., Wang, M., Shen, M., Huang, S., Xue, A., Lin, J., et al. (2020). Deep retinal capillary plexus decreasing correlated with the outer retinal layer alteration and visual acuity impairment in pathological myopia. *Invest. Ophthalmol. Vis. Sci.* 61:45. doi: 10.1167/iovs.61.4.45

Conflict of Interest: The authors declare that the research was conducted in the absence of any commercial or financial relationships that could be construed as a potential conflict of interest.